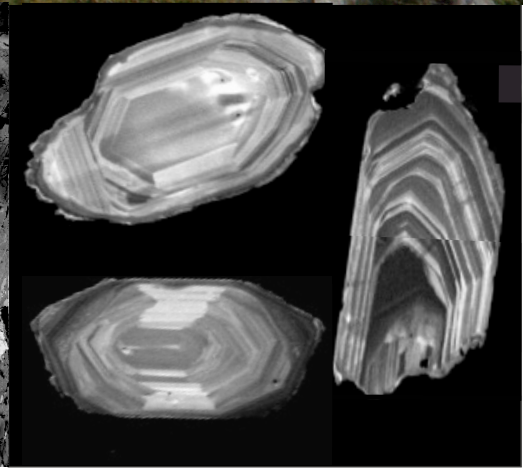
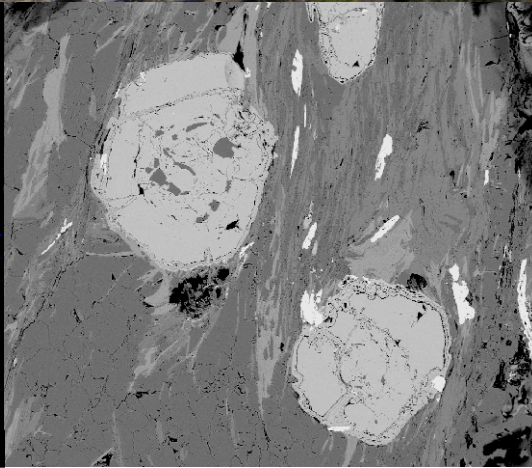
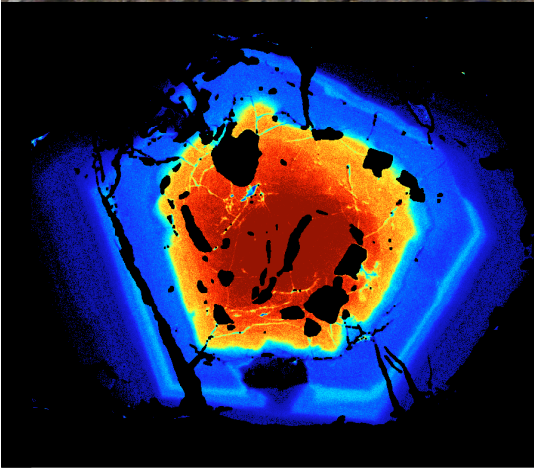
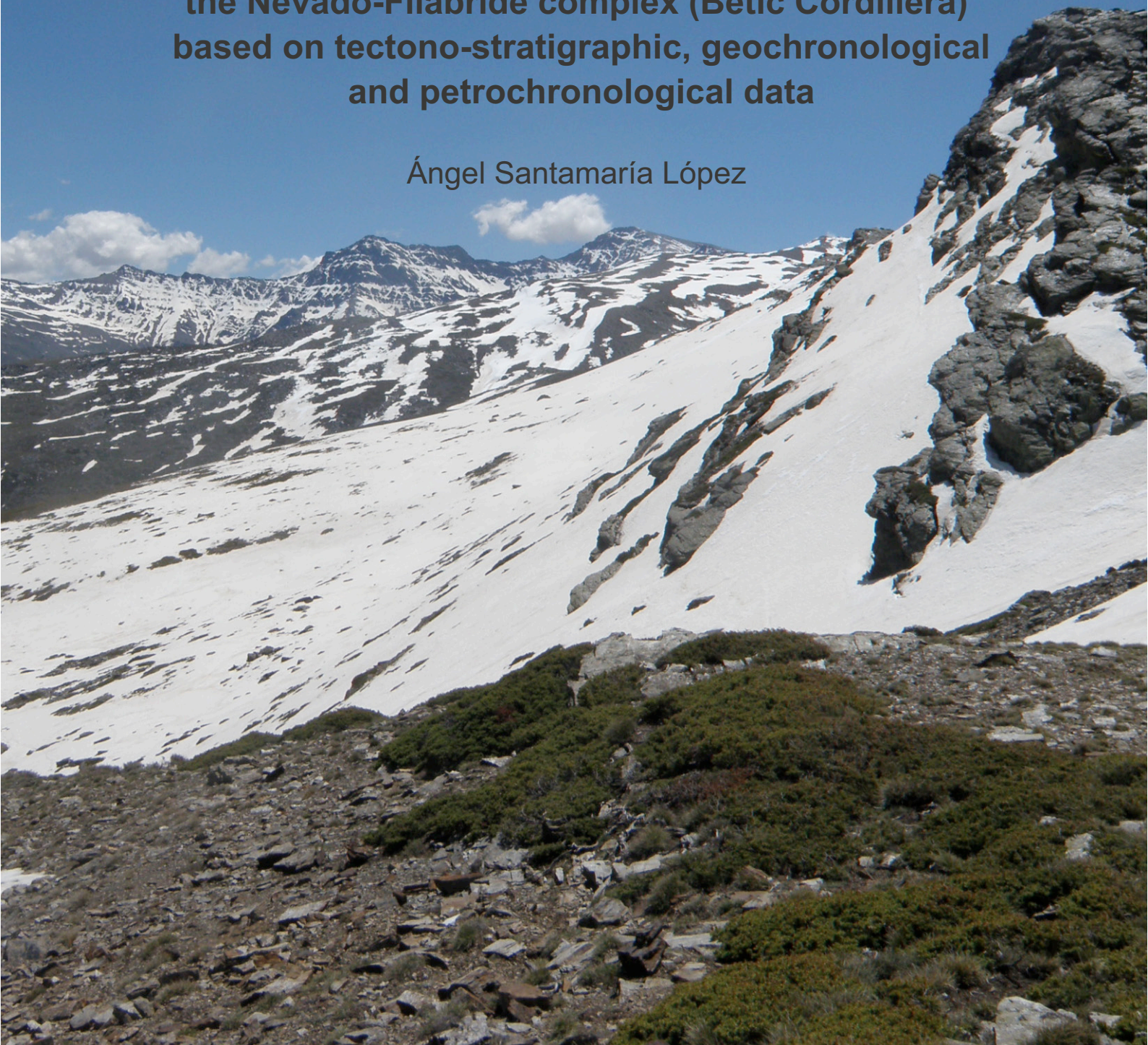




Discussion on the division of the Nevado-Filábride complex (Betic Cordillera) based on tectono-stratigraphic, geochronological and petrochronological data

Ángel Santamaría López



Editor: Universidad de Granada. Tesis Doctorales
Autor: Ángel Santamaría López
ISBN: 978-84-1306-171-9
URI: <http://hdl.handle.net/10481/55476>

Agradecimientos

Esta Tesis Doctoral y todo lo aprendido mientras la llevaba a cabo se lo debo a muchas personas que han estado a lo largo del camino prestándome su ayuda, consejo y confianza. Es complicado reconocerles todo el mérito en tan pocas líneas. Espero que no me lo tengan demasiado en cuenta.

Hay muchas cosas que le debo a mi Director de Tesis, Carlos Sanz de Galdeano. Ha tenido a bien ayudarme en lo científico, ofrecerme su tiempo y poner a mi disposición la grandísima enciclopedia geológica (y botánica) que es su cabeza. Siento que siempre ha buscado guiarme en el camino para que no tropezara (demasiado). Nunca podré terminar de agradecerle su esfuerzo conmigo.

A María Dolores Ruiz de la Universidad de Málaga le agradezco la confianza depositada en mí para llevar a cabo la Tesis. Ella fue la que me inició y encaminó en los senderos más tortuosos de la geología metamórfica.

Debo agradecer a Juan Ignacio Soto de la Universidad de Granada su labor como Tutor durante mi permanencia en el Programa de Doctorado. Sin duda su predisposición para ayudarme en la siempre desagradecida burocracia ha sido completa.

A Pierre Lanari de la Universidad de Berna, por su amabilidad e infinita disponibilidad. A él le agradezco su acogida en Berna, su guía y su mano siempre dispuesta a ayudarme. Sin su ayuda, esta Tesis no se habría podido llevar a cabo.

Sin duda debo mostrar mi agradecimiento a varios doctores del departamento de Química Inorgánica, Cristalografía y Mineralogía Universidad de Málaga. Muchas gracias por la ayuda y acogida a Pedro Maireles, director del departamento. También a María Bentabol por su amabilidad, y a María Dolores Rodríguez por su afecto. En especial me gustaría recordar a Paco Franco en estas líneas. Paco ha sido no solo un maravilloso ejemplo de profesor y científico, si no que desde el primer momento no dudó en entregarse también como un magnífico amigo.

También quiero dar las gracias a varios investigadores de la Universidad de Granada que han contribuido a enriquecer mi Tesis y mi estancia en el aquí. A Jesús Galindo por el tiempo que ha dedicado a aportarme su visión del estudio, además de su siempre apreciado consejo y ayuda. A Patricia Ruano que continuamente me ha sabido escuchar y animar desde el cariño. A Domingo Aerden le agradezco su interés por mi trayectoria y su disponibilidad por aportarme su conocimiento del Nevado-Filábride. Asimismo, agradezco a Fernando Nieto su amabilidad y ayuda. También agradezco al resto de miembros del Departamento de Geodinámica de la Universidad de Granada su interés por mi investigación, en especial a Antonio Jabaloy, Guillermo Booth-Rea, José Miguel Azañón y Manuel López Chicano.

Gracias a Jörg Hermann y a Daniela Rubatto de la Universidad de Berna, por sus estimulantes comentarios sobre este estudio, y a los compañeros investigadores con los que conviví durante la estancia.

Al personal del Centro de Instrumentación Científica de la Universidad de Granada y de los Servicios Centrales de Apoyo a la Investigación de la Universidad de Málaga, que me han facilitado mi trabajo en los diferentes instrumentos analíticos. En particular agradezco a M^a Pilar González Montero del Departamento de Mineralogía y Petrología, su ayuda durante el procesado de los datos de circones.

Gracias a Manuel, Irene, Lourdes, Juampe, Inma, Fran, Idaira, Casto, Lara, Yashmina, Pedro, Ángela, Cristina y Víctor. Ellos no solo han sido compañeros de fatigas de la tesis, si no verdaderos amigos. Gracias a todos por acoger al Nuevo.

Para mostrar mi agradecimiento a mis padres, María Luisa, y Miguel, y mi novia, Carlota, ninguna línea es suficiente. Esperar cada semana hasta el viernes y hacerse fuerte una y otra vez cada domingo sé que ha sido más que duro. Todo lo bueno que esta tesis y yo mismo podemos tener nunca podría haber llegado a existir sin vuestro amor y paciencia.

A todos, de nuevo, muchas gracias por participar en mi formación como investigador.

Esta Tesis Doctoral ha sido financiada por el proyecto CGL 2012-31872 (Ministerio de Economía y Competitividad), el proyecto DAMAGE (AEI/FEDER CGL 2016-80687-R), el Departamento de Química Inorgánica, Cristalografía y Mineralogía Universidad de Málaga, y el Departamento de Geodinámica de la Universidad de Granada.

Abstract

The Nevado-Filábride metamorphic complex is the lowermost part of the Internal zone of the Betic Cordillera (Spain). The complex exhibits a succession of metasediments, orthogneisses and metabasites. Debate still surrounds the age of the rocks, the petrochronological evolution of the complex, and several internal divisions proposed in the literature. This Ph.D. Thesis presents a study concerning the Nevado-Filábride complex based on different methodological approaches, with the objective to determine the validity of the previously proposed divisions.

In the first part of the study, new cartography is proposed for key areas of the complex. The cartography is supported by petrological and mineralogical descriptions of the different schist types existing in the complex. Three lithological formations were identified: the Dark schists Fm in the lower part, the Tahal Fm, and the overlying Schists and marbles Fm. The contact between these formations is stratigraphic, characterized by transitional lithological variations.

U-Pb dating (SHRIMP) was carried out on inherited detrital zircons. The eight dated samples pertain to the lower and upper part of the complex. The youngest age populations in the majority of the samples are Carboniferous. According to the results, the most probable maximum age of deposition of the Dark schists Fm is estimated to be 349.1 ± 1.6 . The most probable maximum age of deposition for the upper part of the complex (Tahal and Schists and marbles Fms) is 334.6 ± 2.9 Ma. The detrital zircon age patterns in most of the studied samples provided common age populations at ca. 480-615 Ma (Cambrian-Ediacaran), ca. 910-1010 Ma (Tonian-Stenian) and ca. 1800-2000 Ma (Orosirian). These age populations are similar to those found in the Cantabrian zone (Iberian Massif) and the Maláguide complex (Betic Cordillera). Hence the results presented in this thesis agree with recent paleogeographic interpretations that consider the Nevado-Filábride complex as part of the south Iberian paleomargin.

Five garnet-bearing schists were investigated to constrain and compare the shape of the P-T paths recorded by the lower and the upper parts of the complex. Quantitative compo-

sitional mapping of garnet was combined with iterative thermodynamic models for garnet and phengite. The resulting P-T trajectories suggest that the upper and lower parts of the complex exhibit similar clockwise P-T path geometries during Alpine metamorphism, but under slightly different conditions. Garnet nucleation took place at high-pressure and low-temperature conditions, ranging ~16 kbar and ~480°C in the Dark schists Fm; ~17.5 kbar and ~490°C in the Tahal Fm; and ~18 kbar and ~520°C in the Schists and marbles Fm. All the samples record a temperature increase of 70-100°C without any significant change in pressure, followed by a stage of isothermal decompression. The garnet rims reflect a high-temperature and low-pressure stage dated at ~13 Ma using allanite U-Th-Pb geochronology (LA-ICP-MS). It is therefore proposed that the isothermal decompression was triggered by slab break-off of the subducting slab. The isothermal decompression also supports rapid exhumation of the Nevado-Filábride rocks. The Nevado-Filábride complex was eventually accommodated below the Alpujárride complex (Betic Cordillera) during the final step of exhumation, describing linear cooling.

The stratigraphic contacts between formations suggest a continuous sequence rather than a tectonically divided complex. This is in line with the detrital zircon data showing a progression from older age populations in the lower part of the complex to younger age populations in the upper part. Additionally, the similarity of the P-T trajectories traced by the three formations implies all three were already closely related during the burial and exhumation stages.

Resumen

El complejo metamórfico Nevado-Filábride constituye la parte inferior de la Zona Interna de la Cordillera Bética (España). El complejo presenta una sucesión de metasedimentos, ortogneises y metabasitas. Existe un debate en torno a la edad de las rocas, la evolución petrocronológica del complejo y su división interna. En esta Tesis Doctoral se presenta un estudio sobre el complejo Nevado-Filábride basado en diferentes aproximaciones metodológicas, con el objetivo de determinar la validez de las divisiones previamente propuestas.

En la primera parte de la tesis se propone una nueva cartografía de áreas clave del complejo. La cartografía está apoyada por descripciones petrológicas y mineralógicas de los diferentes tipos de esquistos existentes en el complejo. Tres formaciones litológicas se han identificado, de abajo arriba: la Formación de Esquistos oscuros, la Formación de Tahal y la Formación de Esquistos y Mármoles. El contacto entre estas formaciones es estratigráfico y caracterizado por una variación transicional entre litologías.

Se ha llevado a cabo una datación de U-Pb de circones detríticos heredados mediante SHRIMP en esquistos de las partes baja y alta del complejo. Las edades máximas más jóvenes estimadas en la mayoría de las muestras son carboníferas. De acuerdo a los resultados, la edad máxima de depósito más probable para el protolito de la formación de Esquistos oscuros es $349,1 \pm 1,6$ Ma. La edad máxima de depósito del protolito de la parte superior del complejo (Formaciones Tahal y de Esquistos y mármoles) se estimó en $334,6 \pm 2,9$ Ma. Los patrones de edades de los circones detríticos en la mayoría de las muestras proporcionan poblaciones comunes en ca. 480-615 Ma (Cámbrico-Ediacarico), ca. 910-1010 Ma (Tónico-Esténico) y ca. 1800-2000 Ma (Orosírico). Estas poblaciones de edad son similares a las que se han encontrado en la Zona Cantábrica del Macizo Ibérico y el Complejo Maláguide (Cordillera Bética).

Cinco muestras de esquistos con granates han sido investigadas para determinar y comparar las trayectorias de presión y temperatura de las partes baja y alta del complejo. Para ello se combinaron mapas composicionales cuantitativos de granate con un modelado ite-

rativo de granate y fengita. Los resultados sugieren que las partes baja y alta del complejo describieron trayectorias horarias con una geometría similar durante el metamorfismo alpino que afectó al complejo. Sin embargo las condiciones de presión y temperatura fueron ligeramente diferentes entre las dos partes. En la Formación de Esquistos oscuros, la nucleación de granate se produjo a ~16 kbar y ~480°C; a ~17,5 kbar y ~490°C en la Formación Tahal; y a ~18 kbar y ~520°C en la Formación de Esquistos y Mármoles. Todas las muestras sufrieron un incremento de temperatura de entre 70 a 100 °C sin un cambio significativo de presión, seguido de una etapa de descompresión isoterma. Los bordes de los granates estudiados se formaron en una etapa de baja presión y alta temperatura. Esta etapa se produjo, de acuerdo a la datación con alanita mediante LA-ICP-MS, hace ~13 Ma. En la Tesis Doctoral se propone que la descompresión isoterma fue desencadenada por la rotura de la lámina subducida. La descompresión isoterma, además, apunta a una rápida exhumación de las rocas del Nevado-Filábride tras la rotura de la lámina. Posteriormente el complejo se acomodó debajo del complejo Alpujarride (Cordillera Bética) durante la etapa final de la exhumación.

Los contactos estratigráficos entre las formaciones sugieren una secuencia continua en vez de una división en unidades tectónicas del complejo. Esto está en la línea de los resultados obtenidos de la datación de circones detríticos, que muestra una progresión desde poblaciones de edad más antiguas en la parte inferior del complejo, y más jóvenes en la parte superior. Además, la similitud entre las trayectorias de presión temperatura entre las formaciones implica que las tres se encontraban estrechamente cercanas durante los eventos de subducción y exhumación.

Index

	<i>Page</i>
<i>Chapter 1: Introduction</i>	1
<i>Chapter 2: Regional setting and background</i>	5
2.1. The Betic Cordillera	5
2.2. The Internal Zone division	7
2.3. The Nevado-Filábride complex	9
2.3.1. Division	9
2.3.2. Lithological succession	11
2.3.2.1. The Dark schists formation	11
2.3.2.2. The Tahal formation.	12
2.3.2.3. The Schists and marbles formation	12
2.3.2.4. Gneisses and metabasites in the Nevado-Filábride complex	12
2.3.3. Metamorphism in the Nevado-Filábride complex	13
2.3.3.1. Metamorphism P-T constraints	13
2.3.3.2. Metamorphism age constraints	15
2.3.4. Nevado-Filábride complex structure	16
2.3.5. Nevado-Filábride complex age constraints	17
2.3.6. Paleogeographic reconstructions of the Nevado-Filábride complex	19
2.3.7. The role of the Nevado-Filábride complex in the Betic Cordillera tectonic configuration	20
<i>Chapter 3: Methodology</i>	23
3.1. Introduction	23
3.2. SHRIMP U-Pb detrital zircon dating	23
3.3. Metamorphic P-T conditions	25
3.3.1. Petrography	25
3.3.2. Bulk rock composition	25
3.3.3. Quantitative compositional mapping on garnet	26
3.3.4. Phase equilibria modelling	27
3.3.5. Th-U-Pb dating in allanites by LA-ICP-MS	30

	<i>Page</i>
<i>Chapter 4: Description on the lithological succession</i>	31
4.1. Introduction	31
4.2. Western part of Sierra Nevada	32
4.2.1. Previous proposed divisions	34
4.2.2. Lithological succession	39
4.2.2.1. Dark schists Fm	39
4.2.2.2. Tahal Fm	40
4.2.2.3. Schists and marbles Fm	41
4.3. Central part of Sierra Nevada	43
4.3.1. Previous proposed divisions	43
4.3.2. Lithological succession	43
4.3.2.1. Dark schists Fm	45
4.3.2.2. Tahal Fm	46
4.4. Central part of Sierra de los Filabres.	47
4.4.1. Previous proposed divisions	47
4.4.2. Lithological succession	49
4.4.2.1. Dark schists Fm	49
4.4.2.2. Tahal Fm	50
4.5. Eastern part of Sierra de los Filabres.	51
4.5.1. Previous proposed divisions	52
4.5.2. Lithological succession	52
4.5.2.1. Tahal Fm	52
4.5.2.2. Schists and marbles Fm	52
4.6. Summary and conclusions	54
<i>Chapter 5: SHRIMP U-Pb detrital zircon dating</i>	59
5.1. Introduction	59
5.2. Description and localization of schist samples	61
5.3. Zircon morphology and inclusions	61
5.3.1. Zircon morphology	61
5.3.2. Deciphering the origin of zircons	63
5.3.3. Description of zircon inclusions	65

	<i>Page</i>
5.4. Geochronology results	67
5.4.1. Lower part of the complex	68
5.4.1.1. Sample SF-1 $^{206}\text{Pb}/^{238}\text{U}$ age populations	68
5.4.1.2. Sample RA-1 $^{206}\text{Pb}/^{238}\text{U}$ age populations	68
5.4.1.3. Sample RA-2 $^{206}\text{Pb}/^{238}\text{U}$ age populations	68
5.4.1.4. Sample VE-1 $^{206}\text{Pb}/^{238}\text{U}$ age populations	68
5.4.1.5. Sample VE-2 $^{206}\text{Pb}/^{238}\text{U}$ age populations	69
5.4.2. Upper part of the complex	70
5.4.2.1. Sample SF-2 $^{206}\text{Pb}/^{238}\text{U}$ age populations	70
5.4.2.2. Sample RA-3 $^{206}\text{Pb}/^{238}\text{U}$ age populations	70
5.4.2.3. Sample VE-3 $^{206}\text{Pb}/^{238}\text{U}$ age populations	71
5.5. Discussion on the geochronology results	71
5.5.1. Age of the deposition of the protolith of the schists	71
5.5.2. Interpretation of older age populations and similarity between the upper and lower parts of the complex	72
5.5.3. Comparison with previous dating. Geological implications	73
5.5.3.1. Lower part of the complex	73
5.5.3.2. Upper part of the complex	73
5.5.3.3. Interval of sedimentation for the protolith of the schists	74
5.6. Origin of inclusions	76
5.6.1. Primary inclusions	76
5.6.2. Secondary inclusions	77
<i>Chapter 6: Conditions of metamorphism</i>	79
6.1. Introduction	79
6.2. Quantitative petrography	80
6.2.1. Mineral assemblages	80
6.2.2. Microstructures	82
6.2.3. Mineral compositions and bulk rock compositions	83
6.3. Results	88
6.3.1. Compositional zoning of garnet	88
6.3.2. Phase equilibria	93

	<i>Page</i>
6.3.3. Allanite dating	96
6.4. Discussion	97
6.4.1. Phase equilibria modelling and quality of predictions	97
6.4.2. Comparison between samples	99
6.4.3. Petrochronology	101
6.4.4. Comparison with literature data	103
6.4.4.1. Dark schists Fm	103
6.4.4.2. Tahal Fm	104
6.4.4.3. Schists and marbles Fm	104
6.4.4.4. Summary	104
<i>Chapter 7: General discussion</i>	107
7.1. Introduction	107
7.2. The paleogeographic provenance of the Nevado-Filábride terranes	107
7.3. Tectono-metamorphic evolution of the Nevado-Filábride complex	110
7.4. Discussion on the proposed divisions in the Nevado-Filábride complex	115
<i>Chapter 8: Conclusions</i>	119
Conclusiones	122
<i>References</i>	127
<i>Appendix</i>	143

Chapter 1

Introduction

The Betic Cordillera (S and SE of the Iberian Peninsula) constitutes, together with the Rif (N of Africa), the western termination of the Mediterranean Alpine belt. The Betic Cordillera is divided in two main domains: the Internal and the External Zones (Fallot, 1948). The Internal zone is divided into three complexes named from bottom to top: Nevado-Filábride, Alpujárride and Maláguide (Egeler and Simon, 1969). The Nevado-Filábride metamorphic complex (Betic Cordillera, Spain) has been interpreted as the E-SE prolongation of the Iberian basement (see, Sanz de Galdeano et al., 2006; Jabaloy et al., 2018). It exhibits a succession of Paleozoic and Mesozoic metasediments (schists, quartzites and marbles), orthogneisses and metabasites. This complex is probably the most controversial of the three. Nowadays, it has not been reached consensus about the internal division of the complex. The age of the sedimentary protolith has just been recently estimated and there is not unanimity regarding the paleogeographic reconstructions of the Nevado-Filábride terranes. Besides, the petrochronological evolution of the complex is not clear as P-T-t conditions differ between authors mainly because of the investigated rock types and the thermobarometric and geochronological techniques applied. Accordingly several tectono-metamorphic models have been proposed in order to explain the role of the complex in the tectonic history of the Betic Cordillera. The debate concerning the number of units forming the complex is probably the most conflictive in the Nevado-Filábride literature. The arguments used in order to identify different tectonic units have been mainly based in metamorphic and structural criteria. These divisions have usually resulted incompatible between them. A complete discussion about the proposed division should take into

account similarities and differences between the proposed units in regards to lithology, affinity, geochronological data and on a better knowledge and comparison of the P-T paths from the different parts of the complex. Accordingly, this Ph.D. Thesis has as main objective to bring light to the debate concerning the existence of the proposed divisions by using different methodologies, and the comparison of the results in different areas of the Nevado-Filábride pile.

Below it is briefly described the content of each chapter, including the methodology and the studies carried out during the Ph.D. Thesis.

Chapter 2. In this chapter is described the geological setting of the studied zones. In the first sections it is summarized the current knowledge of the Betic Cordillera, its division and the models proposed concerning its tectonic story. The following sections review the existing literature focused on the Nevado-Filábride complex regarding its division, metamorphic conditions during the Alpine orogeny, age constraints, structure, and the paleogeographic and tectonic models proposed.

Chapter 3. The methods and analytical techniques used during the Ph.D. Thesis are described in this chapter.

Chapter 4. The aim of this chapter is to provide a new cartography of key areas of the Nevado-Filábride complex. The maps are complemented with cross sections, schemes and field images. It has been carried out a mineralogical characterization focused on the schists and supported by backscattered electron (BSE) images of the studied samples. In the chapter is provided a description of the lithological succession. Finally, the discussion focuses on the characteristics of the contacts of the previously proposed tectonic units.

Chapter 5. In this chapter is presented the results of the Sensitive High Mass-Resolution Ion Microprobe (SHRIMP) U-Pb dating on detrital zircon from eight schist samples of the Nevado-Filábride complex. External and internal zircon grain features have been analyzed by transmitted-light, backscattered, and cathodoluminescence images in order to identify crystal properties which allow interpretation of the former

origin of the zircons. The dating results are discussed in order to provide an estimation of the maximum age of deposition for the complex. The ages obtained have been compared with the results based on previous dating. Additionally, it has been presented a preliminary study of the inclusions found in the zircon grains based in backscattered images.

Chapter 6. In this part is provided the P-T constraints from five schist samples from the Nevado-Filábride complex. The methodology followed combines quantitative compositional mapping of garnet with iterative thermodynamic models in garnet and potassic white mica (mainly phengite). Resulting P-T paths for different parts of the Nevado-Filábride pile are compared between them and with the literature data. The results presented in this chapter are complemented with allanite Laser Ablation Inductively Coupled Plasma Mass Spectrometry (LA-ICP-MS) U-Th-Pb geochronology in order to add time-constraints on the P-T evolution.

Chapter 7. In this chapter are discussed the most remarkable results presented in chapters 4, 5 and 6. In order to provide a complete story of the sedimentary deposition and tectonic evolution of the Nevado-Filábride complex, the discussion focuses in (1) the paleogeographic provenance of the Nevado-Filábride terranes based on the detrital zircon SHRIMP U-Pb dating, (2) the tectono-metamorphic model which fits the P-T-t conditions reached during the subduction and exhumation of the complex. Finally, the conclusions regarding the division of the Nevado-Filábride pile are presented.

Chapter 8. The most remarking conclusions obtained in the Ph.D. Thesis are summarized in this chapter.

Chapter 2

Regional setting and background

2.1. The Betic Cordillera

The western Mediterranean region is formed by a series of segments of the Alpine orogeny: the Betic, the Rif, the Tell, the Apennines, the Alps and the Pyrenees-Basque-Cantabrian mountains (e.g. Royden, 1993; Jolivet and Faccenna, 2000; Jabaloy et al., 2015). The Betic and Rif Cordilleras are connected through the Gibraltar Arc, forming a strongly curved oroclinal. The Betic Cordillera is located in the S and SE of the Iberian Peninsula (Fig. 2.1) and constitutes, with the Rif, the westernmost part of the Mediterranean Alpine Belt. The Betic-Rif Cordillera resulted from the convergence of the African and Iberian plates (e.g. Didon et al., 1973; Durand-Delga and Fontboté, 1980; Bouillin et al., 1986; Dercourt et al., 1986; Stampfli, 2000; Vera and Martín-Algarra, 2004; Aerden et al., 2013), which lead to the collision of several tectonic domains (e.g. Durand-Delga and Fontboté, 1980; Bouillin et al., 1986; Augier, et al. 2005b) during the late Mesozoic to the present. The Iberian Massif is the foreland of the Betic Cordillera. It is included in the central Europe Variscan belt formed during the Paleozoic collision of Gondwana and Laurasia.

The Betic Cordillera undergone a complex evolution including compressional and extensional deformations. Several tectonic models have been proposed to explain the structuring of the area since the studies of Andrieux et al. (1971): slab rollback (Fig. 2.2a) (Morley, 1993; Royden, 1993; Lonergan and White, 1997; Hoernle et al., 1999; Wortel and Spakman, 2000; Gill et al. 2004; Thiebot and Gutscher, 2006; Brun and Faccenna, 2008; Vergés and Fernández, 2012; González-Castillo et al., 2015), delamination (Fig. 2.2b) (Calvert et al., 2000; de Lis Mancilla et al., 2013), convective removal of mantle lithosphere (Fig. 2.2c) (Houseman et al., 1981; Platt and Vissers, 1989; Vissers, 2012;

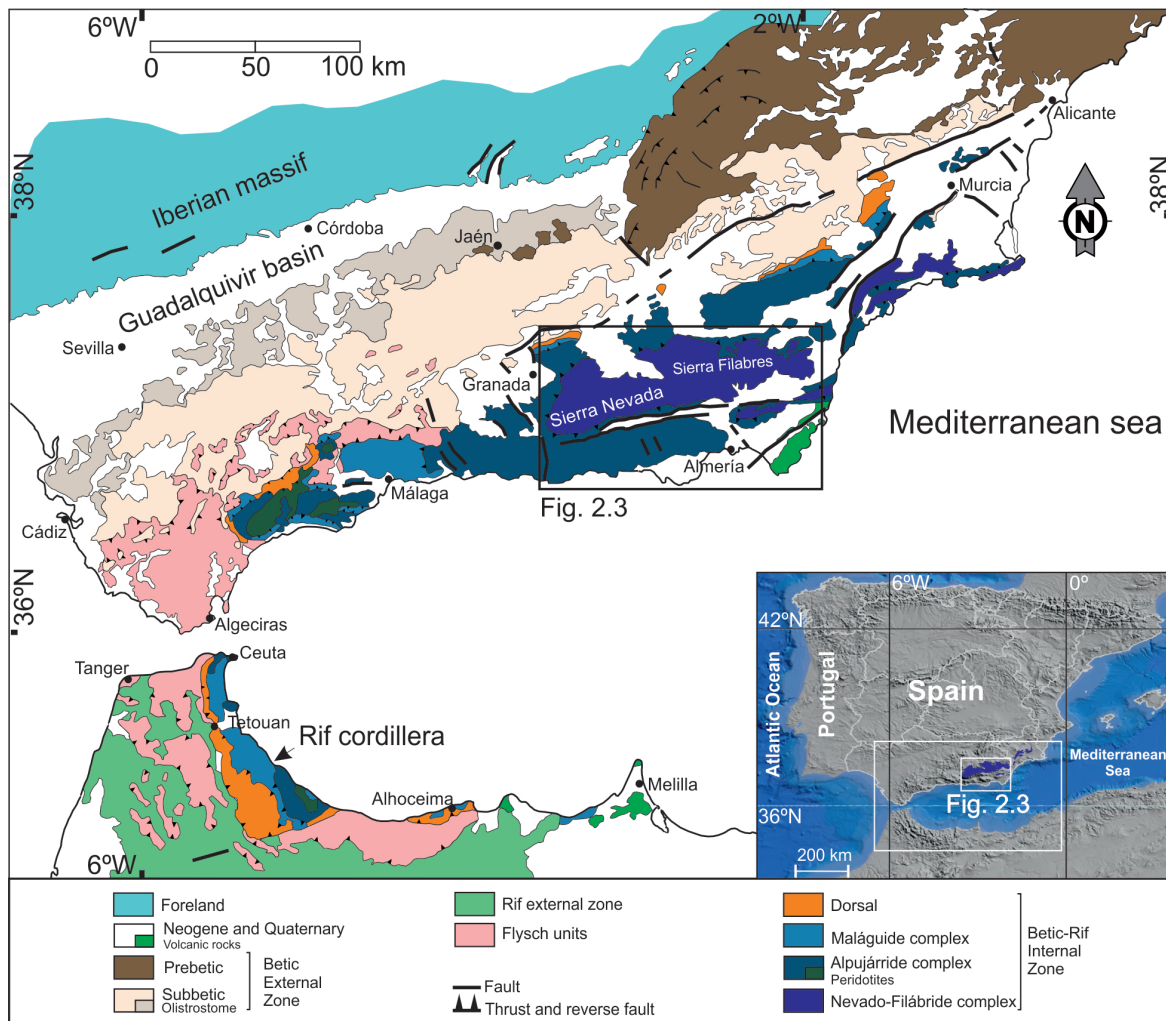


Figure 2.1. Geological map of the Betic Cordillera and northern Rif. Modified from Vera and Martín-Algarra (2004). Inset: Iberian Peninsula topographic map showing the position of the Nevado-Filábride complex.

Williams and Platt, 2018), partial or total break-off and/or tearing (Fig.2.2d) (Buform et al., 1991; Blanco and Spakman, 1993; Zeck, 1996; Spakman and Wortel, 2004; García-Castellanos and Villaseñor, 2011; van Hinsbergen et al., 2014), or a combination of slab rollback and delamination (Bezada et al., 2013).

The Betic Cordillera has been divided into the External Zone, the Internal Zone and the Campo de Gibraltar complex (Durand-Delga and Fontboté, 1980), and several Neogene basins (Fig. 2.1). The External Zone is formed by Mesozoic and Tertiary sedimentary successions constituting the sedimentary cover of the S and SE prolongations of the Iberian Massif. It is divided in two tectonic domains: the Prebetic and the Subbetic. Rocks in both domains are highly deformed but no metamorphosed. The Prebetic is mostly for-

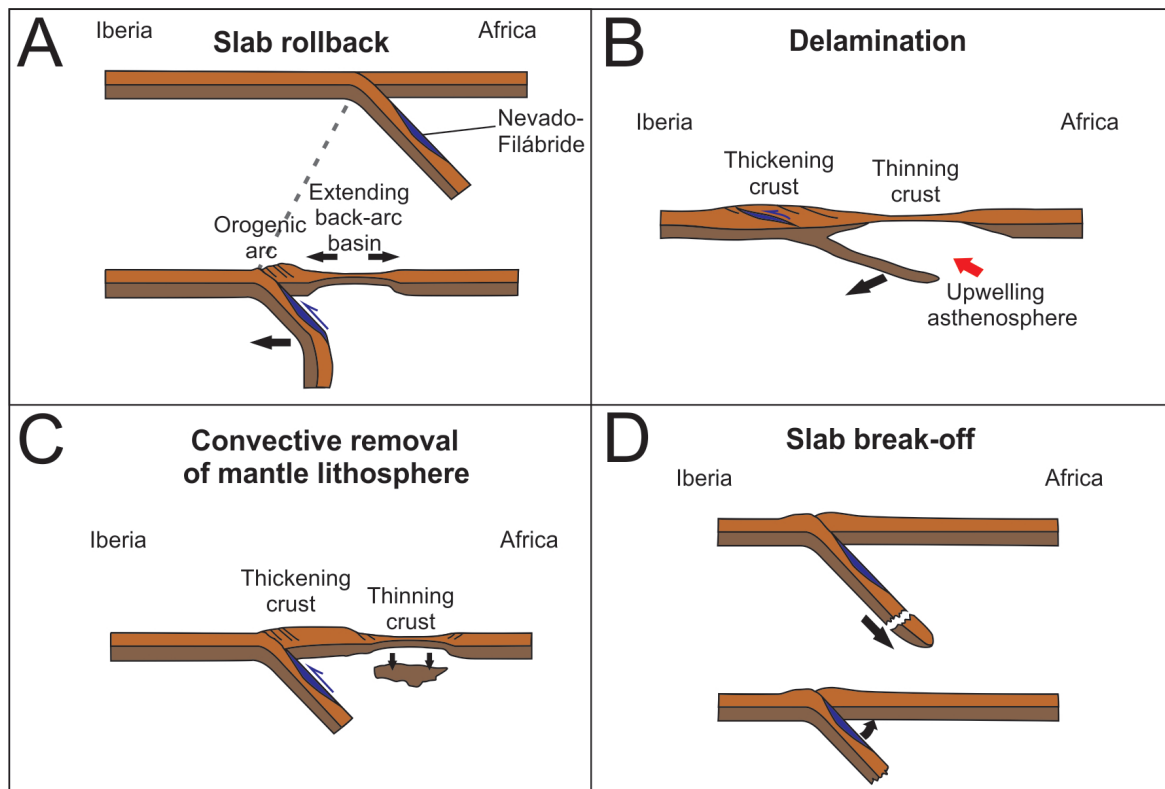


Figure 2.2. Main geodynamic models proposed for the western Mediterranean region. a) Slab rollback. b) Delamination. c) Convective removal of mantle lithosphere. d) Break-off of the subducting slab.

med by shallow marine and continental sediments deposited close to the coast; whilst the Subbetic is formed by deeper marine sediments and overthrusts the Prebetic domain (Vera and Martín-Algarra, 2004). The Internal Zone, also known as “Zona Bética” in old publications, or “Alborán domain” (Balanyá and García-Dueñas, 1987, Casciello et al., 2015) is formed by a Paleozoic basement and a Mesozoic cover. It is present in both the Betic Cordillera and the Rif. This zone is the most deformed region of the Betic Cordillera, and outcrops as a pile of tectonically superposed complexes (see below). The Campo de Gibraltar complex is in the S of the Iberian Peninsula and NW of Africa (in the Rif and the Tell). It is formed by Cretaceous and Tertiary deep marine successions including clays and turbidites (flysch facies) no metamorphosed during Alpine metamorphism (Vera and Martín-Algarra, 2004).

2.2. The Internal Zone division

The Internal Zone has been divided into three main superposed tectono-metamorphic complexes (e.g. Egeler and Simon, 1969; Martínez-Martínez et al., 2002; Puga et al.,

2002; Vera and Martín-Algarra, 2004), in addition to the Dorsal and Predorsal units. The three complexes are from lower to higher position: the Nevado-Filábride (not present in the Rif) (Egeler, 1963), the Alpujárride (called Sébtide in the Rif) (Van Bemmelen, 1927) and the Maláguide (called Ghomáride in the Rif) (Blumenthal, 1927). The Maláguide complex includes Paleozoic marine sediments affected by the Variscan orogeny, covered by marine Mesozoic and Tertiary discontinuous (at present) sediments. Rocks in the Maláguide complex are not metamorphosed or barely metamorphosed (Mäkel, 1985; Chalouan and Michard, 1990; Vera and Martín-Algarra, 2004; Sanz de Galdeano et al., 2006). The Dorsal and Predorsal units are formed by a set of imbricated Mesozoic and Tertiary sedimentary units closely linked to the Maláguide complex.

In the Betic Cordillera, the Alpujárride complex is divided in several units (see Sanz de Galdeano and López-Garrido, 1999; Azañón and Crespo-Blanc, 2000; Vera and Martín-Algarra, 2004) mainly formed by Paleozoic and Mesozoic (mainly Triassic) metasediments including metapelites, quartzites, carbonates and marbles. The higher unit of the complex includes gneisses, and at its base, large peridotite bodies (Vera and Martín-Algarra, 2004). The Alpujárride complex recorded an early HP/LT Alpine metamorphism at 23-20 Ma (Sánchez-Rodríguez and Gebauer, 2000; Janots et al., 2006). Other authors have proposed the HP metamorphism developed at ~50 Ma (Platt et al., 2005) and was followed by a low pressure and locally high temperature stage at 23-21Ma (Platt et al., 2003). Ar-Ar and zircon fission-track data suggest rapid cooling between 20 and 18 Ma (Monié et al. 1994; Sosson et al. 1998; Platt et al. 2003; Platt et al., 2013), and suggest that the rocks reached shallow crustal levels at ~18 Ma.

The Nevado-Filábride complex is formed by a succession of metapelites and marbles, with interlayered orthogneisses and metabasites. The contact with the overlying Alpujárride complex is characterized by brittle low-angle normal regional faults superposing the previous overthrust of the Alpujárride complex over the Nevado-Filábride complex (Galindo-Zaldívar, et al., 1989; Jabaloy et al., 1993; Agard et al., 2011). These faults were formed during late exhumation of the complexes (e.g. Gómez-Pugnaire et al., 2012).

2.3. The Nevado-Filábride complex

The Nevado-Filábride complex was defined by Egeler (1963) for the metamorphic rocks lying under the Alpujárride complex. The complex occupies the lowermost position of the Internal zone, in the core of several antiforms in the sierras Nevada, Baza, de los Filabres, Alhamilla, Cabrera, Almagrera, Almenara, Lomo de Bas, Mazarrón and Cartagena (Fig. 2.3).

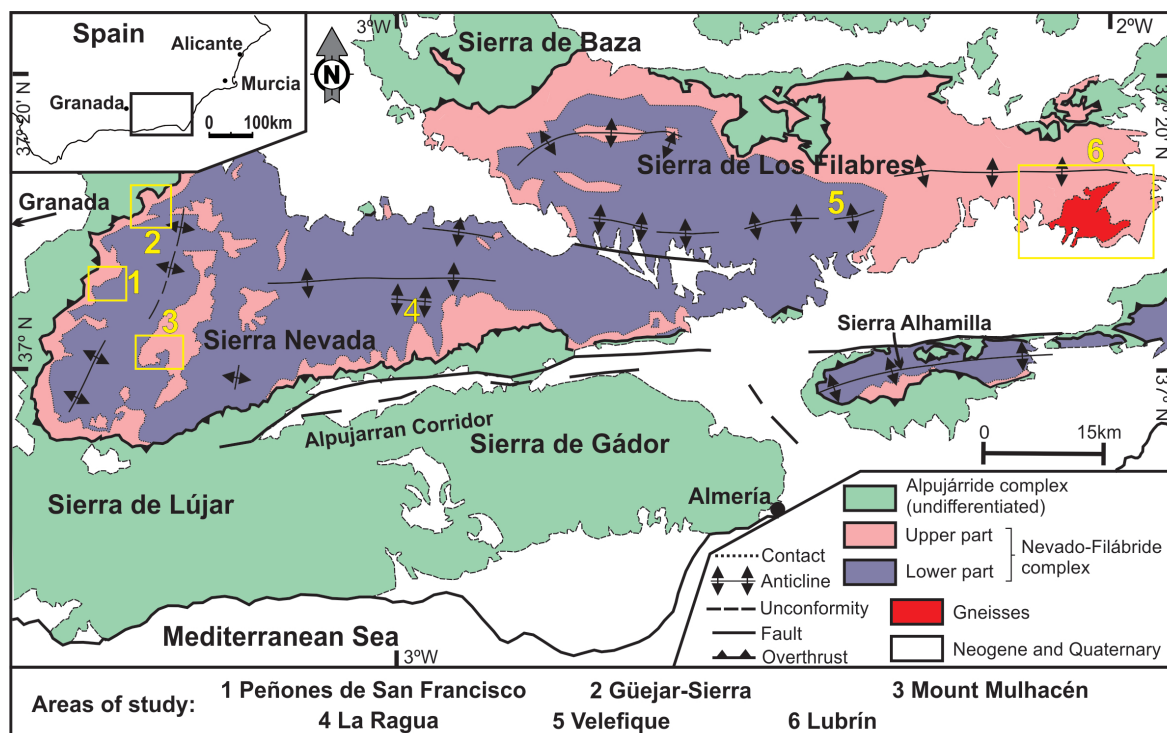


Figure 2.3. Geological map of the Betic Cordillera. In this map the Nevado-Filábride complex rocks crop out primarily in the cores of Sierra Nevada, Sierra de Los Filabres and Sierra Alhamilla. The numbers in yellow mark the studied areas in this Ph.D. Thesis. Modified from Sanz de Galdeano and López-Garrido (2016).

2.3.1. Division

The separation of the complex in two or more lithologic formations and/or tectonic units has remained a matter of debate since the first studies of the area. Nowadays, there is not a unanimously accepted division, as it depends on the criteria used by each author (i.e. petrological, structural and/or metamorphic criteria). Hereafter, it is provided a short summary of the most used divisions over time. Furthermore, in chapter 4 is included a review of the different divisions focused on specific areas of the complex. This presentation of the background allow the comparison of the proposed divisions with the description of

the lithological succession carried out in this Ph.D. Thesis. The Fig. 2.4 shows the correspondence between the most used divisions for comparison.

	Brouwer, 1926	Egeler and Simon, 1969	Puga et al., 2002	Martínez-Martínez et al., 2002	Gómez-Pugnaire et al., 2002	This Ph. D. Thesis		
Nevado-Filábride complex	Mischungszone (Mixed zone)	Almocaizar unit	Mulhacén complex	Sabinas unit	Bédar-Macael unit	Chive formation	Upper part	Schists and marbles Fm
		Bédar unit		Ophiolite unit	Calar-Alto unit			
Chive-Macael unit		Caldera unit		Tahal formation				
Nevado-Lubrín unit		Veleta complex			Montenegro dark schists			
Crystalline of Sierra Nevada	Veleta schists		La Ragua unit	Lower part	Dark schists fm			
	 Stratigraphic contact - - - - Thrust						

Figure 2.4. Comparison of the main Nevado-Filábride complex divisions reported in the literature. The division followed in this Ph.D. Thesis is presented in the right column. Lower and upper parts of the complex are equivalent to the Crystalline of Sierra Nevada and the Mischungszone respectively (Brouwer, 1926). Both parts have been shadowed in purple and pink respectively. Modified from Sanz de Galeano and Santamaria-López et al. (2019).

Brouwer (1926) distinguished two stratigraphic formations based on lithological criteria: a homogeneous metapelite basement, the Crystalline of Sierra Nevada; and a lithologic heterogeneous cover named the Mischungszone (mixed zone). Fallot et al (1959; 1960) raised the possible existence of a disconformity between the Crystalline of Sierra Nevada and the Mischungszone, and discussed the autochthony or allochthony of the last one. Since these initial studies, variations in the Brouwer (1926)'s scheme have been proposed. In general, the existence of the monotonous succession of the Crystalline of Sierra Nevada has been mostly accepted. However, several tectonic units have been described in the Mischungszone (Nijhuis, 1964; Helmers and Voet, 1967; Egeler and Simon, 1969; Vissers, 1977; Linthout and Vissers, 1979; de Jong, 1993; Puga et al., 2002; Martínez-Martínez et al., 2002, 2010). In this respect, probably the most used divisions are those of Puga and Díaz de Federico (1976), Puga et al. (2002) and Martínez-Martínez et al. (2002). According to Puga and Díaz de Federico (1976), the Nevado-Filábride complex is divided into the Veleta and the overlaying Mulhacén nappes (approximately equivalent to the Crystalline of Sierra Nevada and the Mischungszone respectively). The

Veleta nappe includes a monotonous sequence of graphite-bearing schists and quartzites, whereas the Mulhacén nappe is formed by a larger variety of lithologies including schists, quartzites, marbles, gneisses, serpentinites and amphibolites. According to Puga et al. (2002) the differences in metamorphic conditions between these nappes (see section 2.3.3.1) imply they occupied different tectonic settings during the Alpine orogeny. Accordingly these authors reclassified as “complexes” (Fig. 2.4) the “nappes” of Puga and Díaz de Federico (1976). Puga et al. (2002) divided the Mulhacén complex into three tectonic units (Fig. 2.4): the lowermost Caldera unit, the Ophiolite unit and the uppermost Sabinas unit. Martínez-Martínez et al. (2002) renamed the Veleta nappe as Ragua unit (being not exactly equivalent, see Fig. 2.4), and subdivided the Mulhacén nappe into the lowermost Calar-Alto unit and the overlying Bédar-Macael unit (Fig. 2.4). However, it is important to note that according to other authors (Galindo-Zaldívar, 1993; Sanz de Galdeano and López-Garrido, 2016; Sanz de Galdeano et al., 2016; Sanz de Galdeano and Santamaría, 2019) the existence of such tectonic units cannot be reasonably supported by field observations. By the contrary, they proposed a stratigraphically continuous lithological sequence in the Nevado-Filábride complex as was initially proposed by Brouwer (1926).

2.3.2. Lithological succession

Below is summarized, from bottom to top, the lithological succession of the Nevado-Filábride complex. Three main formations have been described: one for the lower part of the complex, equivalent to the Crystalline of Sierra Nevada of Brouwer (1926) and the Veleta complex of Puga et al. (2002); and two for the upper part of the complex, equivalent to the Mischungszone of Brouwer (1926) and the Mulhacén complex of Puga et al. (2002) (Fig. 2.4). The variations of the general succession presented here are discussed in the chapter 4. The section 2.3.2.4 focuses on the igneous rocks found in the complex.

2.3.2.1. The Dark schists formation

The lower part of the complex in the Sierras Nevada and Filabres is formed by a sequence of graphite-rich schists and quartzites. The thickness of the sequence has been estimated in 4000 m (Fallot et al., 1960). The bottom of this sequence does not crop out in these sierras. According to Gómez-Pugnaire et al. (2012) and Laborda-López et al. (2015) the formation shows locally dark low-grade marbles levels up to 80-140 m thick. In the Barranco de San Juan area (W of Sierra Nevada) outcrop scarce metabasite bodies.

2.3.2.2. The Tahal formation.

The upper part of the complex includes in its base a formation of light- and dark mica schists alternating with quartzites, metabasites, marbles and scarce gneisses and metaevaporitic levels, named the Tahal Fm (Fig. 2.4). The thickness of the formation ranges from 500 to 2300 m. The dark mica schists and quartzites are more common in the bottom, whilst the occurrence of light mica schists, marbles, metabasites and gneisses increases upwards (e.g. Vissers, 1981; Gómez-Pugnaire, et al., 2012). In the W of Sierra de los Filabres (area of Escúllar - El Tesorillo - Charches) Sanz de Galdeano and López-Garrido (2016) described apparently not metamorphosed sands (“lutites”) preserving cross laminations. Gómez-Pugnaire et al. (1994) describes the metaevaporites as a discontinuous succession (up to 80 m) of scapolite-gypsum-bearing marbles and fine-grained scapolite-gypsum-anhydrite-barite-bearing metapelites.

2.3.2.3. The Schists and marbles formation

The uppermost formation of the complex (Fig. 2.4) consists of a package of alternating light-, dark schists and layers of marbles and calc-schists. The thickness of the formation varies between 200 and 1300 m. The upper part of the formation includes massive marbles levels, gneisses and scarce metabasite bodies. Above the Schists and marbles Fm formation overthrusts the Alpujárride complex.

2.3.2.4. Gneisses and metabasites in the Nevado-Filábride complex

Gneisses are laterally continuous light layers of variable thickness (from several centimetres to tens of meters) (Martínez-Martínez et al., 2010), showing sharp contacts with the adjacent schists and marbles. Gneisses have been described only in the Tahal and the Schists and marbles Fms. Gómez-Pugnaire et al. (2012) and Ruiz-Cruz et al. (2015) reported the existence of two main types of gneisses: (1) leucocratic gneisses which can be granoblastic tourmaline-rich or porphyritic; and (2) biotitic gneisses, which contain minor amphibole-rich layers. Leucocratic gneisses are more abundant, and according to Gómez-Pugnaire et al. (2012) show textural and field features which prove the intrusive relationships with the surrounding metasediments. Both types are present in the same outcrops (Gómez-Pugnaire et al., 2012), occasionally forming alternations of few cm (Nieto, 1996). Accordingly it has been interpreted as probably cogenetic. Gómez-Pugnaire et al. (2012) interpreted both gneisses as

derived from late Variscan post-collisional leucogranites, recycled during the Alpine orogeny.

Basic and ultrabasic rocks in the Nevado-Filábride complex are associated to light- and dark schists, quartzites, calc-schists and marbles. These rocks are transformed into eclogites, amphibolites and serpentinites (e.g. Nijhuis, 1964; Gómez Pugnare, 1981; Martínez-Martínez, 1986; Puga et al., 2002, Ruiz-Cruz et al., 2015; Puga et al., 2017). They mainly outcrop in the upper part of the complex as discontinuous bodies, locally reaching kilometric length. In some areas occur barely or not metamorphosed igneous rocks surrounded by eclogites. According to Puga et al. (2002) two types of metabasites are present in the Nevado-Filábride complex: (1) intra-plate derived rocks and (2) ocean-floor rocks. Nevertheless, the origin of the basic and ultrabasic association in the Tahal Fm is still under debate, with models ranging from the existence of an ocean floor sequence (the Ophiolitic unit described in Puga et al. 2002; 2017, Fig. 2.4) to continental within-plate type magmatism associated with crustal-thinning (Gómez-Pugnare et al., 2000).

2.3.3. Metamorphism in the Nevado-Filábride complex

2.3.3.1. Metamorphism P-T constraints

Several lines of evidence suggest a two-stage metamorphic history with a HP/LT Alpine event followed by a LP/HT stage during decompression. This latest stage largely overprinted the previous metamorphic record particularly, but not exclusively, in the metasediments. Besides, thermobarometric data generally show higher P and T values were reached in upper part of the complex than in the lower one (e.g. Puga et al., 2002; Augier et al., 2005b; Behr and Platt, 2012; Booth-Rea et al., 2015, Li and Massonne, 2018). Some few metamorphic studies have been focused on metapelites (Augier et al., 2005a, 2005b; Ruiz-Cruz et al., 2015), whilst most of the constraints for the HP/LT stage are provided by studies in mafic and felsic igneous rocks (e.g. Gómez-Pugnare et al., 1994; Puga et al., 2000, 2002; López Sánchez-Vizcaíno et al., 2001, 2005; Padrón-Navarta et al., 2010; Ruiz-Cruz et al., 2015). The resulting P-T paths, strongly differ between authors, in particular for the decompression stage (Fig. 2.5). Puga et al. (2000, 2002) and Behr and Platt (2012) proposed hairpin trajectories (Fig. 2.5a), which show coincidence in the P and T peaks; Augier et al. (2005a, 2005b), Ruiz-Cruz

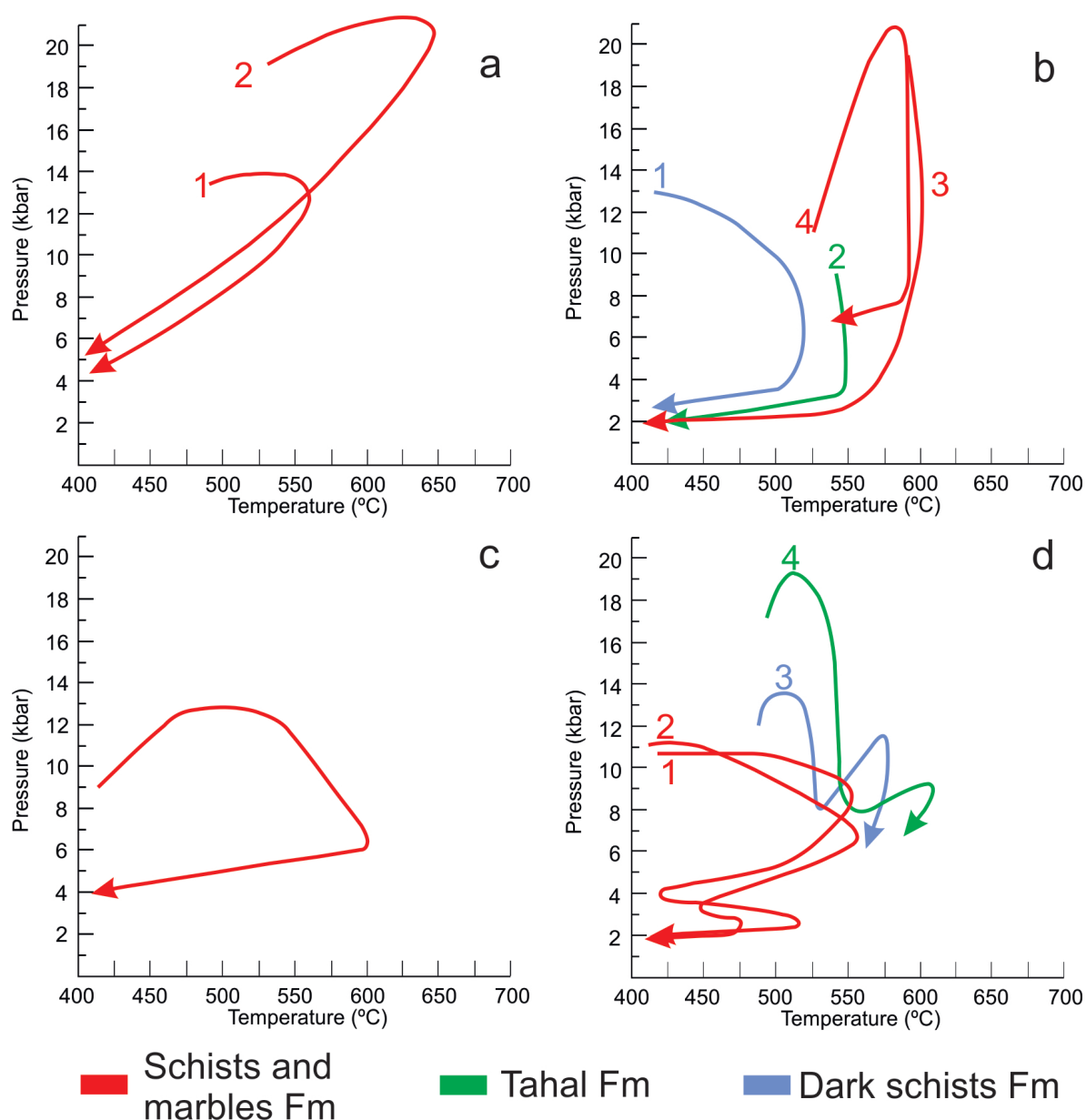


Figure 2.5. *P-T* paths in the available data for the Nevado-Filábride complex. a) Hairpin trajectories, 1: Behr and Platt (2012); 2: Puga et al. (2002). b) Isothermal decompression, 1 and 2: Augier et al. (2005b); 3: Augier et al. (2005a); 4: Ruiz-Cruz et al. (2015). c) Slight heating upon decompression, Gómez-Pugnaire and Fernández-Soler (1987). d) Late reheating, 1: Bakker et al. (1989), 2: Vissers et al. (1995), 3 and 4: Li and Massonne (2018).

et al. (2015) and Laborda-López et al. (2018) suggested an isothermal decompression (Fig. 2.5b); Gómez-Pugnaire and Fernández-Soler (1987) proposed slight heating upon decompression (Fig. 2.5c); and Vissers (1981), Bakker et al. (1989), Booth-Rea et al. (2015) and Li and Massonne (2018) pointed to the existence of late reheating at lower pressure conditions (Fig. 2.5d). The discrepancies have been attributed either to diffe-

rences between thermobarometers, or variations of P-T trajectories throughout the Betic Cordillera (Platt et al., 2013).

2.3.3.2. Metamorphism age constraints

Similarly to the internal division of the Nevado-Filábride complex and its P-T history, there is no consensus regarding the age of each metamorphic stage. Age estimations for both the HP/LT and LP/HT events are reported in Table 2.1. Augier et al. (2005a) applied *in situ* laser $^{40}\text{Ar}/^{39}\text{Ar}$ on phengite in metapelite samples from the Calar-Alto and Bédar-Macael units (Fig. 2.4). They concluded that the HP/LT stage took place at ca. 30 Ma or possibly older, and was followed by the main exhumation between 22-18 Ma and the last step of exhumation between 14-9 Ma. Monié et al. (1991) obtained an integrated $^{40}\text{Ar}/^{39}\text{Ar}$ age range of 48.4 ± 3.3 Ma on amphibole from metabasites for the HP/LT event in the upper part of the complex. de Jong (2003) and Platt et al (2006) yielded Ar-Ar ages for phengite in schists and other lithologies ranging 90 to 13 Ma. However, it is almost unanimously accepted the excess in Ar in the white mica from the Nevado-Filábride schists

Study	HP/LT event age (Ma)	LP/HT event age (Ma)	Method
Augier et al. (2005a)	~30	22 - 18	<i>In situ</i> laser $^{40}\text{Ar}/^{39}\text{Ar}$ on phengite in metapelite
Li and Massonne (2018)	33.9 - 56.0	24.1 ± 0.8 (reheating loop during exhumation)	<i>In situ</i> U-Th-Pb monazite in schists
López Sánchez-Vizcaíno et al. (2001)	15.0 ± 0.6		U-Pb zircon in pyroxenite
Gómez-Pugnaire et al. (2012)	17.3 ± 0.4		U-Pb zircon in gneisses and schists
Platt et al. (2006)	18 - 14		Lu-Hf garnet in mafic eclogites and schists
Kirchner et al. (2016)	~20 - 13		Multimineral $^{87}\text{Rb}/^{86}\text{Sr}$
Monié et al. (1991)	48.4 ± 3.3		$^{40}\text{Ar}/^{39}\text{Ar}$ amphibole in metabasites

Table 2.1. Radiometric ages (in Ma) reported in the literature for the alpine metamorphism affected the Nevado-Filábride complex

(Hebeda et al., 1980; Andriessen et al., 1991; López Sanchez-Vizcaino et al., 2001; de Jong, 2003; Platt et al., 2006; Behr and Platt, 2012; Kirchner et al., 2016). According to several authors (e.g. López Sánchez-Vizcaíno et al., 2001; de Jong, 2003; Platt et al., 2006; Behr and Platt, 2012) the Ar excess prevents this method to be applied because it could lead to ages older than those obtained by other independent radiometric methods (see below), and/or unrealistic highly variable age ranges (e.g. Kelley, 2002). According to Li and Massonne (2018) the HP/LT event occurred during Eocene (~40 Ma), and it was followed by a second P-T loop during exhumation at 24.1 ± 0.8 Ma. Other studies reported younger Miocene ages for the pressure peak conditions including López Sánchez-Vizcaíno et al. (2001) (15.0 ± 0.6 Ma) and Gómez-Pugnaire et al. (2012) (17.3 ± 0.4 Ma) based on U-Pb dating of zircon from the upper part of the complex; Platt et al. (2006) who provided ages ranging between 18 and 14 Ma from Lu-Hf dating of garnet separates in mafic eclogites and schists from several areas of the complex; and Kirchner et al. (2016) who applied multimineral $^{87}\text{Rb}/^{86}\text{Sr}$ geochronology to date the HP/LT event at ~20-13 Ma. Behr and Platt (2012) obtained zircon fission track ages of ~16-13 Ma; and Platt et al. (2006) and Behr and Platt (2012) yielded apatite fission track ages ranging between ~19 and 6 Ma. de Jong (2003) obtained whole-rock-phengite Rb-Sr dates at ~17 and ~14 Ma, representing isotopic re-equilibration during the early stages of exhumation. Johnson et al. (1997) yielded apatite fission track ages at ~12-8 Ma, and proposed the complex reached upper crustal levels by ~8 Ma.

As a summary, the HP/LT event should have occurred not after the Miocene (48 to 13 Ma). On the other hand, the LP/HT stage has not been extensively dated, with the exception of Augier et al. (2005a) and Li and Massonne (2018) (24 to 18 Ma).

2.3.4. Nevado-Filábride complex structure

The Nevado-Filábride complex show two main planar fabrics: S1, parallel to the compositional layering and a crenulation cleavage S2. The first schistosity S1 is mostly overprinted by S2, despite is still recognized, and occasionally unaltered, in rocks from the lowermost levels of the Nevado-Filábride complex (lower part of the Dark schists Fm), and insolated lenses in the upper levels (Tahal and Schists and marbles Fms). The S2 schistosity is associated with a penetrative stretching lineation L2, more intense towards the contact with the overlying Alpujárride complex.

Several shear zones have been described in the Nevado-Filábride complex. The most evident shear zone affects the top of the Nevado-Filábride pile existing below the low-angle normal fault acting as the Alpujárride/Nevado-Filábride detachment. It has been interpreted as late-metamorphic extensional and formed during exhumation of the complex (e.g. Galindo-Zaldívar et al., 1989; Jabaloy et al., 1993; Martínez-Martínez et al., 2002; Augier et al., 2005b; Simancas, 2018) (Fig. 2.3). Kinematic criteria indicate an overall top-to-the-W sense of movement (Galindo-Zaldívar et al., 1989; Jabaloy et al., 1993; De Jong, 1993; Martínez-Martínez et al., 2002; Augier et al., 2005b; Simancas, 2018). Conversely, Behr and Platt (2013) have interpreted this shear zone as produced in a compressional context during exhumation. Martínez-Martínez et al. (2002) and Martínez-Martínez et al. (2010) described several shear zones of similar kinematics but interpreted as contractional, separating their three units (Bédar-Macael, Calar-Alto units and Ragua unit, see Fig. 2.4). The S2 schistosity was deformed by folds (F3) which developed a crenulation cleavage (S3) observed in the whole Nevado-Filábride pile (e.g. Jabaloy et al., 2015).

2.3.5. Nevado-Filábride complex age constraints

The sedimentary age estimations of the Nevado-Filábride complex in the Sierras Nevada and Filabres (Betic Cordillera, Spain) have been traditionally based on stratigraphic correlations with the overlying Alpujárride complex. According to these interpretations the Nevado-Filábride complex is formed by a Paleozoic (or older) lower sequence and a Permo-Triassic cover (e.g. Egeler and Simon 1969). In addition, the deposition of carbonates in the upper part of the complex (now present as marbles in the Schists and marbles Fm) has been assumed as Triassic (de Jong and Bakker, 1991). Gómez-Pugnaire et al. (1982) identified possible pre-Cambrian microfossils in schists from the western part of the Sierra de los Filabres. However, these preliminary results have not been confirmed so far. Tendero et al. (1993) studied the upper part of the complex in Sierra de los Filabres reporting ankeritic “ghosts” interpreted as Cretaceous planktonic foraminifers. Rodríguez-Cañero et al. (2018), in the Sierra de Baza, found Bashkirian (323.2 ± 0.4 to 315.2 ± 0.2 Ma) conodonts in graphite-rich metamorphic limestones included in dark schists (tentatively attributed to the upper part of the complex in this Ph.D. Thesis).

The radiometric age determinations of the complex (Table 2.2) have been mainly based on meta-igneous rocks situated in the upper part of the complex. The first radiometric dating study on the Nevado-Filábride complex rocks provided a Rb-Sr whole-rock age of 269 ± 6 Ma for tourmaline-gneisses and metagranites in the eastern part of Sierra de los Filabres (Priem et al., 1966). Puga (1976) (in the western part of Sierra Nevada), Andriessen et al. (1991) (in the eastern part of the complex) and Gómez-Pugnaire et al. (2000) (in the central part of the complex) proposed Rb-Sr whole-rock from gneisses, ranging between Permian to Triassic. Nieto (1996) and Nieto et al. (1997) reported an age of 307 ± 30 Ma using Sm-Nd whole-rock analyses in orthogneisses. In the western part of the Nevado-Filábride complex U-Pb age determinations include: Gómez-Pugnaire et al.

Study	Age (Ma)	Method	Area
Priem et al. (1966)	269 ± 6	Rb-Sr whole-rock in tourmaline-gneisses	Eastern Sierra de los Filabres
Puga (1976)	215 ± 15	Rb-Sr whole-rock in gneisses	Western Sierra Nevada
Andriessen et al. (1991)	275 ± 30	Rb-Sr whole-rock in gneisses	Eastern part of the complex
Nieto (1996); Nieto et al. (1997)	307 ± 30	Sm-Nd whole-rock in gneisses	Eastern part of the complex
Gómez-Pugnaire et al. (2000)	247 ± 11	Rb-Sr whole-rock in gneisses	Central part of the complex
Gómez-Pugnaire et al. (2004)	301 ± 7	U-Pb zircon in gneisses	Western Sierra Nevada
Martínez-Martínez et al. (2010)	314 ± 7 ; 304 ± 23	U-Pb zircon in gneisses	Western Sierra Nevada
Gómez-Pugnaire et al. (2012)	282 ± 5 ; 295 ± 3	U-Pb zircon in gneisses	Several areas of the complex
Ruiz-Cruz and Sanz de Galdeano (2017)	~ 286	U-Pb zircon in gneisses	Western Sierra Nevada
Jabaloy et al. (2018)	Pennsylvanian MDA (Lower part of the complex)	Detrital U-Pb detrital zircon in schists	Western Sierra de los Filabres
	Early Permian MDA (Upper part of the complex)		Eastern Sierra de los Filabres

Table 2.2. Radiometric ages (in Ma) reported in literature for the Nevado-Filábride complex

(2004) who obtained late Carboniferous age in zircons from orthogneisses (301 ± 7 Ma); Martínez-Martínez et al. (2010), who provided late Carboniferous U-Pb ages in zircons (314 ± 7 and 304 ± 23 Ma) and $^{40}\text{Ar}/^{39}\text{Ar}$ tourmaline ages from gneisses and tourmalinites (319.85 ± 5.81 and 317.85 ± 3.67 Ma); and Ruiz-Cruz and Sanz de Galdeano (2017), who yielded lower Permian U-Pb ages from zircons extracted from orthogneisses (~ 286 Ma). Gómez-Pugnaire et al. (2012) determined lower Permian U-Pb zircon ages in gneisses from various areas of the complex (282 ± 5 to 295 ± 3 Ma).

Till the date, only two studies have been focused in radiometric age determinations of metasedimentary rocks (schists) from the Nevado-Filábride complex, both based on SHRIMP U-Pb detrital zircon dating (Jabaloy et al., 2018; Santamaría-López and Sanz de Galdeano, 2018). Santamaría-López and Sanz de Galdeano (2018) proposed a Carboniferous maximum age of deposition for the lithological sequence of the complex in the Sierras Nevada and de los Filabres (this Ph.D. Thesis, chapter 5). Jabaloy et al. (2018) yielded a Carboniferous age and Early Permian maximum age of deposition for the Dark schists and Tahal Fms respectively in Sierra de los Filabres.

2.3.6. Paleogeographic reconstructions of the Nevado-Filábride complex

The paleogeographic location of the terranes which formed the Internal Zone of the Betic Cordillera is still not well constrained (e.g. Alonso-Chaves et al., 2004; Carminati et al., 2012; Vergés and Fernández, 2012; Jabaloy et al., 2018; Simancas, 2018). However, a probable eastward location for these terranes is commonly accepted. During the Miocene, they probably drifted westward with respect to Iberia and Africa (e.g. Andrieux et al., 1971; Durand-Delga and Fontboté, 1980; Boillot et al., 1984; Sanz de Galdeano, 1990; Rosenbaum et al. 2002; Platt et al. 2003; Williams and Platt, 2018).

Traditionally, the main complexes forming the Internal Zone (the Maláguide, Alpujárride and Nevado-Filábride complexes) have been included in the “Alborán domain” (Balanyá and García-Dueñas, 1987), and would share comparable paleogeographic histories. Recent paleogeographic reconstructions for the Nevado-Filábride complex have challenged this idea. Gómez-Pugnaire et al. (2012) proposed the Nevado-Filábride complex is related to the Central Iberian Zone of the Iberian Massif. This correlation is supported on age and composition similarities between the Nevado-Filábride gneisses and

granitoids from the Central and Northwest Zones of the Iberian Massif. By the contrary, other authors suggest a correlation with the Cantabrian Zone based on similarities in conodont fauna (Rodríguez-Cañero et al., 2018), and detrital zircon age patterns (Jabaloy et al., 2018). Both reconstructions consider the Nevado-Filábride complex to be part of the prolongation of the South Iberian paleomargin. Accordingly, Rodríguez-Cañero et al., (2018) and Jabaloy et al. (2018) proposed redefining the “Alborán domain” as formed by the Alpujárride and Maláguide complexes exclusively. In any case, the significance of the “Alborán domain” is still controversial (Casciello et al., 2015). The Alpujárride and Maláguide terranes would have been located eastwards of the Nevado-Filábride terranes, in the prolongation of the Iberian Massif, but in a more distal position (Sanz de Galdeano et al., 2006).

2.3.7. The role of the Nevado-Filábride complex in the Betic Cordillera tectonic configuration

No consensus has been reached about the subduction and, particularly, the exhumation processes involving the Nevado-Filábride complex. Discrepancies between the models strongly depend on the relative timing of the metamorphic ages estimated for the Nevado-Filábride and Alpujárride complexes.

Conventional studies proposed both complexes developed similar tectono-metamorphic stories. E.g. the studies based in $^{40}\text{Ar}/^{39}\text{Ar}$ on phengite (Augier et al., 2005a) (see section 2.3.3.2) estimated the minimum age for HP/LT metamorphism occurred in the Nevado-Filábride complex at ~30 Ma, and it was followed by exhumation in the Miocene. In this scenario, the subduction of the Nevado-Filábride and Alpujárride complexes are mostly coincident in time, and both complexes shared similar deformational and metamorphic histories

However, recent geochronological studies based on U-Pb dating of zircon, Lu-Hf dating of garnet and multimineral $^{87}\text{Rb}/^{86}\text{Sr}$ pointed to a Miocene age (~20-13 Ma) for the HP/LT event for the Nevado-Filábride Complex (see section 2.3.3.2) (López Sánchez-Vizcaíno et al., 2001; Gómez-Pugnaire et al., 2004, 2012; Platt et al., 2006; Behr and Platt, 2012; Kirchner et al., 2016). This age is almost coincident with the moment that the Alpujárride complex reached shallow crustal levels at ~18-16 Ma (Sosson et al.,

1998; Platt et al., 2003; Platt et al., 2013). Accordingly, the Alpujarride complex suffered pre-Miocene subduction and was later exhumed during early Miocene by the time the Nevado-Filábride underwent HP metamorphism (e.g. López Sánchez-Vizcaíno et al., 2001; Platt et al., 2006, Jabaloy et al., 2015, Kirchner et al., 2016).

Martínez-Martínez et al. (2002) proposed the late exhumation of the Nevado-Filábride complex was controlled by a set of top-to-the-W or SW shear zones. According to Behr and Platt (2012), Behr and Platt (2013) and Platt et al. (2013) the exhumation of the Nevado-Filábride complex took place in two stages: a fast initial exhumation through the subduction channel, followed by a slower accommodation of the complex after being captured by a low-angle detachment fault. Other authors indicate that after the Nevado-Filábride complex reached upper crustal conditions, the exhumation was accommodated by brittle extensional detachments (e.g., Galindo-Zaldívar et al., 1989; Jabaloy et al., 1993; Augier et al., 2013; Do Couto et al., 2014).

Chapter 3

Methodology

3.1. Introduction

In this chapter is described the methodology followed in this Ph.D. Thesis. It includes field work and the use of analytical techniques in selected rock samples. Field work comprehends cartography, identification of minor and major structures and sample collection in the areas of study. In section 3.2 is summarized the methodology followed for the SHRIMP U-Pb dating of detrital zircons (chapter 5). In section 3.3 is provided the procedure followed to estimate the P-T conditions of metamorphism in the Nevado-Filábride complex, and the methodology followed for the LA-ICP-MS Th-U-Pb dating of allanites, (chapter 6).

3.2. SHRIMP U-Pb detrital zircon dating

Eight mica-schist samples have been studied in the U-Pb detrital zircon dating study: SF-1, SF-2, RA-1, RA-2, RA-3, VE-1, VE-2 and VE-3. The UTM coordinates of the samples are given in Appendix 1.

The zircons were analyzed for U-Pb dating by using the SHRIMP IIe/mc ion microprobe at the IBERSIMS laboratory of the University of Granada (Spain) (Fig. 3.1a). A detailed description of the analytical procedures followed during analyses is provided in Appendix 2. A summary of the main steps are presented below. The zircon grains were separated using panning, first in water and then in ethanol, and magnetic techniques followed by handpicking of the concentrates using a binocular microscope. Zircon were mounted in a 3.5 cm diameter epoxy mount and polished. Later they were studied by opti-

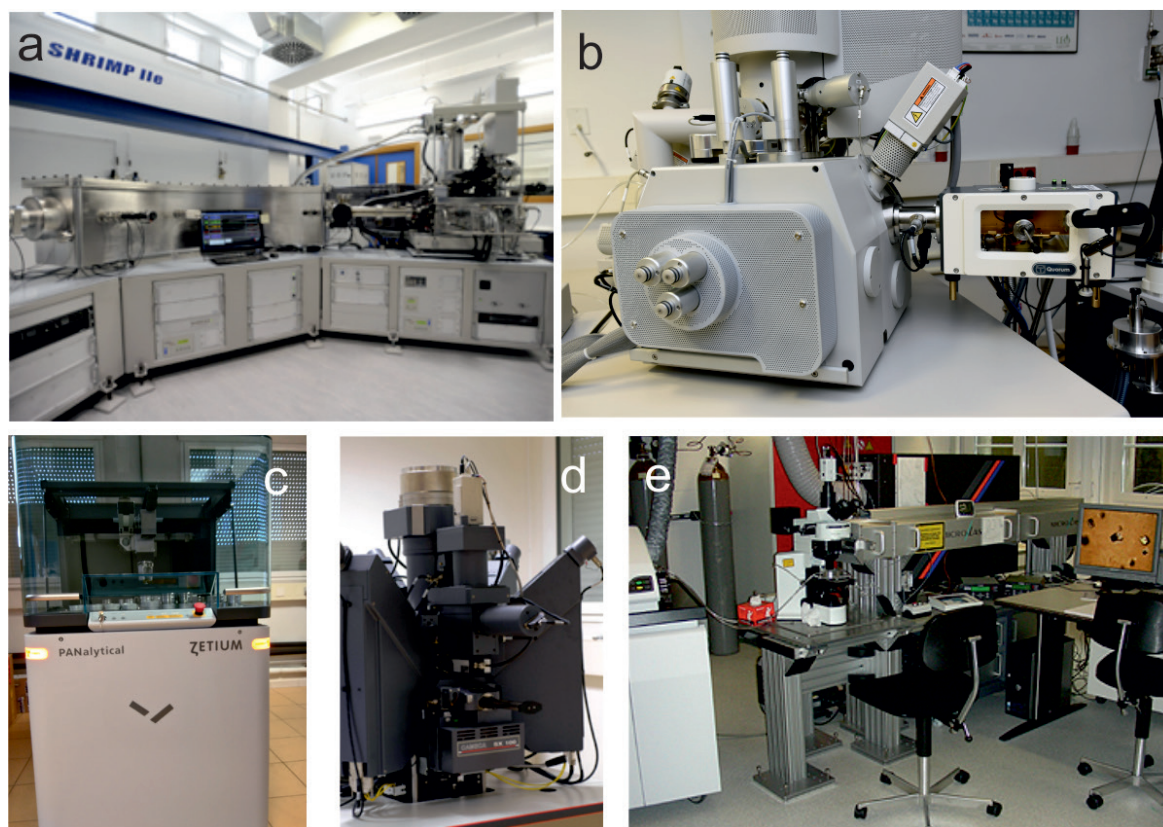


Figure 3.1. Selection of the analytical instruments used during the Ph.D. Thesis. a) Environmental Scanning Electron Microscope (ESEM) FEI model Quanta 400. b) SHRIMP IIe/mc ion microprobe at the IBERSIMS laboratory. c) Philips PW1040/10 spectrometer. d) Cameca SX100. e) ZEISS EVO 50 scanning electron microscope. Sources: www.cic.ugr.es (a, b, c, d); www.geo.unibe.ch (e).

cal and scanning electron microscopy (SEM) using an Environmental Scanning Electron Microscope (ESEM) FEI model Quanta 400, operating at 15–20 keV in Centro de Instrumentación Científica (CIC), Universidad de Granada (Spain) (Fig. 3.1b). Mounts were coated with ultra-pure gold (8–10 nm). In order to select the best location for the SHRIMP study, analyses on the zircons were guided by cathodoluminescence (CL) images (included in Appendix 3). Data reduction was carried out with the SHRIMPTOOLS software (available from www.ugr.es/fbea). SHRIMP results have been provided in Appendix 4. Associated errors are one sigma level. The error in $^{206}\text{Pb}/^{238}\text{U}$ averaging the standard has been already propagated. Th/U ratios are atomic ($^{232}\text{Th}/^{238}\text{U}$), not in weight. Point-to-point errors, calculated on replicates of the TEMORA standard, are: 0.37 % for $^{206}\text{Pb}/^{238}\text{U}$, and 0.44 % for $^{207}\text{Pb}/^{206}\text{Pb}$.

The common lead uncorrected $^{206}\text{Pb}/^{238}\text{U}$ ages (in Ma) were plotted as a combination of Kernel Density Estimates (KDE) diagrams and histograms performed with DENSITYPLOTTER version 8.0 (Vermeesch, 2012). The statistically significant age populations were

identified with the mixture modelling option implemented in the program. The optimal bandwidth automatically calculated by DENSITYPLOTTER resulted in a oversmoothing of the KDE diagrams in various samples, and the age populations obtained with the mixture modelling did not fit the modes in the KDE diagrams. Accordingly, a common bandwidth of 40 Ma was manually set for the KDE in all the studied samples. The resulting modes reasonably fit the age populations obtained by the mixture modelling. Bin width for histograms was set to 100 Ma. Concordia plots in Appendix 5 were displayed with Isoplot version 4.15 (Ludwig, 2008).

3.3. Metamorphic P-T conditions

Five garnet-bearing mica-schists were studied: RA-2, RA-0, 10.1, 16.8 and 16.16, in order to decipher the P-T conditions of the metamorphism affected the Nevado-Filábride complex (chapter 5).

The petrochronology strategy used in this Ph.D. Thesis involved the following steps (see Engi et al., 2017 for a detailed description): (1) classical thin section analysis for petrography (section 3.3.1), (2) quantitative compositional mapping on garnet combined with phase equilibria modelling on garnet and potassic mica (phengite) to retrieve P-T conditions (sections 3.3.2., 3.3.3 and 3.3.4) and (3) *in situ* U-Th-Pb allanite dating to date the exhumation event (section 3.3.5).

3.3.1. Petrography

The studied samples were investigated first by optical microscopy and SEM using an Environmental Scanning Electron Microscope (ESEM) FEI model Quanta 400, operating at 15-20 keV in the Centro de Instrumentación Científica (CIC), Universidad de Granada (Spain) (Fig. 3.1b).

3.3.2. Bulk rock composition

The computational methods used during phase equilibria modelling require obtaining bulk rock composition of the studied samples.

X-ray fluorescence (XRF) analyses of major elements of whole rocks in samples RA-0 and RA-2 were carried out with a Philips PW1040/10 spectrometer in the Centro de Ins-

trumentación (CIC) Universidad de Granada, (Spain) (Fig. 3.1c). The detection limit for major elements was 0.01 wt%. Loss on ignition (LOI) was determined with 0.5 g of powdered sample. Sample was first dried at 110°C and then heated to 1000°C for 1h. Typical precision was better than 51.5 % for an analyte concentration of 10 wt%.

For samples 16.16, 16.8, 10.1 representative bulk rock compositions were determined following the procedure described in Laurent et al. (2018). In order to check the reliability of these estimates the same technique was applied for samples RA-0 and RA-2, and the modelling results were compared with those obtained by XRF for these samples. The estimated bulk rock composition in samples RA-0 and RA-2 obtained by the two different methodologies, and the resulting P-T conditions for garnet were similar within uncertainty.

3.3.3. Quantitative compositional mapping on garnet

Compositional maps for major elements on garnet were obtained by high-resolution electron probe micro-analyser (EPMA). These grains were carefully selected based on backscattered electrons (BSE) images and point analyses. The selection criteria applied in this study included the size of the porphyroblast, the preservation and absence of retrogression and, whenever possible, their low inclusion content. The analyses were carried out at the Institute of Geological Sciences, University of Bern, using a JEOL JXA-8200 superprobe instrument. The detailed analytical procedure is given in Lanari et al. (2013, 2014). The analytical conditions were 15 keV accelerating voltage, 100 nA specimen current, and variable dwell times: 100 ms (samples 10.1 and 16.16); 150 ms (sample RA-0); 200 ms (samples 16.8 and RA-2). The dwell time used in each analytical session was based on the analytical time available and the size of the mapped areas. Map sizes are: 948 x 1228 μm for sample 16.16; 2200 x 2200 μm for sample 16.8; 1800 x 1800 μm for sample RA-0; 770 x 900 μm for sample 10.1; and 800 x 800 μm for sample RA-2. Nine elemental maps were obtained in two passes (Si, Mg, Na, Ca, K and Ti, Al, Fe, Mn). Data processing was performed using the software XMAPTOOLS 2.4.1 (Lanari et al., 2014, 2018). The analytical standardization was performed using the composition of high-quality spot analyses acquired on the same area (de Andrade et al., 2006). Pixels showing mixing compositions, either along the grain boundaries or around mineral inclusions were filtered out using the BRC function of XMAPTOOLS (Lanari et al., 2018). The grossular

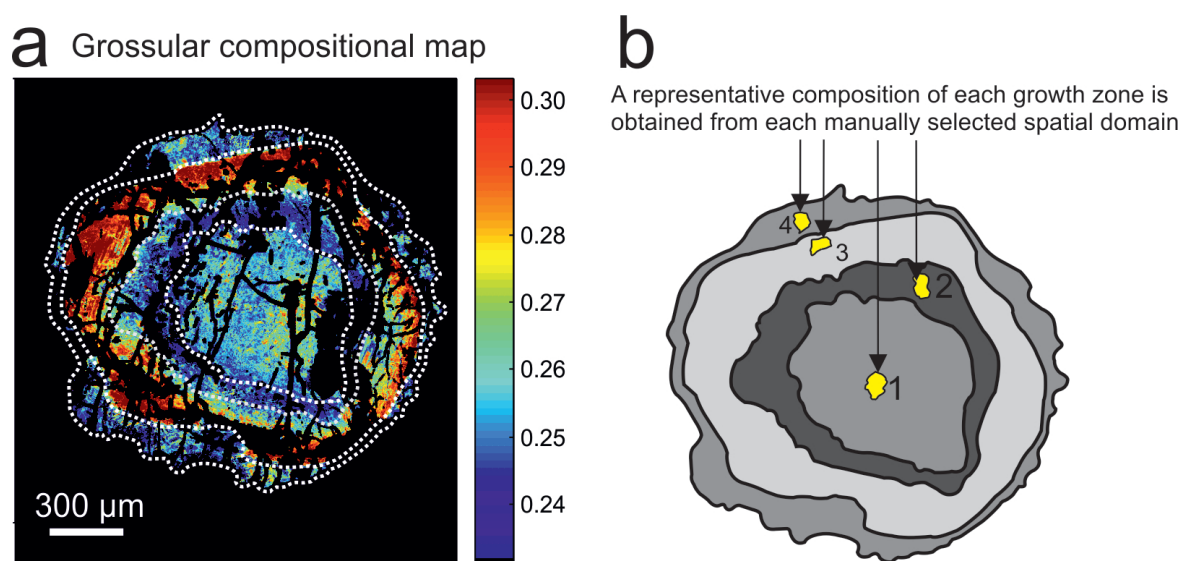


Figure 3.2. Diagrams illustrating the method used to estimate P-T conditions from garnet in sample RA-0. a) Grossular compositional map obtained by EPMA in the studied porphyroblast. Data processing and image display was performed using the software XMAPTOOLS 2.4.1. Dashed lines delimit four growth zones in the garnet. b) Simplified sketch showing the growth zones and the position and size of the selected spatial domains. The representative composition of each growth zone is obtained by averaging pixels of these domains.

compositional map obtained from the studied garnet porphyroblast in sample RA-0 is shown in Fig. 3.2a as an example.

3.3.4. Phase equilibria modelling

Following the strategy described in Lanari et al. (2017), P-T conditions of garnet growth were obtained for each successive growth zone of 5 selected porphyroblasts (one for each studied sample). These growth zones are identified based in compositional zonations observed in the end-member fraction maps, i.e. grossular (Fig. 3.2a), almandine, pyrope and spessartine compositional maps. The representative composition of each growth zone is obtained by averaging pixels from manually selected spatial domains (yellow areas in Fig. 3.2b).

The composition of each successive growth zones were used to model the P-T-X conditions of garnet growth by using the program GRTMOD 1.5.3 (Lanari et al., 2017). This program provides a numerical simulation of the garnet evolution based on the composition of the successive growth zones characterized in the compositional maps, combined with an iterative modelling strategy. This model relies on predictions made by Gibbs free energy minimization and the program THERIAK-DOMINO (version 04.02.2017, and the internally

consistent thermodynamic database of Holland and Powell (1998) and subsequent updates), including an optimization of the reactive bulk composition. Three variables are optimized: pressure (P), temperature (T), and for stages $n+1$, the volume fraction of all the previous growth zones fractionated from the bulk-rock composition. So, the reactive bulk composition of stage $n+1$ is estimated by fractionating a variable amount of the garnet previously formed (see details in Lanari et al., 2017). Previously formed garnet can thus be isolated from the reactive part of the rock (fractionation) or dissolve (resorption), i.e. partly react to form the new garnet generation. The predicted garnet composition for any P-T-X conditions is compared to the reference composition obtained from the map. By minimizing the differences between the measured and the modelled compositions obtained from each effective bulk composition (using the Nelder-Mead algorithm, a heuristic search method; Nelder and Mead, 1965) the program leads to constrain the optimal P-T-X condition for each growth stage. GRTMOD additionally yields a residual value (C_0 in Lanari et al., 2017) during the minimization procedure representing the quality of the isopleths intersection, i.e. the similarity between the observed modelled and garnet compositions. Low residual values (generally <0.04) denote a good fit between the measured and the modelled compositions.

Point analyses of phengites were obtained by EPMA in the Centro de Instrumentación (CIC, Universidad de Granada, Spain) using a Cameca SX100 instrument (Fig. 3.1d) with a beam diameter of 5-7 μm , accelerating voltage of 15 kV and 10-15 nA beam current and variable counting times. The data were reduced using the X-PHI correction (Merlet, 1994). The following standards were used: albite (Na), periclase (Mg), synthetic SiO_2 (Si), Al_2O_3 (Al), TiO_2 (Ti), Fe_2O_3 (Fe), Cr_2O_3 (Cr), NiO (Ni), MnTiO_3 (Mn), sanidine (K) and diopside (Ca). The composition of phengite measured by EPMA was compared with the predictions of THERIAK-DOMINO using the two following compositional variables: Si (atoms per formula unit, apfu) and XMg ($\text{Mg}/(\text{Mg}^+ + \text{Fe}^{2+})$, with Mg and Fe in apfu, assuming no ferric iron, $\text{Fe}^{3+} = 0$). By way of illustration, see results for sample 10.1 in Fig. 3.3. For each Si-XMg pairs (one for each phengite analysed, Fig. 3.3a), the optimal P-T conditions were determined using the intersection between these two isopleths (Fig. 3.3b). P-T estimates from phengites are presented as ellipses (Fig. 3.3b) corresponding to each individual analysis in the P-T diagram with a generic uncertainty of ± 0.01 for both Si (apfu) and XMg (1σ). The relative and absolute uncertainties were estimated using a Monte Carlo simulation and a single phengite composition. The relative uncertainty,

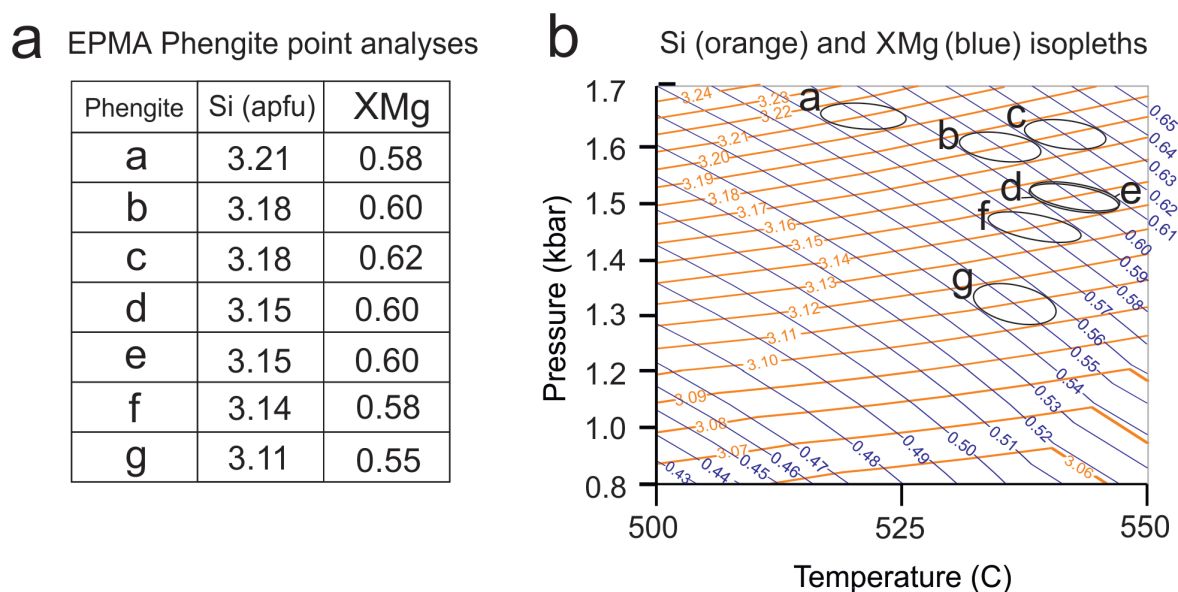


Figure 3.3. Diagrams illustrating the method used to estimate P-T conditions from phengite in sample 10.1 a) EMPA analyses showing Si and XMg values for seven analyzed phengites (a-g). Si content is in atoms per formula unit (apfu). b) P-T diagram showing the Si and XMg isopleths carried out with the program THERIAK-DOMINO. Each Si-XMg pair corresponds to one intersection between the two isopleths. The optimal P-T conditions are presented as ellipses. The uncertainty is ± 0.01 for both Si and XMg (1σ).

based on counting statistics, is 3.151 ± 0.006 apfu for Si^{4+} and 0.541 ± 0.008 for XMg. The total uncertainty including the relative uncertainty and the absolute uncertainty, estimated using the external reproducibility, is 3.151 ± 0.011 apfu for Si^{4+} and 0.541 ± 0.015 for XMg. Therefore the generic uncertainty proposed above (± 0.01) is relevant to visualize how the relative uncertainty in composition (between two spot analyses) affects the P-T conditions. The ellipses only show the uncertainty of the EPMA analyses; they do not reflect the uncertainties of the thermodynamic models.

The procedure with phengites is similar to that followed in garnets, regarding in both cases the most probable P-T is achieved after comparing the EPMA analysis with the predictions of THERIAK-DOMINO. Despite the strategy is similar, in the case of phengite the selection was performed manually, as only two independent variables are involved (leading to a “perfect” P-T solution marked by the intersection of two isolines; Fig. 3.3b) and fractionation effects for white mica are negligible (Airaghi et al., 2017). This is not possible for garnet (3-4 isolines) for which a weighted procedure is required to obtain “optimal” P-T conditions (Lanari and Duesterhoeft, 2019). In addition fractionation effects are strong and can significantly affect the P-T results (Lanari and Engi, 2017 and references therein).

3.3.5. Th-U-Pb dating in allanites by LA-ICP-MS

Allanite grains were identified in BSE images using a ZEISS EVO 50 scanning electron microscope at the Institute of Geological Sciences, University of Bern (Fig. 3.1e). Analyses for the allanite dating were guided by BSE images in order to identify internal texture and compositional zoning in allanites. Allanite dating was performed by using a LAI-CP-MS GeoLas Pro 193 nm ArF excimer laser coupled to an Elan Dynamic Reaction Cell (DRC-e) ICP-MS at the Institute of Geological Sciences, University of Bern (Switzerland). The analytical procedure is described in Burn et al. (2017). Pre-ablation was performed for four to five pulses with an energy density of 2.5 J cm^{-2} , a repetition rate of 1 Hz, and spot sizes of 40 and 32 μm . Ablation was carried out with an energy density of 2.5 J cm^{-2} , a repetition rate of 9 Hz, and spot sizes of 32 and 24 μm . A gas mixture of He (1 L min^{-1}) and H₂ (0.08 L min^{-1}) was used for aerosol transport from the ablation cell to the plasma. Settings on instrument were optimized to increase the sensitivity of heavy masses (e.g. ^{238}U , ^{232}Th , ^{206}Pb , ^{207}Pb , ^{208}Pb). Oxide production (ThO⁺ / Th⁺) was kept lower than 0.5 %. NIST SRM 610 measurements were performed for quantify U and Th concentrations. Plešovice zircon (Sláma et al., 2008) was used as primary standard. In order to minimize instrumental drift the acquisition series were approximately 1 h, including between 8 and 12 unknown analyses bracketed by 8 analyses of the standard Plešovice used for U-Th-Pb ratio calibration and SRM 610 for trace element calibration. Data reduction was performed using the in-house software Trinity (Burn et al., 2017).

Chapter 4

Description on the lithological succession

4.1. Introduction

The study of a large metamorphic complex implies deciphering the succession of the rocks, and to highlight the characteristics of the contacts between the different lithologies (e.g. stratigraphic and tectonic contacts). For that is mandatory the implementation of geological maps, transects and lithological columns of the area of study, accompanied by an appropriate petrological characterization. Only after this previous study has been accomplished, later studies focused on the specific aspects of the metamorphic complex (e.g. thermobarometric and geochronological studies) can be undertaken.

As stated in section 2.3.1, several divisions in tectonics units have been proposed for the Nevado-Filábride through time, and nowadays there is not a unanimous scheme in the literature (Fig. 2.4). Accordingly, the comparison between geological cartographies included in these studies is difficult in the best case or impossible when the adopted division criteria are incompatible. Several of these divisions are mainly supported by petrological and metamorphic criteria exclusively. Although a correct petrological and mineralogical characterization is undoubtedly important, it is practically useless without field data and the appropriate mapping of the complex. Besides, if the division criteria are inconsistent with field data, they lead to improbable tectono-stratigraphic solutions. Additionally, several geological cartographies in different areas of the Nevado-Filábride complex include errors which have been maintained through successive studies. Therefore any tectono-metamorphic study of the Nevado-Filábride can be accomplished without revising the cartography of the complex.

Below it is presented a new cartography of key areas of the Nevado-Filábride complex, and a description of the lithological succession based on field, petrological and mineralogical data. Six studied areas were selected: three in the western part of the Sierra Nevada, one in the central part of the Sierra Nevada, one in the central part Sierra de los Filabres and one in the eastern part of Sierra de los Filabres (Fig. 4.1). The following sections provide a specific background focused in the different divisions reported in each area, followed by a description of the lithological succession of such area. The lithological successions are supported by geological maps, schemes, cross sections, columns and field images. Besides, the present chapter provides a mineralogical characterization and BSE images of the different types of schists (main object of study in this Ph.D. Thesis).

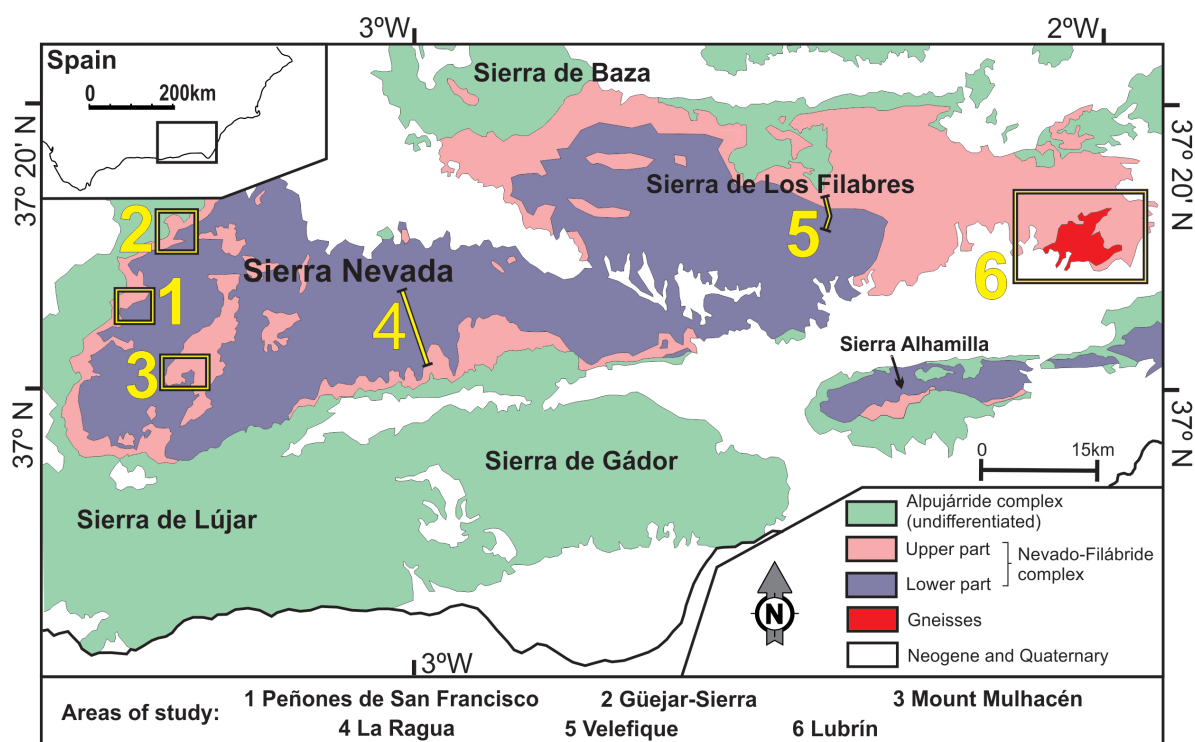


Figure 4.1. Geological map of the Betic Cordillera with the location of the zones studied in chapter 4.

4.2. Western part of Sierra Nevada

Three areas have been investigated in the westernmost part of the Sierra Nevada (Fig. 4.1): (1) the Peñones de San Francisco area which includes the area between the Peñones de San Francisco hills and the NW sector of the Mount Veleta (Fig. 4.2); (2) the Güejar-Sierra area in NE of the town of the same name (Fig. 4.3); and (3) the Mount Mulhacén area and part of its southern hillside (Fig. 4.4).

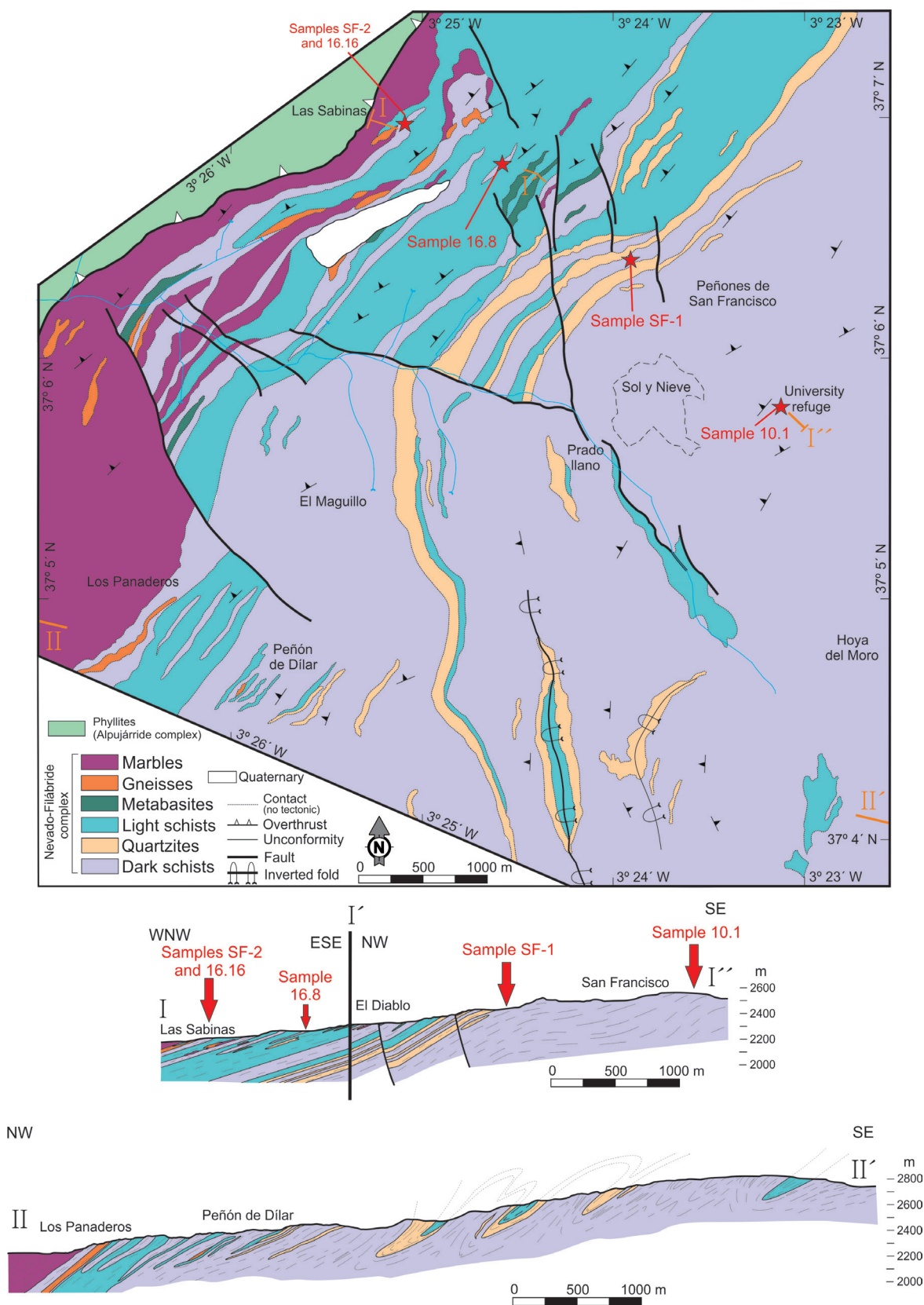


Figure 4.2. Geological map and cross sections of the Peñones de San Francisco area (western part of Sierra Nevada). Red stars and arrows indicate the location of the samples studied in chapters 5 and 6.

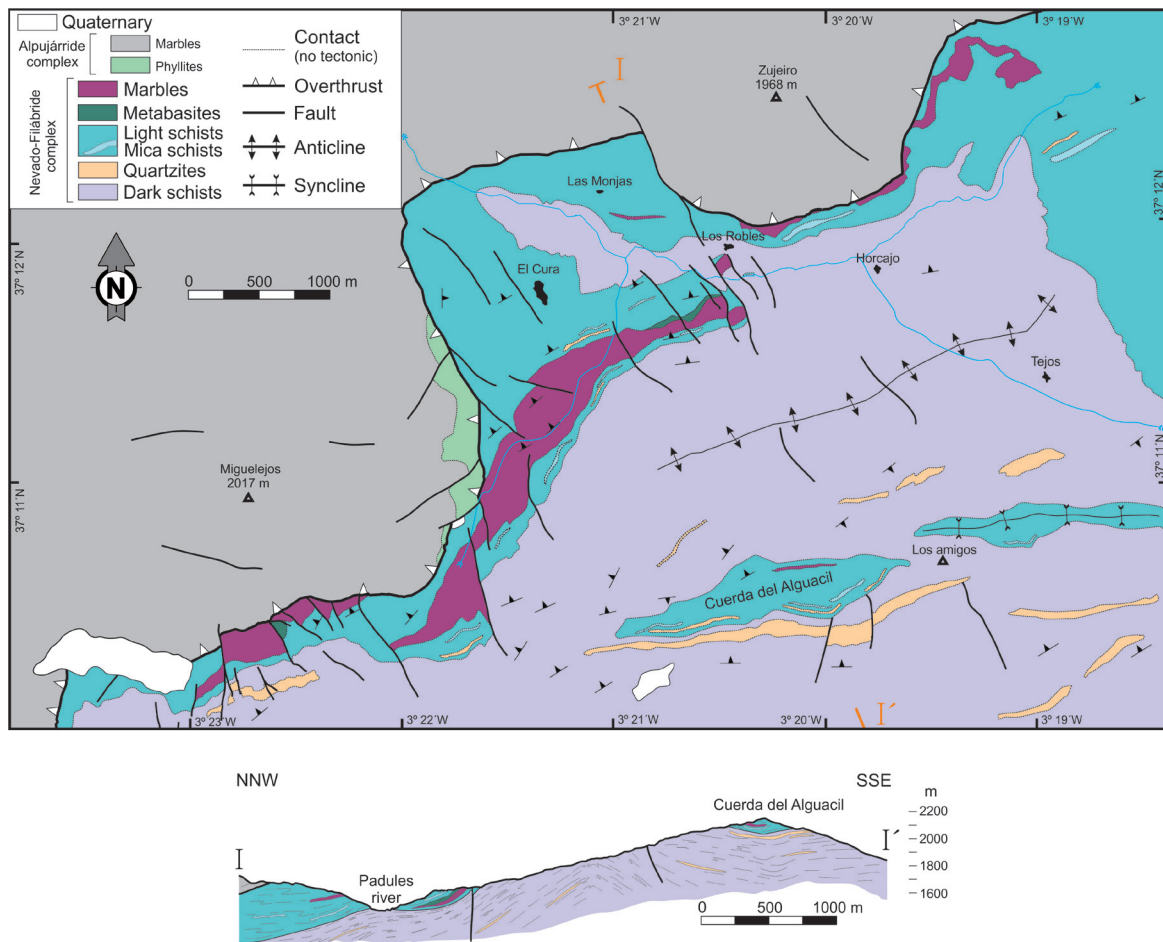


Figure 4.3. Geological map and cross section of the Güéjar-Sierra area (western part of Sierra Nevada).

The column in Fig. 4.5 shows the lithological succession of the Nevado-Filábride complex in the Peñones de San Francisco area (selected as representative for the western part of the complex in Sierra Nevada).

4.2.1. Previous proposed divisions

The previous cartographies in this sector of the Sierra Nevada strongly differ between authors. These disagreements are particularly remarkable in the Peñones de San Francisco area (Fig. 4.2) and they are discussed in the first place. In the cross section of the Peñones de San Francisco to Las Sabinas pass (cross section I - I' in Fig. 4.2), Puga (1971) differentiated two units: the lowermost Sierra Nevada (later named as Veleta unit) and the Sabinas units. Puga et al. (1974) extended this scheme and identified four units, from bottom to top: Yeguas (equivalent to Veleta unit), San Francisco, Caldera and Sabinas. The San Francisco unit was firstly described in this work, and the authors restricted its

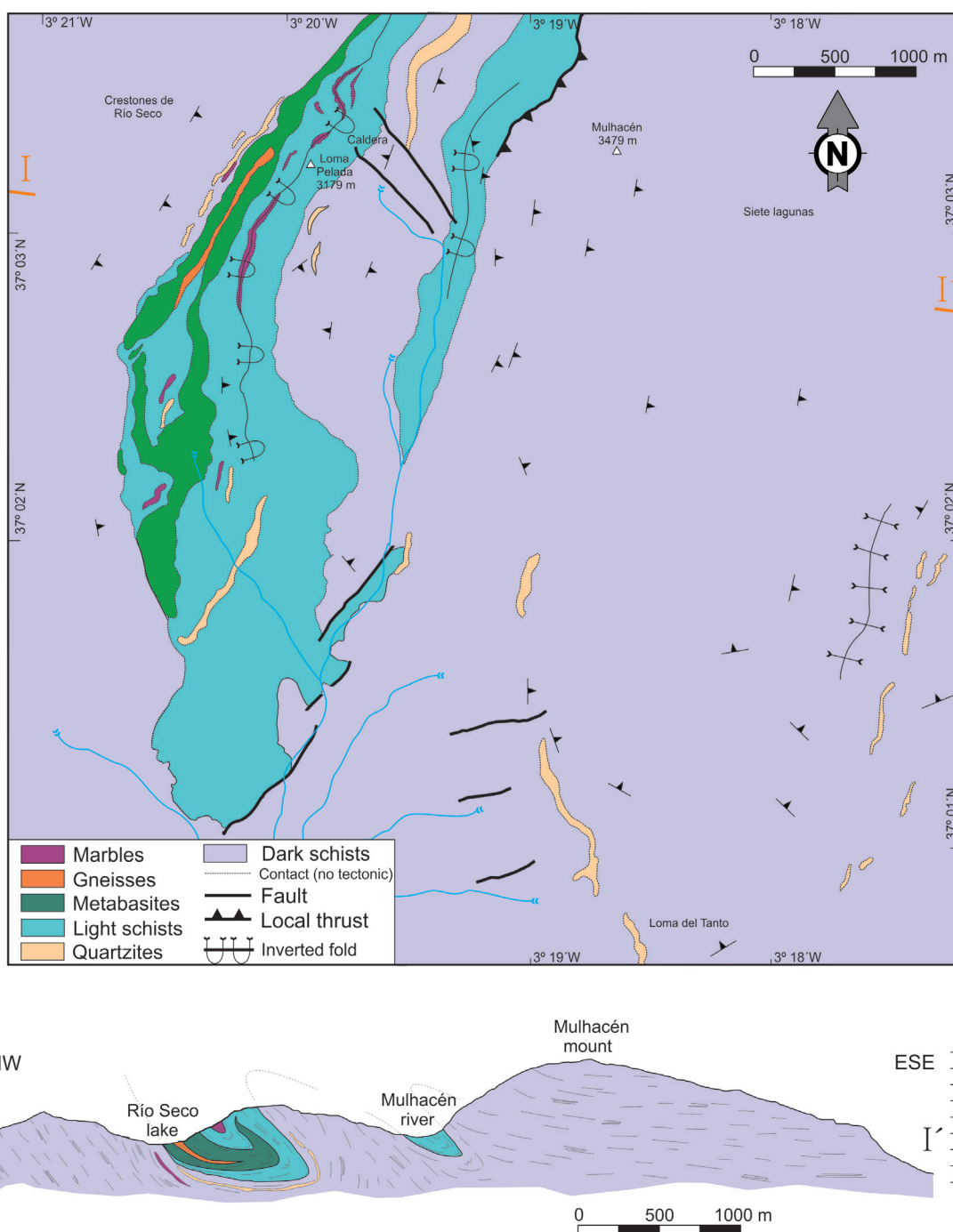


Figure 4.4. Geological map and cross section of the Mount Mulhacén area (western part of Sierra Nevada).

presence to this area of the complex. According to these authors, this unit shares petrological and mineralogical similarities with the overlying Caldera unit. However no clear differences were provided to support the individualization of the San Francisco unit. Díaz de Federico et al. (1980) maintained this last division, but Nieto (1996) did not include

Fig.4.5. (cont.)

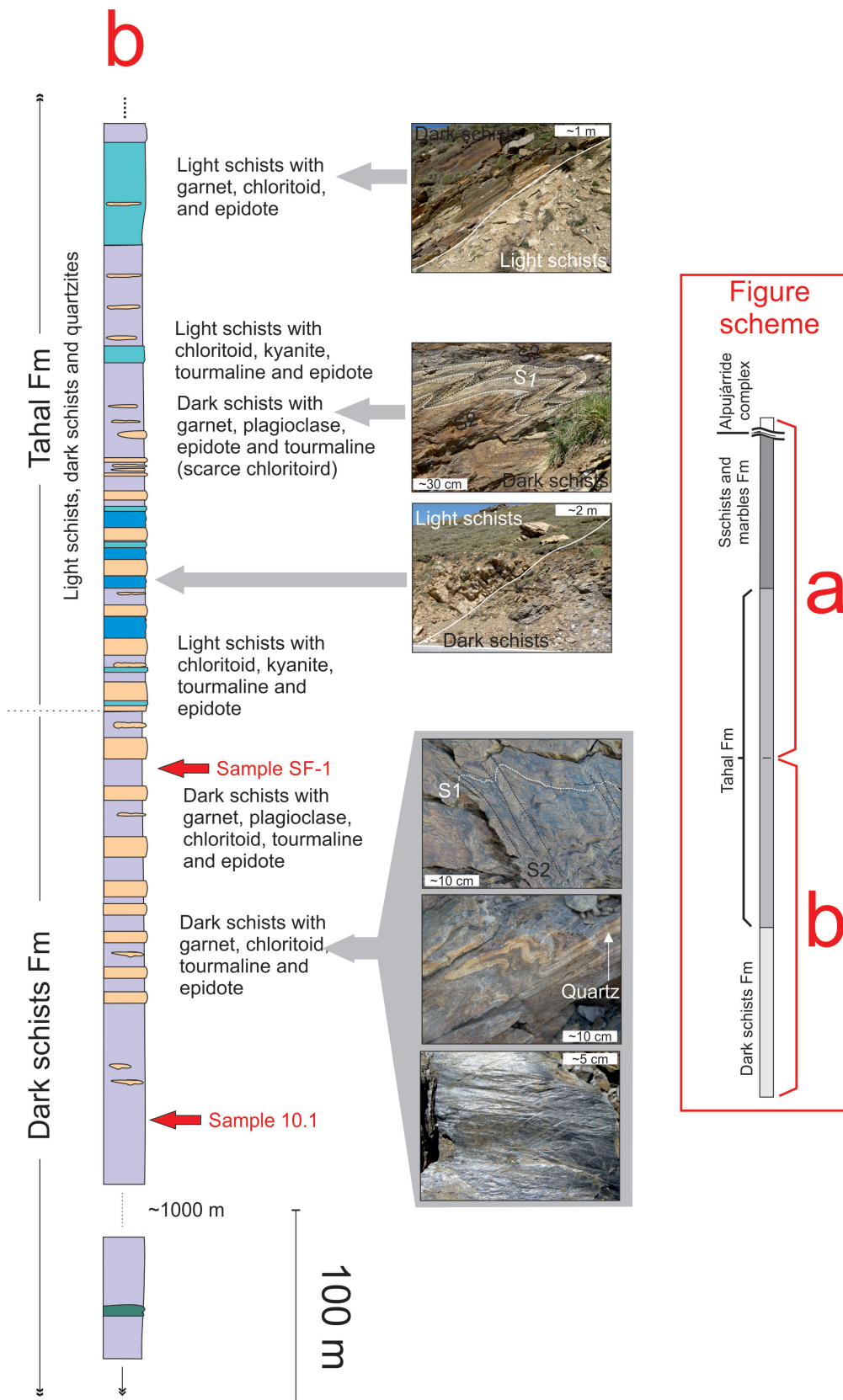


Figure 4.5. Lithological succession and field images of the western part of the Nevado-Filábride complex. Red arrows indicate the location of the samples studied in chapters 5 and 6.

the unit of San Francisco, and Puga (1977) and Puga and Díaz de Federico (1978) included the Ophiolite unit between the Sabinas and Caldera units. Galindo-Zaldívar (1993) did not identify different units in the area but the existence of a continuous lithological succession. Puga et al. (2002) proposed the existence of two tectonic complexes (Veleta and Mulhacén) instead of a unique Nevado-Filábride complex (Fig. 2.4). Their Mulhacén complex comprises the Caldera, Ophiolite and Sabinas units. Martínez-Martínez et al. (2002) and Martínez-Martínez et al. (2010) described three units for the Nevado-Filábride complex in the area: the Ragua, Calar-Alto and Bédar-Macael units (Fig. 2.4). According to these authors, the contacts between these units are ductile-brittle extensional shear zones. According to Martínez-Martínez et al. (2010) these shear zones lead to severe omissions in the sequences from the western area of the complex: the marbles and part of the light schists from the lower part of the Calar-Alto unit were omitted; whilst the Bédar-Macael unit preserves dark schists, gneisses, metabasites and marbles, but the light schists were almost obliterated. Gómez-Pugnaire et al. (2012) provided a succession of lithological formations in this area: the lower, the Tahal, the metaevaporitic and the Marbles and calc-schists Fms. These authors did not report in this area the presence of the uppermost rocks for the Nevado-Filábride complex (the Chive formation according their division, Fig. 2.4).

An example of the discrepancies between the proposed divisions are the differences in cartographies of Puga et al., (2002) and Martínez-Martínez et al., (2002) in the Peñones de San Francisco area. Although the rocks attributed to the Veleta complex (Puga et al., 2002) and La Ragua unit (Martínez-Martínez et al., 2002) are nearly the same (dark schists and quartzites), no equivalence exists regarding the upper limit of these units. The Veleta complex widely outcrops in this area, whilst La Ragua unit is not present and the upper materials of the Veleta unit are included in the Calar-Alto unit of Martínez-Martínez et al. (2002).

In the Mount Mulhacén area, most of previous divisions have been proposed (Díaz de Federico et al., 1980; Puga et al., 2002; Martínez-Martínez et al., 2002; Gómez-Pugnaire et al., 2012) and the discrepancies concerning the extension of the Veleta complex, La Ragua unit and the lower formation of Gómez-Pugnaire et al. (2012) also lead to an irreconcilable equivalence.

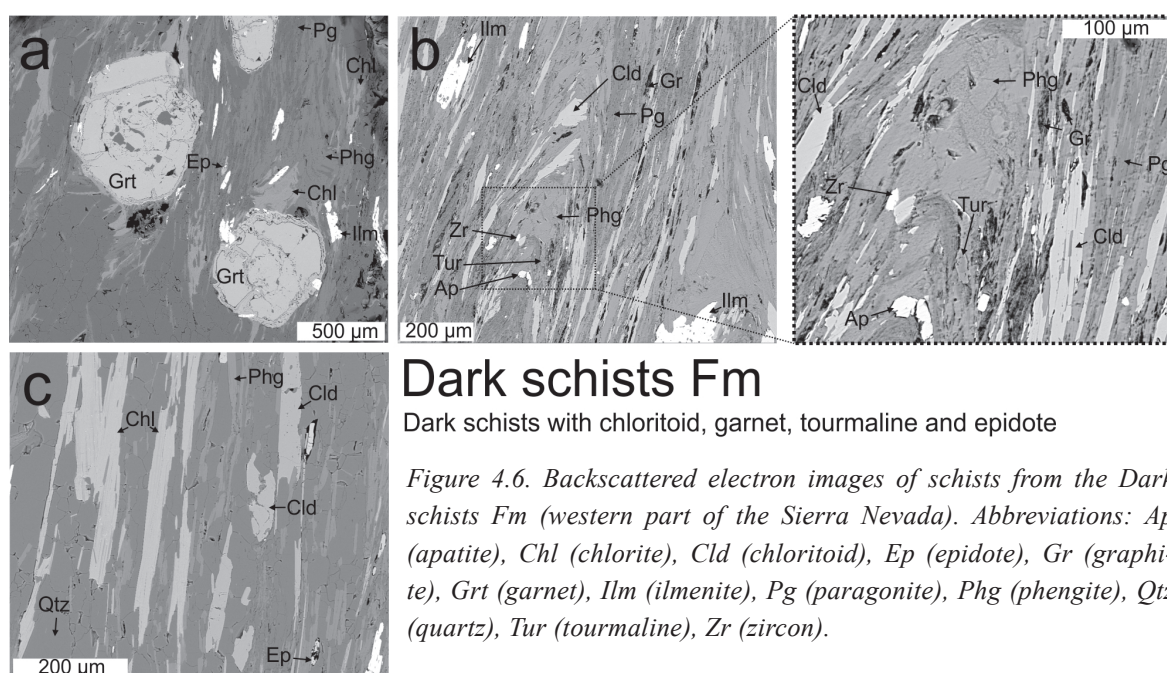
In the Güéjar-Sierra area, García-Dueñas and Navarro-Vilá (1979) distinguished between the Veleta and the Mulhacén units. It is important to note that these authors do not separate the Mulhacén in different sub-units or formations. By the contrary, they identified several lithologies (schists, metabasites, gneisses and marbles) not necessary tectonically superposed.

4.2.2. Lithological succession

The lithological succession of the Nevado-Filábride complex in the Peñones de San Francisco area is described below (Fig. 4.5).

4.2.2.1. Dark schists Fm

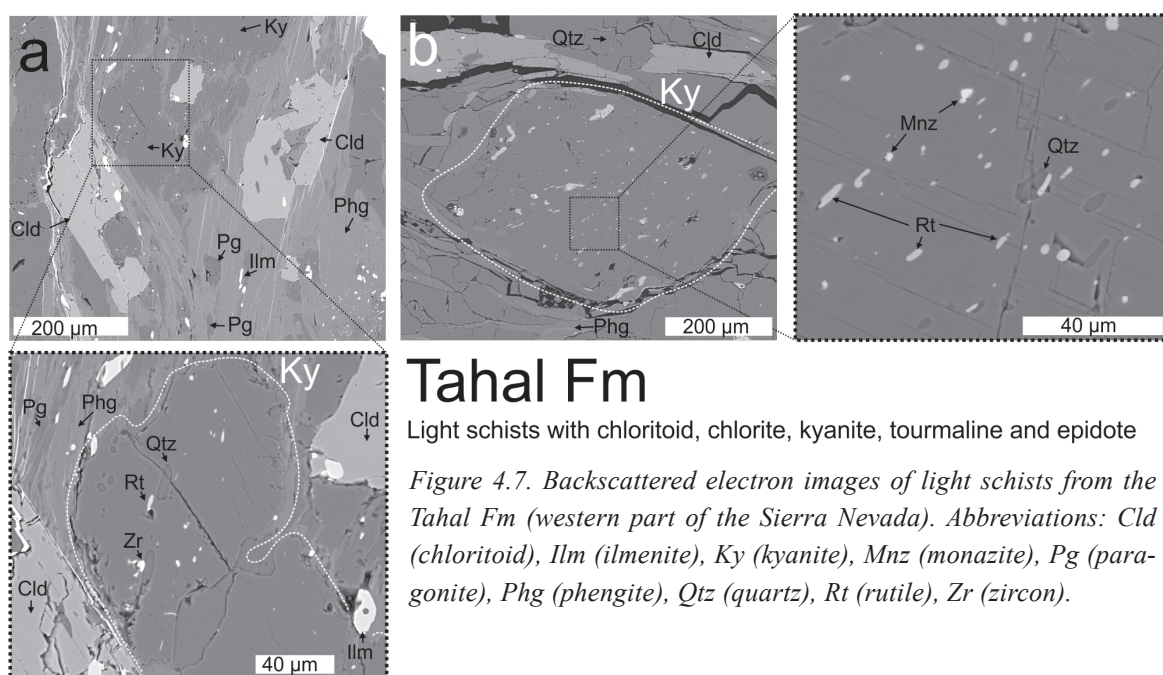
In the western part of the Nevado-Filábride complex the lowermost rocks are mainly graphite-bearing dark schists (Fig. 4.6a) pertaining to the Dark schists Fm. Schists are dark grey- or black coloured and punctually slightly golden coloured. They contain chloritoid (Figs. 4.6b and inset; 4.6c), garnet (Fig. 4.6a), tourmaline (Figs. 4.6b and inset) and epidote (Fig. 4.6a, c). Garnet thickness ranges from 0.5 to 1 cm. Some thin layers (up to 2 m) are garnet-lacking. In the upper part of the formation, in addition to the mentioned phases, the dark schists contain scarce plagioclase.



4.2.2.2. Tahal Fm

The contact between the Dark schists and the Tahal Fms is characterized by an alternating of dark schists and quartzites (Fig. 4.5). The thickness of quartzite layers increases progressively from few meters up to 20 m in the lower part of the Tahal Fm. Remarkably thicker quartzite levels outcrop in the Peñones de San Francisco and Güéjar-Sierra areas (Figs. 4.2 and 4.3). These rocks include quartz and white mica (phengite and paragonite) and scarce feldspar.

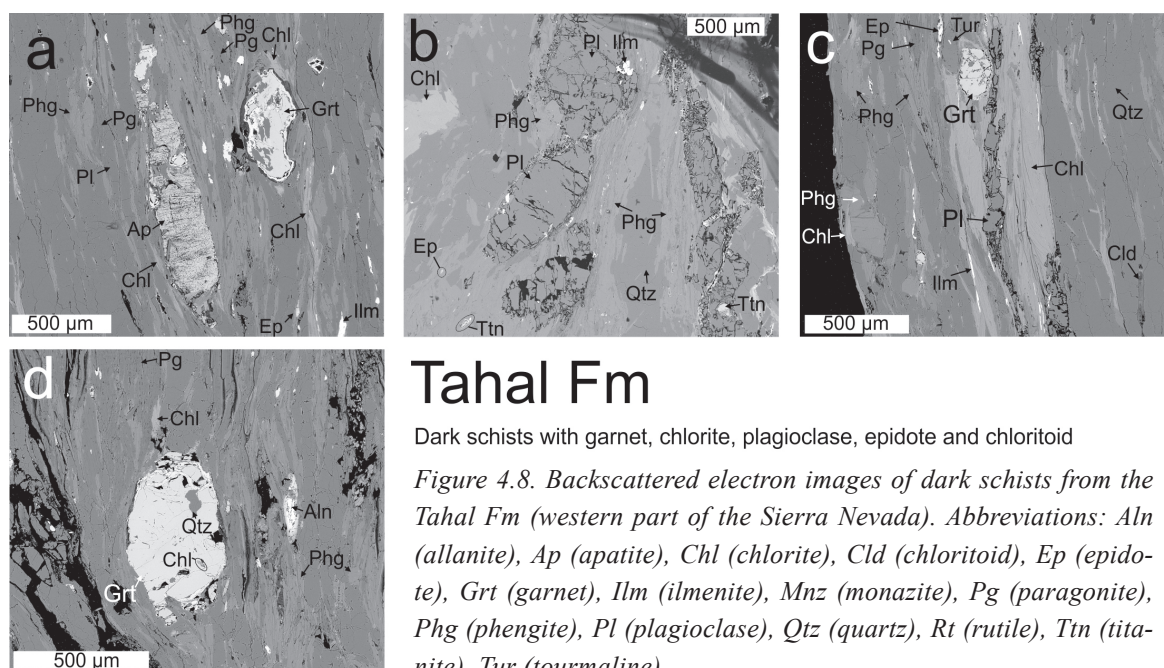
In the lower part of the Tahal Fm, thin levels of light schists are interbedded with the dark ones and the quartzites (Fig. 4.5). The occurrence and thickness of the light schists progressively increases upwards, and reaches hundreds of meters in the Peñones de San Francisco and Güéjar-Sierra areas (Figs. 4.2 and 4.3). The light schists show chloritoid, chlorite, kyanite (Fig. 4.7a and inset; 4.7b and inset), tourmaline and epidote. Towards the top of the formation, the chloritoid, kyanite and tourmaline content in the light schists decreases and they show garnet (up to 1 cm thick). The dark schists are formed by garnet (up to 5 mm) (Fig. 4.8a, c, d), plagioclase (Fig. 4.8a-c), epidote (Fig. 4.8a-c), allanite (Fig. 4.8d), tourmaline and scarce chloritoid (Fig. 4.8c). The chloritoid and plagioclase content strongly varies in the Dark schists being higher in the lower and upper parts of the formation than in the middle part (Fig. 4.5). The quartzite layers (here with albite and chlorite) progressively decrease its thickness up to 3 m in the upper part of the Tahal Fm (Fig. 4.5).



Tahal Fm

Light schists with chloritoid, chlorite, kyanite, tourmaline and epidote

Figure 4.7. Backscattered electron images of light schists from the Tahal Fm (western part of the Sierra Nevada). Abbreviations: Cld (chloritoid), Ilm (ilmenite), Ky (kyanite), Mnz (monazite), Pg (paragonite), Phg (phengite), Qtz (quartz), Rt (rutile), Zr (zircon).



Tahal Fm

Dark schists with garnet, chlorite, plagioclase, epidote and chloritoid

Figure 4.8. Backscattered electron images of dark schists from the Tahal Fm (western part of the Sierra Nevada). Abbreviations: Aln (allanite), Ap (apatite), Chl (chlorite), Cld (chloritoid), Ep (epidote), Grt (garnet), Ilm (ilmenite), Mnz (monazite), Pg (paragonite), Phg (phengite), Pl (plagioclase), Qtz (quartz), Rt (rutile), Ttn (titanite), Tur (tourmaline).

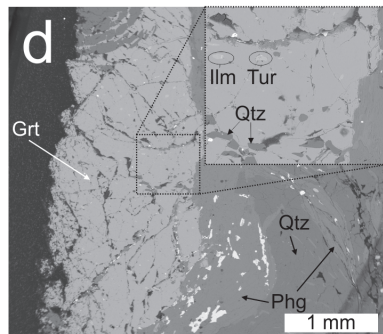
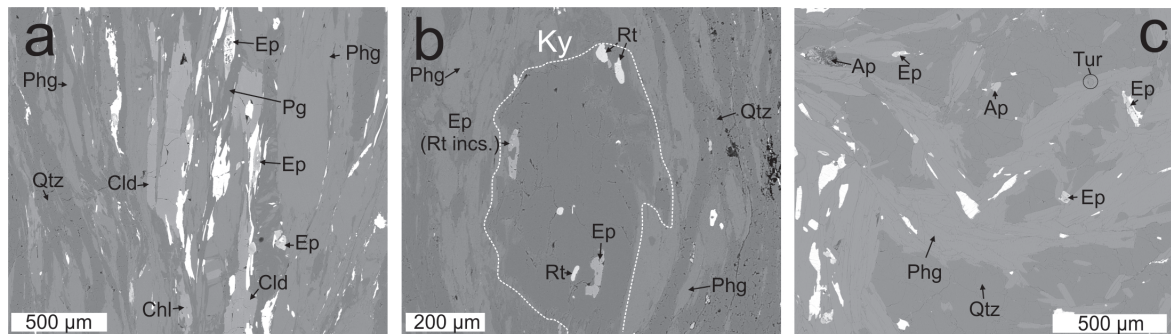
4.2.2.3. Schists and marbles Fm

In the Schists and marbles Fm, the light schists are remarkably bright and white- or green-coloured, and show big white mica grains (phengite and paragonite) (Fig. 4.9a-d), epidote (Fig. 4.9a-c), tourmaline (Fig. 4.9c, d), big garnet porphyroblasts (up to 2 cm thick) (Fig. 4.9d), chloritoid (Fig. 4.9a) and kyanite (Fig. 4.9b). There are levels of micacites of few meters interlayered with the light schists (particularly in the Güéjar-Sierra area, Fig. 4.3). Decametric levels of dark schists are present between the light ones. The dark schists in this formation show garnet (Fig. 4.10a), biotite (Fig. 4.10a inset), epidote and allanite. In Peñones de San Francisco area they also include plagioclase.

In the western part of Sierra-Nevada, the occurrence of metabasic rocks of the Tahal and Schists and marbles Fms strongly varies between areas. In the Peñones de San Francisco and the Mount Mulhacén areas these rocks are common as continuous levels of 2 to 5 m thick, in general preserving general schistosity S2. The levels of gneisses reach thickness of tens of meters and remarkable lateral continuity in the Peñones de San Francisco and Mount Mulhacén areas (Figs. 4.2 and 4.4).

Carbonate rocks are present as marble levels of few centimetres to tens of meters thick in the Tahal and, in particular, the Schists and marbles Fms (Fig. 4.5). They are usually accompanied by calc-schists. Close to the contact with the overlying Alpujárride com-

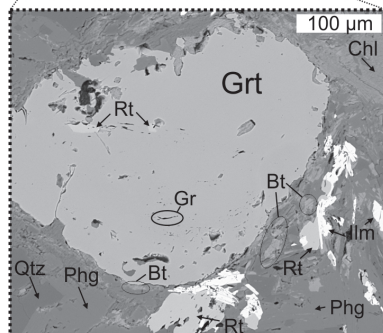
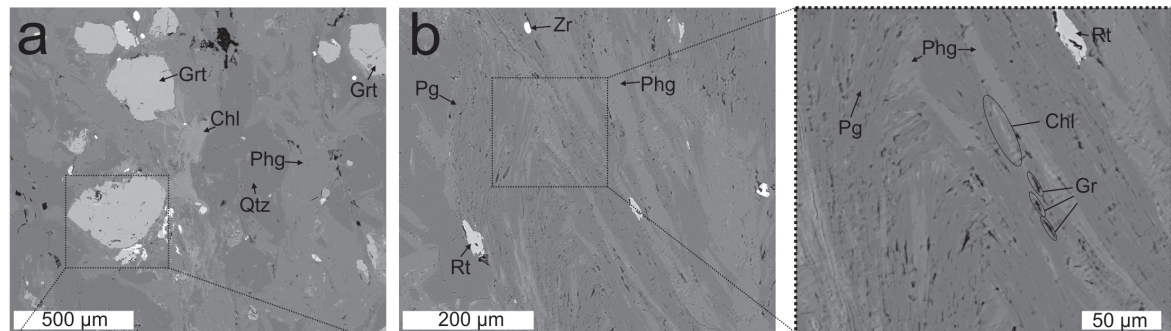
plex, marbles outcrop as remarkably thick banks (up to 30 m) (Fig. 4.5). These rocks are cream- to bluish coloured, and commonly banded. They are formed by calcite, dolomite and scarce white mica grains (mainly phengite) following the main schistosity S2. The marbles are indifferently in contact with light schists, dark schists, gneisses and metabasites. Calc-schists with abundant phengite and paragonite form thin layers of few centimetres interbedded in both light schists and marbles.



Schists and marbles Fm

Light schists with big garnets, chlorite, epidote and tourmaline (scarce kyanite and chloritoid)

Figure 4.9. Backscattered electron images of light schists from the Schists and marbles Fm (western part of the Sierra Nevada). Abbreviations: Ap (apatite), Chl (chlorite), Cld (chloritoid), Ep (epidote), Grt (garnet), Ilm (ilmenite), Ky (kyanite), Pg (paragonite), Phg (phengite), Qtz (quartz), Rt (rutile), Tur (tourmaline).



Schists and marbles Fm

Darks schists with garnet, chlorite, biotite and epidote

Figure 4.10. Backscattered electron images of dark schists from the Schists and marbles Fm (western part of the Sierra Nevada). Abbreviations: Biotite (bt), Chl (chlorite), Gr (graphite), Grt (garnet), Ilm (ilmenite), Pg (paragonite), Phg (phengite), Qtz (quartz), Rt (rutile), Zr (zircon).

4.3. Central part of Sierra Nevada

In the central part of Sierra Nevada it has been studied the area between La Ragua mountain pass and the S of the village of Bayarcal. This area corresponds to the southern flank of the general E-W anticline of Sierra Nevada (Fig. 4.11).

4.3.1. Previous proposed divisions

Several divisions proposed for the western part of Sierra Nevada have been also applied in this area. Initial works include Puga (1971) and Díaz de Federico et al. (1981) who identified in this sector the Veleta, Caldera and Sabinas units. Galindo-Zaldívar (1993) rejected the existence of a division into tectonic units and rather points to a single sequence for the complex in this area. Puga et al. (2002), Aerden et al. (2013) and Puga et al. (2017) reported the Veleta complex, the Caldera unit, the Ophiolite unit and the lower part of the Sabinas unit, these last three included in the Mulhacén complex of Puga et al. (2002). Martínez-Martínez et al. (2002) identified La Ragua and Calar-Alto units, but excluded in this area the Bédar-Macael unit (Fig. 2.4). Gómez-Pugnaire et al. (2012) reported the lower and the Tahal formations of their division, and only locally the Marbles and Calc-schists formation (Fig. 2.4).

In the central part of Sierra Nevada, most of the studies coincide that the uppermost rocks of the Nevado-Filábride pile (equivalent to the Schists and marbles Fm, Fig. 2.4) are severely reduced or obliterated. As in the western part of Sierra Nevada, in the central part there are irreconcilable differences regarding the extensions of the proposed units, in particular for the lower part of the Nevado-Filábride complex. Puga et al. (2002) pointed the lack of major mineralogical and petrological changes through the sequence of their Veleta complex. However, the contact between La Ragua and Calar-Alto units of Martínez-Martínez et al. (2002) is defined inside the Veleta complex of Puga et al. (2002). Likewise, it is impossible find an equivalence in the extension of La Ragua unit, the Veleta complex and the lower formation of Gómez-Pugnaire et al. (2012).

4.3.2. Lithological succession

The lithological succession of the Nevado-Filábride in this area is included in Fig. 4.12.

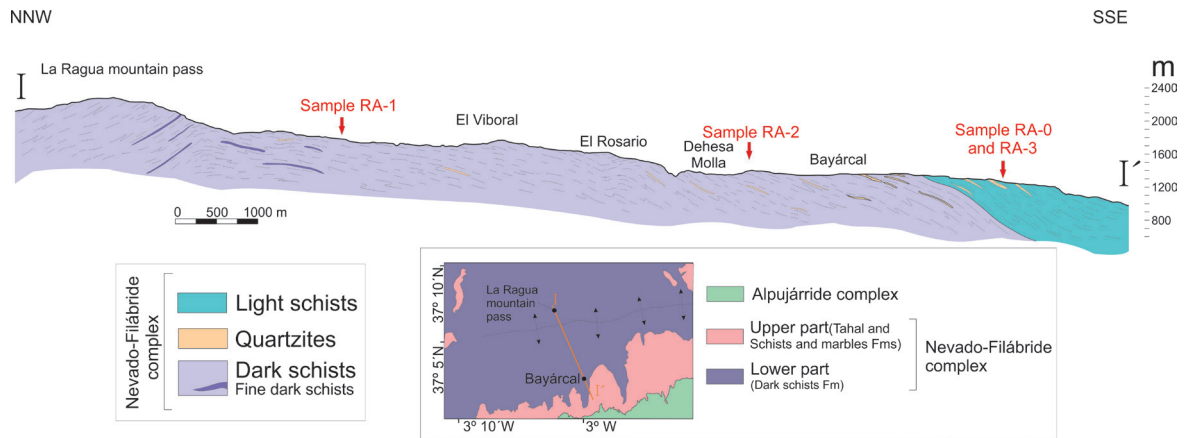


Figure 4.11. Cross section of La Ragua area (central part of the Sierra Nevada). Red arrows indicate the location of the samples studied in chapters 5 and 6.

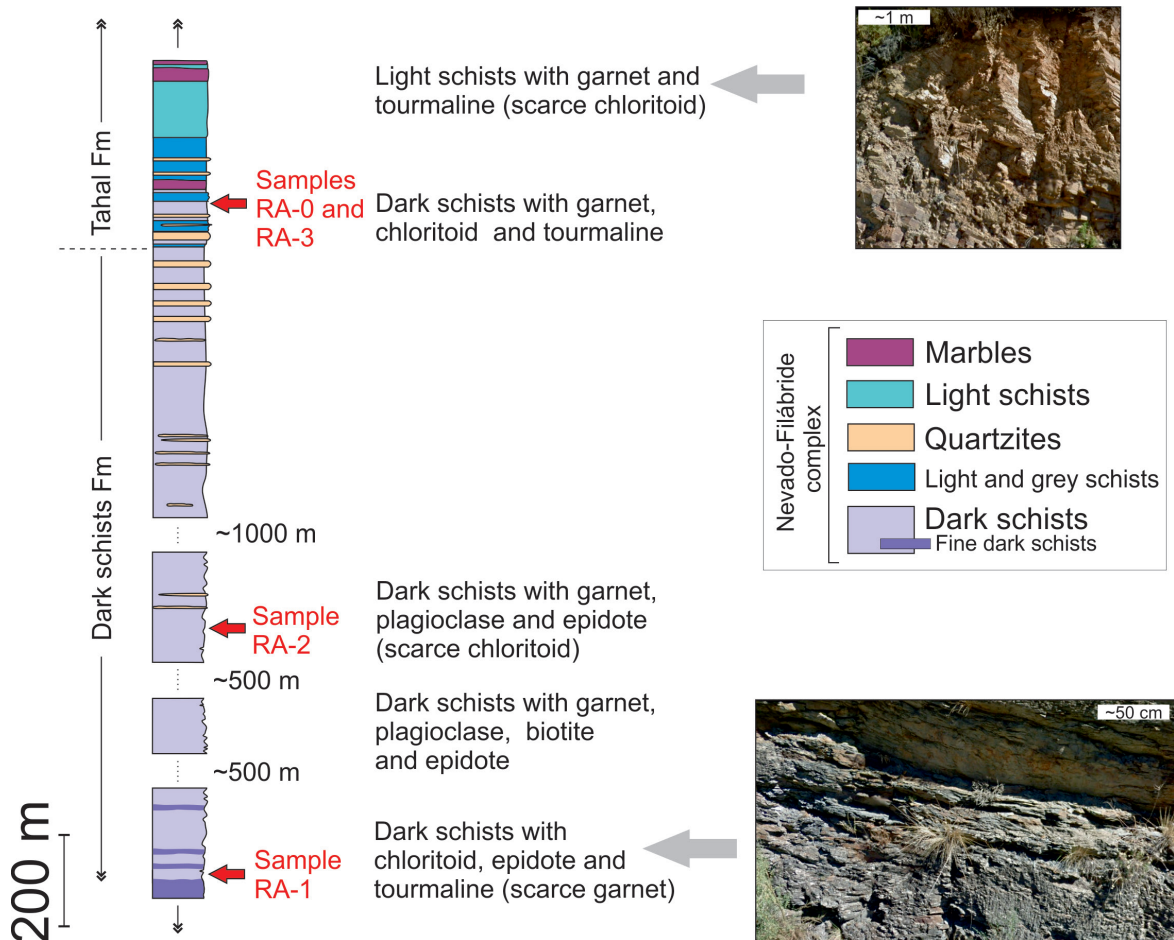
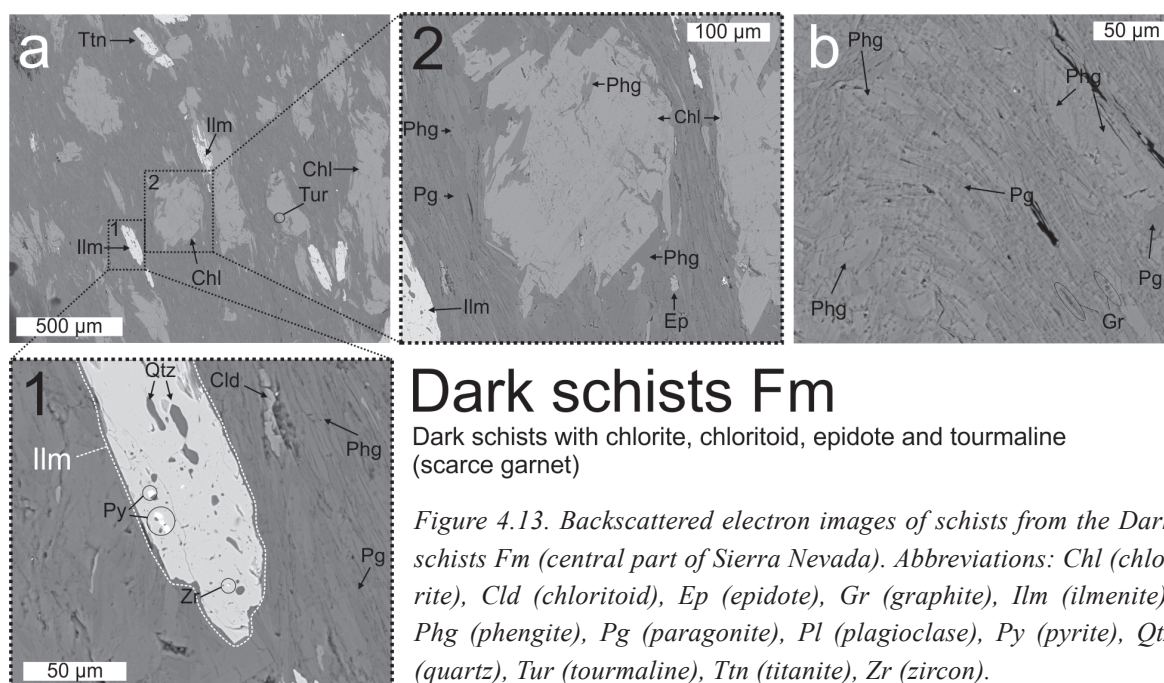


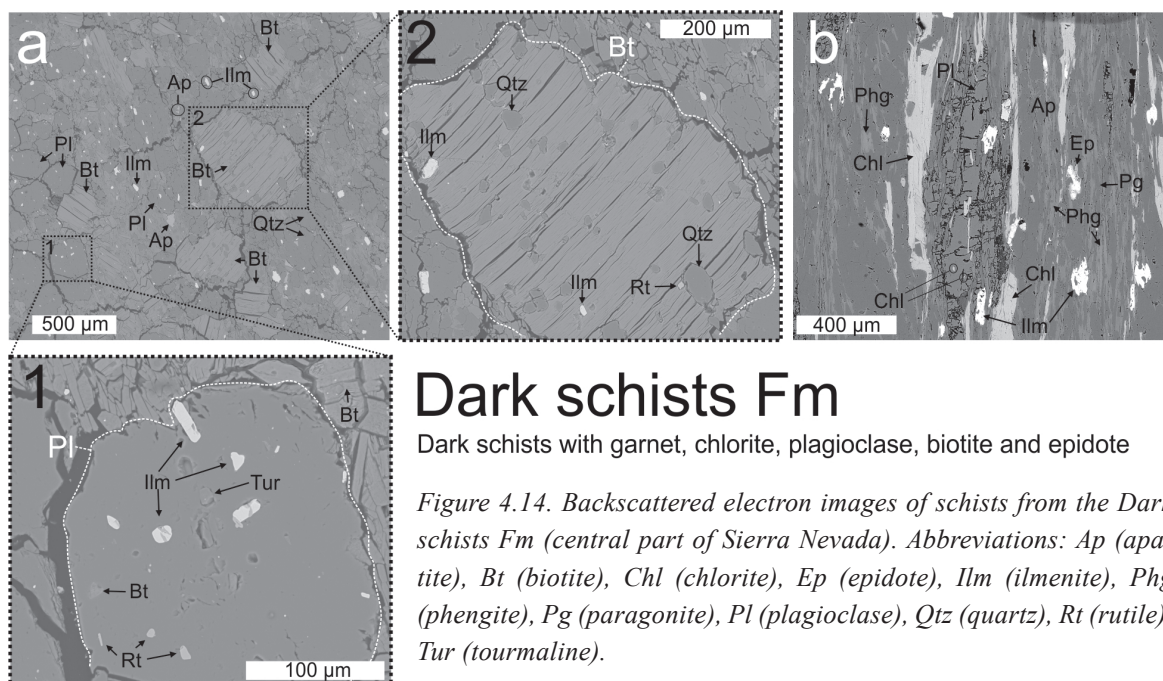
Figure 4.12. Lithological succession and field images of La Ragua area (central part of Sierra Nevada). Red arrows indicate the location of the samples studied in chapters 5 and 6.

4.3.2.1. Dark schists Fm

The Dark schists Fm is formed by graphite-bearing black-, dark grey- and brown colored schists (Fig. 4.13a) and layers (tens of meters thick) of dark slates (Fig. 4.13b). In the lowermost levels of the formation, the dark schists contain chloritoid (Fig. 4.13a and inset 1), epidote (Fig. 4.13a and inset 2) and tourmaline (Fig. 4.13a). Garnet is absent or preserved as small porphyroblasts (up to 1 mm) usually chloritized (Fig. 4.13a and inset 2). The garnet content and grain size both increase upwards, whilst chloritoid content decreases.



In the upper levels of the formation, the dark schists show garnet (up to 8 mm), plagioclase (Fig. 4.14a and inset 1; 4.14b), epidote (Fig. 4.14b) and biotite (Fig. 4.14a and inset 2). At the top of the formation, dark slate levels are not present and there are feldspar-bearing quartzites similar to those of the western part of Sierra-Nevada. Quartzite thickness increases from few centimetres to several tens of meters in the upper part of the formation.



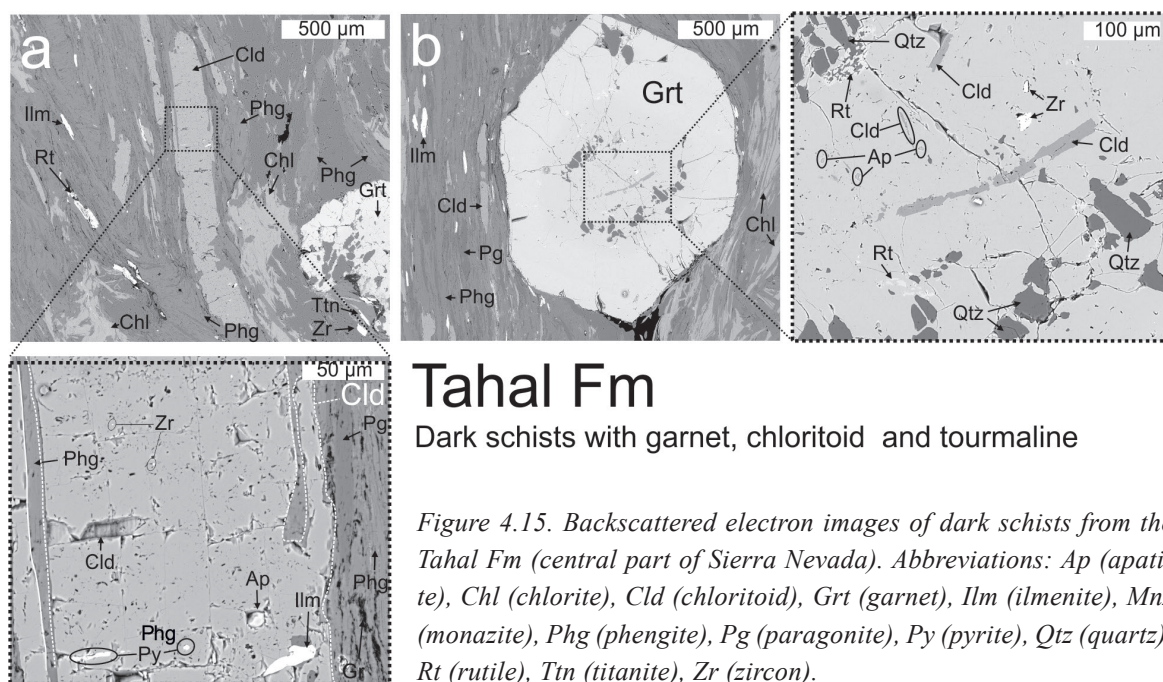
Dark schists Fm

Dark schists with garnet, chlorite, plagioclase, biotite and epidote

Figure 4.14. Backscattered electron images of schists from the Dark schists Fm (central part of Sierra Nevada). Abbreviations: Ap (apatite), Bt (biotite), Chl (chlorite), Ep (epidote), Ilm (ilmenite), Phg (phengite), Pg (paragonite), Pl (plagioclase), Qtz (quartz), Rt (rutile), Tur (tourmaline).

4.3.2.2. Tahal Fm

The lower part of Tahal Fm is formed by an alternation of dark schists, grey schists, quartzite banks and thin layers of light schists. The dark schists contain garnet (Fig. 4.15a; 4.15b and inset), chloritoid (Fig. 4.15a and inset; 4.15b and inset) and tourmaline. Tourmaline content in these rocks decreases upwards. The quartzite banks continue those of the upper part of the Dark schists Fm (Figs. 4.11 and 4.12).

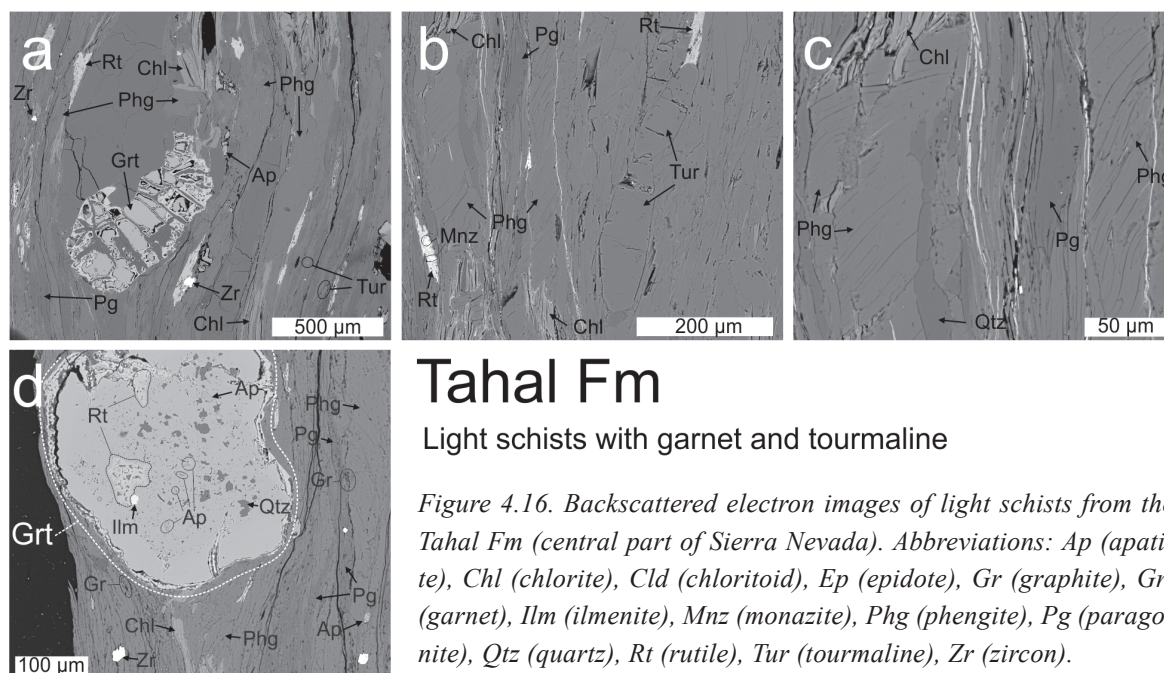


Tahal Fm

Dark schists with garnet, chloritoid and tourmaline

Figure 4.15. Backscattered electron images of dark schists from the Tahal Fm (central part of Sierra Nevada). Abbreviations: Ap (apatite), Chl (chlorite), Cld (chloritoid), Grt (garnet), Ilm (ilmenite), Mnz (monazite), Phg (phengite), Pg (paragonite), Py (pyrite), Qtz (quartz), Rt (rutile), Ttn (titanite), Zr (zircon).

The light- and grey schists contain garnet (up to 1 cm) (Fig. 4.16a, d), tourmaline (Fig. 4.16a, b) and scarce chloritoid. In the upper part of the Tahal Fm the dark schists are progressively replaced by the light ones. Compared with the western part of Sierra Nevada, marbles layers present lower lateral continuity and thickness in this area. The marbles contain calcite, dolomite and phengite.



4.4. Central part of Sierra de los Filabres.

In the central part of Sierra de los Filabres has been studied the lithological succession outcropping in the village of Velefique. This area corresponds to the northern flank of the general E-W anticline in Sierra de los Filabres (Fig. 4.17).

4.4.1. Previous proposed divisions

García-Monzón et al., (1975) proposed the existence of four formations in the Sierra de los Filabres, from bottom to top: the Nevada, Tahal, Huertecica and Las Casas formations. According to these authors the contacts between these formations are mostly stratigraphic in origin, although they could have been tectonically altered later. Vissers (1981) reported two units, the lowermost Nevado-Lubrín unit and the Chive unit. García-Dueñas et al. (1988), de Jong and Bakker (1991) and Martínez-Martínez et al. (2010) only identified the Calar-Alto and Bédar-Macael units (Fig. 2.4). In the area, several authors

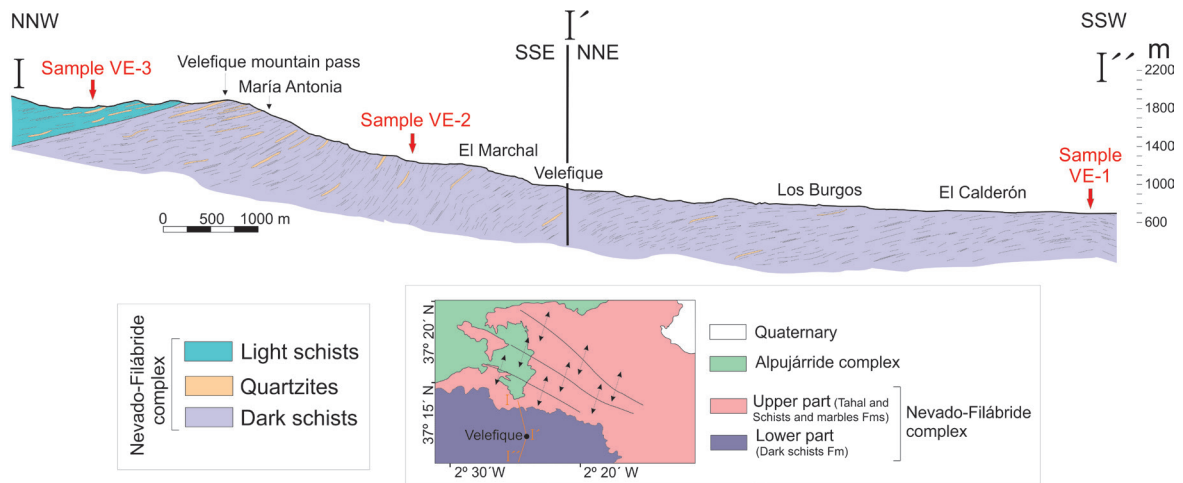


Figure 4.17. Cross section of the Velefique area (central part of Sierra de los Filabres). Red arrows indicate the location of the samples studied in chapter 5.

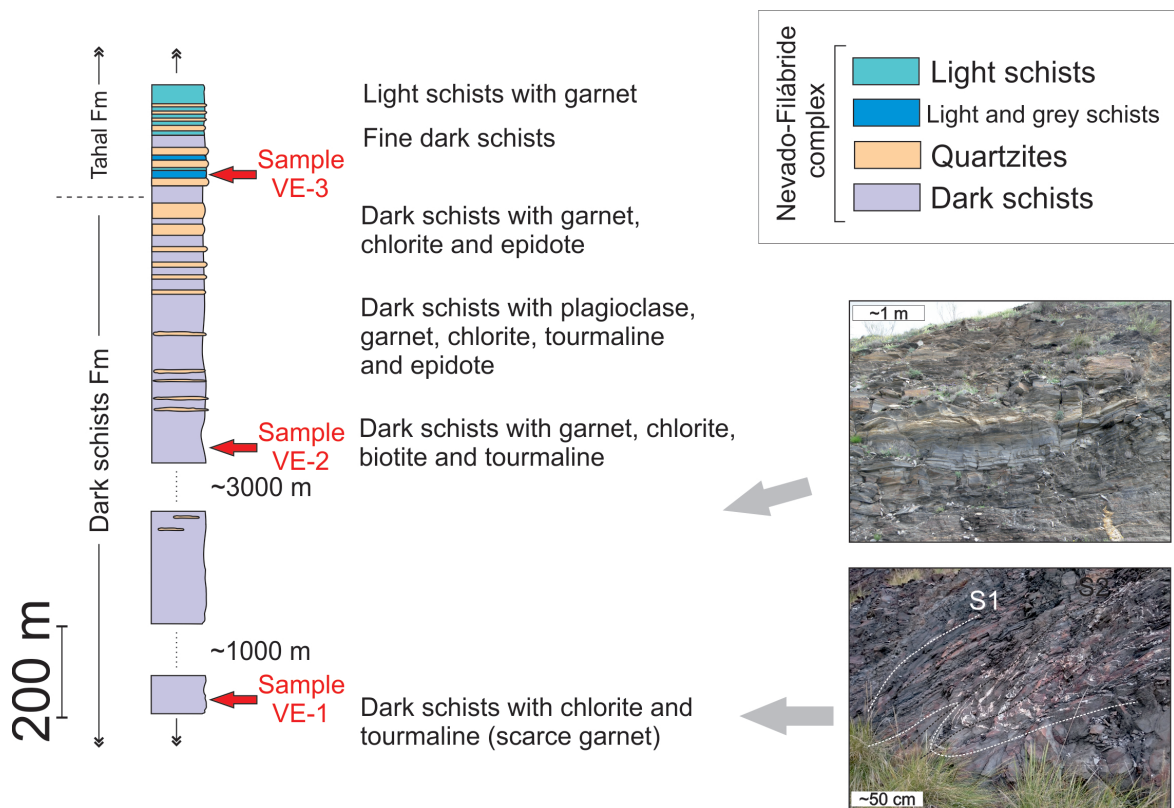


Figure 4.18. Lithological succession and field images of the Velefique area (central part of Sierra de los Filabres). Red arrows indicate the location of the samples studied in chapter 5.

(e.g. García-Dueñas et al., 1988; Martínez-Martínez et al., 2010; Booth-Rea et al., 2015) includes the contact between the Calar-Alto and Bédar-Macael units in a synmetamorphic shear zone (the Marchal shear zone, 500 m thick). According to Martínez-Martínez et al.

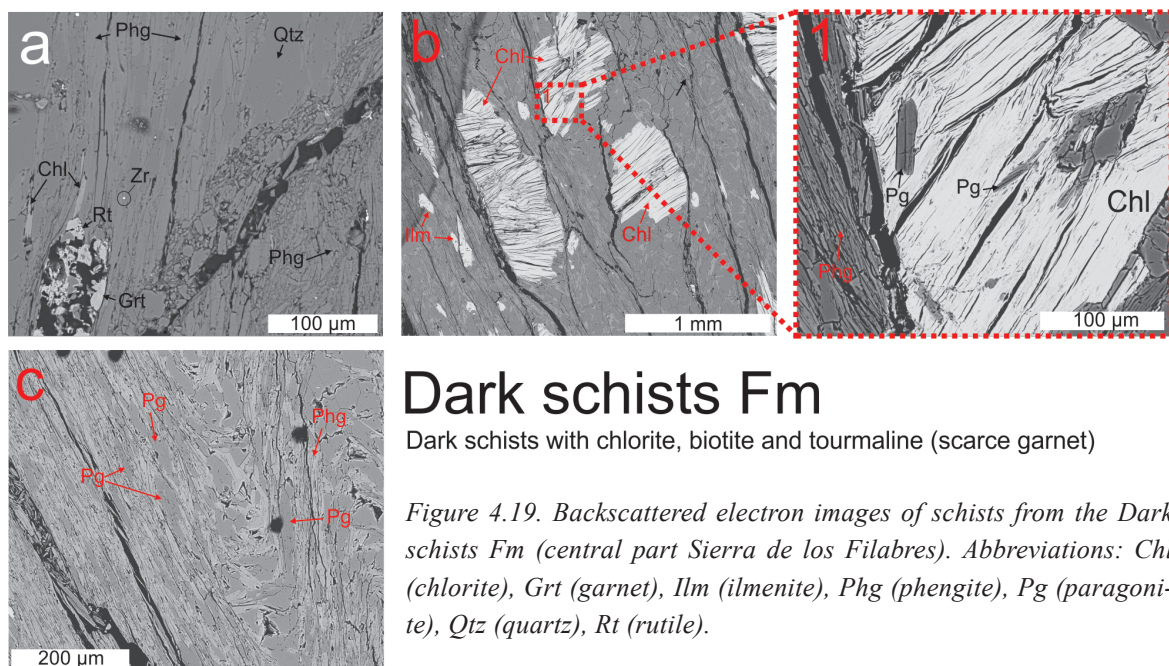
(2010), both units reach significantly bigger thickness in this area, than in the western part of the Nevado-Filábride complex. Despite Martínez-Martínez et al. (2010) did not report the Ragua unit in the area, authors as Puga et al. (2002) and Gómez-Pugnaire et al. (2012) accept in the area the existence of the dark schists from the lower part of the complex.

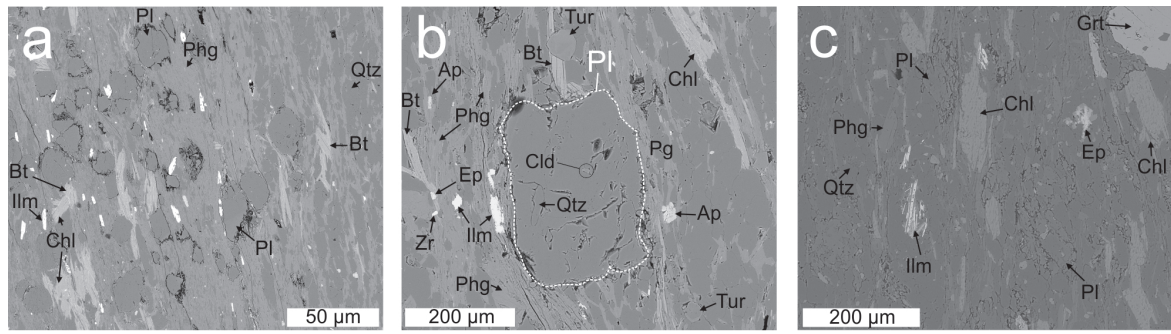
4.4.2. Lithological succession

The Nevado-Filábride lithological succession of this area is included in Fig. 4.18.

4.4.2.1. Dark schists Fm

In this area widely outcrops the Dark schists Fm including a monotonous succession of graphite-bearing dark schists and quartzites (Figs. 4.17). In the lowermost part of the studied succession the schists show chlorite (Fig. 4.19a), usually as stacks up to 1.5 mm thick (Fig. 4.19b and inset), small garnets (up to 0.2 mm thick) (Fig. 4.19a), tourmaline and variable content of biotite. Towards the top of the formation the schists are dark grey-, grey-, or brown colored, and show plagioclase (Fig. 4.20a-c), and variably content of garnet porphyroblasts (up to 0.5 mm thick), tourmaline (Fig. 4.20b) and epidote (Fig. 4.20c; 4.21b and inset). Close to the contact with the Tahal Fm the garnet size increases up to 3 mm (Fig. 4.21a and inset), and plagioclase is not present. Quartzites from the upper part of the formation include quartz and white mica (phengite and paragonite).

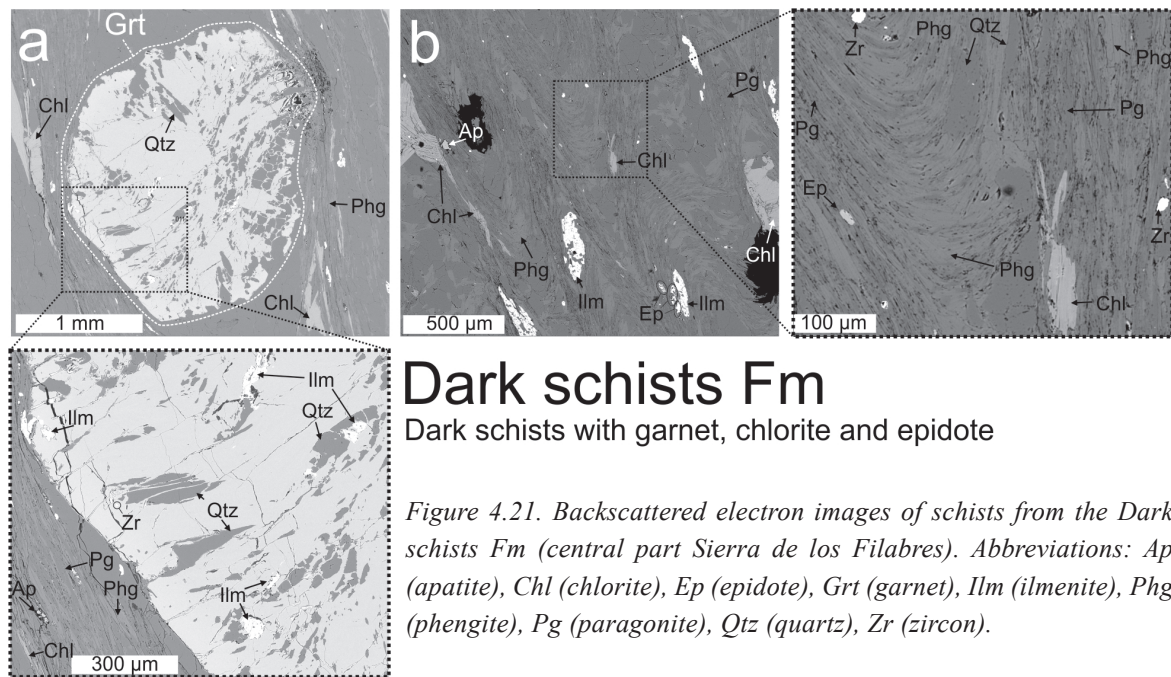




Dark schists Fm

Dark schists with plagioclase, garnet, chlorite, tourmaline and epidote

Figure 4.20. Backscattered electron images of schists from the Dark schists Fm (central part Sierra de los Filabres). Abbreviations: Ap (apatite), Bt (biotite), Chl (chlorite), Cld (chloritoid), Ep (epidote), Grt (garnet), Ilm (ilmenite), Phg (phengite), Pl (plagioclase), Qtz (quartz), Tur (tourmaline).



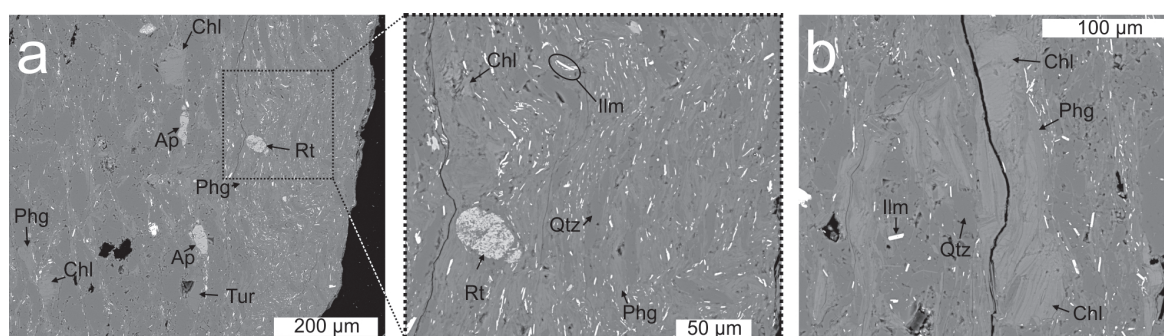
Dark schists Fm

Dark schists with garnet, chlorite and epidote

Figure 4.21. Backscattered electron images of schists from the Dark schists Fm (central part Sierra de los Filabres). Abbreviations: Ap (apatite), Chl (chlorite), Ep (epidote), Grt (garnet), Ilm (ilmenite), Phg (phengite), Pg (paragonite), Qtz (quartz), Zr (zircon).

4.4.2.2. Tahal Fm

The lower part of the Tahal Fm is formed by dark schists with garnet similar to those of the Dark schists Fm. The upper part of the formation is mostly formed by light grey schists with intercalations of levels of fine-grained bluish-schists (Fig. 4.22a, b) and quartzites. The light grey schists and the bluish-schists contain quartz, phengite, paragonite and chlorite (Fig. 4.22a, b). The Schists and marbles Fm outcrops northwards (not studied in this area).



Tahal Fm Fine dark schists

Figure 4.22. Backscattered electron images of schists from the Tahal Fm (central part Sierra de los Filabres). Abbreviations: Ap (apatite), Chl (chlorite), Ilm (ilmenite), Phg (phengite), Qtz (quartz), Rt (rutile), Tur (tourmaline).

4.5. Eastern part of Sierra de los Filabres.

In order to investigate the Nevado-Filábride succession in the eastern part of the Sierra de los Filabres it has been selected the area around the village of Lubrín (Fig. 4.23).

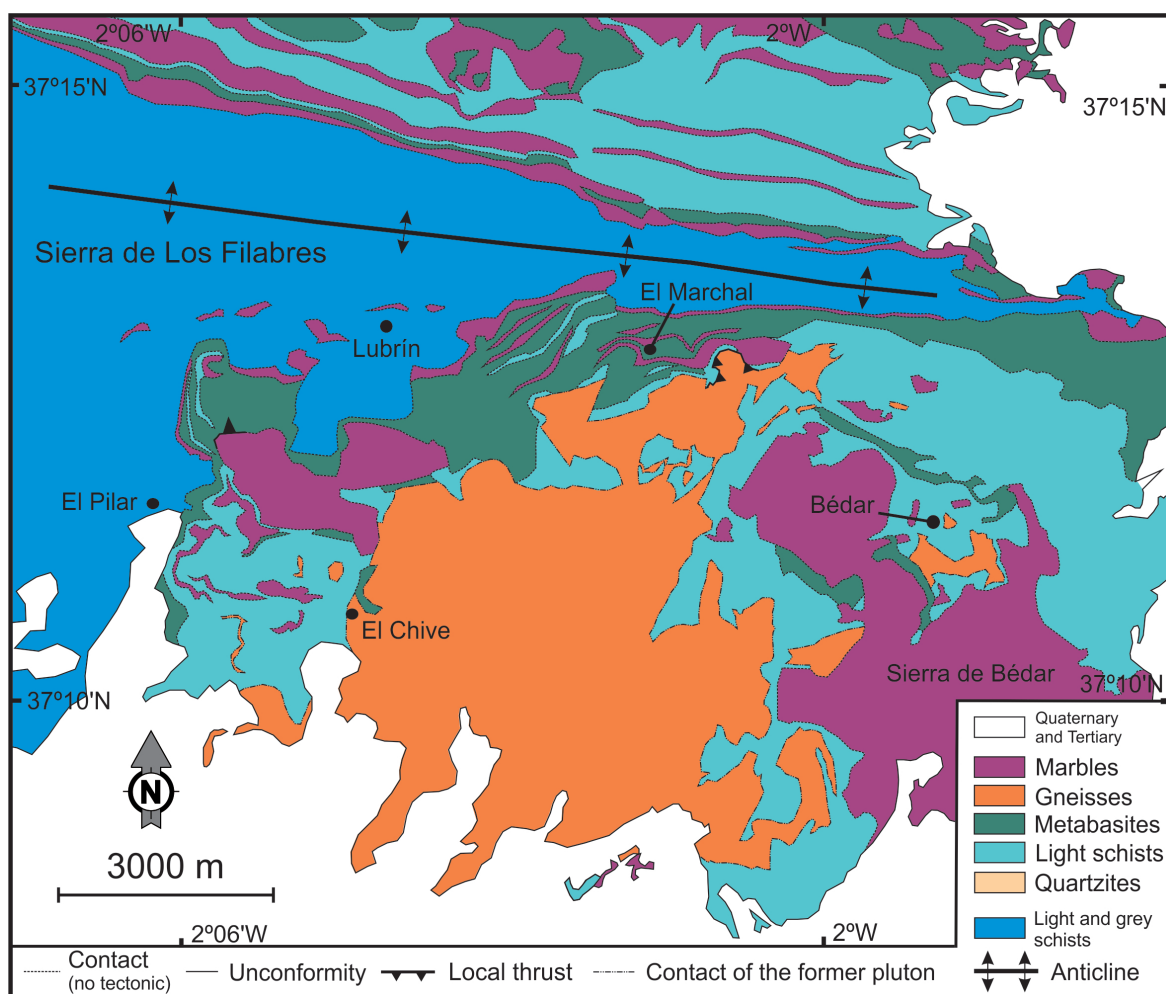


Figure 4.23. Geological map of the Lubrín area (eastern part of Sierra de los Filabres).

4.5.1. Previous proposed divisions

In this area is one of the most noteworthy exposures of the upper part of the Nevado-Filábride complex (Figs. 4.23). García-Monzón and Kampschuur (1975) reported in this area the Nevada (which covers materials approximately equivalent to those of Veleta complex of Puga, 2002), Tahal, Huertecicas and Las Casas formations. According to these authors, the contact between the Nevada and Tahal formations is stratigraphic, whilst the contact between the Tahal and Huertecicas, and the Huertecicas and Las Casas is nowadays mostly tectonic, but probably stratigraphic in origin. Martínez-Martínez et al. (2002) distinguished in the area the Calar-Alto and Bédar-Macael units (Fig. 2.4). According to these authors, this Bédar-Macael unit is almost completely affected by the Marchal shear zone. Puga et al. (2002) and Puga et al. (2017) reported the Mulhacén complex, whilst Gómez-Pugnaire et al. (2012) identified the Tahal, the metaevaporitic, the marbles and calc-schists and the Chive formations (Fig. 2.4). Therefore, most of the authors did not recognize the lower part of the complex in the area.

4.5.2. Lithological succession

The lithological succession outcropping in this area starts with the rocks attributed to the Tahal Fm (Fig. 4.24).

4.5.2.1. Tahal Fm

The lower part of the formation is a thick alternation of dark and light schists. Both rocks are formed by chloritoid, and variable content of garnet, plagioclase, amphibole, epidote and kyanite; with decametric layers of grey to white quartzites with white mica (phengite) chlorite and scarce epidote. The upper part of the Tahal Fm includes thin marbles levels with calcite, dolomite, phengite and paragonite (Fig. 4.24).

4.5.2.2. Schists and marbles Fm

The lower part of the Schists and marbles Fm includes an alternation of marbles, calc-schists, light schists and metabasite levels and few thin levels of dark schists (Fig. 4.24). The metabasite bodies appear as 20 to 50 m thick layers with a remarkable lateral continuity, or as thin levels of few centimetres interlayered in light schists, marbles and calc-schists. Most of the bigger metabasic bodies preserve a basaltic texture in the inner part, whilst the border is clearly metamorphic. Several levels, described as ultramafic rocks (e.g. Puga et al., 2002; Puga et al., 2017) contain thin layers of schists and few marbles.

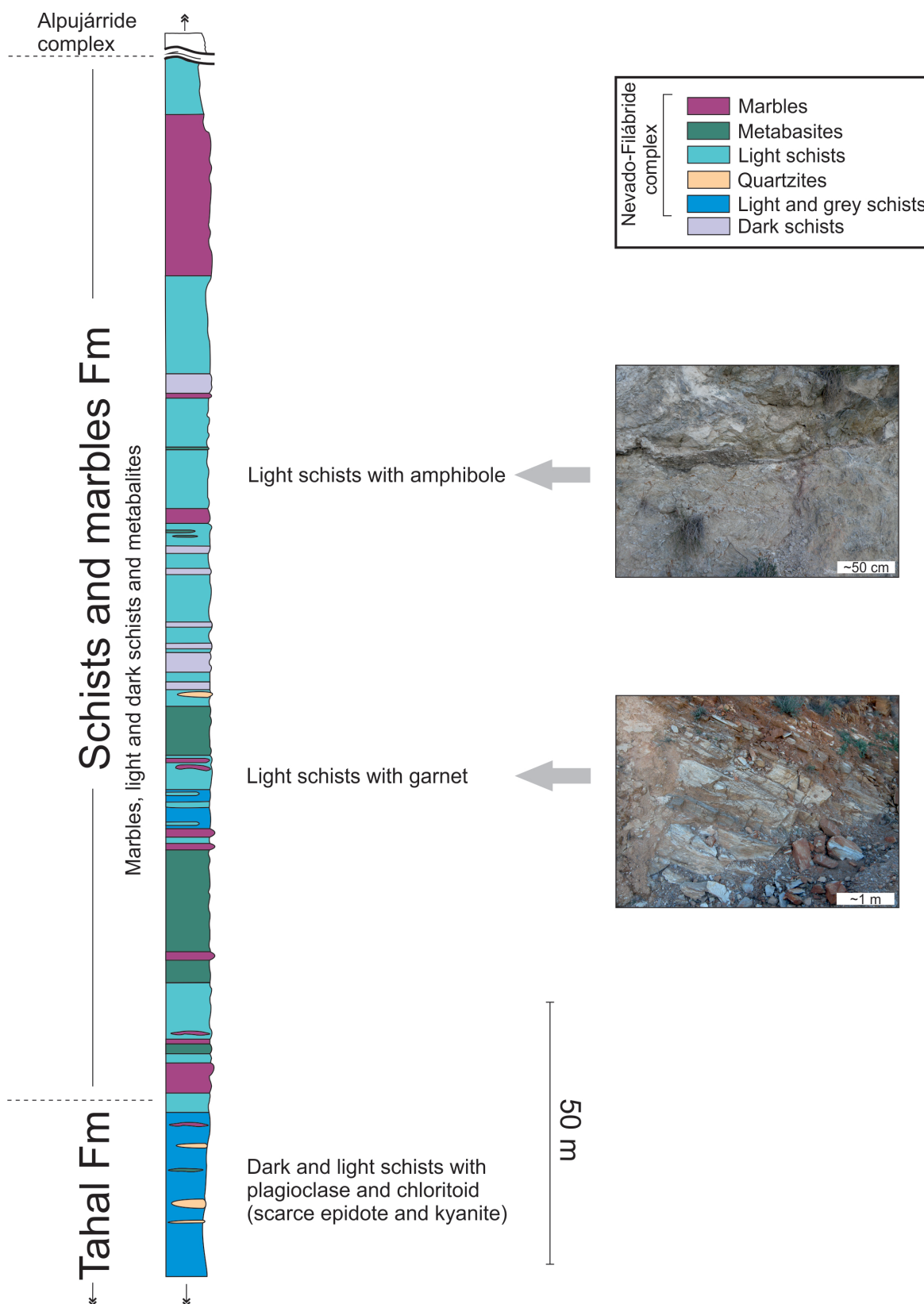


Figure 4.24. Lithological succession and field images of the Lubrin area (eastern part of Sierra de los Filábrides).

The upper part of the Schists and marbles Fm is mainly formed by light schists with garnet up to 5 mm thick, green light schists with amphibole, calc-schists and dark schists (Fig. 4.24). In these rocks the kyanite, epidote and tourmaline content strongly varies between sectors. The formation culminates with marbles banks up 100 m thick. These rocks contain albite and amphibole, and are white-, yellow-, bluish- or brownish-coloured. Commonly they include metric levels of calc-schists (sometimes with garnet) or impure marbles.

It is remarkable the presence in the area of a metagranite body up to 6 km width, and more than 400 m thick, which lower part does not outcrop. The body intrudes the previous described materials (Fig. 4.23), and is partially covered in some sectors by the uppermost rocks of the Schists and marbles Fm. Additionally, there are sectors showing thinner gneiss levels of tens of meters mainly interbedded with light schists from the Schists and marbles Fm (e.g. in the village of Bédar, Fig. 4.23).

4.6. Summary and conclusions

The Nevado-Filábride complex shows comparable lithological successions in the all the studied areas. The Fig. 4.25 summarizes the results presented in this chapter by including the lithological columns for the western and central part of the Sierra Nevada and the eastern and central part of Sierra de los Filabres. In this figure is proposed a lithologic correlation between the Nevado-Filábride formations identified in the areas of study.

In the sierras Nevada and Filabres, the Dark schists Fm is characterized by a monotonous formation of graphite-bearing dark schists and quartzites. The lowermost schists of this formation (widely outcropped in La Ragua and Velefique areas) are fine grained and include scarce small garnets. Upwards the grain size of the schists increases, and these rocks show plagioclase, epidote and tourmaline. Close to the contact between the Dark schists and Tahal Fms, in the central and western parts of Sierra Nevada area, the plagioclase content decreases, and chloritoid increases. In Sierra de los Filabres area it has not been found the chloritoid-bearing schists. The uppermost meters of the Dark schists Fm is formed by an alternation of dark schists and quartzites. The quartzite thickness increases upwards from the order of centimeters to tens of meters.

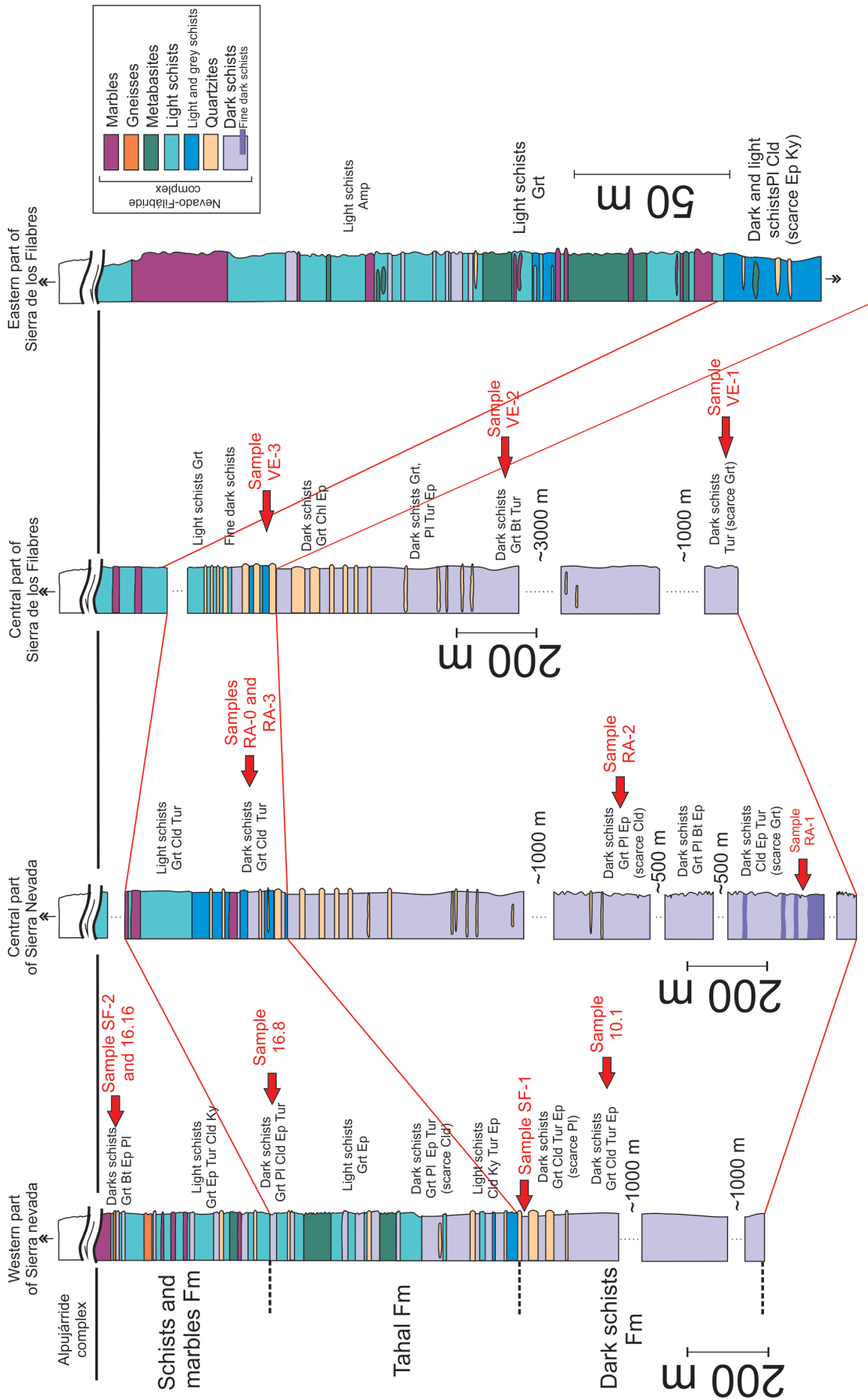


Figure 4.25. Comparative of the lithological successions of the studied areas. Abbreviations: Bt (biotite), Chl (chloritoid), Ep (epidote), Grt (garnet), Ky (kyanite), Pl (plagioclase), Py (pyrite), Tur (tourmaline).

The upper part of the complex is formed by a succession of several lithologies included in the lower Tahal and the Schists and marbles Fms. The main difference existing between these Fms is the occurrence and thickness of marbles, metabasites and gneisses. In general, the studied lithological successions (particularly in the Western part of Sierra Nevada) show several metabasite bodies in the Tahal Fm, whilst the Schists and marbles Fm show thicker gneisses and marbles.

The lowermost part of the Tahal Fm is formed by an alternation of dark schists, quartzites, and thin levels of light schists. Dark schists are similar to those of the Dark schists Fm (i.e. mostly chloritoid-bearing schists) and light schists show chloritoid, tourmaline, epidote and kyanite (this last phase observed in the western part of the Sierra Nevada area). The alternation of schists and quartzites existing in the contact between the Dark schists and Tahal Fms is common through the Nevado-Filábride complex (see the western and central parts of Sierra Nevada and the central part of Sierra de los Filabres in Fig. 4.25). This contact is mostly stratigraphic and points to a transition between both formations rather than a tectonic contact. The upper part of the Tahal Fm show dark schists with garnet, epidote and tourmaline and variable content in chloritoid, plagioclase and allanite; light schists with garnets; marble and calc-schists layers; metabasite bodies and quartzites.

The Schists and marbles formation is characterized by the presence of thick levels of light- grey- and dark schists and marbles. The light schists include big garnet porphyroblasts, epidote, tourmaline and variable content of kyanite, chloritoid, plagioclase and amphibole (this last only found in the eastern part of Sierra de los Filabres). The marbles contain white mica (phengite and paragonite) and are remarkably thick (tens of meters) in the uppermost part of the formation, close to the contact with the Alpujarride complex. In the Schists and marbles Fm, the thickness of the dark schists is comparatively lower than in the underlying formations. These schists include garnet, epidote and variable content of plagioclase and allanite. In both the western part of Sierra Nevada and the eastern part of Sierra de los Filabres outcrop several layers of gneisses.

The main reason which have led to the differentiation of the complex in various structural units (e.g. Puga and Díaz de Federico, 1976; Puga et al., 2002) is the difference in metamorphism conditions between the upper and lower part of the complex. An essential

question to check the existence of these divisions is to determinate how are the contact between the supposed units in the field. The observations during fieldwork showed that the contact between the different proposed units or complexes do not occur as lithological “jumps”, but as a transition. For example, the supposed contact between the Veleta and Mulhacén complexes of Puga et al. (2002), mostly equivalent to the Dark schists Fm, and the Tahal and Schists and marbles Fms respectively, is characterized by the occurrence of quartzite levels and light schists interbedded in the dark ones. Towards the upper part of the Nevado-Filábride complex, the light schists are progressively more abundant, and the dark schists decrease (but do not disappear). No proves have been found of the existence of large shear zones in the Nevado-Filábride complex units as previously proposed by Martínez-Martínez et al. (2002). Conversely, the shear zones found during the study are interpreted as local and not as generalized structures. The results presented in this chapter lead to a continuous lithological sequence rather than a succession divided in different tectonic units.

Chapter 5

SHRIMP U-Pb detrital zircon dating

5.1. Introduction

An essential topic in the study of lithological successions is the age dating of rocks which allow geologists to accomplish a better understanding of the processes leading to formation and evolution of the stratigraphic sequences. Paleontological approach is one of the primary tools to determinate the age of the rocks. But in absence of fossils, as usually occurs in metamorphic and igneous rocks, age determinations based on radiometric dating methods are usually implemented in the studies (e.g. dating methods based on Rb-Sr, Sm-Nd, U-Th, U-Pb, etc).

U-Pb geochronology applied to zircon is widely used nowadays to estimate probable age constraints in lithological successions. This is due to the remarkable resistance of zircon grains to deformation and metamorphism processes, and the consequent abundance of this mineral in sedimentary, metamorphic and igneous rocks (e.g. Fedo et al., 2003; Dickinson and Gehrels, 2009; Díez-Fernández et al., 2010; Gehrels 2012, 2014; Meinhold et al., 2013; Schoene, 2014; Litty et al., 2017; Pérez-Cáceres et al., 2017; Thomson, 2017). Dating of zircons formed in metamorphic and igneous rocks allows estimating the age of geological events involving the hosting rock (e.g. metamorphic stages during orogenies, intrusion of igneous bodies, etc.). In sedimentary and metamorphic successions, dating of inherited detrital zircons can be used for determining the most likely maximum age of deposition (MDA) of the sedimentary protolith. This interpretation relies in the assumption that the inherited zircons must have grown before the deposition of the hosting sedimentary protolith. Accordingly, dating of these zircons yields necessary a maximum age for the deposition event. This interpretation is based on the identification of the youngest age

population and requires a large number of analyses to ensure the results to be statistically representative (e.g. Andersen, 2005; Fedo, 2003; Gehrels, 2012). Ion microprobe (SIMS) and Laser Ablation Inductively Coupled Plasma Mass Spectrometry (LA-ICP-MS), which both permit the analysis of large number of zircon grains (see Davis et al., 2003; Fedo et al., 2003; Kosler and Sylvester, 2003 for a historical review of these methods), constitute optimal tools in order to determinate the most probable MDAs. The determination of age populations in samples from different lithologic sequences allows comparison between them, and provides results useful to verify or reject proposed sub-divisions which have been previously based on lithological and tectonic criteria (e.g. Rónadh et al., 2004; Kirkland et al., 2008).

The radiometric age determinations in the Nevado-Filábride complex have been mainly based on meta-igneous rocks (mostly gneisses) (section 2.3.5) resulting from igneous intrusive events (Priem et al., 1966; Puga and Díaz de Federico, 1976; Andriessen et al., 1991; Nieto, 1996; Nieto et al., 1997; Gómez-Pugnaire et al., 2000; Gómez-Pugnaire et al., 2004; Martínez-Martínez et al., 2010; Gómez-Pugnaire et al., 2012; Ruiz-Cruz and Sanz de Galdeano, 2017). These rocks were intruded after the sedimentary protolith deposited, accordingly the age estimations obtained from meta-igneous rocks can only provide minimum deposition ages (mDA) for the complex. Additionally, the studies based on meta-igneous rocks have been mainly focused in the Tahal and Schists and marbles Fms, due to the scarcity of these rocks in the Dark schists Fm. Therefore a comparison between radiometric ages from the upper part of the complex with those of the lower part has remained incomplete. Until recent times, the dataset of detrital zircon ages was limited to the study of a tourmaline-rich mica-schist sample situated in the Tahal Fm (see Gómez-Pugnaire et al., 2012, sample PC-3, which yielded $^{206}\text{Pb}/^{238}\text{U}$ dates at ~ 336 , ~ 700 and ~ 2050 Ma). Recently, Santamaría-López and Sanz de Galdeano (2018) and Jabaloy et al. (2018) have yielded new U-Pb dating on inherited detrital zircons from the Nevado-Filábride schists. These studies allowed for the first time to estimate MDAs for the protolith of the Nevado-Filábride schists.

In this chapter are presented and discussed the results of the SHRIMP U-Pb detrital zircon dating carried out during the Ph.D. Thesis, and published in the *International Journal of Earth Sciences* journal (Santamaría-López and Sanz de Galdeano, 2018). The com-

parison of the age populations obtained in samples from different areas of the complex and parts of their lithological sequence have been used to check the proposed divisions traditionally based on tectono-metamorphic observations (e.g. de Jong 1991, 1993; Martínez-Martínez, et al., 2002; Puga et al., 2002; Augier et al., 2005a; Behr and Platt, 2012; Booth-Rea et al., 2015;).

5.2. Description and localization of schist samples

Eight mica-schist samples have been studied: SF-1, SF-2, RA-1, RA-2, RA-3, VE-1, VE-2 and VE-3. Samples SF-1 and SF-2 were collected in the Peñones de San Francisco (see Figs. 4.1 and 4.2); samples RA-1, RA-2, in La Ragua area (see Figs. 4.1 and 4.11); and samples VE-1, VE-2 and VE-3 in the Velefique area (see Figs. 4.1 and 4.17). Their stratigraphic relative positions are shown in the schematic lithological succession in Fig. 4.25. The UTM coordinates of the samples are given in Appendix 1. It is important to note that VE-1 and RA-1 were taken in the lower outcropping part of the Dark schists Fm in the Sierra de los Filabres and Sierra Nevada respectively; i.e. the lower visible points of the lithological sequence studied in this Ph.D. Thesis. The rest of the samples were taken progressively in higher positions of the lithological succession. The sample SF-2 was taken in the highest position of the Nevado-Filábride complex succession studied in this Ph.D. Thesis; i.e. in the Schists and marbles Fm visible in the Peñones de San Francisco area.

The studied samples are dark-gray schists, with the exception of VE-3 being a fine-grained bluish-schist. The major mineral phases are quartz, phengite, paragonite, and chlorite. Chloritoid is in samples SF-1, RA-1; garnet in samples SF-2, RA-2, RA-3; and epidote and allanite in samples SF-2, RA-2, RA-1. Graphite, biotite, apatite, ilmenite, rutile, xenotime, and zircons appear as minor phases. Zircons grains were observed both in the matrix and as inclusions in other minerals such as garnet, phengite and paragonite.

5.3. Zircon morphology and inclusions

5.3.1. Zircon morphology

In Fig. 5.1 is shown a selection of optical images of the several zircon grains. Optical and CL images of all studied zircons are supplied in Appendix 3.

The zircons from the Peñones de San Francisco samples are commonly anhedral or subhedral. The occurrence of euhedral grains is occasional. The grain size differs between the samples of this area: sample SF-1 exhibits sizes between 60 and 200 μm , and in SF-2 between 40 and 120 μm . Some green- and pink-colored grains occur in sample SF-1 (Fig. 5.1a, c) but generally the grains are colorless, and transparent (Fig. 5.1b) or translucent (Fig., 5.1c).

The zircons from La Ragua area samples are anhedral or subhedral (Fig. 5.1d, f). In all samples, the grain size is between 60 and 200 μm . In general, they are translucent or transparent, and colorless (Fig. 5.1d). There are few green-, pink-, blue- and brown-colored grains (Fig. 5.1e, f).

In the Velefique area the studied zircons are anhedral (Fig. 5.1g) or subhedral (Fig. 5.1h). The size of zircon grains varies between 10 and 180 μm . Samples VE-1 and VE-2

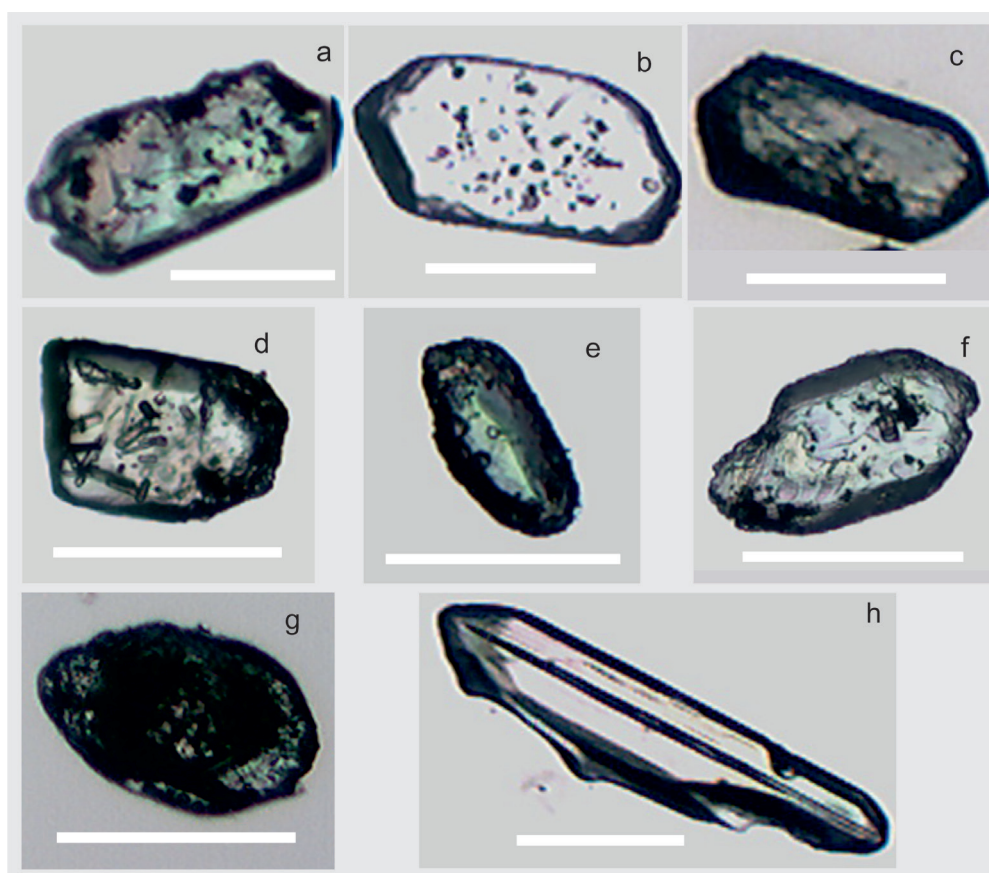


Figure 5.1. Selection of optical images of zircons from Peñones de San Francisco area (a, b, c), La Ragua area (d, e, f) and Velefique area (g, h). Scale bars correspond to 100 μm .

include a population of elongated grains up to 300 μm long (Fig. 5.1h). The grains are mainly colorless, and transparent or translucent, although some opaque grains are also observed in sample VE-2 (Fig. 5.1g).

5.3.2. Deciphering the origin of zircons

Only inherited zircons can be used for determining the MDA of the sedimentary protolith. Indeed, the zircon grains identified as igneous in origin were necessarily inherited in the Nevado-Filábride protolith. Alike, metamorphic grains formed before metamorphism of the sedimentary protolith can be used for the MDA estimation. Conversely, as it was pointed in the introduction, metamorphic zircons formed after the deposition of sediments should be discarded. The use of CL images of the zircon has proved to be a useful tool in order to determine the possible former origin. This is based on the interpretation of the zoning preserved in the grains (Corfu et al., 2003; Rubatto and Scambelluri, 2003; Wu and Zheng, 2004; Belousova et al., 2006). Besides, the rounded edges observed in several grains can be interpreted as proving of sedimentary transport (i.e. inherited) regardless of their former origin (Gärtner et al., 2013).

In the CL images the most common texture observed in the core and rim has been an oscillatory zone (in some cases slightly blurred) (Figs. 5.2 and 5.3), which usually supports an igneous origin (Corfu et al., 2003). Some grains show blurred oscillatory zone and non-oscillatory patches which can be common features formed during a partial metamorphic recrystallization process (see below) (Corfu et al., 2003; Hoskin and Schaltegger, 2003). In a few cases the observed oscillatory zone can be slightly deformed, leading to convolute zoning (cores in Fig. 5.2f, j).

Few zircons show a xenocrystic core surrounded by variably well-preserved oscillatory zoned rims (Fig. 5.2n; Fig. 5.3k, l, m, o). In some cases the rim preserves radial fractures formed by the expansion of a U-rich core due to metamictization process (Fig. 5.3l) (Corfu et al., 2003; Ewing et al., 2003). However, in other examples the zircon preserves a U-rich rim, not fractured (Fig. 5.3k). The origin of xenocrystic cores cannot always be deduced, but few of them show abrasion on their edges (Fig. 5.3k). In these cases, xenocrystic cores should probably record a detrital episode after its formation, followed by the new rim growth. Accordingly, these grains can be interpreted as inherited.

Some zircons can be recognized as metamorphic zircons based on textural features pointing to this origin (e.g. Rubatto 2002, 2017; Wu and Zheng 2004). These characteristics include the anhedral morphology of the zircon grain and features in the CL images as: weak zoning (Fig. 5.3m), the presence of no-zoned patches (arrows in Fig. 5.2c, e, k, l, p; Fig. 5.3a, g, h, i, j, k, l, m, n, p), and fir-tree zoned areas (bottom side of the grain in Fig. 5.3d). Additionally to textural characteristics, it has been found zircons yielding $\text{Th}/\text{U} < 0.1$, these being commonly attributed to metamorphic zircons (Rubatto, 2001). However, several examples of metamorphic zircons with $\text{Th}/\text{U} > 0.1$ have also been documented (see Rubatto, 2017 and references herein). The Alpine metamorphism which affected the Nevado-Filábride complex has been dated as Oligocene and/or Miocene (see section 2.3.3.2). In this sense, probably the thin external no-luminescent rims (Fig. 5.2e, l, m, o; Fig. 5.3a, b, e, f, l, m, n) were formed during metamorphism, and accordingly they were ignored in the SHRIMP study.

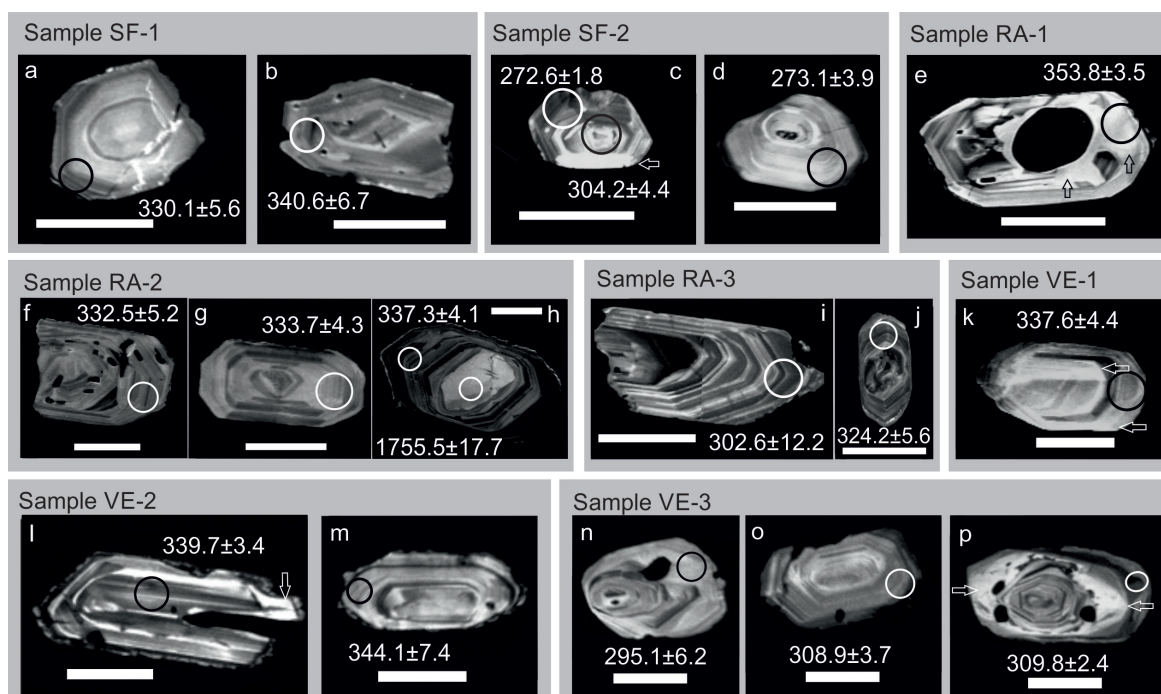


Figure 5.2. Selection of cathodoluminescence images of zircons yielding Permian and Carboniferous $^{206}\text{Pb}/^{238}\text{U}$ zircon ages. See text for a detailed description. Circles correspond to SHRIMP analysis points and ages are in million years. Arrows show no-zoned patches. Scale bars correspond to $50\ \mu\text{m}$.

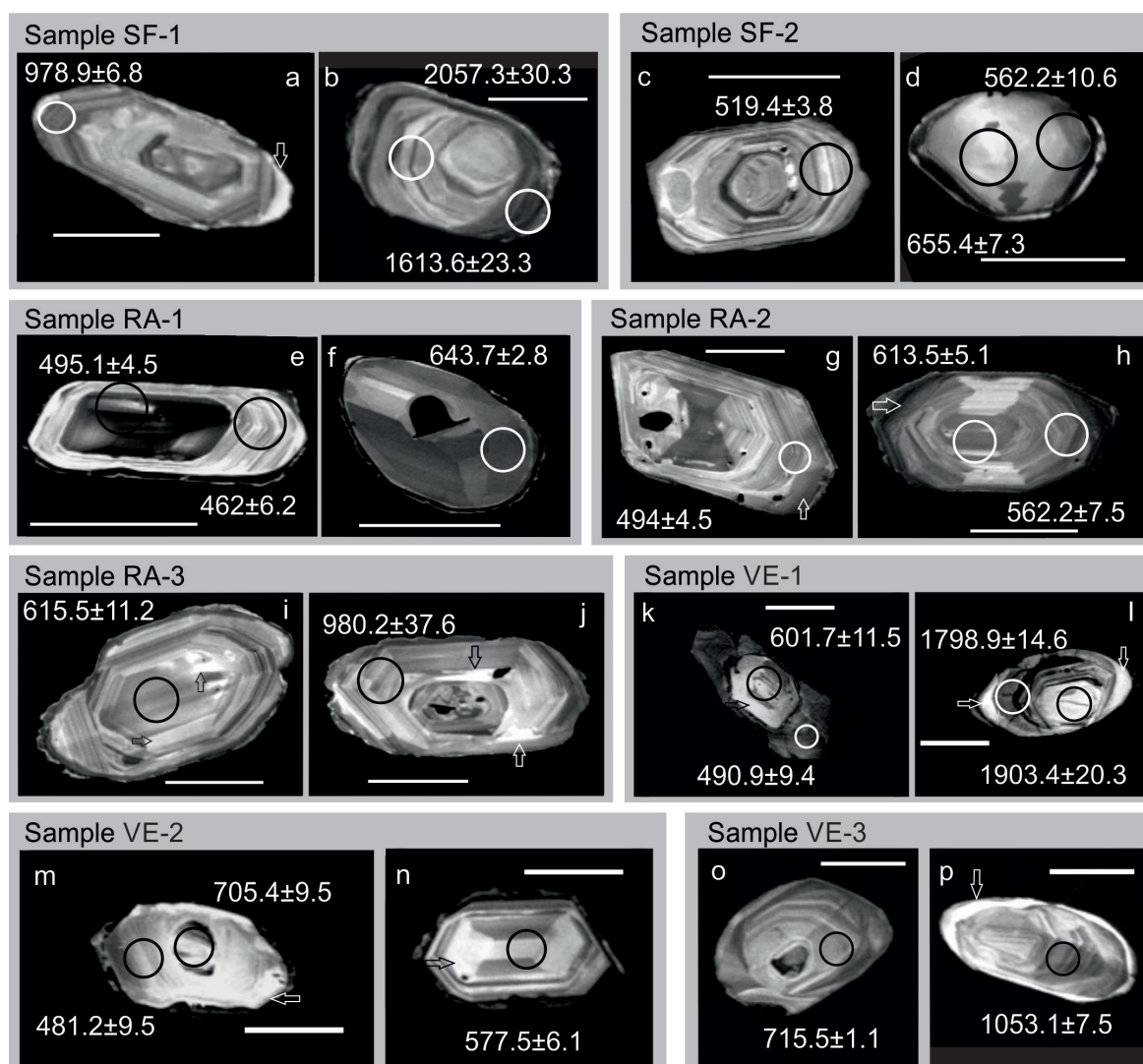


Figure 5.3. Selection of cathodoluminescence images of zircons yielding pre-Carboniferous $^{206}\text{Pb}/^{238}\text{U}$ zircon ages. See text for a detailed description. Circles correspond to SHRIMP analysis points and ages are in million years. Arrows show no-zoned patches. Scale bars correspond to $50\ \mu\text{m}$.

Finally, no-luminescent spots (Fig. 5.2b, e, f, j, l, m, n, o, p; Fig. 5.3f, g, h, j) have been attributed to inclusions (see below).

5.3.3. Description of zircon inclusions

BSE images combined with EDX analyses allowed to determine the morphology, size, and composition of the inclusions. In zircons from sample SF-1, there are quartz inclusions with a size $\leq 20\ \mu\text{m}$ in diameter, (Fig. 5.4a), apatite $\leq 25\ \mu\text{m}$ (Fig. 5.4a and insets), and xenotime $\leq 30\ \mu\text{m}$ (Fig. 5.4b and inset). Sample SF-2 zircons show inclusions of quartz with a size $\leq 15\ \mu\text{m}$ in diameter (Fig. 5.4c), phengite $\leq 30\ \mu\text{m}$ (Fig. 5.4c inset), pa-

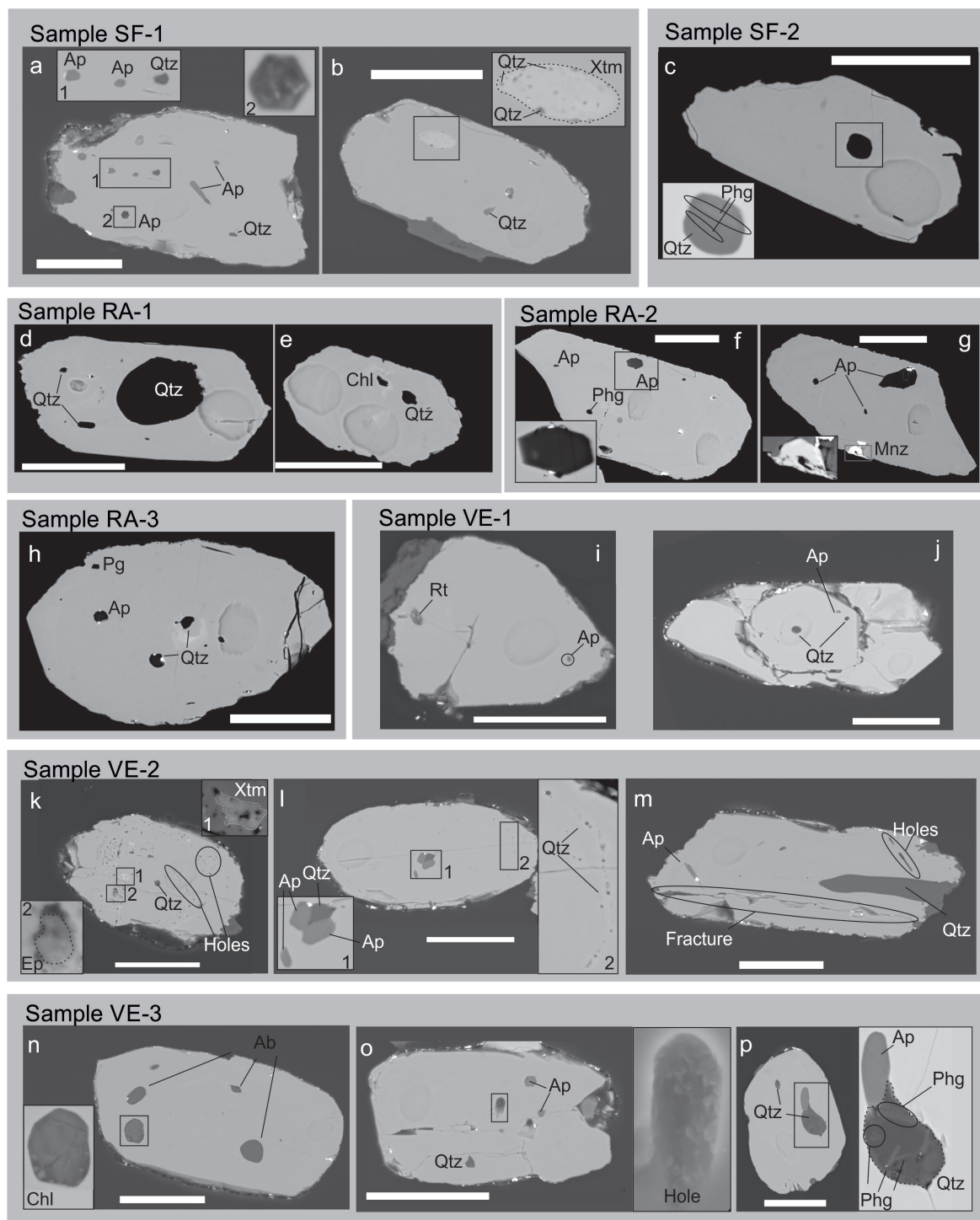


Figure 5.4. Selection of backscattered electron images of the zircons showing the most significant inclusions observed. Abbreviations: Qtz (quartz), Phg (phengite), Ap (apatite), Xtm (xenotime), Chl (chlorite), Mnz (monazite), Pg (paragonite), Rt (rutile), Ep (epidote), Ab (albite). Scale bars correspond to 50 μm .

ragonite $\leq 30 \mu\text{m}$, apatite $\leq 12 \mu\text{m}$, albite ($\leq 10 \mu\text{m}$), and xenotime $\leq 10 \mu\text{m}$. The zircons in sample RA-1 have common quartz inclusions (particularly in the youngest age zircon populations) with a size $\leq 45 \mu\text{m}$ in diameter (Fig. 5.4d-e) and, to a lower extent, chlorite $\leq 7 \mu\text{m}$ (Fig. 5.4e). Zircons in sample RA-2 have inclusions of quartz with a size $\leq 40 \mu\text{m}$ in diameter, phengite $\leq 6 \mu\text{m}$ (Fig. 5.4f), apatite $\leq 25 \mu\text{m}$ (Fig. 5.4f and inset; Fig. 5.4g), and monazite $\leq 30 \mu\text{m}$ (Fig. 5.4g and inset). In sample RA-3, quartz inclusions were found with a size $\leq 10 \mu\text{m}$ in diameter, apatite $\leq 20 \mu\text{m}$ and paragonite $\leq 4 \mu\text{m}$ (Fig. 5.4h). The main inclusions present in zircon grains from sample VE-1 are quartz (5-10 μm) (Fig. 5.4j) and apatite (4 μm) (Fig. 5.4i-j). Rutile inclusions $\leq 5 \mu\text{m}$ are less common (Fig. 5.4i). Sample VE-2 zircons exhibits quartz as main inclusion, showing a wide variability of sizes. In general, quartz inclusions are small, $\leq 7 \mu\text{m}$ in diameter (Fig. 5.4k-l) but a few other ones are significantly larger (e.g. 75 μm in the zircon grain shown in Fig. 5.4m). Apatite ($\leq 8 \mu\text{m}$) (Fig. 5.4l-m), xenotime (5 μm) (Fig. 5.4k and inset 1) and epidote (5 μm) (Fig. 5.4k and inset 2) inclusions were also found. In sample VE-3, the inclusions are quartz $\leq 25 \mu\text{m}$ (Fig. 5.4o-p), apatite $\leq 15 \mu\text{m}$ (Fig. 5.4o-p), chlorite $\leq 20 \mu\text{m}$ (Fig. 5.4n and inset), albite $\leq 15 \mu\text{m}$ (Fig. 5.4n) and phengite of 5 μm (Fig. 5.4p and inset). The zircons studied in the eight samples exhibit holes, tentatively attributed to fluid inclusions, or fractures on the surface (e.g. Fig. 5.4k, m, o). Some of these holes have been filled by gold coating in the images.

5.4. Geochronology results

Below it is summarize the SHRIMP $^{206}\text{Pb}/^{238}\text{U}$ zircon ages provided from each sample and grouped by age populations. The distribution histogram and the KDE plots are shown in Fig. 5.5 for the lower part of the complex (Dark schists Fm) (samples SF-1, RA-1, RA-2, VE-1 and VE-2), and Fig. 5.6 for the upper part of the complex (samples RA-3 and VE-3 from the Tahal Fm; and sample SF-2 from the Schists and marbles Fm). In Figs. 5.5 and 5.6 the age populations obtained after mixture modelling are marked for each sample (arrows). Appendix 4 and Appendix 5 correspond to the SHRIMP results, and the Wheterill plots respectively.

The majority of the analyses were acquired on the outermost rim of each zircon grain (excluding the last Alpine metamorphic event). Some zircon grains were analyzed twice for core and rim. In most cases, the ages obtained for these two domains are different,

but sometimes core and rim analyses yield the same age within error. Zircon grains that may have lost lead, according to the high U concentration observed (>3000 ppm), were therefore rejected from the analyses. Analyses with a discordance value > 10% were discarded.

5.4.1. Lower part of the complex

5.4.1.1. Sample SF-1 $^{206}\text{Pb}/^{238}\text{U}$ age populations

In sample SF-1, 78 analyses (70 in rims and 8 in cores) were obtained; three of them were rejected because of their high discordance (>10%). The youngest analysis, 330 ± 6 Ma, is included in an age population of 354.7 ± 1.9 Ma. Two prominent probability peaks are present at 590.2 ± 1.1 and 997.5 ± 3.2 Ma; and several Paleoproterozoic analyses define an age population at 2004 ± 4.3 Ma (Fig. 5.5a).

5.4.1.2. Sample RA-1 $^{206}\text{Pb}/^{238}\text{U}$ age populations

In sample RA-1, 48 analyses (34 in rims and 14 in core) were obtained; seven of them were rejected because their high discordance (>10%). The youngest analysis is 300 ± 4 Ma. The youngest statistical significant population yield an age of 524.1 ± 1.1 Ma, followed by scattered Neoproterozoic and Mesoproterozoic analyses (Fig. 5.5b).

5.4.1.3. Sample RA-2 $^{206}\text{Pb}/^{238}\text{U}$ age populations

In sample RA-2, 64 analyses (49 in rims and 15 in cores) were obtained; two of them were rejected because of their high discordance (>10%). The youngest analysis, 309 ± 6 Ma, is included in a population at 338.9 ± 1.1 Ma. The most prominent probability peak is 593.1 ± 1.3 Ma, and is followed by a smaller population at 982.3 ± 2.9 Ma. Finally, a minor amount of analyses show Paleoproterozoic ages (Fig. 5.5c).

5.4.1.4. Sample VE-1 $^{206}\text{Pb}/^{238}\text{U}$ age populations

In sample VE-1 86 analyses (77 in rims and 9 in cores) were obtained; three of them have been rejected because of their high discordance (>10%). The youngest analysis is 338 ± 4 Ma. The youngest age population is present at 349.1 ± 1.6 Ma. The most prominent probability peak is 574.8 ± 1.2 Ma. A broad population is present at 966.2 ± 2.3 Ma, and 1875.2 ± 4.9 Ma. There is some representation of Archaean ages (Fig. 5.5d).

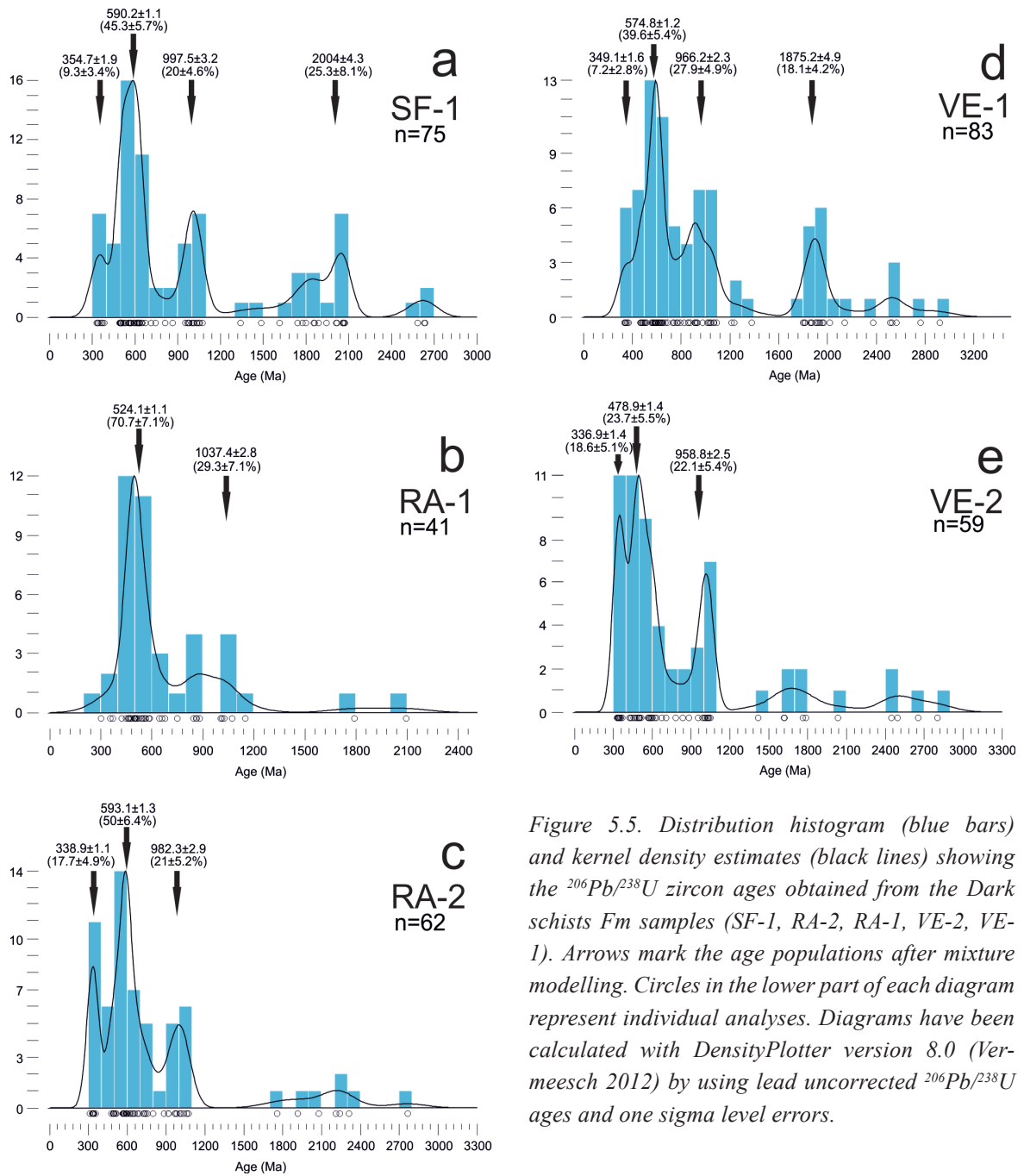


Figure 5.5. Distribution histogram (blue bars) and kernel density estimates (black lines) showing the $^{206}\text{Pb}/^{238}\text{U}$ zircon ages obtained from the Dark schists Fm samples (SF-1, RA-2, RA-1, VE-2, VE-1). Arrows mark the age populations after mixture modelling. Circles in the lower part of each diagram represent individual analyses. Diagrams have been calculated with DensityPlotter version 8.0 (Vermeesch 2012) by using lead uncorrected $^{206}\text{Pb}/^{238}\text{U}$ ages and one sigma level errors.

5.4.1.5. Sample VE-2 $^{206}\text{Pb}/^{238}\text{U}$ age populations

In sample VE-2, 70 analyses (58 in rims and 12 in cores) were obtained; eleven of them were rejected because of their high discordance (>10%). The youngest analysis, 326 ± 4 Ma, is included in an age population of 336.9 ± 1.4 Ma, closer to a probability peak at 478.9 ± 1.4 Ma. A smaller age population is found at 958.8 ± 2.5 Ma (Fig. 5.5e).

5.4.2. Upper part of the complex

5.4.2.1. Sample SF-2 $^{206}\text{Pb}/^{238}\text{U}$ age populations

In sample SF-2, 52 zircon analyses (39 in rims and 13 in cores) were obtained; six of them were rejected because of their high discordance ($>10\%$). The youngest analysis is 232 ± 1 Ma. In this sample, analyses defined an age population at 269.6 ± 0.9 Ma, followed by a prominent age population at 601.2 ± 0.9 Ma (Fig. 5.6a).

5.4.2.2. Sample RA-3 $^{206}\text{Pb}/^{238}\text{U}$ age populations

In sample RA-3, 54 analyses (38 in rims and 16 in cores) were obtained; four of them were rejected because of their high discordance ($>10\%$). The youngest analysis is 303 ± 12 Ma. A younger age population is observed at 334.6 ± 2.9 Ma, followed by two prominent probability peaks at 602.1 ± 3.1 and 999.3 ± 5.3 Ma. A remarkable Paleoproterozoic population is observable at 2088 ± 11 Ma (Fig. 5.6b).

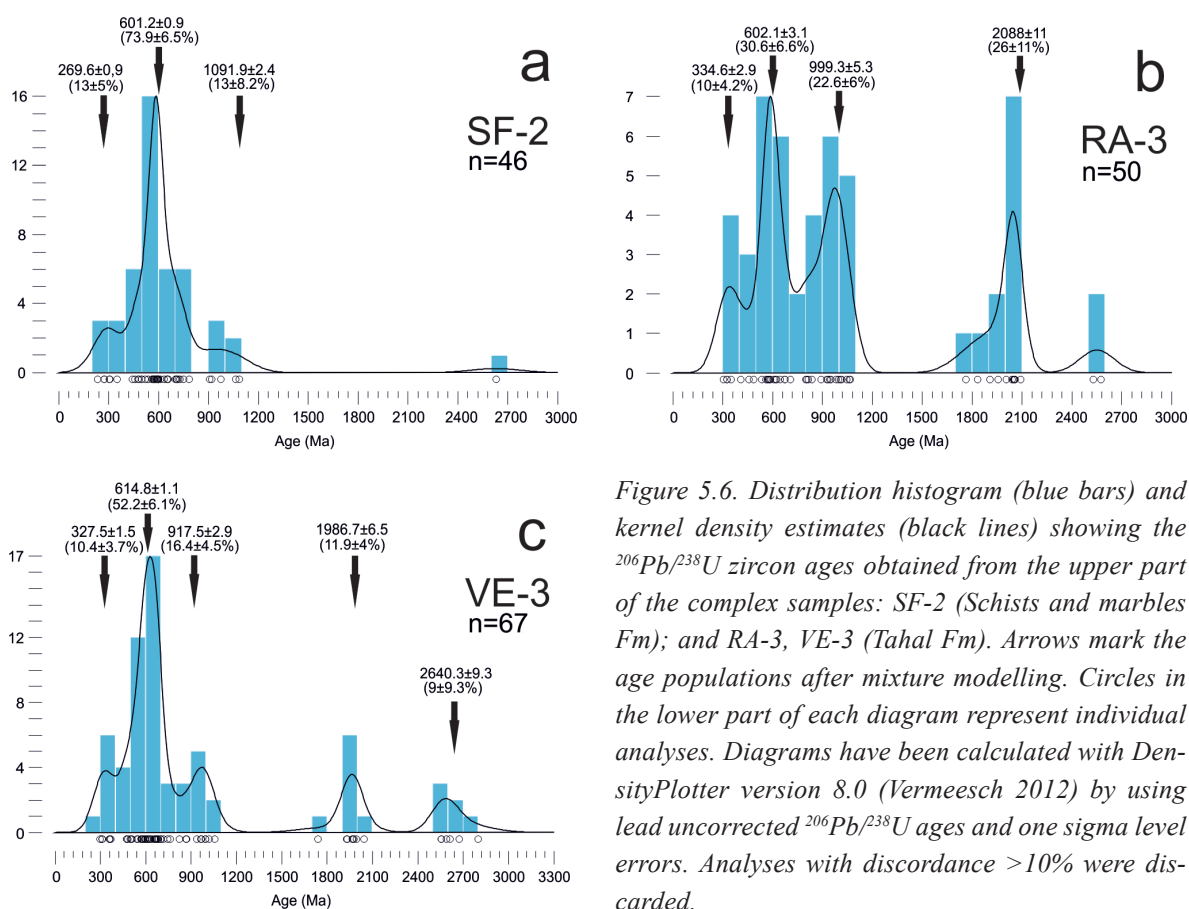


Figure 5.6. Distribution histogram (blue bars) and kernel density estimates (black lines) showing the $^{206}\text{Pb}/^{238}\text{U}$ zircon ages obtained from the upper part of the complex samples: SF-2 (Schists and marbles Fm); and RA-3, VE-3 (Tahal Fm). Arrows mark the age populations after mixture modelling. Circles in the lower part of each diagram represent individual analyses. Diagrams have been calculated with DensityPlotter version 8.0 (Vermeesch 2012) by using lead uncorrected $^{206}\text{Pb}/^{238}\text{U}$ ages and one sigma level errors. Analyses with discordance $>10\%$ were discarded.

5.4.2.3. Sample VE-3 $^{206}\text{Pb}/^{238}\text{U}$ age populations

In sample VE-3, 70 analyses (63 in rims and 7 in cores) were obtained; three of them were rejected because of their high discordance (>10%). The youngest analysis is 295 ± 6 Ma. The youngest age population is 327.5 ± 1.5 Ma. The biggest age population is 614.8 ± 1.1 Ma, and is followed by small populations at 917.5 ± 2.9 , 1986.7 ± 6.5 and 2640.3 ± 9.3 Ma (Fig. 5.6c).

5.5. Discussion on the geochronology results

5.5.1. Age of the deposition of the protolith of the schists

The youngest age populations that are statistically significant (formed by number of analyses ≥ 3) for each sample are shown in Table 5.1. The youngest age populations identified in the lowermost sample in both the upper and lower parts of the complex can be used in order to estimate MDAs.

Sample	Youngest age population (Ma)	Formation	
SF-2	269.6 ± 0.9	Schists and marbles Fm	Upper part of the complex
RA-3	334.6 ± 2.9	Tahal Fm	
VE-3	327.5 ± 1.5		
SF-1	354.7 ± 1.9	Dark schists Fm	Lower part of the complex
RA-2	338.9 ± 1.1		
RA-1	524.1 ± 1.1		
VE-2	336.9 ± 1.4		
VE-1	349.1 ± 1.6		

Table 5.1 Youngest statistically significant age populations obtained in the studied samples

In the lower part of the complex four of the five samples (SF-1, RA-2, VE-1 and VE-2) show Carboniferous youngest age populations (Table 5.1). In particular, the sample VE-1 which was taken in the lowest part of the Dark schists Fm shows a youngest age population of 349.1 ± 1.6 Ma. This age can be interpreted as the most probable MDA for the lower part of the complex in Sierra Nevada and Sierra de los Filabres.

In the upper part of the complex two of the three samples show Carboniferous youngest age populations (RA-3 and VE-3) (Table 5.1). Sample RA-3 was taken in the lowermost position and the youngest age population in this sample is 334.6 ± 2.9 Ma. Accordingly it can be interpreted as the most probable MDA for the upper part of the complex in Sierra Nevada and Sierra de los Filabres.

In samples SF-2 and RA-1 the number of Carboniferous analyses is insufficient ($n < 3$) to define statistically representative age populations. Nevertheless, a Carboniferous participation is still present in these two samples (Figs. 5.5b and 5.6a), and are in line with the previous Carboniferous estimations in other samples.

5.5.2. Interpretation of older age populations and similarity between the upper and lower parts of the complex

In addition to the Carboniferous age populations, other common age populations have been identified. All the samples show a clear domain ranging at ca. 480-615 Ma (Cambrian-Ediacaran). All samples, and to a lower extent the sample SF-2, exhibit an age population at ca. 910-1010 Ma (Tonian-Stenian). In samples SF-1, RA-3, VE-1 there is a particularly relevant age population at ca. 1800-2000 Ma, also present in samples RA-2, VE-2 and VE-3, almost absent in sample RA-1 and absent in sample SF-2. These last two samples reported few analyses > 1200 Ma, insufficient to define age populations. Finally, there is a representation of Archaean analyses ca. 2600 Ma in all samples, although it is remarkable only in sample VE-3.

The similarity between various population ages in samples attributed to the lower part of the complex (samples SF-1, RA-1, RA-2, VE-1 and VE-2), and the upper part (samples SF-2, RA-3 and VE-3,) implies a common source area (or areas) for the detrital zircons. However it is important to note that samples SF-1 and RA-1 did not yielded identical age patterns compared the other samples. The reason is probably the lower number of analyses obtained from these two samples (52 in sample SF-2, and 48 in sample RA-1).

5.5.3. Comparison with previous dating. Geological implications

5.5.3.1. Lower part of the complex

The lack of radiometric dating based in igneous rocks in the Dark schists Fm prevents to compare the MDA estimated for this formation (349.1 ± 1.6 Ma) with any existing mDA. No-radiometric estimations for this formation include pre-Cambrian (Gómez-Pugnaire, 1981) and Devonian (Lafuste and Pavillon, 1976; Laborda-López et al., 2015) fossils from the eastern part of the Betic Cordillera, older than youngest ages populations in samples SF-1, RA-2, VE-1 and VE-2, and in any case similar to sample RA-1 youngest age population. A possible explanation is that these fossils were taken in deeper levels of the formation, which do not outcrop in Sierra Nevada and Sierra de los Filabres. In Sierra de Baza, Rodríguez-Cañero et al. (2018) identified early Bashkirian (323.2 ± 0.4 to 315.2 ± 0.2 Ma) conodont fauna slightly younger than the age populations presented here. These differences are not incompatible because detrital zircons can be older than the fauna included in the sediment. Jabaloy et al. (2018) yielded SHRIMP U-Pb data from detrital zircons obtained in four samples of schists taken in the western Sierra de los Filabres area. These authors assign the samples to the Aulago unit (mostly equivalent to the Dark schists Fm) and proposed a MDA of 359 ± 5 Ma for the lower part of the complex. This age mostly coincides with the MDA proposed in this Ph.D. Thesis for this part (349.1 ± 1.6 Ma). Older age populations yielded by these authors are: Ediacaran (~ 596 Ma), Cryogenian (~ 788 Ma), Late Stenian (1031 Ma), Paleoproterozoic (1810 and 1910 Ma) and Neoproterozoic (~ 2620 Ma). With the exception of the Cryogenian populations, our age patterns resemble the results of Jabaloy et al. (2018). Although, analyses yielding Cryogenian dates are present in the samples from the Dark schists Fm, they are insufficient to define an independent age population. In this sense the patterns presented here are similar to the sample SN-31b of Jabaloy et al. (2018) which does not present this age population.

5.5.3.2. Upper part of the complex

The youngest age populations in the upper part of the complex (Tahal and Schists and marbles Fms) (Table 5.1), have been compared with the ages determined for these formations in previous works. Recent studies have been oriented to dating of zircons included in orthogneisses. Age estimations comprise: Gómez-Pugnaire et al. (2000) of 247 ± 11 Ma in the central part of the complex; Gómez-Pugnaire et al. (2004) of 301 ± 7 Ma, and Martínez-Martínez et al. (2010), of 304 ± 23 and 314 ± 7 Ma in the western part of

Sierra Nevada; and those of Gómez-Pugnaire et al. (2012), of 282 ± 5 to 295 ± 3 Ma, and Ruiz-Cruz and Sanz de Galdeano (2017) of ~ 286 Ma, in the south-western area of Sierra Nevada. Youngest age populations in samples RA-3 and VE-3 are older than the cited. The differences between our results and literature can be attributed to the different origin of the zircons: detrital zircons are inherited in the sediment, while zircons obtained from the orthogneisses yield ages later the deposition. Only youngest age population in sample SF-2 is younger than the ages reported by those authors.

Jabaloy et al. (2018) yielded LA-ICP-MS data from detrital zircons obtained in four schist samples taken in the eastern Sierra de los Filabres area (close to the Velefique area, sample VE-3). These authors assign these samples to the Tahal Fm. The youngest populations they obtained show $^{206}\text{Pb}/^{238}\text{U}$ ages ranging between 274 ± 3 and 295 ± 3 Ma. Accordingly they proposed an Early Permian MDA for this formation. These age populations are younger than those from Tahal samples, RA-3 and VE-3. Although, it is important to note that the youngest analyses in samples RA-3 and VE-3 yielded Early Permian ages (303 ± 12 and 295 ± 6 Ma respectively). Results of Jabaloy et al. (2018) are nearly coincident with sample SF-2 from the Schists and marbles Fm. Likewise, Jabaloy et al. (2018) results also record older age populations at Early Permian-Carboniferous (295-320 Ma) Ediacaran (~ 594 Ma), Cryogenian (~ 650 Ma) and Tonian (992 Ma), Mesoproterozoic (~ 1052 Ma), in addition to two minor Paleoproterozoic populations (~ 1880 and ~ 1960 Ma), and a minor Neoproterozoic population (~ 2610 Ma). Most of these age populations have been identified in the patterns obtained from samples SF-2, RA-3 and VE-3. However, the Ediacaran and Cryogenian analyses are partially merged defining a single age population in the KDE plots (Fig. 5.6). Besides, in sample SF-2 no Paleoproterozoic analyses were found.

5.5.3.3. Interval of sedimentation for the protolith of the schists

Most of the youngest age populations presented here are Carboniferous in age. This finding does not imply that the totally of the sedimentary protolith was deposited during this period. As the dating of detrital zircons only provides MDAs, a younger age for the sedimentary protolith cannot be excluded and, therefore, it prevents to estimate an interval for the sedimentation of the schists protolith.

An approach to narrow the interval of sedimentation of the Nevado-Filábride schists protolith (comprising both the upper and lower parts of the complex) relies on combining

the mDAs obtained in the literature with the MDAs obtained in the present study. Gómez-Pugnaire et al. (2012) age estimations in orthogneisses from the Schists and Marbles Fm allowed obtaining mDA of 282 ± 5 Ma for the schists (see their sample CB-4). As the youngest age population obtained in the lowermost sample studied (VE-1) is 349.1 ± 1.6 Ma, the deposition of the sediments probably happened between ca. 282 to 349 Ma (Fig. 5.7).

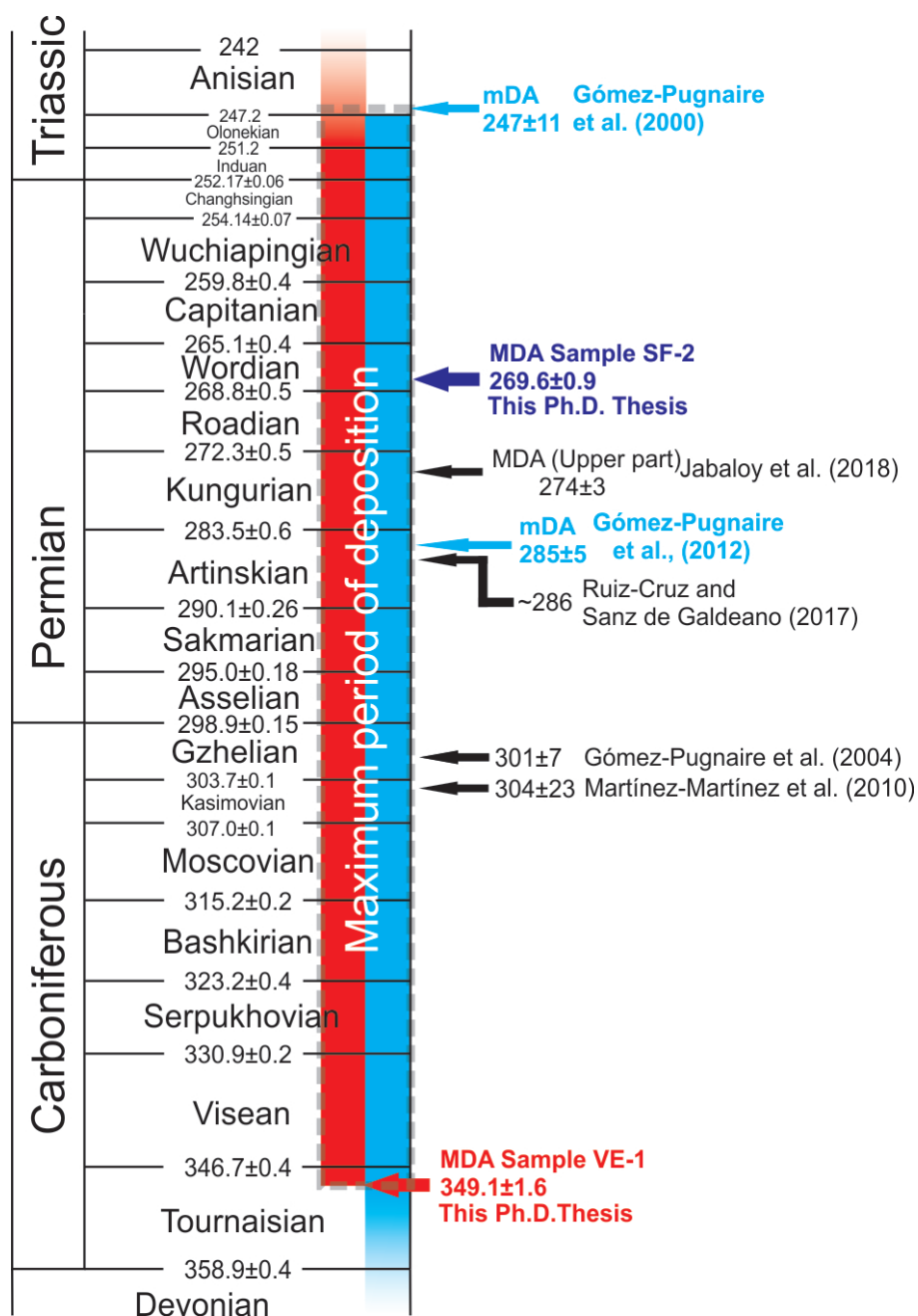


Figure 5.7. Recent age estimations from Nevado-Filábride gneisses in the literature compared with the maximum deposition age obtained after detrital zircon dating in this Ph.D. Thesis. Inset shows a probable maximum period for the deposition of the sedimentary protolith (see text).

However this interval excludes the youngest age population estimated in sample SF-2, 269.6 ± 0.9 Ma and accordingly this tentatively range should be taken into account with precaution. A more conservative lapse of deposition ranges between the mDA of Gómez-Pugnaire et al. (2000), 247 ± 11 Ma, and 349.1 ± 1.6 Ma (Fig. 5.7). The present thickness existing between the stratigraphic positions of the samples from Gómez-Pugnaire et al. (2012) and the sample VE-1 is ~ 4000 - 5000 m. As the sequence could present several tectonic repetitions, the actual estimation of the deposited sediment volume, even if it can be high, cannot be estimated with certainty in this study.

The Nevado-Filábride complex succession culminates with marbles resulted from deposition of carbonates probably during Triassic (de Jong and Bakker, 1991).

5.6. Origin of inclusions

The study of SEM images and EDX patterns, combined with the CL images, permitted constraining the former origin of the inclusions and their relationship with the host zircon. Initial approach focused on deciphering the primary or secondary origin of the inclusions. Primary inclusions can be present in both igneous zircons and metamorphic regrowth. In the first case, the CL image shows a mostly unaltered oscillatory pattern (characteristic of the igneous zircons) around the inclusion. The common interpretation is that the inclusion was trapped during the growth of the igneous zircon. Otherwise, inclusions can be found in metamorphic regrowth, recrystallizations, or in metamorphic rims surrounding xenocrystic igneous cores. In these cases the oscillatory pattern does not necessary occur, and inclusions are related to textural features pointing to metamorphic conditions (e.g. no-zoned patches, weak zoning, etc.). Inclusions related to fractures can be interpreted as secondary inclusions formed after precipitation from fluids. The mineral composition of the secondary inclusion is not necessary dependent of the former origin of the zircon. In these cases the CL images show patched zoning and/or disturbed textures formed after the zircon-secondary inclusion interaction (Wu and Zheng 2004).

5.6.1. Primary inclusions

Most of the primary inclusions reported in this Ph.D. Thesis are inclusions trapped in oscillatory zoned zircons interpreted as igneous in origin. Quartz (Fig. 5.2i, o) and apatite (Fig. 5.4f, g o) are the most common primary inclusions. Phengite (Fig. 5.4c, f), monazi-

te and xenotime (which in some cases is included by small quartz grains, see Fig. 5.4b) are scarce. Apatite, monazite and xenotime are not always present in the sample matrix. Therefore their inclusion in zircons during the igneous phase seems plausible. Quartz, apatite and phengite occupy positions in cores and rims, while xenotime and monazite usually are found in mantle and rim. Some quartz and apatite are present in cores showing oscillatory pattern partially fainted. In those cases an igneous origin has been attributed to inclusions and cores, later affected by a metamorphic event which led to alteration of the oscillatory pattern. In general, igneous primary inclusions have been found in zircons which yield SHRIMP analyses of ca. 300-380 Ma. Only few inclusions of quartz, apatite and xenotime are included in zircons showing analyses ca. 520 Ma, and quartz inclusions have been found in a rim showing analyses of ca. 620 Ma.

Zircons showing metamorphic regrowth are occasionally included by metamorphic minerals as paragonite (Fig. 5.4h), albite (Fig. 5.4n) and chlorite (Fig. 5.4n). The regrowth surround oscillatory zoned cores interpreted as igneous and commonly fainted and included by quartz and apatite (Fig. 5.4j). SHRIMP analyses in the regrowth yield dates ranging ca. 310-350 Ma, interpreted as the age when paragonite, plagioclase and chlorite were probably formed during metamorphism. The igneous cores show analyses ~350, ~600 and ~1000 Ma, which point to the age of previous igneous phases. The zircon in Fig. 5.4e preserves an obliterated oscillatory zoned core included by quartz and chlorite, surrounded by an oscillatory rim. In this case, a more complex story can be inferred, including an initial igneous event followed by possible alteration during metamorphism and, finally, new growth under igneous conditions. Accordingly, observations support the complex growth story of various grains including several crystallization steps under different conditions.

5.6.2. Secondary inclusions

Inclusions related with fractures are quartz (Figs. 5.4d; 5.4l and insets; 5.4m), apatite (Figs. 5.4l and insets; 5.4m, o), phengite (occasionally included in quartz, see Fig. 5.4p), paragonite, rutile (Fig. 5.4i), monazite (Fig. 5.4g), xenotime and epidote (Fig. 5.4k and insets). Samples including these inclusions additionally show them as phases in the matrix. The precipitation of inclusions probably occurred during the Alpine metamorphism.

Chapter 6

Conditions of metamorphism

6.1. Introduction

Pressure-Temperature-time (P-T-t) paths have been previously used in order to summarize the changes in pressure and temperature conditions recorded in a rock during an orogeny. Accordingly determining P-T-t paths for metamorphic rocks of several units has proved to be a valid method to decipher mountain-building tectonic processes such as the subduction and exhumation of metamorphic complexes (e.g. Ernst, 1988; Guillot et al., 2009; Rolland et al., 2012). Identification and quantification of the differences or similarities in conditions recorded by several tectonic units (as those previously proposed for the Nevado-Filábride complex, see section 2.3.1), allow to constrain tectonic and thermal histories and propose tectonic scenarios (e.g. Thompson and England, 1984; Jamienson, 1991; Foster and Parrish, 2003; Brown, 2014). Our ability to construct portions of P-T paths have been improved by the development of analytical and modelling techniques in metamorphic petrology which have opened new possibilities in order to estimate the P-T conditions (e.g. Brown, 2007, 2014; Lanari and Duisterhoeft, 2019). Nowadays there are several thermobarometric methods to estimate P-T conditions including: empirical thermobarometers (e.g. Hodges and Crowley, 1985), multi-equilibrium or average P-T approach (e.g. Berman, 1991; Holland and Powell, 1998), equilibrium phase diagrams (e.g. Holland and Powell, 1998, 2011), Raman spectrometry in carbonaceous material (e.g. Beyssac et al., 2002). Several of these techniques are based on the assumption of chemical equilibrium and have absolute uncertainties of ± 50 °C (Kohn and Spear, 1991). By contrast, relative thermobarometry between units to be performed in a much precise way (Worley and Powell, 2000) due to relative errors are smaller. Additionally, thermobarometric methods require estimating the composition of minerals assumed to have been

in chemical equilibrium at one specific stage of the metamorphic history. In this sense, it is common to rely in porphyroblasts which, in some cases preserve chemical and textural record of metamorphic conditions affected the rock due to their remarkable resilience (e.g. Lanari et al., 2017; Yakymchuk et al., 2017). An excellent example for this is garnet which is a common rock-forming mineral (and is usually present in the Nevado-Filábride schists). Garnet often preserve compositional zoning interpreted to reflect changes in equilibrium conditions, and therefore related to changes in P-T conditions during metamorphism (Gaidies et al., 2008; Caddick and Kohn, 2013; Cheng and Cao, 2015; Baxter et al. 2017; Lanari et al., 2017). In order to determinate the mentioned compositional zoning it is common the application of quantitative compositional mapping (Lanari et al., 2013, 2014, 2018). A problem arises as garnet grows, as it becomes isolated from the reactive part of the rock and, therefore, the thermobarometric reconstruction based on the bulk rock compositions are biased (Spear, 1988; Evans, 2004; Tinkham and Ghent, 2005). The strategy proposed by Lanari et al. (2017) (described in section 3.3) confronts this problem and allows predicting P-T conditions based on the composition of each successive growth zones by taking into account the resorption and fractionation of garnet formed previously. Therefore, this methodology takes into account the possible variations of the reactive bulk composition. In this chapter is presented a set of EPMA compositional mapping of garnet from five garnet-bearing schists taken from different areas of the Nevado-Filábride complex. These data was combined with iterative thermodynamic models (Lanari et al., 2017) to obtain the P-T conditions of garnet and phengite growth in the studied rocks using the same modelling technique and thermodynamic data. The samples were collected from the Dark schists, Tahal and Schists and marbles Fms. The thermobarometric results obtained from garnet and phengite allowed the P-T paths to be reconstructed. These P-T paths were combined with *in situ* U-Th-Pb allanite dating in an attempt to add time-constraints on the P-T evolution.

6.2. Quantitative petrography

6.2.1. Mineral assemblages

Five garnet-bearing mica-schists were studied: RA-2, RA-0, 10.1, 16.8 and 16.16. Three of the five investigated samples, 10.1, 16.8 and 16.16, were collected in the Peñones de San Francisco area (see Figs. 4.1 and 4.2). Samples RA-2 and RA-0 were collected from La Ragua area (see Figs. 4.1 and 4.11). Their stratigraphic relative positions are shown in the schematic lithological succession in Fig. 4.25. The UTM coordinates of

samples are included in Appendix 1. Samples are described below from lower to higher position in the Nevado-Filábride pile.

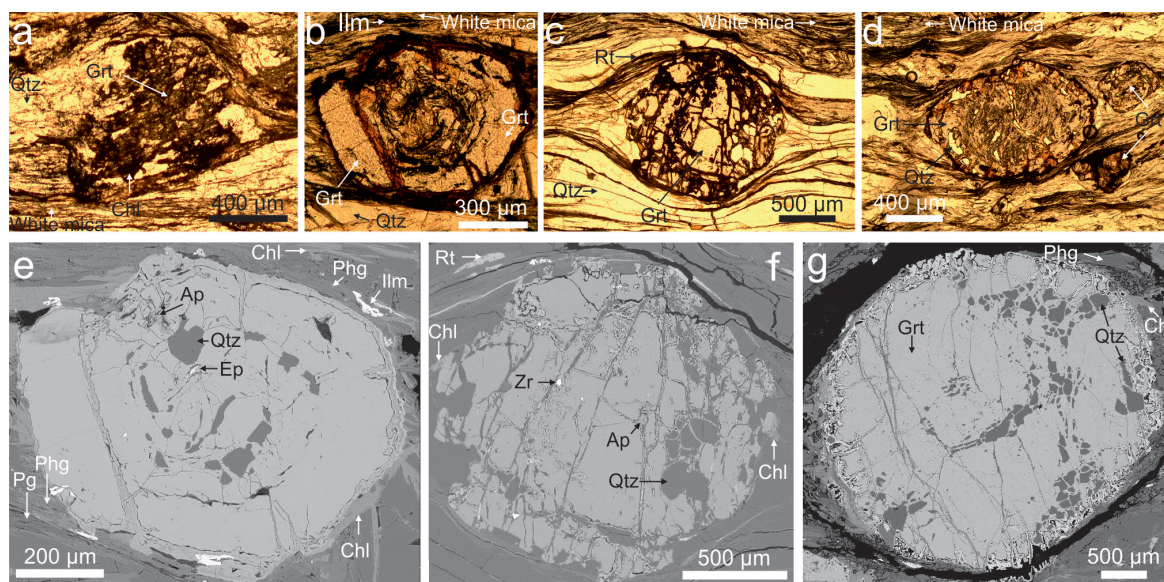


Figure 6.1. Optical microscopy (a, b, c, d) and backscattered electron (e, f, g) images of garnet porphyroblast and the mineral matrix in the studied samples. Abbreviations: Ap (apatite), Chl (chlorite), Ep (epidote), Grt (garnet), Ilm (ilmenite), Pg (paragonite), Phg (phengite), Qtz (quartz), Rt (rutile), Zr (zircon).

Sample RA-2 (Dark schists Fm) is a fine grained dark schist (Fig. 6.1a) made of major phases of quartz, albite, phengite, paragonite, chlorite and garnet; and graphite, epidote, rutile, ilmenite, apatite, titanite and zircon as accessory phases. Most of the garnet porphyroblasts have been partially or completely replaced by chlorite (Fig. 6.1a). The preserved garnet grains are relatively small (<1 mm). These porphyroblasts contain inclusions of quartz, ilmenite, epidote, zircon and titanite.

Sample 10.1 (Dark schists Fm) is a dark schist (Fig. 6.1b, e) consisting of major phases of quartz, phengite, paragonite, chlorite, chloritoid and garnet; and ilmenite, rutile, epidote and allanite as accessory phases. The size of the garnet porphyroblasts is up to 800 μm . They show inclusions of quartz (mainly located in the core) (Fig. 6.1e), graphite, apatite (Fig. 6.1e), ilmenite, epidote (Fig. 6.1e), allanite, zircon and titanite.

Sample RA-0 (Tahal Fm) is a dark-grey schist (Fig. 6.1c, f) formed by major phases of quartz, phengite, paragonite, chlorite, chloritoid and garnet; and the accessory phases

apatite, zircon, rutile, tourmaline, ilmenite and monazite. Garnet porphyroblasts have a size of up to 1 mm and they are frequently fractured (Fig. 6.1c, f). The porphyroblasts are slightly deformed and contain numerous inclusions of quartz (Fig. 6.1f) and in lower amount of graphite, apatite (Fig. 6.1c, f), rutile and zircon.

Sample 16.8 (Tahal Fm) is a grey mica-schist (Fig. 6.1g) containing quartz, albite, phengite, paragonite, chloritoid, chlorite and garnet; and accessory phases of graphite, ilmenite, rutile, apatite, epidote, allanite, tourmaline and biotite. Garnet porphyroblasts have a size up to 3 mm. They are highly deformed (Fig. 6.1g) and show numerous fractures. The inclusions in garnet are quartz (Fig. 6.1g), rutile, zircon, biotite and apatite.

Sample 16.16 (Schists and marbles Fm) is a dark grey mica-schist (Fig. 6.1d) showing major phases of quartz, albite, phengite, paragonite, chloritoid, chlorite and garnet; and graphite, titanite, biotite, ilmenite, rutile, epidote, apatite and allanite as accessory phases. Garnet porphyroblasts have a size of up to 2 mm and inclusions of quartz, graphite, ilmenite, allanite, rutile and chlorite. Snowball and atoll garnets are commonly observed.

In samples pertaining to the Tahal and Schists and marbles Fms the graphite content is lower than in samples from the Dark schists Fm, leading to schists comparatively light-coloured than those from the Dark schists Fm. Allanite was found in samples 16.8 and 16.16, with comparable features. Allanite size ranges between 40 and 160 μm and the grains are generally located in the mineral matrix. Few of them were observed as inclusion in the outer rim of garnet.

6.2.2. Microstructures

The samples RA-0, 10.1, 16.8, and 16.16 exhibit either the two main planar fabrics S1 and S2. However, sample RA-2 exhibits a single foliation Sp corresponding to S2. The first cleavage S1 is parallel to the compositional layering and it was folded during formation of a crenulation cleavage defined as S2 (section 2.3.4). In the Dark schists Fm, S1 is preserved in sample 10.1 in which phengite and paragonite (up to 100 μm long) form aggregates intergrown by graphite lamellas. In the Tahal Fm, S1 is preserved in sample RA-0 with phengite (up to 300 μm), paragonite (up to 200 μm) and chlorite (up to 200 μm); and in sample 16.8 with interbedded thin grains of phengite and paragonite (up to

300 μm). In the Schists and marbles Fm, S1 is preserved in sample 16.16 as intergrowths of phengite (200 μm), paragonite (100 μm), chlorite (50 μm) and fine lamellas of graphite. It has already been proposed that the S1 cleavage formed during the prograde history under greenschist facies conditions (e.g. Martínez-Martínez, 1986; de Jong, 1991). Despite possible partial re-equilibrations at higher grade (e.g. Airaghi et al., 2017), local mineral assemblage described before for S1 (when it is visible) support the conclusion that it was formed under greenschist facies conditions.

In the Dark schists Fm, S2 is underlined in sample RA-2 by thick aggregates of chlorite (up to 600 μm long), plagioclase (250 μm) and intergrowths of phengite and paragonite (200 μm); and in sample 10.1 by chlorite (500 μm), chloritoid (100 μm), phengite (400 μm) and paragonite (200 μm) showing graphite inclusions. In the Tahal Fm the following mineral phases are observed into S2: in sample RA-0, phengite (up to 400 μm) included by graphite lamellas, paragonite (up to 200 μm), and chlorite (up to 300 μm); in sample 16.8, phengite (up to 800 μm), paragonite (up to 300 μm), plagioclase (up to 300 μm) and chlorite (up to 500 μm) which includes phengite. In sample 16.16, pertaining to the Schists and marbles Fm, S2 is underlined by phengite (up to 400 μm), chlorite (up to 100 μm), and paragonite (up to 200 μm) include graphite lamellas. The crenulation-cleavage S2 has been proposed to have formed during exhumation and cooling (Martínez-Martínez, 1986; Platt and Behrmann, 1986; García-Dueñas et al., 1988; Augier et al., 2005b). The local mineral assemblages described above for S2 suggest that it developed under greenschist facies conditions in both the upper and lower part of the complex.

In garnet cores of samples 16.16 and 10.1 there are inclusion trails recording the geometry of the S1 cleavage. Besides, the porphyroblasts are deformed by S2 in sample 16.8. These observations suggest that garnet nucleated and grew significantly after S1 and before S2. In sample RA-0, garnet porphyroblasts are undeformed preventing the relative timing to be established, as it is for sample RA-2 in which garnet has been replaced by chlorite.

6.2.3. Mineral compositions and bulk rock compositions

The bulk rock compositions from studied samples used for modelling are included in Table 6.1. The representative analyses of minerals are listed in Table 6.2. The structural formulae of white mica were calculated assuming all the iron to be Fe^{2+} .

K-white mica in S1 show a Si^{4+} content of 3.10 to 3.19 apfu, whereas those in S2 have values ranging between 3.07 and 3.28 apfu (Fig. 6.2). Higher Si^{4+} content is observed in samples from the upper part of the complex, 16.16: 3.23 - 3.24 in S1 and 3.13 - 3.22 in S2 (triangles in Fig. 6.2); and in sample 16.8: 3.15 - 3.21 in S1 and 3.18 - 3.28 in S2 (pentagons in Fig. 6.2); followed by sample RA-0: 3.10 - 3.18 in S1 and 3.09 - 3.15 in S2 (circles in Fig. 6.2). Lower values are found in samples from the lower part of the complex, sample 10.1: 3.18 in S1 and 3.12- 3.21 in S2 (squares in Fig. 6.2); and sample RA-2: 3.07- 3.23 in S2 (stars in Fig. 6.2).

K-white mica yielded Na^+ content in S1 ranging between 0.09 and 0.19 apfu, and 0.10 and 0.40 apfu in S2 (Fig. 6.2). In sample 16.16, the Na^+ content of K-white mica varies from 0.11 - 0.13 in S1 and 0.14 - 0.21 in S2 (triangles in Fig. 6.2); in sample 16.8, 0.12 - 0.17 in S1, and 0.10 - 0.14 in S2 (pentagons in Fig. 6.2); in sample RA-0, 0.10 - 0.19 in S1, and 0.15 - 0.18 in S2 (circles in Fig. 6.2); in sample 10.1, is 0.13 in S1, and 0.10 - 0.19 S2 (squares in Fig. 6.2); and in sample RA-2 results are 0.09 - 0.17 in S2 (stars in Fig. 6.2).

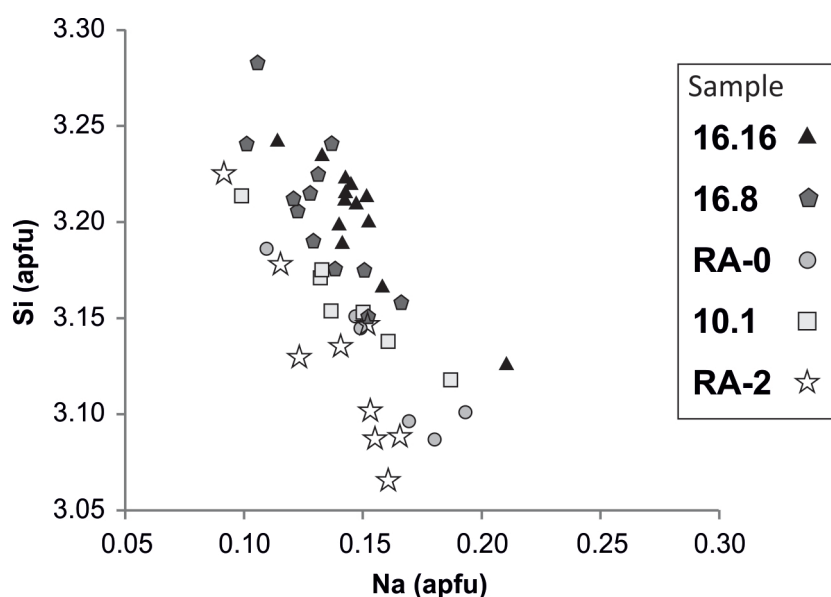


Figure 6.2. Phengite chemical diagram Si^{4+} vs Na^+ content in analysed phengites. Si^{4+} and Na^+ content in atoms per formula unit (apfu).

XMg in K-white mica developed in S1 varies between 0.49 and 0.71, and 0.43 and 0.73 in S2. Higher values of XMg are observed in samples from samples 16.16 (Schists and marbles Fm), 0.65 - 0.71 in S1, and 0.61 - 0.73 in S2; in sample 16.8 (Tahal Fm), 0.61 - 0.65 in S1, and 0.63 - 0.67 in S2. Lower values of XMg are observed in sample RA-0

(Tahal Fm) showing 0.57 - 0.58 in S1 and 0.43 - 0.54 in S2; and samples from the Dark schists Fm, 10.1, 0.59 in S1, and 0.48 - 0.62 in S2; and RA-2, 0.49 - 0.56 in S2.

Paragonite composition shows Na⁺ content in S1 varying between 0.80 and 0.86 apfu and from 0.75 to 0.90 apfu in S2. The Na⁺ content in paragonite in sample 16.16 are ~0.84 in S1, and 0.70 - 0.90 in S2; in sample 16.8 from 0.80 - 0.83 in S1, and 0.87 - 0.91 in S2, in sample RA-0 is 0.86 in S1, and 0.75 - 0.92 in S2; and in sample 10.1 is 0.88 in S1, and 0.87 - 0.89 in S2.

Chlorite developed in S1 has a Si⁴⁺ content ranging from 2.57 to 2.85 apfu and XMg from 0.42 to 0.52. In S2, chlorite exhibits higher Si⁴⁺ content varying from 2.57 to 3.26 apfu, and XMg from 0.33 to 0.57. In sample 16.16, Si⁴⁺ content varies between 2.68 - 3.07 in S1, and a value of 2.84 was obtained in S2; in sample 16.8 between 2.68 - 2.86 in S2; in sample RA-0 ranges between 2.57 - 2.64 in S1, and 2.58 - 2.64 in S2; in sample 10.1 between 2.63-2.88 in S2; and in sample RA-2 from 2.57 - 3.26 in S2. XMg in chlorite is 0.50-0.52 in S1, and 0.45 in S2 from sample 16.16; in sample 16.8 of 0.46 - 0.57 in S2; in sample RA-0 of 0.42 in S1, and 0.42- 0.43 in S2, in sample 10.1 varies between 0.41 and 0.49 in S2; and in sample RA-2 of 0.33 - 0.42 in S2.

	Sample 16.16	Sample 16.8	Sample RA-0	Sample 10.1	Sample RA-2
SiO ₂	60.19	57.24	53.00	59.33	75.10
TiO ₂	0.42	0.50	1.46	0.61	0.80
Al ₂ O ₃	20.35	19.91	23.29	19.18	12.04
FeO	10.86	7.60	8.93	9.44	4.49
MnO	0.12	0.30	0.12	0.41	0.04
MgO	2.51	2.10	1.24	2.30	1.00
CaO	0.82	2.29	0.30	1.27	0.25
Na ₂ O	1.29	1.99	0.89	1.29	0.65
K ₂ O	2.55	2.14	3.29	2.24	1.81

Table 6.1. Bulk rock compositions from studied samples used for modelling.

Table 6. 2.

Mineral	Sample 16.16										Sample 16.8										Sample RA-0											
	K white mica		K white mica		Pg		Chl		P-shadow		K white mica		K white mica		Pg		Chl		P-shadow		K white mica		K white mica		Pg		Ph		Chl		Chl	
	S1	S2	S1	S2	S2	S2	S1	S1	S1	P-shadow	S2	S2	S1	S1	S1	S1	S1	S2	S2	P-shadow	S2	S2	S1	S1	S2	S2	S2	S1	S1	S2	S1	
SiO ₂	48.91	46.60	47.81	46.30	45.52	25.59	30.08			46.96	47.22	45.75	46.32	27.51	26.73					46.87	46.90	46.75	46.35	47.98	24.80	23.89						
TiO ₂	0.37	0.39	0.35	0.08	0.08	0.02	0.20			0.48	0.47	0.49	0.15	0.05	0.07					0.30	0.16	0.08	0.05	0.31	0.04	0.05						
Al ₂ O ₃	31.90	32.33	31.44	39.52	38.84	21.81	20.10			28.76	30.56	31.73	38.77	23.47	22.34					34.06	36.61	38.82	39.42	33.83	23.76	23.57						
FeO	1.58	1.54	1.49	0.31	1.03	26.22	26.61			2.09	1.99	1.74	0.36	23.30	22.35					1.45	0.95	0.25	0.18	1.52	26.89	27.81						
MnO	0.01	0.00	0.01	0.00	0.02	0.06	0.07			0.02	0.00	0.00	0.00	0.10	0.07					0.00	0.08	0.00	0.00	0.00	0.07	0.09						
MgO	2.16	1.75	2.26	0.09	0.10	14.56	12.19			2.44	2.18	1.71	0.22	12.39	15.20					0.96	0.44	0.09	0.07	1.12	11.61	11.43						
CaO	0.01	0.00	0.00	0.37	0.35	0.01	0.11			0.05	0.01	0.05	0.20	0.08	0.03					0.03	0.02	0.06	0.02	0.03	0.02	0.04						
Na ₂ O	1.04	1.20	1.11	6.78	7.14	0.00	0.00			0.78	0.99	1.24	6.61	0.01	0.00					1.13	1.41	6.97	7.38	0.85	0.03	0.17						
K ₂ O	9.44	9.27	9.33	0.81	0.87	0.02	0.55			8.86	9.43	9.06	1.50	0.04	0.05					8.59	8.53	0.60	0.54	8.81	0.21	0.10						
Cations																																
Si	3.23	3.17	3.22	2.99	2.97	2.68	3.08			3.28	3.22	3.16	3.00	2.86	2.78					3.15	3.09	3.03	2.99	3.19	2.64	2.57						
Ti	0.02	0.02	0.02	0.00	0.00	0.00	0.02			0.03	0.02	0.03	0.01	0.00	0.01					0.02	0.01	0.00	0.00	0.02	0.00	0.00						
Al	2.49	2.59	2.49	3.01	2.98	2.70	2.42			2.37	2.46	2.58	2.96	2.87	2.74					2.70	2.84	2.96	3.00	2.65	2.98	2.99						
Fe	0.09	0.09	0.08	0.02	0.06	2.30	2.27			0.12	0.11	0.10	0.02	2.02	1.94					0.08	0.05	0.01	0.01	0.08	2.39	2.50						
Mn	0.00	0.00	0.00	0.00	0.00	0.01	0.01			0.00	0.00	0.00	0.00	0.01	0.01					0.00	0.00	0.00	0.00	0.00	0.01	0.01						
Mg	0.21	0.18	0.23	0.01	0.01	2.28	1.86			0.25	0.22	0.18	0.02	1.92	2.36					0.10	0.04	0.01	0.01	0.11	1.84	1.83						
Ca	0.00	0.00	0.00	0.03	0.02	0.00	0.01			0.00	0.00	0.00	0.01	0.01	0.00					0.00	0.00	0.00	0.00	0.00	0.00	0.00						
Na	0.13	0.16	0.15	0.85	0.90	0.00	0.00			0.11	0.13	0.17	0.83	0.00	0.00					0.15	0.18	0.88	0.92	0.11	0.01	0.03						
K	0.80	0.80	0.80	0.07	0.07	0.00	0.07			0.79	0.82	0.80	0.12	0.00	0.01					0.74	0.72	0.05	0.04	0.75	0.03	0.01						
XMg	0.71	0.67	0.73	0.34	0.15	0.50	0.45			0.67	0.66	0.64	0.52	0.49	0.55					0.54	0.43	0.40	0.41	0.57	0.43	0.42						

Table 6. 2. (cont.)

		Sample 10.1						Sample RA-2					
Mineral	Location	K white mica		Pg		Chl		K white mica		Pg		Chl	
		S2	S2	S2	S2	S2	P-shadow	S2	S2	S2	S2	S2	P-shadow
SiO ₂		47.72	46.74	46.90	24.64	27.79	46.82	46.72	45.98	47.74	27.55	23.46	
TiO ₂		0.33	0.40	0.06	0.05	0.06	0.40	0.31	0.21	0.07	0.10	0.10	
Al ₂ O ₃		30.47	32.36	38.38	22.00	22.81	31.75	35.51	36.32	39.42	21.30	22.96	
FeO		2.79	1.91	0.57	25.83	26.72	1.71	1.14	1.05	0.22	28.15	30.66	
MnO		0.00	0.00	0.00	0.03	0.05	0.00	0.00	0.00	0.00	0.18	0.18	
MgO		2.14	1.59	0.40	13.28	11.29	1.19	0.63	0.56	0.15	8.85	8.75	
CaO		0.01	0.00	0.11	0.04	0.04	0.07	0.06	0.02	0.08	0.10	0.09	
Na ₂ O		0.76	1.04	7.01	0.24	0.05	0.69	1.19	1.24	6.59	0.03	0.07	
K ₂ O		9.57	9.35	1.97	0.15	0.02	8.43	8.48	8.66	0.56	0.04	0.00	
Cations													
Si		3.21	3.15	3.02	2.65	2.88	3.23	3.10	3.07	3.04	2.97	2.59	
Ti		0.02	0.02	0.00	0.00	0.00	0.02	0.02	0.01	0.00	0.01	0.01	
Al		2.42	2.57	2.91	2.79	2.78	2.58	2.78	2.85	2.96	2.70	2.99	
Fe		0.16	0.11	0.03	2.33	2.31	0.10	0.06	0.06	0.01	2.54	2.83	
Mn		0.00	0.00	0.00	0.00	0.00	0.00	0.00	0.00	0.00	0.02	0.02	
Mg		0.21	0.16	0.04	2.13	1.74	0.12	0.06	0.06	0.01	1.42	1.44	
Ca		0.00	0.00	0.01	0.00	0.00	0.01	0.00	0.00	0.01	0.01	0.01	
Na		0.10	0.14	0.87	0.05	0.01	0.09	0.15	0.16	0.81	0.01	0.01	
K		0.82	0.81	0.16	0.02	0.00	0.74	0.72	0.74	0.05	0.01	0.00	
X _{Mg}		0.58	0.60	0.55	0.48	0.43	0.55	0.50	0.49	0.55	0.36	0.34	

Table 6.2. Representative mineral compositions of phengite, paragonite and chlorite from the analysed samples. $X_{Mg} = Mg/(Mg^{+} + Fe^{2+})$.

6.3. Results

6.3.1. Compositional zoning of garnet

The compositional variability of garnet has been analysed using quantitative compositional mapping (the methodology followed is described section 3.3.3). The maps of end-member fraction for the studied garnet porphyroblasts are shown in Fig. 6.3 for the samples of the Tahal and Schists and marbles Fms, and Fig. 6.4 for samples of the Dark schists Fm.

Several growth zones of garnet were defined for each sample based on the compositional zonations. These growth zones are delimited by dashed lines in Figs. 6.3 and 6.4. The limit of each growth zone was set using the grossular map as reference (first compositional map for each set of maps in Figs. 6.3 and 6.4). Smother transitions between growth zones in almandine and pyrope maps suggest that the original composition may have been locally affected by diffusion (e.g. between core and first rim in sample RA-0's almandine map, Fig. 6.3). As these effects are restricted to ~10-40 μm around the limit (see below), it is assumed in the following that the central part of each growth zone was not significantly affected by diffusion allowing the growth composition to be preserved (other examples at similar conditions are given in Chapman et al., 2011). As it is described in section 3.3.4, the average composition of each growth zone was determined by integrating the pixel compositions of each domain selected in the central part of the growth zone. The size of the domain varies between 330 and 7200 μm^2 depending on the thickness of the growth zone. The garnet domains were carefully selected, avoiding mixing pixels, mineral inclusions and contact between zones that could have been affected by diffusion. The corresponding compositions and their analytical uncertainties were exported and are reported in Table 6.3. For comparison among samples, these average compositions are plotted in a ternary diagram (Fig. 6.5).

Garnet porphyroblasts in sample 16.16 (Fig. 6.3a) exhibit a core with typical growth zoning. Grossular (X_{grs}) and spessartine (X_{sps}) proportions decrease outward (0.18 to 0.10 and 0.029 to 0.015 respectively). Almandine (X_{alm}) and pyrope (X_{prp}) proportions both increase (0.69 to 0.76 and 0.09 to 0.14 respectively). The porphyroblast core is surrounded by two narrow rims. These rims are not thicker than 100 μm and both show lower X_{grs} and X_{sps} and higher X_{alm} and X_{prp} . A 50 μm thick fracture crosscuts the garnet

core. This fracture is sealed by garnet with similar composition of the outermost rim (Fig. 6.3a). Three garnet domains were selected in this sample. The first domain Grt₁ corresponds to the core of the porphyroblast. The average composition was obtained far away from the fracture (Fig. 6.3a). Two additional garnet domains were selected, Grt₂ for the inner rim and Grt₃ for the outer rim and the sealed fracture (Fig. 6.3a).

As shown by the X_{grs} map, garnet in sample 16.8 does not exhibit significant variations in Ca (0.87 ± 0.03 apfu) (Fig. 6.3b). By contrast, both X_{alm} and X_{prp} maps show lower values in the core (0.61 and 0.04 respectively) than in the rim (0.66 and 0.08). This chemical zonation is counterbalanced by a decrease of X_{sps} from 0.09 in the core to 0.01 in the rim. Three garnet domains were selected for modelling: the core, Grt₁; the mantle, Grt₂; and the rim, Grt₃ (Fig. 6.3b).

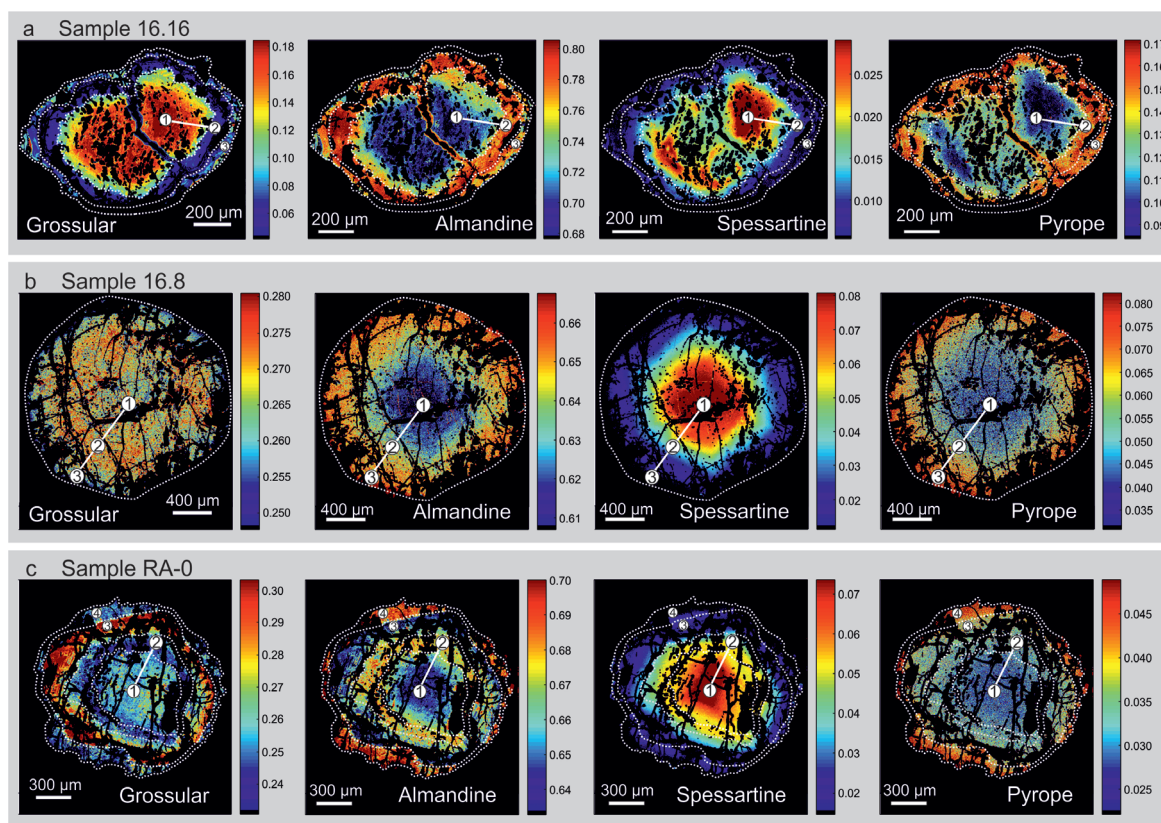


Figure 6.3. Compositional maps of end-member fractions for garnet porphyroblast analysed from the upper part of the complex: a) samples 16.16 (Schists and marbles Fm), b) sample 16.8 (Tahal Fm), c) sample RA-0 (Tahal Fm). Dashed lines delimit growth zones in the garnet. Circles show the location of the domains used for extracting the representative composition of each growth zone (see text). Continuous lines show where compositional profiles reported in Fig. 6.8 were obtained.

Garnet porphyroblasts in sample RA-0 display a more complex zoning pattern. It includes a core surrounded by three rings (Fig. 6.3c). The first ring (i.e. the innermost ring) and the second one are up to 300 μm thick. The outermost is up to 150 μm . Garnet shows an oscillatory pattern in both X_{grs} and X_{alm} maps. The core and the second ring are enriched in X_{grs} and depleted in X_{alm} ; the first and the outermost ring are both enriched in X_{alm} and depleted in X_{grs} . By contrast, X_{prp} gently increases from core (0.03) to the outermost rim (0.05). X_{sps} decreases from core (0.08) to the outermost rim (0.01) (Fig. 6.3c). Four garnet domains were selected each corresponding to a single growth zone. Grt_1 was defined in the core, Grt_2 in the first ring, Grt_3 in the second ring and Grt_4 in the outermost rim (Fig. 6.3c). It is remarkable to note the sharp compositional transition between Grt_3 and Grt_4 in Ca, Fe and Mg. This finding supports the assumption that post-growth intragranular diffusion was limited to a distance of less than 10-40 μm .

In sample 10.1 garnet porphyroblasts show three compositional domains delimited by roughly straight boundaries (Fig. 6.4a). The core is surrounded by a mantle 50-80 μm thick, and a rim up to 160 μm thick. The core shows low X_{alm} , X_{grs} and X_{prp} (0.62, 0.22 and 0.05 respectively) and high X_{sps} (0.09-0.12). The two rims are enriched in X_{alm} , X_{grs} and X_{prp} , and depleted in X_{sps} . The spessartine map shows small-scale diffusion between the core and the first rim, but not larger than 15 μm (Fig. 6.4a). The slight increase in Mn between the mantle and the rim from 0.02 to 0.05 suggests garnet resorption (see the brighter line existing between mantle and rim in the spessartine map in Fig. 6.4a). This feature is only observed on the bottom side of the grain around a lobate structure generally interpreted as evidence of garnet resorption (e.g. Giuntoli et al., 2018). Two garnet domains were selected in the core for this sample: Grt_1 near the centre and Grt_2 in the outer part (Fig. 6.4a). Two additional garnet domains were chosen, Grt_3 for the mantle and Grt_4 for the rim (Fig. 6.4a).

The selected garnet porphyroblast from sample RA-2 are clustered of mineral inclusion (Fig. 6.4b) making the zoning pattern more difficult to read and interpret. Nevertheless, two zones were identified: a core surrounded by a thin rim (<100 μm thick). The core shows a growth zoning where X_{grs} and X_{sps} decrease outward (from 0.03 to 0.02 and from 0.12 to 0.04 respectively), and X_{alm} and X_{prp} increase (from 0.59 to 0.69 and from 0.02 to 0.03) (Fig. 6.4b). The rim is enriched in X_{alm} , X_{grs} and X_{prp} (0.67, 0.27, 0.03) and depleted

in X_{sps} (0.04) (Fig. 6.4b). Two garnet compositions were defined for this grain: a core Grt_1 and a rim Grt_2 (Fig. 6.4b).

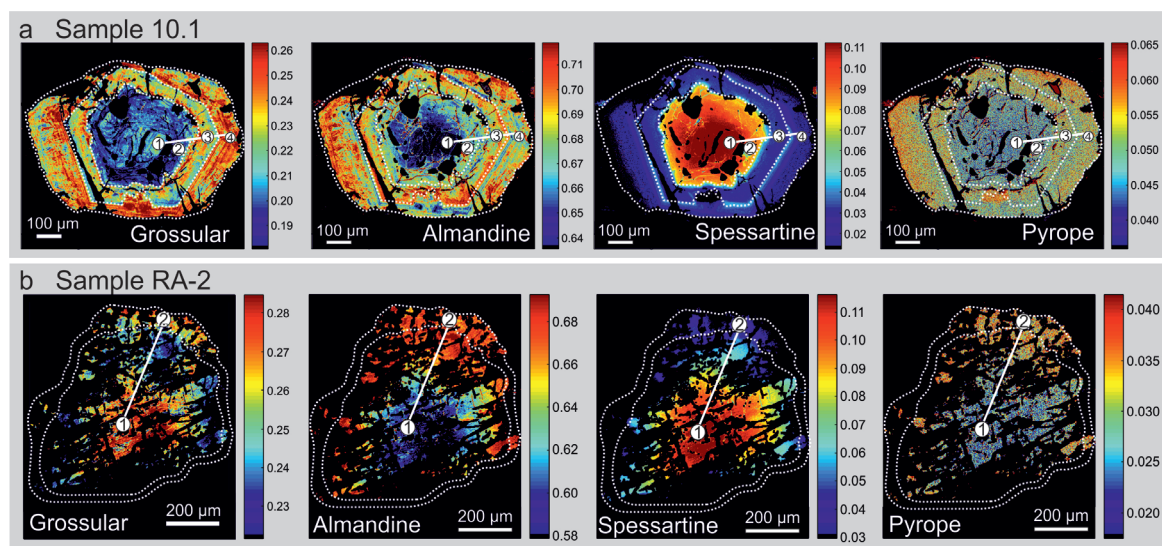


Figure 6.4. Compositional maps of end-member fractions for garnet porphyroblast analysed from the Dark schists Fm: a) samples 10.1, b) sample RA-2. Dashed lines delimit growth zones in the garnet. Circles show the location of the domains used for extracting the representative composition of each growth zone (see text). Continuous lines show where compositional profiles reported in Fig. 6.8 were obtained.

Garnets from samples 16.8, RA-0, 10.1 and RA-2 yielded similar compositional zoning between core and rim (Fig. 6.3 and Fig. 6.4). Only garnet from sample 16.16 shows a separate trend characterized a remarkable enrichment in Fe towards the rim (Fig. 6.3a).

As a summary, garnet porphyroblasts of every sample show typical growth zoning in core and mantle with limited post-growth modification by diffusion. Accordingly the selected domains from these growth zones were used in the following to model the P-T conditions using equilibrium thermodynamics (next section). It is important to note that the garnet rims in samples 16.16 and RA-0 show more complex compositional zonation with oscillatory zoning (Fig. 6.3a, b). These features suggest non-equilibrium processes; however an attempt to model these rims with equilibrium thermodynamics is made in the following. The goal of this test is to determine if equilibrium thermodynamics remain a reasonable assumption (or if it does not).

Grt	Sample 16.16				Sample 16.8				Sample RA-0				Sample 10.1				Sample RA-2		
	Grt ₁	Grt ₂	Grt ₃		Grt ₁	Grt ₂	Grt ₃	Grt ₄	Grt ₁	Grt ₂	Grt ₃	Grt ₄	Grt ₁	Grt ₂	Grt ₃	Grt ₄	Grt ₁	Grt ₂	
SiO ₂	38.727	38.419	38.575		37.328	37.595	37.702		37.853	37.668	38.209	38.032		37.422	36.588	37.616	37.741	38.072	37.880
Al ₂ O ₃	21.425	21.356	21.478		20.629	20.738	20.784		21.905	21.867	22.159	21.995		20.657	20.359	20.713	20.788	21.307	21.455
FeO	31.007	36.171	35.600		26.648	28.525	29.748		28.479	30.139	28.726	30.567		27.669	29.460	30.927	31.013	26.499	30.140
MnO	1.879	0.447	0.207		3.990	1.631	0.461		3.480	2.280	0.760	0.557		5.133	3.810	1.327	0.680	5.488	1.625
MgO	1.903	3.954	3.836		0.951	1.395	1.994		0.682	0.776	0.918	1.169		1.138	1.163	1.301	1.344	0.605	0.806
CaO	6.976	2.168	2.786		9.057	9.461	8.838		8.907	8.249	10.793	8.776		7.498	6.554	8.306	8.965	9.515	9.344
Na ₂ O	0.023	0.015	0.014		0.120	0.090	0.132		0.066	0.045	0.039	0.041		0.041	0.047	0.027	0.026	0.060	0.043
K ₂ O	0.003	0.002	0.003		0.015	0.008	0.007		0.023	0.023	0.024	0.023		0.010	0.020	0.009	0.009	0.013	0.008
Atom site distribution (12 anhydrous-oxygen basis)																			
Si(OT)	3.031	3.002	3.007		3.021	3.014	3.012		2.988	2.986	2.988	2.995		3.019	3.008	3.013	3.008	3.006	2.996
Al(Y)	1.976	1.967	1.974		1.967	1.960	1.957		2.038	2.043	2.043	2.042		1.964	1.973	1.955	1.953	1.982	2.000
Fe(X)	2.030	2.364	2.321		1.804	1.913	1.988		1.880	1.998	1.879	2.014		1.867	2.026	2.072	2.068	1.750	1.994
Mg(X)	0.222	0.461	0.446		0.115	0.167	0.238		0.080	0.092	0.107	0.137		0.137	0.143	0.155	0.160	0.071	0.095
Mn(X)	0.125	0.030	0.014		0.273	0.111	0.031		0.233	0.153	0.050	0.037		0.351	0.265	0.090	0.046	0.367	0.109
Ca(X)	0.585	0.181	0.233		0.785	0.813	0.757		0.753	0.701	0.904	0.741		0.648	0.577	0.713	0.766	0.805	0.792
XAlm	0.685	0.779	0.770		0.606	0.637	0.660		0.638	0.679	0.639	0.688		0.622	0.673	0.684	0.680	0.585	0.667
XPrp	0.075	0.152	0.148		0.039	0.056	0.079		0.027	0.031	0.036	0.047		0.046	0.047	0.051	0.053	0.024	0.032
XSpS	0.042	0.010	0.005		0.092	0.037	0.010		0.079	0.052	0.017	0.013		0.117	0.088	0.030	0.015	0.123	0.036
XGrs	0.198	0.060	0.077		0.264	0.271	0.251		0.256	0.238	0.308	0.253		0.216	0.192	0.235	0.252	0.269	0.265

Table 6.3. Representative mineral compositions of garnet.

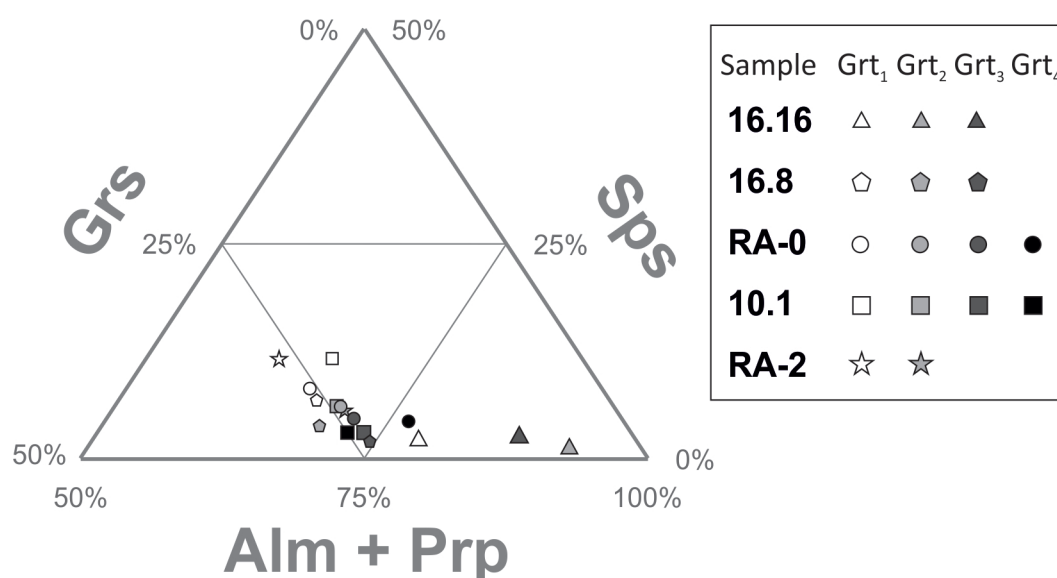


Figure 6.5. Ternary compositional diagram of garnet: Grs (grossular fraction content), Sps (spessartine fraction content), Alm + Prp (almandine + pyrope fraction content).

6.3.2. Phase equilibria

Following the methodology described in section 3.3.4, the optimal P-T conditions for garnet were determined using iterative forward models and the program GRTMOD (Lanari et al., 2017). A similar approach was followed for phengite (see section 3.3.4). The results for all the studied samples are reported in Fig. 6.6. As the uncertainty envelopes are rarely symmetrical in both P and T for garnet, only the optimal solution is discussed in the following. Uncertainties are shown in Fig. 6.6 using the method proposed by Lanari et al. (2017) with a tolerance factor on C_0 of 1.5.

In sample 16.16 (Fig. 6.6a), garnet nucleation is predicted at 518 °C and 18.2 kbar using the composition of Grt₁. By contrast, Grt₂ is predicted to have formed at higher temperature and lower pressure conditions of 591 °C and 6.0 kbar. 4.39 vol% of Grt₁ was fractionated to model Grt₂. No satisfactory solution was found for Grt₃ showing a complex oscillatory zoning (a minimum residual value of 0.082 was reached at 585 °C and 6.3 kbar). The P-T estimates for K-white mica form a cluster around ~580 °C and ~18 kbar, with two analyses showing lower pressures around 14 kbar.

In sample 16.8 (Fig. 6.6b), garnet nucleation is predicted at 489 °C and 17.1 kbar using the composition of Grt₁. This stage is followed by two episodes of garnet growth occurring at higher temperature and lower pressure conditions. Garnet mantle (Grt₂)

is predicted to have formed at 546 °C and 8.3 kbar (fractionation of 3.11 vol% of Grt₁). Garnet rim (Grt₃) is predicted at 566 °C and 7.4 kbar (fractionation of 3.11 vol% and 3.66 vol% of Grt₁ and Grt₂ respectively). K-white mica P-T estimates form a cluster around 530-550 °C and 12-15 kbar with two outliers at 530 °C and 15-20 kbar.

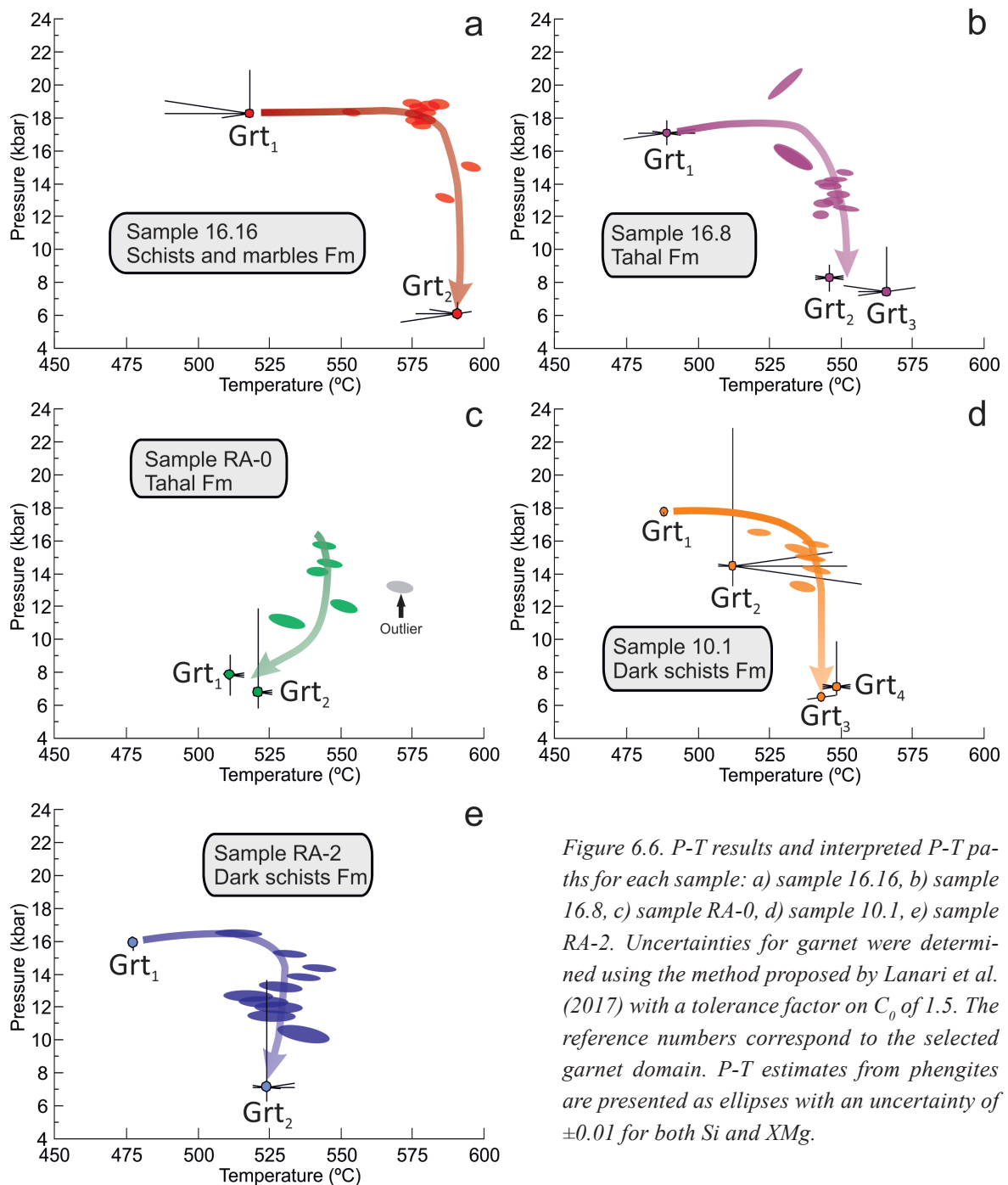


Figure 6.6. P-T results and interpreted P-T paths for each sample: a) sample 16.16, b) sample 16.8, c) sample RA-0, d) sample 10.1, e) sample RA-2. Uncertainties for garnet were determined using the method proposed by Lanari et al. (2017) with a tolerance factor on C_0 of 1.5. The reference numbers correspond to the selected garnet domain. P-T estimates from phengites are presented as ellipses with an uncertainty of ± 0.01 for both Si and XMg.

In sample RA-0 (Fig. 6.6c), garnet is predicted to have nucleated at 511 °C and 7.8 kbar using the composition of Grt₁. The crystallization of Grt₂ is predicted at 521 °C and 6.7 kbar (fractionation of 0.57 vol% of Grt₁). No satisfactory solutions were found for Grt₃ and Grt₄ ($C_0 = 0.088$ at 527 °C, 7.1 kbar for Grt₃ and $C_0 = 0.078$ at 529 °C, 11.3 kbar for Grt₄). The P-T estimates for K-white mica suggest higher P-T conditions of ~11-16 kbar at ~530-575 °C.

In sample 10.1 (Fig. 6.6d), four domains of garnet were investigated (Fig. 6.4a). Garnet nucleation is predicted at 488 °C and 17.8 kbar using the composition of Grt₁. The outer part of the core (Grt₂) is predicted to have formed at 512 °C and 14.5 kbar (fractionation of 0.012 vol% of Grt₁) with large asymmetrical uncertainties in both temperature and pressure. The mantle (Grt₃) is predicted at 543 °C and 6.5 kbar (fractionation of 0.01 vol% of Grt₁ and 6.402 vol% of Grt₂). The rim Grt₄ is modelled at 548 °C and 7.2 kbar (fractionation of 0.01 vol% of Grt₁, 5.503 vol% of Grt₂, and 0.069 vol% of Grt₃). The P-T estimates for K-white mica are around 540 °C and 13-16 kbar with two outliers around 520 °C and 11 kbar.

In sample RA-2 (Fig. 6.6e), only two garnet domains have been modelled (Fig. 6.4b). Garnet nucleation is predicted at 477 °C and 15.9 kbar using the composition of Grt₁. The garnet rim is predicted at lower pressure and higher temperature conditions of 524 °C and 7.1 kbar (fractionation of 0.03 vol% of Grt₁). The P-T conditions of phengite are between 515 and 540 °C and ~10-16 kbar.

As a summary, in most of the samples, except for RA-0, garnet nucleation is modelled at high-pressure conditions, above ~16 kbar and temperatures ranging between 480 and 525 °C (Fig. 6.6). The phengite compositions are modelled in general at higher temperatures and lower pressures than those of the garnet nucleation. The phengite composition display a range of pressure comprised between 4 and 7 kbar. All the following growth stages of garnet, involving mantle and rims, yield lower pressure and slightly higher temperature conditions. However, garnet in sample RA-0 apparently recorded nucleation at lower pressure conditions below 8 kbar at 511 °C (Grt₁ in Fig. 6.6c). Additionally, it was not possible to model with reasonable residuals the outer rim(s) respectively of samples 16.16 (Grt₃) and RA-0 (Grt₃ and Grt₄).

6.3.3. Allanite dating

The dating results of allanite for samples 16.16 and 16.8 are summarized in Fig. 6.7. The data were plotted in (1) uncorrected Terra-Wasserburg diagrams to estimate the $^{207}\text{Pb}/^{206}\text{Pb}$

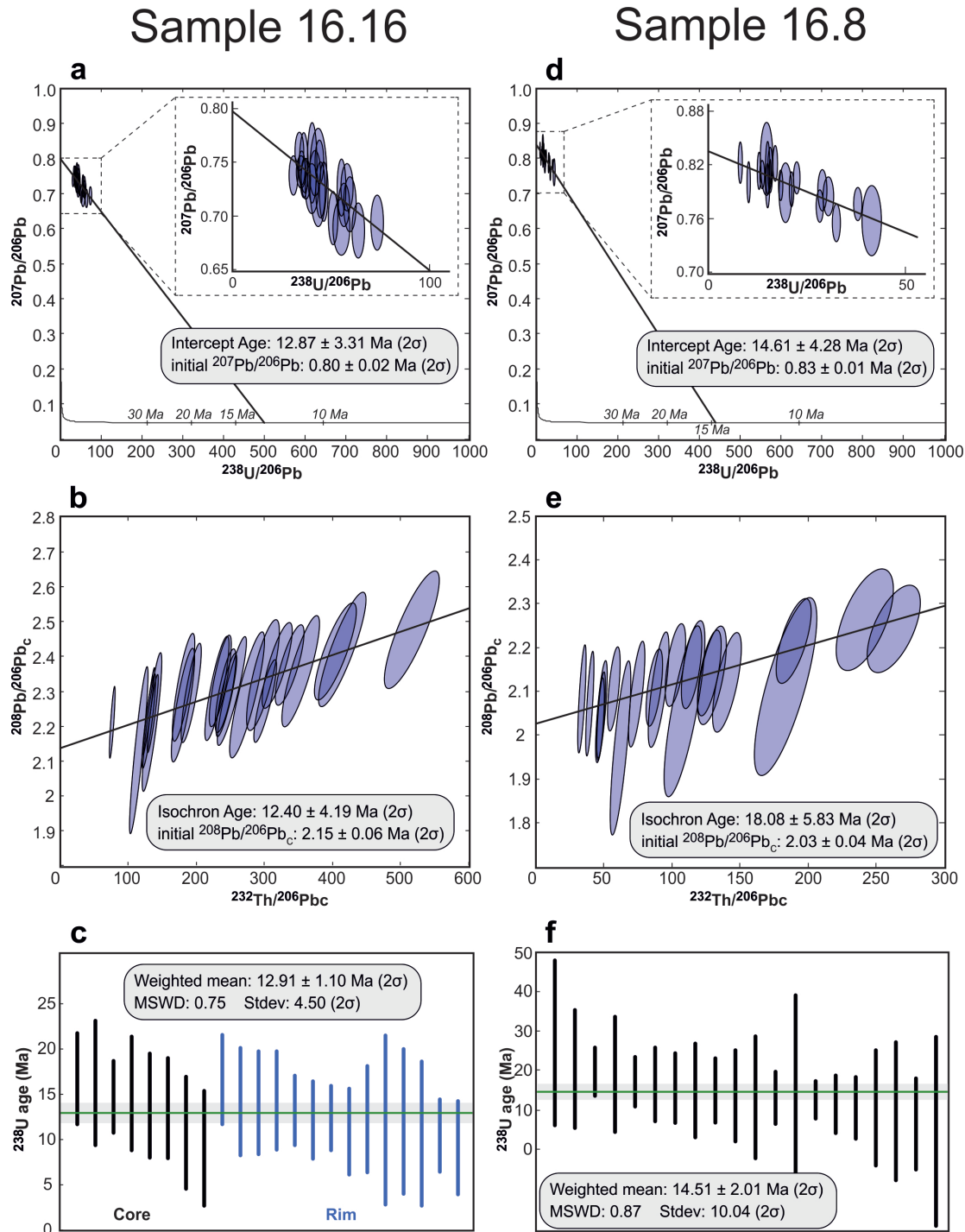


Figure 6.7. LA-ICP-MS Th-U-Pb allanite dating results. The figure shows the Terra-Wasserburg and Th-isochron diagrams as well as the weighted mean U-Pb age for samples 16.16 (a, b, c) and 16.8 (d, e, f).

common lead composition; (2) Th-isochron diagrams, in which the uncertainty on the common lead fraction (f_{206}) was propagated through the age calculation procedure using a Monte-Carlo technique (Burn et al., 2017); and as (3) common lead corrected U ages using the common lead compositions from (1) and (2).

In sample 16.16, the U- and Th- isochrons defined by 21 allanite analyses yield the intercept ages of 12.87 ± 3.31 Ma (2σ , Fig. 6.7a) and 12.40 ± 4.19 Ma (2σ , Fig. 6.7b). The corresponding weighted mean U-Pb age is of 12.91 ± 1.10 Ma (2σ). Allanite core and rim analyses returns the same age within uncertainty (MSWD = 0.75, see Fig. 6.7c).

In sample 16.8, the U- and Th- isochrons defined by 20 allanite analyses yield the intercept ages of 14.61 ± 4.28 Ma (2σ , Fig. 6.7d), and 18.08 ± 5.83 Ma (2σ , Fig. 6.7e). The corresponding weighted mean U-Pb age is of 14.51 ± 2.01 Ma (2σ , Fig. 6.7f).

6.4. Discussion

6.4.1. Phase equilibria modelling and quality of predictions

In this Ph.D. Thesis, garnet and phengite were modeled using iterative thermodynamic models based on Gibbs free energy minimizations. The garnet interiors are the only relicts of the first stage at HP conditions. Accordingly, the predicted mineral assemblages for this stage were not considered to refine the P-T conditions. In fact, this technique is for Grt_1 similar in essence to isopleth thermometry without considering the coexisting assemblage. The main advantages of methodology based in GRTMOD are: (1) to enable garnet fractionation and (2) resorption in order to compute a suitable reactive bulk composition at each stage and (3) the weighting procedure included in the inversion (Lanari et al., 2017), allowing “optimal” P-T conditions to be derived in a quantitative way (see Fig. 11 in Lanari and Duesteroheft, 2019 for a comparison between the weighted and unweighted procedure).

The robustness of the model predictions, such as the garnet compositions and the volume fractions, was tested along a profile (the positions of these profiles are shown as white lines in Figs. 6.3 and 6.4). The results are given in Fig. 6.8. The chemical composition of garnet was extracted using XMAPTOOLS (points in Fig. 6.8). The distances between each pixel was transformed into a volume fraction of garnet assuming a total of 4.89 vol% in sample 16.16; 11.07 vol% in sample 16.8; 1.74 vol% in sample RA-0; 11.89 vol% in

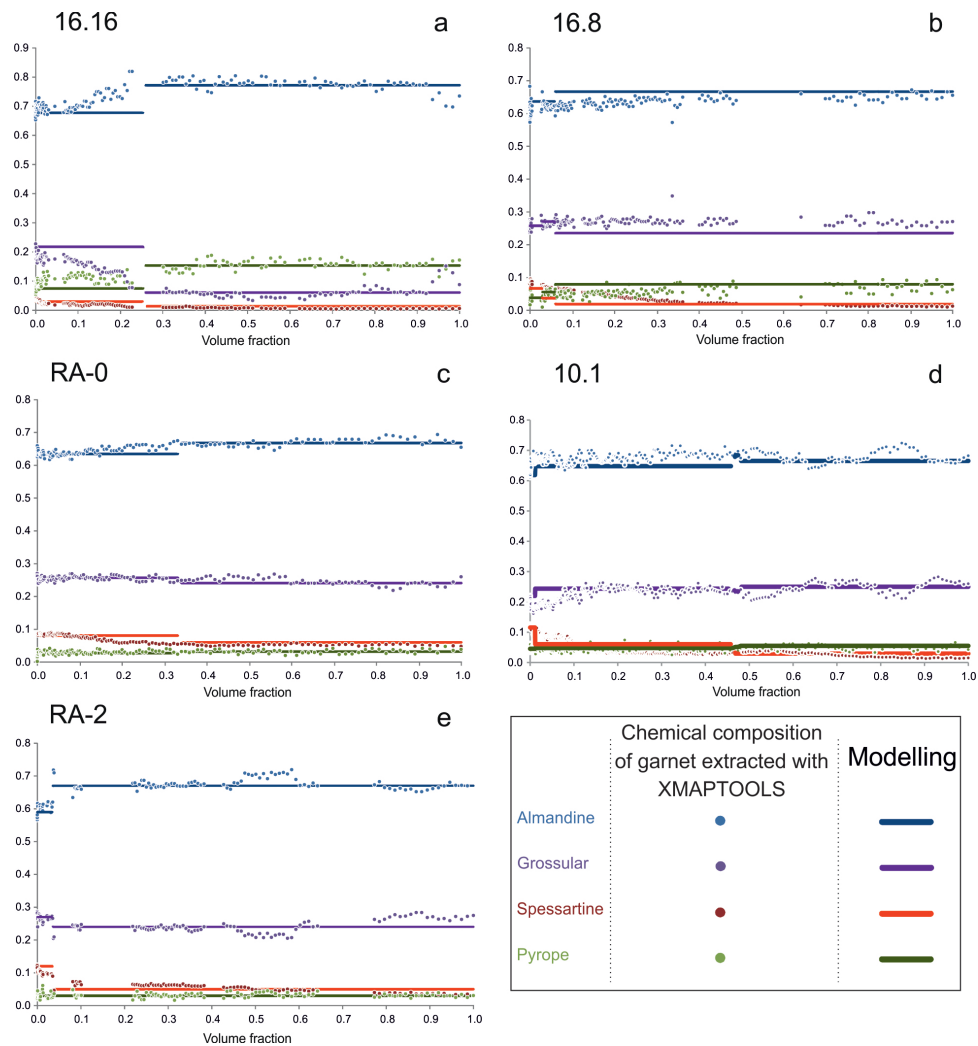


Figure 6.8. Modelled garnet composition in the selected domains compared with the extracted chemical composition through a profile. The chemical composition of garnet was extracted using XMAPTOOLS. The continuous lines in the compositional maps from Figs. 6.3 and 6.4 show where the compositional profiles were obtained. The distances between each pixel was transformed into a volume fraction.

sample 10.1; and 0.71 vol% in sample RA-2, of garnet being produced. These modeled values are in line with the observations in each sample (Fig. 6.8). This procedure allows the zoning profiles and predictions to be compared assuming a single-size population of garnet (e.g. Lanari et al., 2017). The modeled garnet zoning profiles are in line with the observation for most samples (Fig. 6.8) and, accordingly suggesting an overall good quality of the models. Minor discrepancies are caused by chemical variations within a single growth zone due to Rayleigh fractionation (e.g. core in sample 16.16, Fig. 6.8a) or by small oscillations in chemical composition within a single growth zone (e.g. rim in sample 10.1, Fig. 6.8d). These were probably controlled by kinetics rather than chemical

equilibrium and cannot be modeled using Gibbs free energy minimizations relying on the assumption of chemical equilibrium.

As presented in section 6.3.2, the outer rims of garnet in samples 16.16 and RA-0 yielded high residual values. The observed garnet compositions cannot be modelled with our model based on equilibrium thermodynamics; these are interpreted to reflect disequilibrium processes such as transport-controlled growth and they are excluded from the comparison shown above.

6.4.2. Comparison between samples

The combination of thermobarometric results obtained for garnet and K-white mica allows the P-T paths of each sample to be reconstructed (see Figs. 6.6 and 6.9). The absolute uncertainty on any P-T estimate is commonly assumed to be close to ± 50 °C and ± 2 kbar. However, as the same modelling technique and thermodynamic properties are used, the relative uncertainty is assumed to be much smaller (between 5-15 °C, see the uncertainty envelopes in Fig. 6.6). This permits to perform relative thermobarometry (e.g. Worley and Powell, 2000).

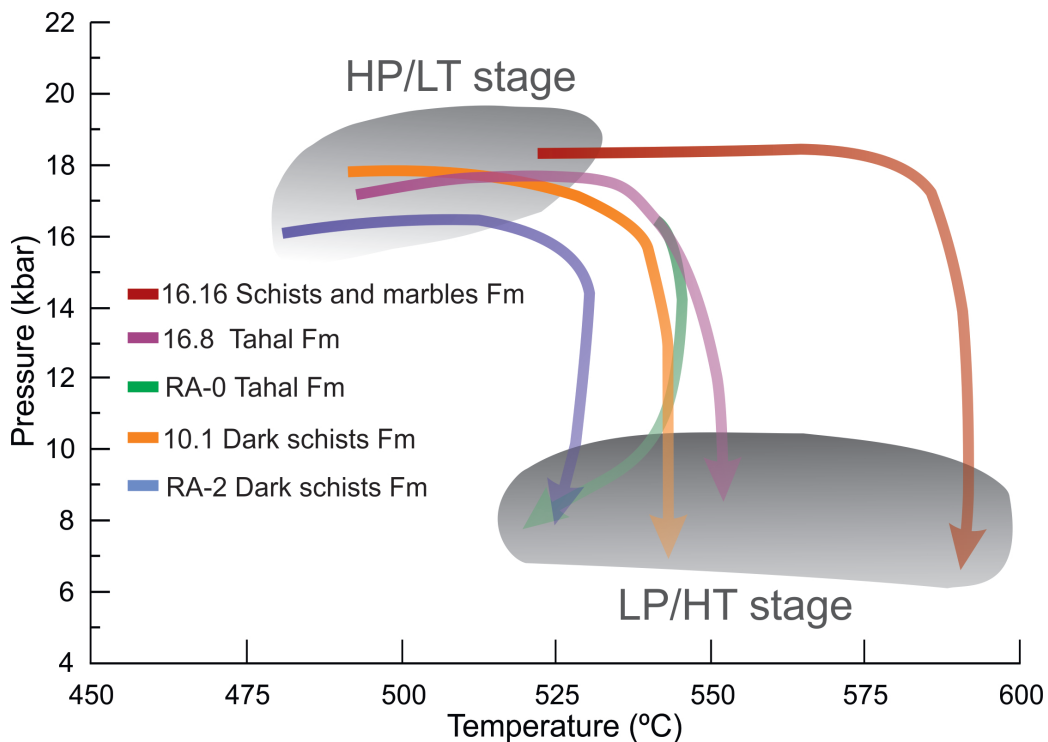


Figure 6.9. Comparison between the P-T paths of the studied samples.

The P-T paths exhibit similar shapes of clockwise (Fig. 6.9). The prograde part is isobaric. The HP/LT stage is followed by a nearly isothermal decompression to reach the LP/HT stage (Fig. 6.9). A difference of $\sim 40^{\circ}\text{C}$ and 2 kbar is observed between samples RA-2 (Dark schists Fm) and 16.16 (Schists and marbles Fm) for the HP/LT stage. The temperature difference between these samples slightly increases during heating to reach $\sim 70^{\circ}\text{C}$ for the LP/HT stage. The difference between sample 16.16 (Schists and marbles Fm) and 16.8 (Tahal Fm) for the HP/LT stage is $\sim 30^{\circ}\text{C}$ and 1.1 kbar. Again, the difference of temperature in those samples increases during heating up to $\sim 40^{\circ}\text{C}$ in the LP/HT stage. The burial trajectory however cannot be reconstructed as no relic was found in any sample. Garnet nucleation occurred at high-pressure conditions and phengite was re-equilibrated after garnet started to grow.

It is remarkable to note that the differences in P-T conditions between samples (Fig. 6.9) are correlated with the structural position. For example, in the Peñones de San Francisco area, sample 16.16, recording the higher conditions, was taken in the upper part of the Schists and marbles Fm, whereas 16.8 and 10.1, recording lower conditions were taken in the Tahal and Dark schists Fms respectively, i.e. in progressively lower positions of the Nevado-Filábride pile (see Fig. 4.25).

Samples 16.8 and 10.1, from the Tahal and Dark schists Fms respectively, exhibit identical P-T paths within uncertainty (Fig. 6.9). This result questions the divisions proposed in the literature, and particularly the differences in the division existing in Puga et al. (2002) and Martínez-Martínez et al. (2002) (Fig. 2.4). Sample 10.1 can be assigned to the highest levels of the Veleta unit according to the division of Puga et al. (2002). However, according to the division of Martínez-Martínez et al. (2002) this sample can be associated to the Calar-Alto unit, approximately equivalent to the lower part of the Mulhacén unit of the Puga et al. (2002)'s division.

As a summary, the results presented in this Ph.D. Thesis suggest that the samples 16.16, 16.8, 10.1 and RA-2 followed P-T trajectories with identical shapes. Only sample RA-0 does not record the HP/LT stage as Grt₁ is predicted to grow at LP/HT conditions. The results also suggest that Schists and marbles Fm reached slightly higher-pressure conditions than the Tahal and the Dark schists Fms (differences of ~ 1.1 and ~ 2.3 kbar res-

pectively). The difference in temperature between within the complex is maintained and slightly increased during decompression. The Nevado-Filábride pile thus display an inverted metamorphism, as already suggested in previous studies (e.g. Augier et al., 2005a, 2005b; Behr and Platt, 2012; Booth-Rea et al., 2015). However, the mentioned similarity in the shape of the P-T paths indicate that, despite the differences in pressure and temperature, the studied formations underwent a similar heating and exhumation history but at different structural levels.

6.4.3. Petrochronology

Allanite dating can be used to estimate the age of a single metamorphic stage, provided that growth episodes can be correlated to major phases (Rubatto et al., 2011; Cenko-Tok

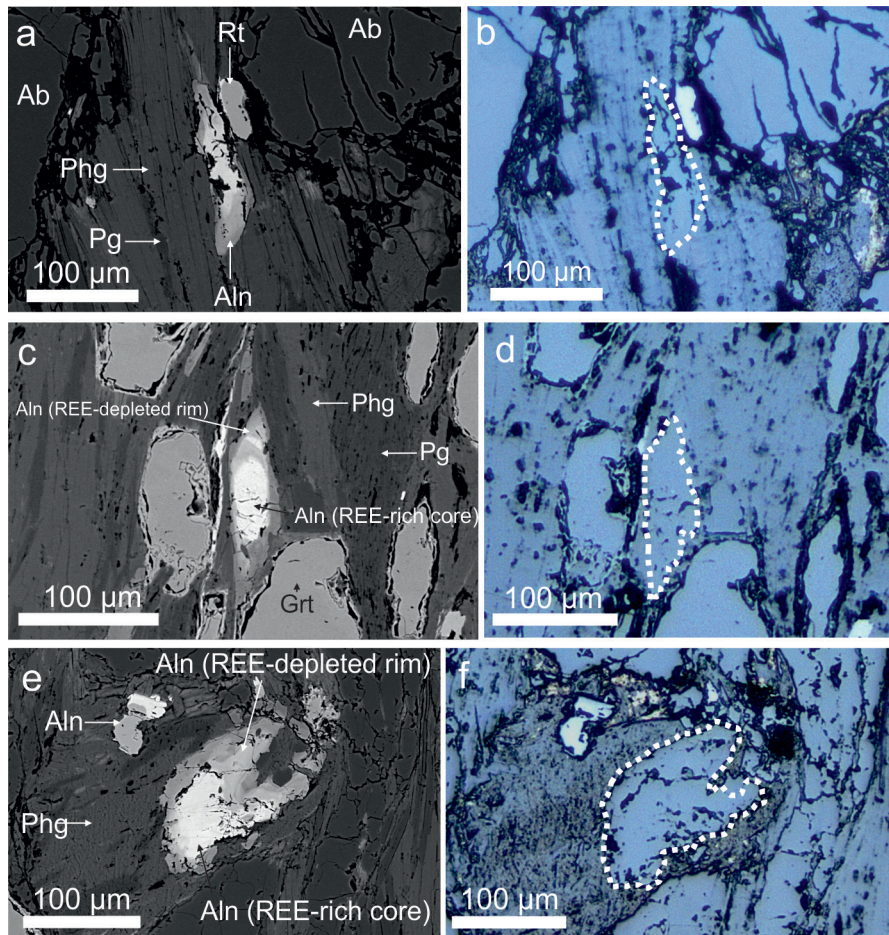


Figure 6.10. Backscattered electron (a, c, e) and optical microscopy (b, d, f,) images of allanite grains from samples 16.16 and 16.8 matrix. Abbreviations: Ab (albite), Aln (allanite), Grt (garnet), Pg (paragonite), Phg (phengite), Qtz (quartz), Rt (rutile).

et al., 2014; Loury et al., 2016; Engi, 2017). Allanite from samples 16.16 and 16.8 crystallized during Miocene at 12.91 ± 1.10 Ma and 14.51 ± 2.01 Ma respectively (Fig. 6.7c, f). In these two samples, allanite is present in the matrix (Fig. 6.10) and as inclusion in the outer rim of garnet (Fig. 6.11).

No age difference was found between these two locations as well as between the REE-rich core and the REE-depleted rim of single grains (Fig. 6.7c and Fig. 6.10c, e). In both samples, those allanites included in garnet were found in the garnet rim (Fig. 6.11a) as well as along late fractures cross-cutting the previous growth zones. For example, in sample 16.16, allanite was found only in the outer rim (Grt₃) showing oscillatory zoning (see Fig. 6.3a). These observations show that allanite formed before or syn Grt₃ and allanite dating provides a maximum age for the formation of the garnet rim in these samples. These rims correspond to the garnet domains that were not modelled properly because of too high residuals, i.e. Grt₃ in sample 16.16 (see section 6.3.2). The textural relationships and

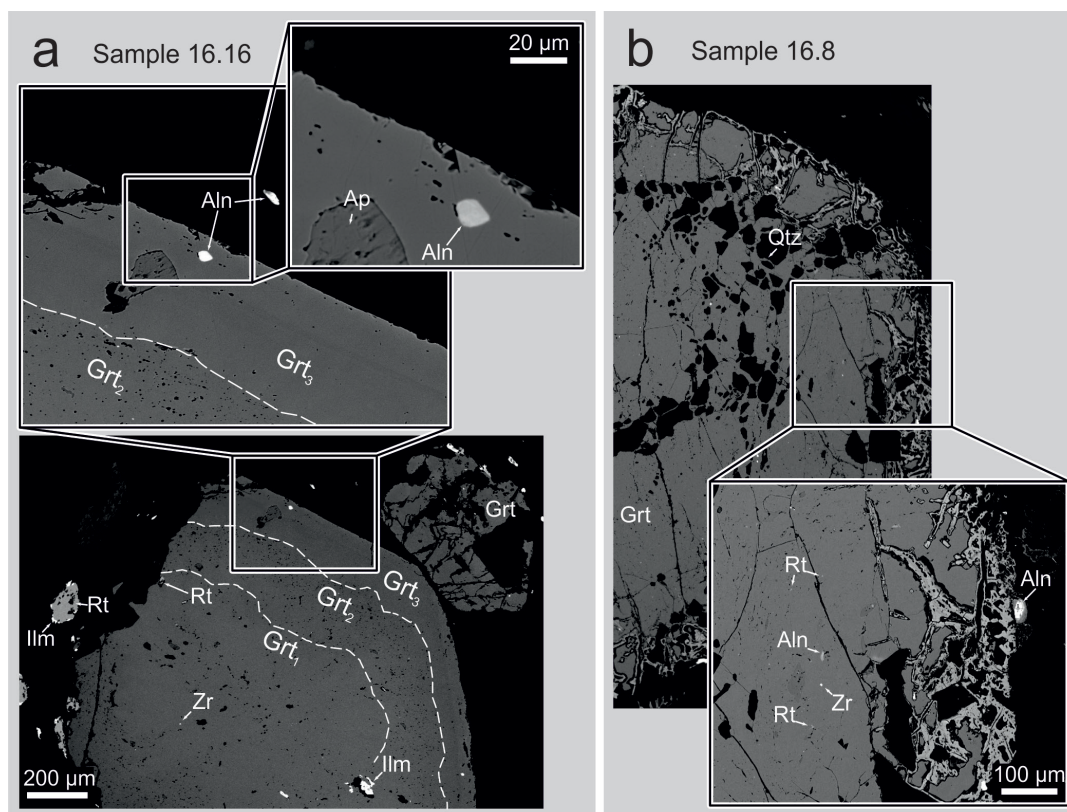


Figure 6.11 Backscattered electron images of allanite inclusions in garnets from samples 16.16 (a) and 16.8 (b). Abbreviations: Aln (allanite), Ap (apatite), Grt (garnet), Ilm (ilmenite), Qtz (quartz), Rt (rutile), Zr (zircon).

the potential presence of reactive fluids to form the last garnet rims in these samples suggest that the allanite formed during the LP/HT stage at ca. 13 Ma. Accordingly, the HP/LT stage should take place earlier as proposed by other authors (e.g. Monié et al., 1991; López-Sánchez-Vizcaíno et al., 2001; Gómez-Pugnaire et al., 2004; Augier et al., 2005a; Platt et al., 2006; Kirchner et al., 2016; Li and Massonne, 2018).

Li and Massonne (2018) recognized two monazite age populations formed at 40.2 ± 1.7 and 24.1 ± 0.8 Ma. According to these authors, a first HP event took place before the first monazite population formed, whereas the exhumation and a second P-T loop coincide with the age of the younger population. These events are all older than the LP/HT stage recorded by allanite. On the other hand, other studies reported a Miocene HP metamorphism (ranging between 18 to 13 Ma) (e.g. López-Sánchez-Vizcaíno et al., 2001; Platt et al., 2006; Gómez-Pugnaire et al., 2012; Kirchner et al., 2016). These estimations are previous or nearly coincident with the allanite data for the LP/HT stage. Finally, the results of de Jong (2003), ~ 14 and ~ 17 Ma for the early stages of exhumation are previous or nearly coincident with the allanite data.

6.4.4. Comparison with literature data

The P-T trajectories obtained in this Ph.D. Thesis are compared in the following sections with the P-T paths proposed in the previous studies (Fig. 6.12).

6.4.4.1. Dark schists Fm

The shape of the P-T path obtained by Augier et al. (2005b) (path 1 in Fig. 6.12a) for this formation is quite similar to the P-T path of sample RA-2, whereas the pressure conditions obtained by garnet are slightly higher of ~ 3 kbar. Li and Massonne (2018) reported a clockwise P-T loop (with similar P-T conditions to our results) followed by a second burial stage (path 2 in Fig. 6.12a). The second loop is assumed to have been caused by the overlying of the hotter Alpujarride complex above the Nevado-Filábride complex. This does not agree the P-T path presented in this Ph.D. Thesis. By the contrary, in all the samples investigated, neither garnet, nor phengite recorded such complex P-T path with two burial stages (see Rubatto et al., 2011 and Regis et al., 2014 for examples of phengite zoning recording pressure cycling).

6.4.4.2. Tahal Fm

Augier et al. (2005b) proposed a P-T path showing similar exhumation shapes and peak temperature conditions for the Tahal Fm (path 1 in Fig. 6.12b). The results presented in this Ph.D. Thesis are also similar to the first part of the P-T path of Li and Massonne (2018) (path 2 in Fig. 6.12b). P-T conditions predicted from mantle and rim in sample 16.8 (Grt₂ and Grt₃ in Fig. 6.6b), and from core and rim in RA-0 (Grt₁ and Grt₂ Fig. 6.6c) are almost the same within uncertainty. Therefore, the possible increase in temperature and the reheating event of 60 °C proposed by Li and Massonne (2018) (their second loop) was apparently not recorded by garnet and phengite in our samples, or it cannot be clearly distinguished.

6.4.4.3. Schists and marbles Fm

Gómez-Pugnaire and Fernández-Soler (1987), Bakker et al. (1989) and Vissers et al. (1995) (paths 1, 2 and 3 respectively in Fig. 6.12c) yielded values for the HP/LT between 5 and 7 kbar, significantly lower than the estimates from garnet modelling in sample 16.16. The continuous heating during exhumation proposed in these studies is also not observed. The P-T estimates of Augier et al. (2005a) (path 4 in Fig. 6.12c) are in line with the estimates presented here. A hairpin P-T path was proposed by Behr and Platt (2012) (path 5 in Fig. 6.12c). This P-T path shows a pressure and temperature maxima remarkably lower than the results presented here (differences of ~4 kbar and ~35 °C). By contrast, Ruiz-Cruz et al. (2015) yielded a P-T path (path 6 in Fig. 6.12c) showing an increase of both pressure and temperature during burial with a pressure peak ~3 kbar higher than the estimates from garnet, but identical temperature during decompression. Considerably higher values for both pressure and temperature peaks were obtained by López-Sánchez-Vizcaíno et al. (2001) in ultramafic rocks (difference of ~3 kbar and ~150 °C) (path 7 in Fig. 6.12c). Puga et al. (2002) (path 8 in Fig. 6.12c) proposed a P-T path shape different to the one obtained in this Ph.D. Thesis (difference of ~5 kbar and ~75 °C respectively).

6.4.4.4. Summary

The P-T paths obtained here show similarities to the studies of Augier et al. (2005a, 2005b); Ruiz-Cruz et al. (2015); and the first part of the decompression trajectory of Li and Massonne (2018). The differences existing in pressure conditions between the model used in this Ph.D. Thesis and those of these authors are due to different thermobarometric

methods used, as well as different positions studied in Nevado-Filábride pile. In several previous studies (e.g. Puga et al., 2002) it has been proposed that the Dark schists Fm does not recorded HP metamorphism. However, the results presented here for this formation confirm the HP metamorphism proposed by Augier et al. (2005b) and Li and Massonne (2018) (P-T paths in samples 10.1 and RA-2 in Figs. 6.6 and 6.9). A stage of isothermal decompression is obtained for all the studied samples for the three formations. This is in line with the results from several previous studies (Augier et al., 2005a, 2005b; Ruiz-Cruz et al., 2015; and the first part of the decompression trajectory of Li and Massonne, 2018). Our samples and our petrochronological data do not show any evidence of two successive loops (Li and Massonne, 2018) or strong reheating during exhumation (Bakker et al., 1989, Vissers et al., 1995; Aerden et al., 2013).

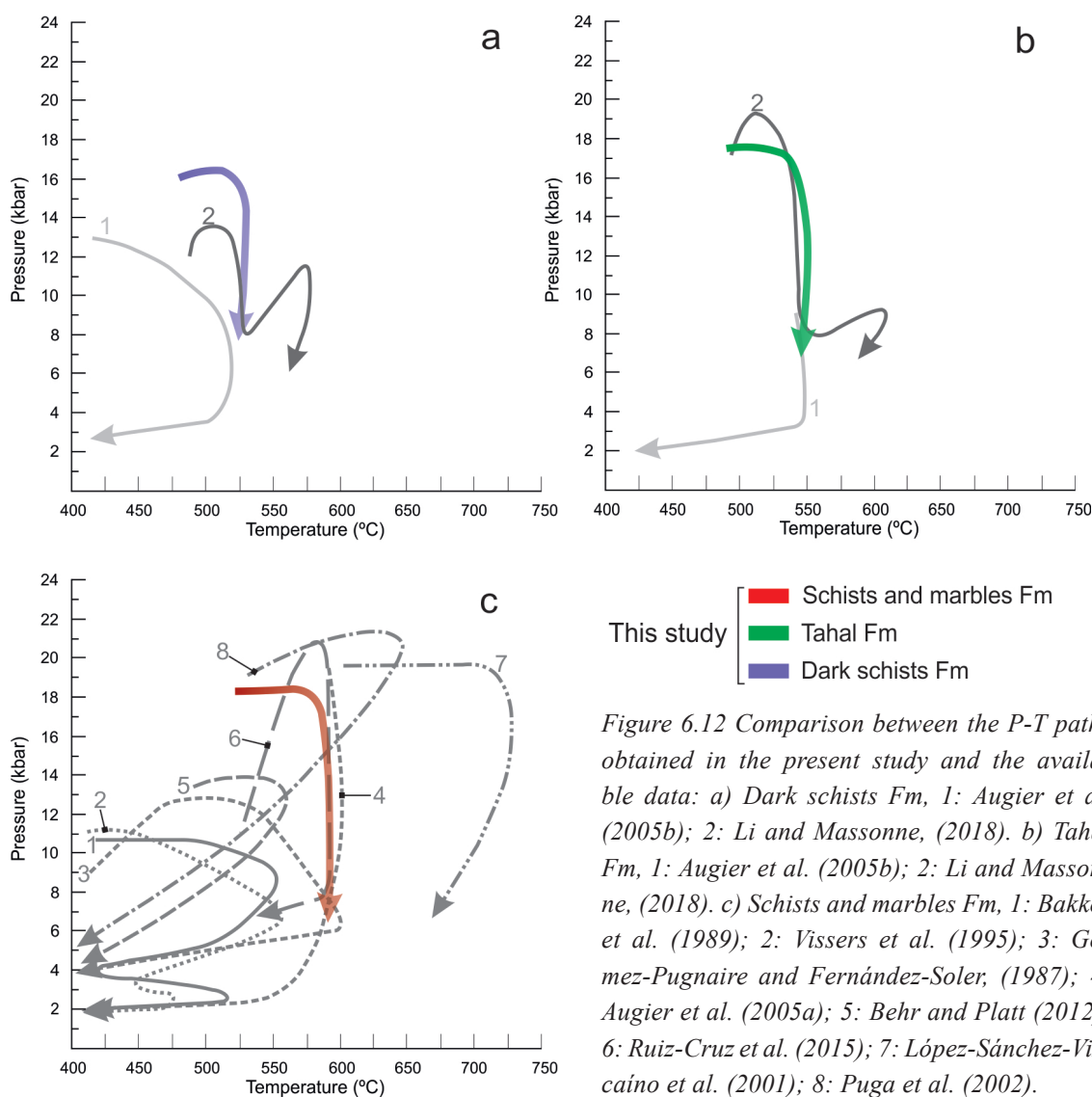


Figure 6.12 Comparison between the P-T paths obtained in the present study and the available data: a) Dark schists Fm, 1: Augier et al. (2005b); 2: Li and Massonne, (2018). b) Tahal Fm, 1: Augier et al. (2005b); 2: Li and Massonne, (2018). c) Schists and marbles Fm, 1: Bakker et al. (1989); 2: Vissers et al. (1995); 3: Gómez-Pugnaire and Fernández-Soler, (1987); 4: Augier et al. (2005a); 5: Behr and Platt (2012); 6: Ruiz-Cruz et al. (2015); 7: López-Sánchez-Vizcaino et al. (2001); 8: Puga et al. (2002).

Chapter 7

General discussion

7.1. Introduction

Results presented in the previous chapters draw a framework for revision of the existing data and processes proposed for the formation and tectonic evolution of the Nevado-Filábride complex, as well as its role in the western Mediterranean tectonic configuration. The discussion in sections 7.2 and 7.3 is presented in chronologic order (i.e. from the initial deposition of the sedimentary protolith, to the subduction of the Nevado-Filábride terranes and subsequent exhumation of the complex). In section 7.2, the SHRIMP U-Pb detrital zircon age patterns are examined to identify the sources of the schists' protolith, and provide paleogeographic constraints for the Nevado-Filábride complex. A comparison is made between the age populations identified in the Ph.D. Thesis and the dataset existing in the literature for other Iberian areas. In section 7.3 the subduction and exhumation history of the complex was refined based on the comparison of the shape of the P-T paths of the different formations. Finally, in section 7.4 the results obtained in Ph.D. Thesis are integrated and discussed in light of the debate concerning the division of the complex.

7.2. The paleogeographic provenance of the Nevado-Filábride terranes

The SHRIMP U-Pb age populations obtained from the studied samples are: ca. 328-355 Ma (Carboniferous), ca. 480-615 Ma (Cambrian-Ediacaran), ca. 910-1010 Ma (Tonian-Stenian) and ca. 1800-2000 Ma (Orosirian) (see section 5.5.2). To be taken into account, moreover, is the Permian age population obtained in sample SF-2, ca. 270 Ma.

The Permian age population identified in the Nevado-Filábride complex was attributed by Jabaloy et al. (2018) to the Late-Variscan magmatic event (~275-300 Ma, see Vai et al., 1984; Cassinis et al., 2000; Fernández-Suárez et al., 2011; Gutiérrez-Alonso et al., 2011). In this study, only sample SF-2 yielded a Permian age population, at 269.6 ± 0.9 Ma. This finding is consistent because this sample pertains to the upper part of the Schists and marbles Fm (Fig. 4.25), whose sedimentary protolith was deposited after those of the Tahal and Dark schists Fms. This age population is present in the Permian units studied by Pastor-Galán et al. (2013) in the Cantabrian zone and in the Middle-Late Permian and Middle Triassic of the Iberian range (Sánchez Martínez et al., 2012).

The age population ca. 328-355 Ma can be attributed to a tectonic denudation of igneous rocks formed during early stages of the Variscan orogeny (e.g. Fernandez-Suarez et al., 2000; Valle-Aguado et al., 2005; Dinis et al., 2012; Pastor-Galán et al., 2013). Similar age populations are present in the carboniferous units of the Cantabrian zone (Pastor-Galán et al., 2013), in southeastern France and northeastern Spain (Martínez et al., 2016) and in the Middle-Late Permian and Middle Triassic rocks of the Iberian range (Sánchez Martínez et al., 2012).

The zircons yielding ages ranging 480-615 Ma can be attributed to different sources. The upper Ordovician zircons (~480) probably formed during magmatic events that occurred along the northern margin of Gondwana, associated with the opening of the Rheic Ocean (Pastor-Galán et al., 2013; Jabaloy et al. 2018); while the zircons showing Ediacaran to Cryogenian ages point to the Cadomian and Pan-African orogeny, ascribed to the north of Gondwana (Nance and Murphy, 1994; Linnemann et al., 2008; Pastor-Galán et al., 2013; Pérez-Cáceres et al., 2017; Jabaloy et al., 2018). Although all of the samples provided ~480 Ma analyses, mixture modelling only yielded a clear probability peak at 478.9 ± 1.4 in sample VE-2 (Fig. 5.5e). Conversely, the strong detrital input from Cadomian/Pan-African igneous sources is easily identified in all the studied samples.

The Tonian-Stenian analyses included in the ca. 910-1010 Ma age population can be ascribed to the Sahara Metacraton and the Arabian-Nubian Shield (Bea et al., 2010; Jabaloy et al., 2018).

The age population ca. 1800-2000 Ma could be integrated by zircons derived from the amalgamation of the supercontinent Nuna (Bradley, 2011; Pastor-Galán et al., 2013), or the Eburnean orogeny in North Gondwana (Pérez-Cáceres et al., 2017).

The ca. 480-615 Ma and the ca. 1800-2000 Ma age populations are common in several Iberian areas including the Cantabrian (Pastor-Galán et al., 2013), West Astur-Leonese (Cambeses, 2015), Central Iberian (Talavera et al., 2012; Cambeses et al., 2017), Ossa-Morena (Cambeses et al., 2017), and South Portuguese zones (Pereira et al., 2012; Pérez-Cáceres et al., 2017), southeastern France and northeastern Spain (Martínez et al., 2016), and the Middle-Late Permian and Middle Triassic rocks of the Iberian range (Sánchez Martínez et al., 2012).

The ca. 910-1010 Ma age population is probably the most interesting for discerning relationships of the Nevado-Filábride terranes with other areas of the Iberian Peninsula. This age population is likewise preserved in the Cantabrian (Pastor-Galán et al., 2013) and Central Iberian zones (Bea et al., 2010; Cambeses et al., 2017), and in the Iberian range (Sánchez Martínez et al., 2012). To the contrary, the Tonian-Stenian imprint is testimonial in the Ossa-Morena zone (Cambeses et al., 2017) and in southeastern France and northeastern Spain (Martínez et al., 2016), while also ascribed to a unique formation in the South Portuguese zone (Horta da Torre Fm, see Pérez-Cáceres et al., 2017).

In view of the comparisons drawn above, one may conclude that the Nevado-Filábride complex and the Cantabrian zone were closely related (Fig. 7.1), as they provide similar detrital zircon age patterns (Pastor-Galán et al., 2013, Jabaloy et al., 2018). This is in agreement with previous paleogeographic reconstructions including those by Sanz de Galdeano et al. (2006) and Jabaloy et al. (2018).

The relation of the Nevado-Filábride complex with the Alpujárride and Maláguide complexes is not clear. Esteban et al. (2017) provided LA-ICP-MS U-Pb detrital zircon analyses obtained from the Marbella conglomerate (Maláguide complex). These authors proposed an MDA of ~286 Ma based on the youngest age population. Furthermore, they obtained three Paleozoic main age clusters at ca. 280-310 Ma, 320 Ma, and 345 Ma, a high proportion of Ediacaran ages (~590 Ma), small age populations ca. 1000, and several

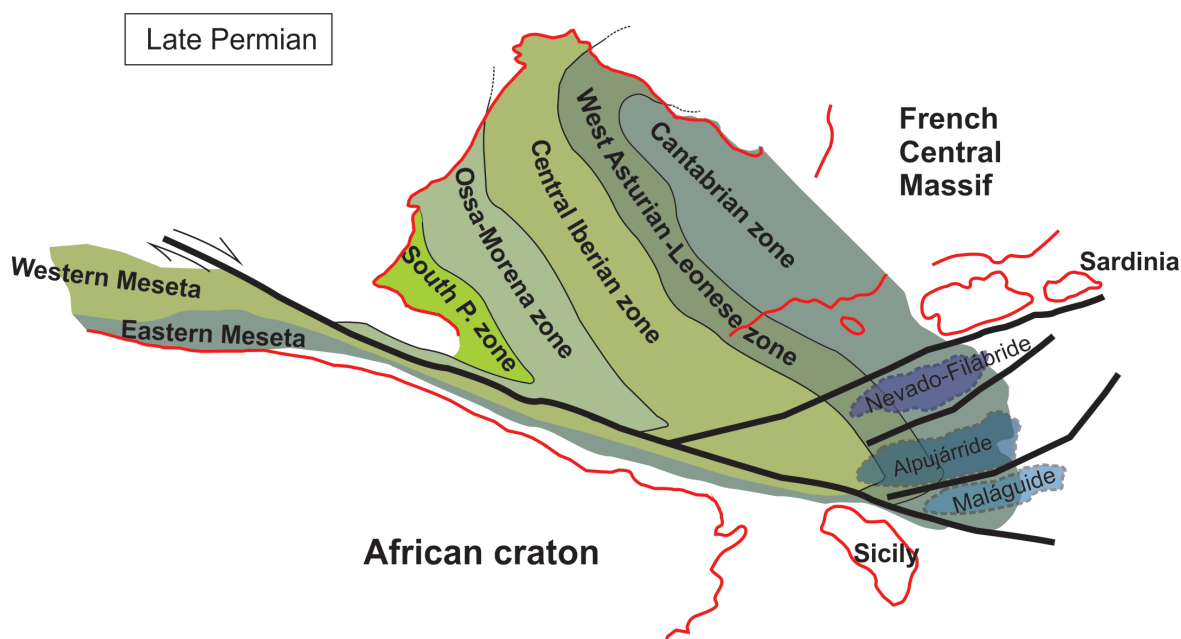


Figure 7.1. Paleogeographic reconstruction of the Iberian terranes in the late Permian. Modified from Sanz de Galdeano et al. (2006).

Paleoproterozoic analyses ranging 1800-2400 Ma. This age pattern resembles those from the Nevado-Filábride complex presented herein. Accordingly, both complexes would have been close during the deposition of the sedimentary protolith. In Fig. 7.1 is shown a probable paleogeographic position for the Maláguide terranes during the Late Permian. In this reconstruction the Nevado-Filábride complex is in the prolongation of the Cantabrian zone, while the Alpujarride and Maláguide complexes are situated to the ESE or SE, in the prolongation of the Iberian Massif.

7.3. Tectono-metamorphic evolution of the Nevado-Filábride complex

Any model proposed to explain the tectono-metamorphic story of the Nevado-Filábride complex must reconcile several remarks presented in chapter 6: the similarity of the P-T paths in the upper and lower parts of the complex, the prograde isobaric heating followed by isothermal decompression, and the LP/HT stage at ~13 Ma.

The results expounded in chapter 6 prove that the three studied formations of the Nevado-Filábride complex shared similar metamorphic histories during subduction and exhumation. Accordingly, they were already closely related during the burial and exhumation stages. Despite the similar P-T path trajectories, the uppermost rocks of the Nevado-Filábride complex recorded higher P-T conditions than the lowest ones. This difference in P-T

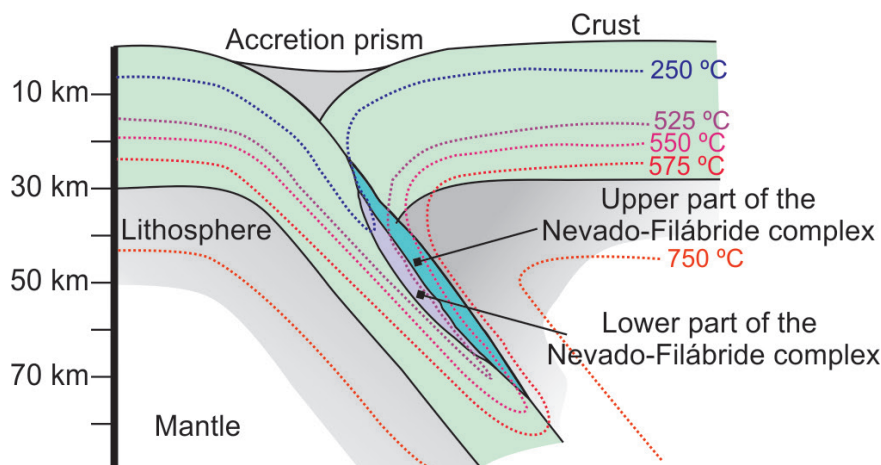


Figure 7.2. Simplified sketch showing the probable distribution of the isotherms in the subducting slab.

conditions has been pointed out previously (e.g. Puga et al., 2002; Augier et al., 2005b; Behr and Platt, 2012; Booth-Rea et al., 2015; Li and Massonne, 2018). The inverted thermal gradient has been attributed to factors including: the proximity of the top to a hot hanging wall (e.g. Behr and Platt, 2012); a late-stage thermal overprint (Bakker et al., 1989) involving either shear heating or hot fluid flow (Aerden et al., 2013); and the upwelling of hot mantle material followed by magmatism (de Jong, 2003). Since the data presented in this Ph.D. Thesis do not signal late thermal overprint and/or reheating assisted by fluid (see sections 6.4.2 and 6.4.4), the hypothesis proposed by Behr and Platt (2012) best fits our observations —i.e. the rocks in the upper part of the complex were closer to the hot upper plate during subduction, for which reason they underwent higher T than the rocks from the lower part. Fig. 7.2 depicts a probable distribution of the isotherms in the subducting slab. The small difference in pressure between the upper and lower part of the complex (2 kbar between samples RA-2, Dark schists Fm, and 16.16, Schists and marbles Fm, for the HP/LT stage) could have been caused by the effect of the directed tectonic pressure exerted in the top of the subducted slab by the upper plate.

The subduction of the Nevado-Filábride complex would not have started before ~ 30 Ma (Figs. 7.3 and 7.4a, b). The dataset presented in this Thesis does not allow for a reconstruction of the burial trajectory, as no garnet relict was found. However, it was possible to estimate a prograde isobaric heating at HP conditions at a depth of ~ 60 - 66 km (Figs. 7.3 and 7.4c).

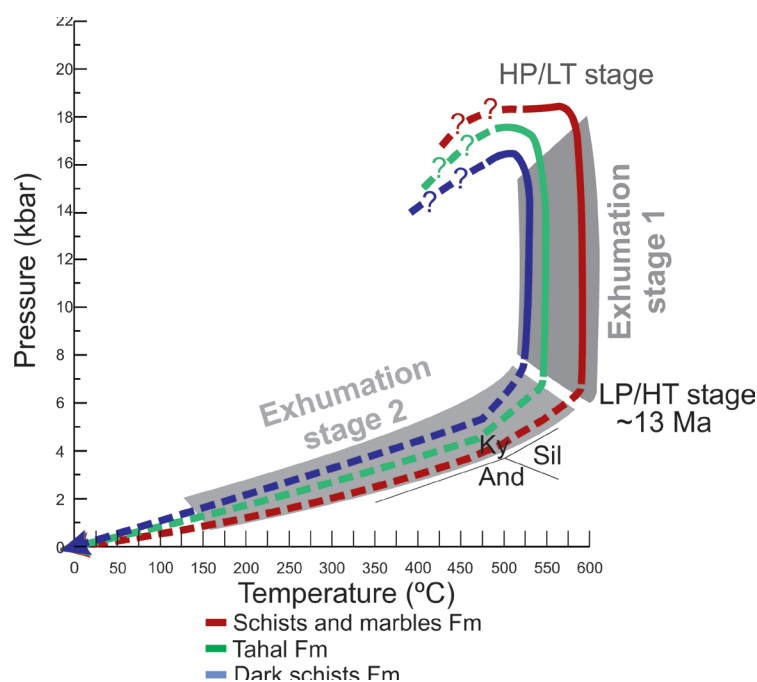


Figure 7.3. Comparison between the P-T paths obtained in the Ph.D. Thesis for the Dark schists (blue), Tahal (green) and Schists and marbles (red) Fms. Continuous lines are reconstructed based on the combination of thermobarometric results obtained for garnet and phengite. Dashed lines for the exhumation stage 2 are proposed based on the absence of andalusite and sillimanite in the studied rocks.

Following the isobaric stage, the P-T paths in all the studied samples draw an isothermal decompression trajectory attributed to the initial stage of exhumation (exhumation stage 1 in Figs. 7.3 and 7.4d). In this sense, the results presented in this Ph.D. Thesis do not fit with other studies proposing hairpin trajectories (i.e. linear cooling, Behr and Platt, 2012), or heating and/or reheating during decompression (Vissers, 1981; Gómez-Pugnaire and Fernández-Soler, 1987; Bakker et al., 1989; de Jong 2003; Aerden et al., 2013; Booth-Rea et al., 2015, Li and Massonne, 2018). A break-off of the subducting slab is evoked as the probable mechanism triggering the exhumation of the Nevado-Filábride complex (Fig. 7.4d). Indeed, slab break-off has been cited to explain the exhumation of high pressure rocks (Andersen et al., 1991; Babist et al., 2006; Xu et al., 2010; Duretz et al., 2012; Duretz and Gerya, 2013, Yamato and Brun, 2016), but also isothermal decompression following trajectories without significant cooling, as shown in Fig. 7.3 (Andersen et al., 1991; Duretz et al., 2012; Duretz and Gerya, 2013; Warren, 2013; Petersen and Buck, 2015). Such a conclusion for the Nevado-Filábride complex is furthermore in line with models invoking slab break-off and/or tearing of the subducting Iberian plate

(Bufoorn et al., 1991; Blanco and Spakman, 1993; Zeck, 1996; Spakman and Wortel, 2004; García-Castellanos and Villaseñor, 2011; Rosell et al., 2011; Vergés and Fernández, 2012; van Hinsbergen et al., 2014).

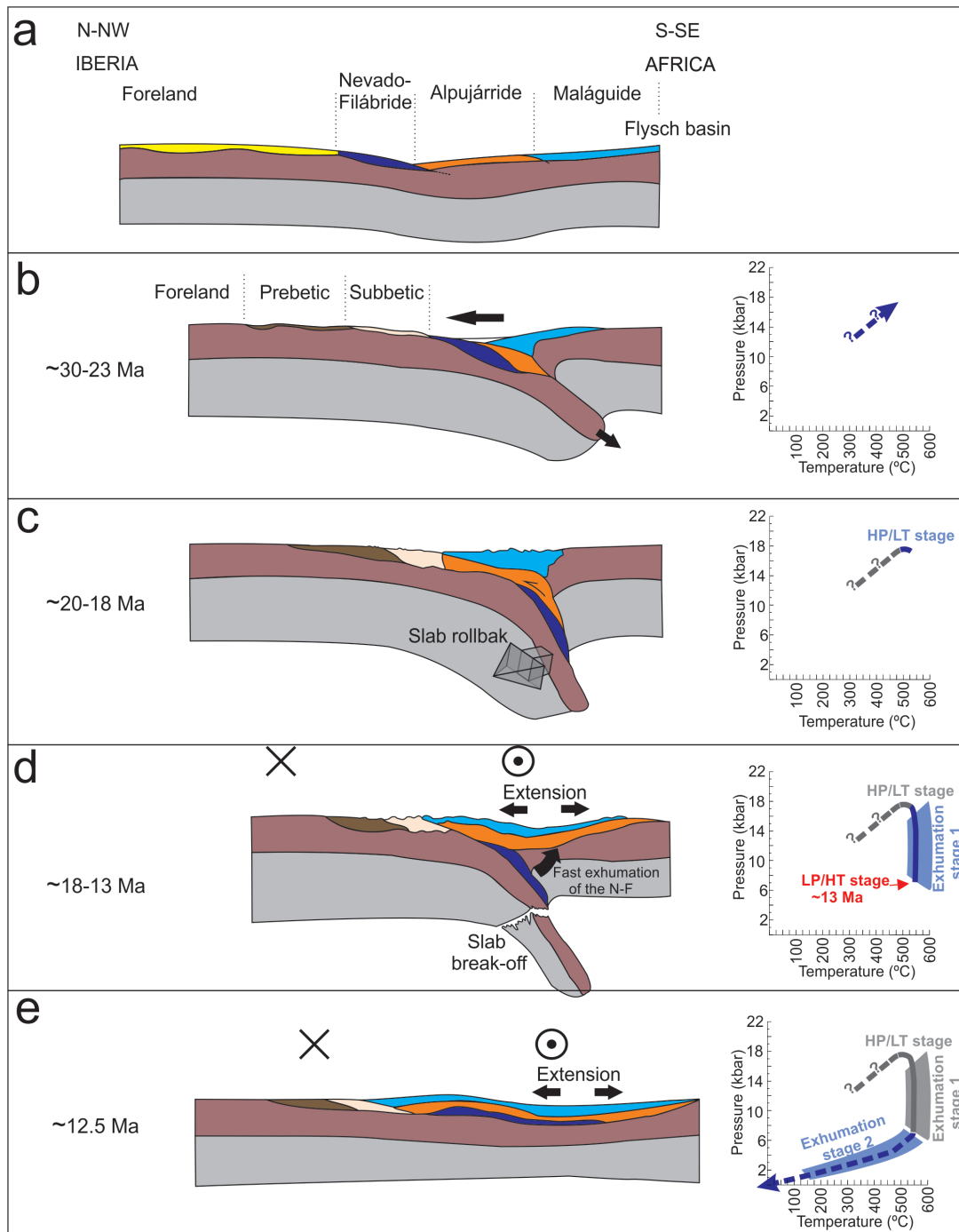


Figure 7.4. Reconstruction over time of the subduction and exhumation of the Nevado-Filábride complex.

Fig. 7.5 illustrates the position of the subducted Nevado-Filábride under the Alpujarride and Maláguide complexes at the time the slab probably broke.

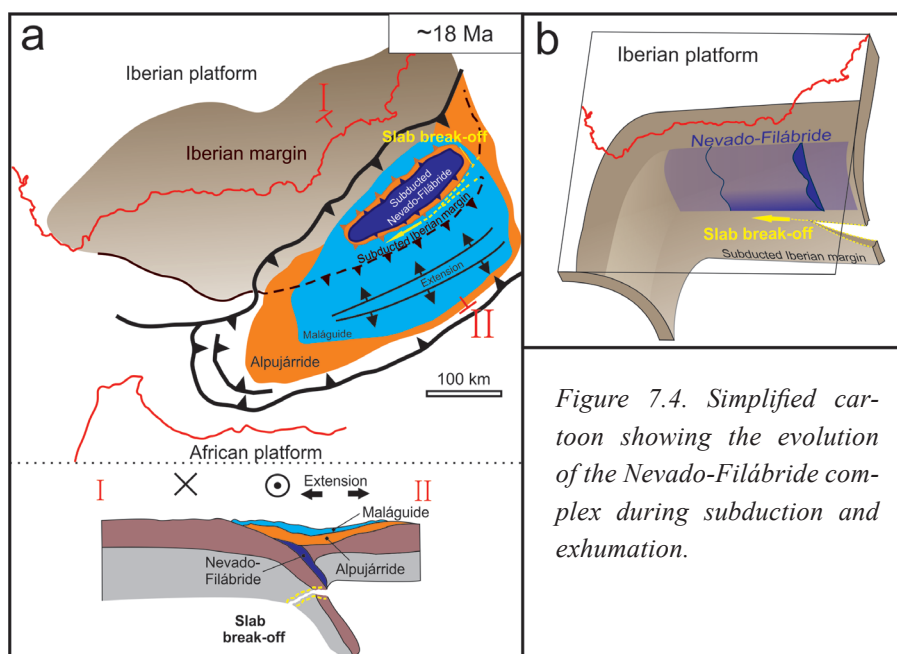


Figure 7.4. Simplified cartoon showing the evolution of the Nevado-Filábride complex during subduction and exhumation.

Regarding the age of metamorphism, allanite dating results from samples 16.16 (12.91 ± 1.10 Ma) and 16.8 (14.51 ± 2.01 Ma) made it possible to constrain the timing of the LP/HT stage at ca. 13 Ma. This age is comparable with the two main estimations for the HP/LT metamorphism existing in the literature: early Miocene (~ 20 –13 Ma) (e.g. López Sánchez-Vizcaíno et al., 2001; Gómez-Pugnaire et al., 2004; Platt et al., 2006; Kirchner et al., 2016), and Eocene to Early Oligocene (Monié et al., 1991; Augier et al., 2005a; Li and Massonne, 2018). The time frame between the Miocene ages suggested for the HP/LT event and the allanite data implies a rapid exhumation of the Nevado-Filábride complex (as previously surmised, e.g., López Sánchez-Vizcaíno et al., 2001; de Jong, 2003; Platt et al., 2006; Behr and Platt, 2012; Kirchner et al., 2016). Rapid exhumation made the Nevado-Filábride complex avoid significant cooling during the first part of decompression (up to ~ 20 –30 km) and supports the isothermal trajectory observed in the P-T diagrams (exhumation stage 1 in Fig. 7.3). Additionally, it is compatible with the slab break-off model (Davies and von Blanckenburg, 1995; O'Brien, 2001; Leech et al., 2005; Duretz et al. 2012; Petersen and Buck, 2015). In contrast, the results pointing to an Eocene or Early Oligocene age for the HP/LT event would require much longer subduction and exhumation processes, which do not agree with our results.

The allanite dating of the LP/HT (and the acceptance of a Miocene age for the HP/LT event) has important implications regarding the tectonic relation between the Nevado-Filábride and Alpujárride complexes. According to the results presented in this Ph.D. Thesis, the two complexes underwent different tectono-metamorphic histories, since the Alpujárride complex was already exhumed in the Early Miocene (~20 Ma), when the Nevado-Filábride complex was affected by the HP metamorphism, and the LP/HT event was about to start.

After ~13 Ma the retrograde part of the P-T path probably changed from isothermal to describe a linear cooling trajectory. Other proposed P-T paths enter the field of andalusite (Bakker et al., 1989; Vissers et al., 1995; Augier et al., 2005a, 2005b) or sillimanite (Augier et al., 2005a, 2005b) during decompression. However (see chapter 4), kyanite is the only Alpine-age aluminosilicate recorded in the Nevado-Filábride complex (e.g. Behr and Platt, 2013). Accordingly, this Ph.D. Thesis proposes a P-T trajectory for the late exhumation that remains inside the kyanite stability field (exhumation stage 2 in Figs. 7.3 and 7.4e). This part of the P-T trajectory probably coincides with the final emplacement of the Nevado-Filábride complex under the Alpujárride (Fig. 7.4e). Johnson et al. (1997) yielded apatite fission-track ages at 11 Ma for the Nevado-Filábride complex, implying the complex was exhumed by this time. Reconciling this age with the allanite dating necessarily implies fast cooling during stage 2 of exhumation.

To sum up, according to the petrochronological results presented in this Ph.D. Thesis, the Nevado-Filábride complex was subducted up to ~60-66 km below the Alpujárride complex at ~30 Ma, and reached HP conditions at ~20-18 Ma. The break-off of the subducted slab triggered the rapid isothermal exhumation of the complex, which underwent LP/HT conditions at ca. 13 Ma. The last stage of exhumation described linear cooling while the Nevado-Filábride complex acquired its final position under the Alpujárride complex.

7.4. Discussion on the proposed divisions in the Nevado-Filábride complex

The results presented in this Ph.D. Thesis challenge the general opinion that the Nevado-Filábride complex is divided into several tectonic units.

The study of the lithological succession, supported by petrological and mineralogical data, demonstrates that the contacts between different the lithological formations are stratigraphic ones. The supposed tectonic contacts between previously proposed tectonic units are imprecise and poorly defined in the literature, and their acceptance leads to incoherencies with the field data. The contacts between the Dark schists and the Tahal Fms, and between the Tahal and the Dark and marble Fms (or the equivalent units in the literature) are generally transitional. In particular, the contact between the Dark schists and the Tahal Fms is characterized, in the studied areas, by alternating dark and light schists and quartzites, with an upward increase in the light schists. Similarly, the contact between the Tahal and the Schists and marbles Fms has a stratigraphic character and is marked by the beginning of thin interlayered levels of marbles, which become progressively more abundant upwards. Previous shear zones existing between these units (e.g. Martínez-Martínez et al., 2002; Augier et al., 2005a; Martínez-Martínez et al., 2010) can be explained as local and not generalized structures.

The upper and lower parts of the Nevado-Filábride complex show comparable detrital zircon age patterns. Notwithstanding, this similarity does not necessarily support the existence of several tectonic units. Nor does it reject their existence, because similar age signatures have been described in other areas of the Iberian Peninsula (e.g. the Cantabrian zone, Pastor-Galán et al., 2013). Conversely, the youngest age populations identified in the studied samples correlate with their structural position: i.e. the youngest age population in the overlying Schists and marbles Fm (269.6 ± 0.9 Ma, sample SF-2) is younger than those of the Tahal Fm (334.6 ± 2.9 Ma, sample RA-3; and 327.5 ± 1.5 Ma, VE-3), and those of the underlying Dark schists Fm (354.7 ± 1.9 Ma, sample SF-1; 524.1 ± 1.1 , sample RA-1; 338.9 ± 1.1 Ma, sample RA-2; 349.1 ± 1.6 Ma, sample VE-1; 336.9 ± 1.4 Ma, sample VE-2). This finding does not fit with the formerly proposed tectonic differentiation of the Nevado-Filábride complex. Instead, it may be interpreted as a result of continuity in the sequence, the Dark schists Fm being the older part of the complex in the Sierra Nevada and Filabres, whereas the Tahal and Schists and marbles Fms, on the top, are the younger parts.

The similarities between the P-T trajectories of the schists from the upper and lower parts of the complex do not support the tectonic model of superposed independent com-

plexes based on tectono-metamorphic criteria (e.g. Puga et al., 2002). Again, a model without major tectono-metamorphic discontinuities is in line with the results. In this scenario, the upper and lower parts of the complex were subducted and exhumed together. The progressive increase of P-T conditions towards the top of the succession (Fig. 7.2) could be the consequence of an inverted thermal gradient in the complex produced by the proximity of the upper rocks to the hot plate during subduction (Fig. 7.2).

This Ph.D. Thesis, in summary, proposes that the existence of a tectonic division in the Nevado-Filábride complex can be rejected in light of the evidence described. Rather, it is strongly suggested that the Nevado-Filábride pile is formed by a succession of three formations preserving mainly stratigraphic contacts in between. The conclusions provided in previous paragraphs, taken independently, may not constitute sufficient evidence for a stratigraphic continuity of the complex. The robustness of what is concluded here lies in the combination of different methodological approaches. Stratigraphic, petrological, mineralogical, geochronological and petrochronological criteria are further supported by a comparison of data from samples collected in different sectors of the Nevado-Filábride pile.

Chapter 8

Conclusions

This chapter summarizes the results compiled in the previous chapters in order to underline the main contribution of this Ph.D. Thesis for a better understanding of the Nevado-Filábride complex and its evolution during the Betic Cordillera configuration.

The lithological succession of the Nevado-Filábride complex is formed, from bottom to top, by a lower part including a monotonous succession of dark schists and quartzites (the Dark schists Fm), and a more heterogeneous upper part showing dark schists, light schists, calc-schists, marbles, quartzites, gneisses and metabasites (the Tahal and the overlying Schists and marbles Fms). The contact between these formations is stratigraphic, with a transitional character.

Schist samples taken from different areas of the complex underwent a SHRIMP U-Pb detrital zircon study. The youngest age population estimated in the lowermost sample from the Dark schists Fm, 349.1 ± 1.6 Ma (Carboniferous), was interpreted to be the most probable maximum deposition age for the lower part of the complex in the area of Sierra Nevada and Filabres. Furthermore, the youngest age population yielded by the lowermost sample from the Tahal Fm, 334.6 ± 2.9 Ma (Carboniferous), is held to be the most probable maximum deposition age of the upper part of the complex protolith. The sample taken in the Schists and marbles Fm (upper part of the complex) provided a youngest age population of 269.6 ± 0.9 Ma (Permian). Overall, the youngest age populations were found in the upper part of the complex, and they are progressively older downward in the succession.

Hence, the protolith of the Nevado-Filábride schist would have been deposited in a nearly continuous lapse of time: the Dark schists Fm was probably deposited firstly, followed by the Tahal Fm and finally the Schists and marbles Fm. Combining the estimated maximum deposition age of the Dark schists Fm with the minimum age of deposition previously obtained from orthogneisses made it possible to constrain the deposition of the Nevado-Filábride sediments in a period of 67 Ma (between ca. 282 to 349 Ma) or a more conservative period of 102 Ma (between ca. 247 to 349 Ma).

Comparison of detrital zircon patterns led to the identification of common age populations at 480-615 Ma (Cambrian-Ediacaran), ca. 910-1010 Ma (Tonian-Stenian) and ca. 1800-2000 Ma (Orosirian), suggesting a common source area for the schists' protolith. These age populations are similar to those previously provided for the Cantabrian zone (Iberian Massif) and the Maláguide complex (Internal Zone of the Betic Cordillera). Accordingly, it can be interpreted that the Nevado-Filábride terranes were part of the Iberian paleomargin, in the ESE or SE prolongation of the Iberian Massif.

The petrochronological study based on thermo-barometric estimates of garnet and phengite, combined with U-Th-Pb allanite dating, confirmed that the Nevado-Filábride complex displays an inverted metamorphism, characterized by higher P-T conditions in the upper part of the complex.

The Darks schists, the Tahal, and the Schists and marbles Fms exhibit similar clockwise P-T trajectories characterized by prograde isobaric heating at HP/LT conditions reached after burial, and followed by an isothermal decompression leading to a LP/HT stage. During the HP/LT stage, the Dark schists Fm reached ~16 kbar and ~480 °C. The temperature difference increased during decompression up to ~47 °C during the LP/HT stage. In the Tahal Fm, the HP/LT stage was recorded at ~17.5 kbar and ~490 °C, and the temperature difference increased during the decompression up to ~50 °C in the LP/HT stage. For the Schists and marbles Fm the HP/LT stage was estimated at ~18 kbar and ~520 °C, and the temperature increase in decompression was ~70 °C during the LP/HT stage. Despite such differences in pressure and temperature between formations, the similarities in the shape of P-T paths indicate that they underwent a similar subduction and exhumation history, but at different structural levels.

Based on the allanite dating of two samples from the upper part of the complex (Schists and marbles and Tahal Fms), the age of the LP/HT stage could be constrained at ca. 13 Ma. A rapid exhumation is proposed for the Nevado-Filábride complex, characterized by an initial fast isothermal decompression, followed by linear cooling. This rapid isothermal exhumation was probably triggered by the break-off of the subducting south Iberian paleomargin.

The combination of cartographic, stratigraphic, geochronological, and petrochronological results presented in this Ph.D. Thesis lead to an interpretation for the Nevado-Filábride complex as a continuous metamorphic sequence showing an inverted metamorphism, rather than a tectonically divided complex.

Conclusiones

Este capítulo resume los resultados presentados en los capítulos anteriores, con el objetivo de resaltar la contribución de esta Tesis Doctoral al conocimiento del complejo Nevado-Filábride y su evolución durante la configuración tectónica de la Cordillera Bética.

La sucesión litológica del complejo Nevado-Filábride presenta una parte inferior formada por una sucesión monótona de esquistos oscuros y cuarcitas (Formación de Esquistos oscuros), y una parte superior más heterogénea que incluye esquistos oscuros, esquistos claros, calcoesquistos, mármoles, cuarcitas, gneises y metabasitas (formaciones Tahal y, por encima, la formación de Esquistos y Mármoles). El contacto entre estas formaciones es estratigráfico y transicional.

Las muestras de esquisto tomadas de diferentes áreas del complejo, que abarcan desde las partes más bajas a las más altas de la sucesión litológica, se sometieron a un estudio SHRIMP U-Pb para datar circones detríticos. La edad más joven estimada en la muestra más baja de la Formación de Esquistos oscuros es $349,1 \pm 1,6$ Ma (Carbonífero). Esta edad se ha interpretado como la edad máxima de depósito del protolito sedimentario en la parte inferior del complejo en las Sierras Nevada y Filabres. Por otro lado, la población de edad más joven estimada para la muestra más baja de la Formación Tahal, $334,6 \pm 2,9$ Ma (Carbonífero), es la edad máxima de depósito más probable para la parte superior del complejo. La muestra tomada en la parte más alta de la secuencia del Nevado-Filábride (Formación de Esquistos y Mármoles) proporcionó una población de edad más joven, $269,6 \pm 0,9$ Ma (Pérmico). En general, las poblaciones de edad más joven se encontraron en la parte superior del complejo, y son progresivamente mayores hacia abajo en la sucesión. Por lo tanto, el protolito del esquisto se debió depositar en un lapso de tiempo casi continuo. Así, el protolito de la Formación de Esquistos oscuros se depositó en primer lugar, seguido del de la Formación Tahal y finalmente por el de la Formación de Esquistos y Mármoles. El periodo de sedimentación del protolito debió tener lugar en un periodo aproximado de 67 Ma (entre ca. 282 a 349 Ma), o bien un periodo menos restrictivo de 102 Ma (entre ca. 247 a 349 Ma), a tenor de la comparativa entre las eda-

des de deposición máximas obtenidas en esta Tesis Doctoral y las edades de deposición mínimas obtenidas en la literatura a partir de ortogneises.

La comparación de los patrones de circones detríticos condujo a la identificación de poblaciones de edades comunes ca.480-615 Ma (Cámbrico-Ediacárico), ca. 910-1010 Ma (Tónico-Sténico) y ca. 1800-2000 Ma (Orosírico), lo que sugiere un área fuente común para el protolito de los esquistos. Estas poblaciones de edad son similares a las proporcionadas previamente para la Zona Cantábrica (Macizo Ibérico) y el complejo Maláguide (Zona Interna de la Cordillera Bética). En consecuencia, se puede interpretar que el área donde se sedimentó el Nevado-Filábride eran parte del paleomargen ibérico, y se encontraba en la prolongación hacia el ESE o SE del Macizo Ibérico.

El estudio petrocronológico basado en estimaciones termo-barométricas en granate y fengita, combinado con la datación de alanita U-Th-Pb, confirmaron que el complejo Nevado-Filábride muestra un metamorfismo inverso, caracterizado por condiciones de presión y temperatura más altas en la parte superior del complejo.

Las formaciones estudiadas exhiben trayectorias horarias de presión y temperatura en sentido horario, similares entre sí y caracterizadas por un calentamiento isobárico en condiciones AP / BT, seguido de una descompresión isotérmica que conduce a una etapa de BP / AT. Durante la etapa de AP / BT, la Formación de Esquistos oscuros alcanzó ~ 16 kbar y ~ 480 °C. La diferencia de temperatura aumentó durante la descompresión hasta ~ 47 ° C durante la etapa de BP / AT. En la Formación Tahal, la etapa de AP / BT se registró a ~ 17.5 kbar y ~ 490 °C, y la diferencia de temperatura aumentó durante la descompresión hasta ~ 50 ° C durante la etapa BP / AT. Por último, en la Formación de Esquistos y Mármoles la etapa HP / LT se estimó en ~ 18 kbar y ~ 520 °C, y el aumento de temperatura en la descompresión fue de ~ 70 °C durante la etapa BP / AT. A pesar de estas diferencias en la presión y la temperatura entre las formaciones, las similitudes en la forma de las trayectorias indican que éstas estuvieron sometidas a un proceso de enterramiento y exhumación similares, pero en diferentes niveles estructurales.

A partir de los datos de datación de alanita (LA-ICP-MS) de dos muestras de la parte superior del complejo (Formaciones Tahal y de Esquistos y Mármoles), la edad de la

etapa de BP / AT se estimó en ca. 13 Ma. Se ha propuesto una exhumación rápida para el complejo Nevado-Filábride, caracterizada una primera etapa de descompresión isotérmica, seguida de una segunda etapa de enfriamiento describiendo una trayectoria lineal. La exhumación isotérmica mencionada probablemente se desencadenó tras la ruptura de la lámina subducida del paleomargen Ibérico.

La combinación de resultados cartográficos, estratigráficos, geocronológicos y petrocrónológicos presentados en esta Tesis Doctoral señalan que el complejo Nevado-Filábride presenta una secuencia continua que muestra un metamorfismo invertido, en lugar de ser un complejo dividido tectónicamente.

References

- Aerden, D., Bell, T.H., Puga, E., Sayab, M., Lozano, J.A., Díaz de Federico, A., 2013. Multi-stage mountain building vs. relative plate motions in the Betic Cordillera deduced from integrated microstructural and petrological analysis of porphyroblast inclusion trails. *Tectonophysics* 587, 188-206.
- Aerden, D., Sayab, M., 2008. From Adria- to Africa-driven orogenesis: Evidence from porphyroblasts in the Betic Cordillera, Spain. *J. Struct. Geol.* 30, 1272-1287.
- Agard, P., Augier, R., Monié, R., 2011. Shear band formation and strain localization on a regional scale: Evidence from anisotropic rocks below a major detachment (Betic Cordilleras, Spain). *J. Struct. Geol.* 33, 114-131.
- Airaghi, L., Lanari, P., de Sigoyer, J., Guillot, S., 2017. Microstructural vs compositional preservation and pseudomorphic replacement of muscovite in deformed metapelites from the Longmen Shan (Sichuan, China). *Lithos* 282-283, 262-280.
- Alonso-Chaves, F., Soto, J.I. Orozco, M., Kiliyas, A.A., Tranos, M.D., 2004. Tectonic evolution of the Betic cordillera: an overview. *Bull. Geol. Soc. Greece* 36, 1598-1607.
- Andersen, T., 2005. Detrital zircons as tracers of sedimentary provenance: limiting conditions from statistics and numerical simulation. *Chem. Geol.* 216, 3-4, 249-270.
- Andersen, T.B., Jamtveit, B., Dewey, J.F., 1991. Subduction and eduction of continental crust: major mechanisms during continent – continent collision and orogenic extensional collapse, a model based on the south Norwegian Caledonides. *Terra Nova* 3 (3), 303-310.
- Andriessen, P.A.M., Hebeda, E.H., Simon, O.J., Verschure, R.H., 1991. Tourmaline K-Ar ages compared to other radiometric dating systems in Alpine anatectic leucosomes and metamorphic rocks (Cyclades and Southern Spain). *Chem. Geol.* 91, 33-48.
- Andrieux, J., Fontbote, J.M., Mattauer, M., 1971. Sur un modèle explicatif de l'Arc de Gibraltar. *Earth Planet. Sc. Lett.* 12, 191-198.
- Augier, R., Agard, P., Monié, P., Jolivet, L., Robin, C., Booth-Rea, G., 2005a. Exhumation, doming and slab retreat in the Betic Cordillera (SE Spain): in situ Ar-40/Ar-39 ages and P-T-d-t paths for the Nevado-Filabride complex. *J. Metamorph. Geol.* 23, 357-381.
- Augier, R., Booth-Rea, G., Agard, P., Martínez-Martínez, J.M., Jolivet, L., Azañón, J.M., 2005b. Exhumation constraints for the lower Nevado- Filabride Complex (Betic Cordillera, SE Spain): A Raman thermometry and Tweeku multiequilibrium thermobarometry approach. *Bull. Soc. Geol. France* 176, 403-416.
- Augier, R., Jolivet, L. 2005c. Late Orogenic doming in the eastern Betic Cordilleras: Final exhumation of the Nevado-Filabride complex and its relation to basin genesis. *Tectonics*, 24.
- Augier, R., Jolivet, L., Do Couto, D., Negro, F., 2013. From ductile to brittle, late- to post-orogenic evolution of the Betic Cordillera: Structural insights from the North-eastern Internal Zones. *Bull. Soc. Geol. France* 184, 4-5, 405-425.
- Azañón, J.M., Goffé, B., 1997. Ferro-Magnesiocarpholite-kyanite assemblages as record of the high-pressure, low-temperature metamorphism in central Alpujarride units, Betic cordillera (SE Spain). *Eur. J. Mineral.* 9, 1035-1051.
- Azañón, J.M., Crespo-Blanc, A., 2000. Exhumation during a continental collision inferred from the tectonometamorphic evolution of the Alpujarride Complex in the Central Betics (Alboran Domain, SE Spain). *Tectonics* 19, 549-565.
- Babist, J., Handy, M.R., Konrad-Schmolke, M., Hammerschmidt, K., 2006. Pre-collisional, multistage exhumation of subducted continental crust: The Sesia Zone, western Alps. *Tectonics* 25, TC6008.

- Bakker, H., de Jong, K., Helmers, H., Biermann, C., 1989. The geodynamic evolution of the Internal Zone of the Betic Cordilleras (south-east Spain): A model based on structural analysis and geothermobarometry, *J. Metamorph. Geol.* 7, 359-38.
- Balanyá, J.C., García-Dueñas, V. 1987. Les directions structurales dans le domaine d'Alborán de part et d'autre du détroit de Gibraltar. *C. R. Acad. Sci. II* 304, 929-932.
- Baxter, E.F., Caddick, M.J., Dragovic, B., 2017. Garnet: A Rock-Forming Mineral Petrochronometer. *Rev. Mineral. Geochem* 83(1), 469-533.
- Bradley, D.C., 2011. Secular trends in the geologic record and the supercontinent cycle. *Earth-Sci. Rev.* 108 (1-2), 16-33.
- Bea, F., Montero, P., Talavera, C., Abu Anbar, M., Scarrow, J., Molina, J.F., Moreno, J.A., 2010. The palaeogeographic position of Central Iberia in Gondwana during the Ordovician: evidence from zircon geochronology and Nd isotopes. *Terra Nova* 22, 341-346.
- Behr, W.M., Platt, J.P., 2012. Kinematic and thermal evolution during two-stage exhumation of a Mediterranean subduction complex. *Tectonics* 31, TC4025.
- Behr, W.M., Platt, J.P., 2013. Rheological evolution of a Mediterranean subduction complex. *J. Struct. Geol.* 54, 136-155.
- Belousova, E.A., Griffin, W.L., O'Reilly, S.Y., 2006. Zircon crystal morphology, trace element signatures and Hf isotope composition as a tool for petrogenetic modelling: Examples from Eastern Australian Granitoids. *J. Petrol.* 47, 329-353.
- Berman, R.G., 1991. Thermobarometry using multi-equilibrium calculations: a new technique, with petrological applications. *Can. Mineral.* 29, 833-855.
- Beyssac, O., Goffé, B., Chopin, C., Rouzaud, J.N., 2002. Raman spectra of carbonaceous material in metasediments: a new geothermometer. *J. Metamorph. Geol.* 20, 859-871.
- Bezada, M.J., Humphreys, E.D., Toomey, D.R., Harnafi, M., Dávila, J.M., Gallart, J., 2013. Evidence for slab rollback in westernmost Mediterranean from improved upper mantle imaging. *Earth Planet. Sc. Lett.* 368, 51-60.
- Black, L.P., Kamo, S.L., Allen, C.M., Aleinikoff, J.N., Davis, D.W., Korsch, R.J., Foudoulis, C., 2003. TEMORA 1: A new zircon standard for Phanerozoic U-Pb geochronology. *Chem. Geol.* 200, 155-170.
- Blanco, M.J., Spakman, W., 1993. The P-wave velocity structure of the mantle below the Iberian Peninsula: evidence for subduction lithosphere below southern Spain. *Tectonophysics* 221, 13-34.
- Blumenthal, M., 1927. Versuch einer tektonischen Gliederung der Betischen Kordilleren von central und Südwest Andalusien. *Eclogae Geol. Helv.* 20, 487-532.
- Boillot, G., Montadert, L., Lemoine, M., Biju-Duval, B., 1984. Les marges continentales actuelles et fossiles autour de la France. Masson, Paris, 342 p.
- Booth-Rea, G., Azañón, J.M., Goffé, B., Vidal, O., Martínez-Martínez, J.M., 2002. High-pressure, low-temperature metamorphism in the Alpujarride units outcropping in southeastern Betics (Spain). *C. R. Geosci.* 334 (Série II), 857-865.
- Booth-Rea, G., Martínez-Martínez, J.M., Giaconia, F., 2015. Continental subduction, intracrustal shortening and coeval upper-crustal extension: P-T evolution of subducted south-Iberian paleomargin metapelites. *Tectonophysics* 663, 122-139.
- Bouillin, J., Durand-Delga, M., Olivier, P., 1986. Betic-Rif and Tyrrhenian distinctive features, genesis and development stages. In: Wezel, F.C. (ed). *The origin of arcs*. Elsevier, Amsterdam, pp 281-304.
- Brouwer, H.A., 1926. Zur Tektonik der betischen Kordilleren. *Geol. Rundsch.* 17, 332-336.
- Brown, M., 2007. Metamorphic conditions in orogenic belts: a record of secular change. *Int. Geol. Rev.* 49, 193-234.
- Brown, M., 2014. The contribution of metamorphic petrology to understanding lithosphere evolution and geodynamics. *Geosci. Front.* 5, 553-569.

- Brun, J.P., Faccenna, C., 2008. Exhumation of high-pressure rocks driven by slab rollback. *Earth Planet. Sc. Lett.* 272, 1-7.
- Bufo, E., Udias, A., Madariaga, R., 1991. Intermediate and deep earthquakes in Spain. *Pure Appl. Geophys.* 136, 375-393.
- Burn, M., Lanari, P., Pettke, T., Engi, M., 2017. Non-matrix-matched standardisation in LA-ICP-MS analysis: General approach and application to allanite Th-U-Pb age-dating. *J. Anal. Atom. Spectrom.* 32, 1359-1377.
- Caddick, M.J., Kohn, M.J., 2013. Garnet: Witness to the evolution of destructive plate boundaries. *Elements* 9, 427-432.
- Calvert, A., Sandvol, E., Seber, D., Barazangi, M., Roecker, S., Mourabit, T., Vidal, F., Alguacil, G., Jabour, N., 2000. Geodynamic evolution of the lithosphere and upper mantle beneath the Alboran region of the western Mediterranean: constraints from travel time tomography. *J. Geophys. Res.* 105, 898.
- Cambeses, A., 2015. Ossa-Morena Zone Variscan 'Calc-Alkaline' Hybrid Rocks: Interaction of Mantle- and Crustal-Derived Magmas as a Result of Intra-Orogenic Extension Related Intraplating. Universidad de Granada, Ph.D. Thesis (450 pp).
- Cambeses, A., Scarrow, J.H., Montero, P., Lázaro, C., Bea, F., 2017. Palaeogeography and crustal evolution of the Ossa-Morena Zone, southwest Iberia, and the North Gondwana margin during the Cambro-Ordovician: a review of isotopic evidence. *Int. Geol. Rev.* 59, 94-130.
- Casciello, E., Fernández, M., Vergés, J., Cesarano, M., Torne, M., 2015. The Alboran Domain in the Western Mediterranean evolution: the birth of a concept. *Bull. Soc. Geol. France* 186, 371-384.
- Cassinis, G., Di Stefano, P., Massari, F., Neri, C., Venturi, C., 2000. Permian of South Europe and its interregional correlation. In: Yin, H.F., Dickins, J.M., Shi, G.R., et al. (eds). *Permian-Triassic Evolution of Tethys and Western Circum-Pacific*. Elsevier Science, Amsterdam, pp 37-70.
- Carminati, E., Lustrino, M., Doglioni, C., 2012. Geodynamic evolution of the central and western Mediterranean: Tectonics vs. igneous petrology constraints. *Tectonophysics* 579, 173-192.
- Cathelineau, M., Nieva, D., 1985. A chlorite solid solution geothermometer the Los Azufres (Mexico) geothermal system. *Contrib. Mineral. Petrol.* 91, 235-244.
- Cenki-Tok, B., Darling, J., Rolland, Y., Dhuime, B., Storey, C.D., 2014. Direct dating of mid-crustal shear zones with synkinematic allanite: New in situ U-Th-Pb geochronological approaches applied to the Mont Blanc Massif. *Terra Nova* 26(1), 29-37.
- Centro de Instrumentación Científica de la Universidad de Granada. IBERSIMS: the Shrimp Ion-Microprobe Laboratory of the University of Granada. Available from <http://www.ugr.es/~ibersims> (Last access: 2 November 2017).
- Chalouan, A., Michard, A., 1990. The Ghomarides nappes, Rif coastal range, Morocco: a variscan chip in the Alpine belt. *Tectonics* 9, 1565-1583.
- Chapman, A., Luffi, P., Saleeby, J., Petersen, S., 2011. Metamorphic evolution, partial melting and rapid exhumation above an ancient flat slab: insights from the San Emigdio Schist, southern California. *J. Metamorph. Geol.* 29(6), 601-626.
- Cheng, H., Cao, D., 2015. Protracted garnet growth in high-P eclogite: constraints from multiple geochronology and P-T pseudosection. *J. Metamorph. Geol.* 33, 613-632.
- Corfu, F., Hanchar, J.M., Hoskin, P.W.O., Kinny, P., 2003. Atlas of zircon textures. In: Hanchar, J.M., Hoskin, P.W.O. (eds). *Zircon. Rev. Mineral. Geochem.* 53. Mineralogical Society of America. Washington DC, pp 469-500.
- Davies, J.H., von Blanckenburg, F., 1995. Slab breakoff: a model of lithosphere detachment and its test in the magmatism and deformation of collisional orogens. *Earth. Planet. Sci. Lett.* 129, 85-102.
- Davis, D.W., Williams, I.S., Krogh, T.E., 2003. Historical development of U-Pb geochronology. In: Hanchar, J.M., Hoskin, P.W.O. (eds). *Zircon. Rev. Mineral. Geochem.* 53. Mineralogical Society of America. Washington DC, pp 145-181.

- Dercourt, J., Zonenshain, L.P., Ricou, L.E., Le Pichon, X., Knipper, A.L., Grandjaquet, C., Sbertshikov, I.M., Geussant, J., Lepvrier, C., Pechersku, D.H., Boulin, J., Bazhenov, M.L., Lauer, J.P., Biju-Duval, B., 1986. Geological evolution of the Tethys belt from the Atlantic to the Pamirs since the Lias. *Tectonophysics* 123, 241-315.
- de Andrade, V., Vidal, O., Lewin, E., O'Brien, P., Agard, P., 2006. Quantification of electron microprobe compositional maps of rock thin sections: an optimized method and examples. *J. Metamorph. Geol.* 24, 655-668.
- de Jong, K., 1991. Tectonometamorphic studies and radiometric dating in the Betic Cordilleras (SE Spain) - with implications for the dynamics of extension and compression in the western Mediterranean area. Thesis Vrije Universiteit. Amsterdam, 204 p.
- de Jong, K., 1993. The tectono-metamorphic evolution of the Veleta Complex and the development of the contact with the Mulhacen Complex (Betic Zone, SE Spain). *Geol. Mijnbouw* 71, 227-227.
- de Jong, K., 2003. Very fast exhumation of high-pressure metamorphic rocks with excess ^{40}Ar and inherited ^{87}Sr , Betic Cordilleras, southern Spain. *Lithos* 70, 91-110.
- de Jong, K., Bakker, H.E., 1991. The Mulhacen and Alpujarride complexes in the Sierra de los Filabres, SE Spain: Litho-stratigraphy. *Geol. Mijnbouw* 70, 93-103.
- de Lis Mancilla, F., Stich, D., Berrocoso, M., Martín, R., Morales, J., Fernández-Ros, A., Páez, R., Pérez-Peña, A., 2013. Delamination in the Betic Range: Deep structure, seismicity, and GPS motion. *Geology* 41, 307-310.
- Díaz de Federico, A., Burgos J., Almarza, J., Orozco, M., 1981. Mapa Geológico de España, Serie Magna 1:50.000, hoja 1028 (Aldeire), Instituto Geológico y Minero de España, Madrid.
- Díaz de Federico, A., Puga, E., Burgos, J., Gallegos, J.A., Sanz de Galdeano, C., 1980. Mapa Geológico de España, Serie Magna 1:50.000, hoja 1027 (Güéjar-Sierra). Instituto Geológico y Minero de España, Madrid.
- Dickinson, W.R., Gehrels, G., 2009. Use of U–Pb ages of detrital zircons to infer maximum depositional ages of strata: A test against a Colorado Plateau Mesozoic database. *Earth Planet. Sc. Lett.* 288, 115-125.
- Didon, J., Durand-Delga, M., Kornprobst, J., 1973. Homologies géologiques entre les deux rives du Déroit de Gibraltar. *B. Soc. Geol. Fr.* 15(7), 77-105.
- Díez-Fernández, R., Martínez-Catalán, J.R., Gerdes, A., Abati, J., Arenas, R., Fernández-Suárez, J. 2010. U–Pb ages of detrital zircons from the Basal allochthonous units of NW Iberia: Provenance and paleoposition on the northern margin of Gondwana during the Neoproterozoic and Paleozoic. *Gondwana Res.* 8, 2-3, 385-399.
- Dinis, P., Andersen, T., Machado, G., Guimaraes, F., 2012. Detrital zircon U-Pb ages of a late-Variscan carboniferous succession associated with the Porto-Tomar shear zone (West Portugal): provenance implications. *Sediment, Geol.* 273-274, 19-29.
- Do Couto, D., Gumiaux, C., Augier, R., Lebret, N., Folcher, N., Jouannic, G., Jolivet, L., Suc, J.-P., Gorini, C., 2014. Tectonic inversion of an asymmetric graben: Insights from a combined field and gravity survey in the Sorbas basin. *Tectonics* 33(7), 1360-1385.
- Durand-Delga, M., Fontboté, J.M., 1980. Le cadre structural de la Méditerranée occidentale. 26 Congrès. Géol. Intern., Paris. Les Chaînes alpines issues de la Téthys. *Mém. B.R.G.M.* 115, 67-85.
- Duretz, T., Gerya, T.V., 2013. Slab detachment during continental collision: Influence of crustal rheology and interaction with lithospheric delamination. *Tectonophysics* 602, 124-140.
- Duretz, T., Gerya, T.V., Kaus, B.J.P., Andersen T.B., 2012. Thermomechanical modeling of slab eduction. *J. Geophys. Res.* 117.
- Egeler, C. G., 1963. On the tectonics of the eastern Betic Cordilleras. *Geol. Rundsch.* 53, 260-269.
- Egeler, C.G., Simon, O.J., 1969. Orogenic evolution of the Betic zone (Betic cordilleras, Spain), with emphasis on the nappe structures. *Geol. Mijnbouw* 48, 296-305.

- Engi, M., 2017. Petrochronology based on REE-minerals: monazite, allanite, xenotime, apatite. *Rev. Mineral. Geochem.* 83, 365-418.
- Engi, M., Lanari, P., Kohn, M. J., 2017. Significant Ages — An Introduction to Petrochronology. *Rev. Mineral. Geochem.* 83 (1), 1-12.
- Ernst, W.G., 1988. Tectonic history of subduction zones inferred from retrograde blueschist P-T paths. *Geology* 16, 1081-1084.
- Esteban, J.J., Cuevas, J., Tubía, J.M., Gutiérrez-Alonso, G., Larionov, A., Sergeev, S., Hofmann, M., 2017. U–Pb detrital zircon ages from the Paleozoic Marbella Conglomerate of the Malaguide Complex (Betic Cordilleras, Spain): Implications on Paleotethyan evolution. *Lithos* 290-291, 34-47.
- Evans, T.P., 2004. A method for calculating effective bulk composition modification due to crystal fractionation in garnet-bearing schist: implications for isopleth thermobarometry. *J. Metamorph. Geol.* 22, 547-557.
- Ewing, R., Meldrum, A., Wang, L., Weber, W., Corrales, L. 2003. Radiation effects in zircon. *Rev. Mineral. Geochem.* 53, 387-425.
- Fallot, P., 1948. Les Cordillères bétiques. *Estud. Geol.* 4, 83-173.
- Fallot, P., Faure-Muret, A., Fontboté, J.M., Solé Sabarís, L., 1959. Profil géologique à travers le massif du Veleta (Sierra Nevada, Andalousie). *C. R. Acad. Sci. Paris* 248, 3247-3252.
- Fallot, P., Faure-Muret, A., Fontboté, J.M., Solé Sabarís, L., 1960. Estudio sobre las series de Sierra Nevada y de la llamada Mischungzone. *Boletín del Instituto Geológico y Minero España* 81, 347-557.
- Fedo, C.M., Sircombe, K.N., Rainbird, R.H. 2003. Detrital zircon analysis of the sedimentary record. *Rev. Mineral. Geochem.* 53, 277-303.
- Fernández-Suárez, J., Dunning, G.R., Jenner, G.A., Gutiérrez-Alonso, G., 2000. Variscan collisional magmatism and deformation in NW Iberia: constraints from U/Pb geochronology of granitoids. *J. Geol. Soc.* 157, 565-576.
- Fernández-Suárez, J., Gutierrez-Alonso, G., Johnston, S.T., Jeffries, T.E., Pastor-Galán, D., Jenner, G.A., Murphy, J.B., 2011. Iberian late-Variscan granitoids: Some considerations on crustal sources and the significance of “mantle extraction ages”. *Lithos* 123, 1-4, 121-132.
- Foster, G., Parrish, R.R., 2003. Metamorphic monazite and the generation of P-T-t paths. *Geol. Soc. London Spec. Publ.* 220, 25-47.
- Gaidies, F., de Capitani, C., Abart, R., Schuster, R., 2008. Prograde garnet growth along complex P–T–t paths: results from numerical experiments on polyphase garnet from the Wölz Complex (Austroalpine basement). *Contrib. Mineral. Petrol.* 155, 673-688.
- Galindo-Zaldívar, J., 1993. Geometría de las deformaciones neógenas en Sierra Nevada (Cordilleras Béticas). Tesis Universidad de Granada. Monografía Tierras del Sur, 249 p.
- Galindo-Zaldívar, J., González-Lodeiro, F., Jabaloy, A., 1989. Progressive extensional shear structures in a detachment contact in the western Sierra Nevada (Betic Cordilleras, Spain). *Geodin. Acta* 3, 73-85.
- García-Castellanos, D., Villaseñor, A., 2011. Messinian salinity crisis regulated by competing tectonics and erosion at the Gibraltar arc. *Nature* 480, 359-363.
- García-Dueñas, V., Martínez-Martínez, J.M., Orozco, M., Soto, J., 1988. Plis-nappes, cisaillements syn- à post-métamorphiques et cisaillements ductiles-fragiles en distension dans les Nevado- Filabrides (Cordillères bétiques, Espagne). *C. R. Geosci.* 307, Série II, 1389-1395.
- García-Dueñas, V., Navarro-Vilá, F., Pérez-Rojas, A., González-Donoso, J. M., Martínez-Gallego, J., 1979. Mapa Geológico de España, Serie Magna 1:50.000, hoja 1010 (La Peza). Instituto Geológico y Minero de España, Madrid.
- García-Monzón, G., Kampschuur, W., 1975. Mapa Geológico de España 1:50.000, hoja 1014 (Vera), Instituto Geológico y Minero de España, Madrid.

- Gärtner, A., Linnemann, U., Sagawe, A., Hofmann, M., Ullrich, B., Kleber, A., 2013. Morphology of zircon crystal grains in sediments-characteristics, classifications, definitions. *Journal of Central European Geology* 59, 65-73.
- Gehrels, G., 2012. Detrital zircon U-Pb geochronology: Current methods and new opportunities. In: Busby, C., Azor, A. (eds). *Tectonics of Sedimentary Basins: Recent Advances*. Wiley-Blackwell, Chichester, pp 47-62.
- Gehrels, G., 2014. Detrital zircon U-Pb geochronology applied to tectonics. *Annu. Rev. Earth Pl. Sc.* 42, 127-149.
- Gill, R., Aparicio, A., El Azzouzi, M., Hernandez, J., Thirlwall, M., Bourgois, J., Marriner, G., 2004. Depleted arc volcanism in the Alboran Sea and shoshonitic volcanism in Morocco: geochemical and isotopic constraints on Neogene tectonic processes. *Lithos* 78, 363-388.
- Giuntoli, F., Lanari, P., Engi, M., 2018. Deeply subducted continental fragments – Part 1: Fracturing, dissolution–precipitation, and diffusion processes recorded by garnet textures of the central Sesia Zone (western Italian Alps). *Solid Earth* 9(1), 167-189.
- Goffé, B., Michard, A., García-Dueñas, V., González-Lodeiro, F., Monié, P., Campos, J., Galindo-Zaldívar, J., Jabaloy, A., Martínez-Martínez, J.M., Simancas, F., 1989. First evidence of high-pressure, low temperature metamorphism in the Alpujarride nappes, Betic Cordillera (SE Spain). *Eur. J. Mineral.* 1, 139-142.
- Gómez-Pugnaire, M.T., 1981. La evolución del metamorfismo Alpino en el Complejo Nevado-Filábride de la Sierra de Baza (Cordilleras Béticas, España). *Tecniterrae*, pp 1-130.
- Gómez-Pugnaire, M.T., Braga, J.C., Martín, J.M., Sassi, F.P., del Moro, A., 2000. Regional implications of a Palaeozoic age for the Nevado–Filábride Cover of the Betic Cordillera, Spain. *Schweiz. Miner. Petrogr. Mitt.* 80, 45-52.
- Gómez-Pugnaire, M.T., Chacón J., Mitrofanov, F., Timofeev, V., 1982. First report on pre-Cambrian rocks in the graphite-bearing series of the Nevado-Filábride Complex (Betic Cordilleras, Spain). *N. Jb. Geol. Paliönt. Mh.* 3, 176-180.
- Gómez-Pugnaire, M.T., Fernández-Soler, J.M., 1987. High-pressure metamorphism in metabasite from the Betic Cordilleras (SE Spain) and its evolution during the Alpine orogeny. *Contrib. Mineral. Petrol.* 95, 231-244.
- Gómez-Pugnaire, M.T., Franz, G., López Sánchez-Vizcaíno, V.L., 1994. Retrograde formation of NaCl- scapolite in high pressure metaevaporites from the Cordilleras Béticas (Spain). *Contrib. Mineral. Petrol.* 77, 619-640.
- Gómez-Pugnaire, M.T., Galindo-Zaldívar, J., Rubatto, D., González-Lodeiro, F., López Sánchez-Vizcaíno, V., Jabaloy, A., 2004. A reinterpretation of the Nevado-Filábride and Alpujarride Complexes (Betic Cordillera): field, petrography and U-Pb ages from orthogneisses (western Sierra Nevada, S Spain). *Schweiz. Miner. Petrogr. Mitt.* 84, 303-322.
- Gómez-Pugnaire, M.T., Rubatto, D., Fernández-Soler, J.M., Jabaloy, A., López Sánchez-Vizcaíno, V., González-Lodeiro, F., Galindo-Zaldívar, J., Padrón-Navarta, J.A., 2012. Late Variscan magmatism in the Nevado-Filábride Complex: U-Pb geochronologic evidence for the pre-Mesozoic nature of the deepest Betic complex (SE Spain). *Lithos* 146-147, 93-111.
- Gómez-Pugnaire, M.T., Ulmer, P., López Sánchez-Vizcaíno, V., 2000. Petrogenesis of the mafic igneous rocks of the Betic Cordilleras: A field, petrological and geochemical study. *Contrib. Mineral. Petrol.* 139, 436-457.
- González-Castillo, L., Galindo-Zaldívar, J., de Lacy, M.C., Borque, M., Martínez-Moreno, F., García-Armenteros, J., Gil, A.J., 2015. Active rollback in the Gibraltar Arc: Evidences from CGPS data in the Western Betic Cordillera. *Tectonophysics* 663, 310-321.
- Guillot, S., Hattori, K., Agard, P., Schwartz, S., Vidal, O., 2009. Exhumation processes in oceanic and continental subduction contexts: a review. In: Lallemand, S., Funicello, F. (eds). *Subduction Zone Dynamics*. Springer-Verlag, Berlin Heidelberg, pp 175-204.
- Gutiérrez-Alonso, G., Fernández-Suárez, J., Jeffries, T.E., Johnston, S.T., Pastor-Galán, D., Murphy, J.B., González, M.P.F., Gonzalo, J.C., 2011. Diachronous post-orogenic magmatism within a developing orocline in Iberia, European Variscides. *Tectonics* 30, TC5008.
- Hebeda, E., Boelrijk, N., Priem, H., Verdurmen, E., Verschure, R., Simon, O. 1980. Excess radiogenic Ar and undisturbed Rb-Sr systems in basic intrusives subjected to Alpine metamorphism in southeastern Spain. *Earth Planet. Sc. Lett.* 47, 81-90.

- Helmets, H., Voet, H.W., 1967. Regional extension of the Nevado-Filábride nappes in the eastern and central Sierra de los Filabres (Betic Cordilleras, SE Spain). *Proc. Kon. Ned. Akad. Wetensch. Ser. B* 70, 239-253.
- Hoernle, K., van den Bogaard, P., Duggen, S., Mocek, B., Garbe-Schönberg, D., 1999. Evidence for Miocene subduction beneath the Alboran Sea (Western Mediterranean) from $^{40}\text{Ar}/^{39}\text{Ar}$ age dating and the geochemistry of volcanic rocks from holes 977A and 978A. In: Zahn, R., Comas, M. C., Klaus, A. (eds). *Proceedings of the Ocean Drilling Project, Scientific Results 161*. Ocean Drilling Project, College Station, TX, pp 357-373.
- Hodges, K.V., Crowley, P.D., 1985. Error estimation and empirical geothermobarometry for pelitic systems. *Am. Mineral.* 70(7-8), 702-709.
- Holland, T.J.B., Powell, R., 1998. An internally consistent thermodynamic data set for phases of petrological interest. *J. Metamorph. Geol.* 16, 309-343.
- Holland, T., Powell, R., 2011. An improved and extended internally consistent thermodynamic dataset for phases of petrological interest, involving a new equation of state for solids. *J. Metamorph. Geol.* 29, 333-383.
- Hoskin, P.W.O., Schaltegger, U., 2003. The composition of zircon and igneous and metamorphic petrogenesis. In: Hanchar, J.M., Hoskin, P.W.O. (eds). *Zircon: Rev Mineral Geochem 53*, Mineralogical Society of America, Washington DC, pp 27-62.
- Houseman, G.A., McKenzie, D.P., Molnar, P., 1981. Convective instability of a thickened boundary layer and its relevance for the thermal evolution of continental convergence belts. *J. Geophys. Res.* 86, 6115-6132.
- Jabaloy, A., 1993. La estructura de la región occidental de la Sierra de los Filabres (Cordilleras Béticas). Thesis Univ. Granada. Colección monográfica Tierras del Sur. 2, 200 p.
- Jabaloy, A., Galindo-Zaldívar, J., González-Lodeiro, F., 1993. The Alpujarride-Nevado-Filábride extensional shear zone, Betic Cordilleras, SE Spain. *J. Struct. Geol.* 15, 555-569.
- Jabaloy, A., Gómez-Pugnaire, M.T., Padrón-Navarta, J.A., López Sánchez-Vizcaíno, V., Garrido, C.J., 2015. Subduction- and exhumation-related structures preserved in metaserpentinities and associated metasediments from the Nevado-Filábride Complex (Betic Cordillera, SE Spain). *Tectonophysics* 644-645, 40-57.
- Jabaloy, A., Talavera, C., Gómez-Pugnaire, M.T., López Sánchez-Vizcaíno, V., Vázquez-Vílchez, M., Rodríguez-Peces, M., Joyce Evans, N., 2018. U-Pb ages of detrital zircons from the Internal Betics: A key to deciphering paleogeographic provenance and tectono-stratigraphic evolution. *Lithos*, 318-319.
- Jamienson, R.A., 1991. P-T-t paths of collisional orogens. *Geol. Rundsch.* 80, 2, 321-332.
- Janots, E., Negro, F., Brunet, F., Goffé, B., Engi, M., Bouybaouène, M.L., 2006. Evolution of REE Mineralogy in HP-LT Metapelites of the Septide Complex, Rif, Morocco: Monazite Stability and Geochronology. *Lithos* 87, 214-234.
- Johnson, C., Harbury, N., Hurford, A. J., 1997. The role of extension in the Miocene denudation of the Nevado-Filábride-Complex, Betic Cordillera (SE Spain). *Tectonics* 16, 189-204.
- Jolivet, L., Faccenna, C., 2000. Mediterranean extension and the Africa-Eurasia collision. *Tectonics* 19, 1095-1109.
- Kelley, S., 2002. Excess argon in K-Ar and Ar-Ar geochronology. *Chem. Geol.* 188, 1-22.
- Kirchner, K.L., Behr, W.M., Loewy, S., Stockli, D.F., 2016. Early Miocene subduction in the western Mediterranean: Constraints from Rb-Sr multimineral isochron geochronology. *Geochem. Geophys. Geosyst.*, 17, 1842-1860.
- Kirkland, C.L., Strachan, R.A., Prave, A.R., 2008. Detrital zircon signature of the Moine Supergroup, Scotland: Contrasts and comparisons with other Neoproterozoic successions within the circum-North Atlantic region. *Precambrian Res.* 163, 332-350.
- Kohn, M.J., Spear, F.S., 1991. Error propagation for barometers; 2, Application to rocks. *Am. Mineral.* 76(1-2), 138-147.
- Kosler, J., Sylvester, P.J., 2003. Present trends and the future of zircon in U-Pb geochronology: laser ablation ICPMS. In: Hanchar, J.M., Hoskin, P.W.O. (eds). *Zircon: Rev Mineral Geochem 53*, Mineralogical Society of America. Washington DC, pp 243-275.

- Laborda-López, C., Aguirre, J., Stephen, K., Donovan, S.K., Navas-Parejo, P., Rodríguez, S. 2015. Fossil assemblages and biostratigraphy of metamorphic rocks of Nevado-Filábride Complex from the Águilas tectonic arc (SE Spain). *Spanish Journal of Palaeontology* 30(2), 275-292.
- Labord-López, C., López Sánchez-Vizcaíno, V., Marchesi, C., Gómez-Pugnaire, M.T., Garrido, C.J., Jabaloy-Sánchez, A., Padrón-Navarta, J.A., Hidas, K., 2018. High pressure metamorphism of rodingites during serpentinite dehydration (cerro del almirez, southern Spain): implications for the redox state in subduction zones. *J. Metamorph. Geol.* 36, 9, 1141-1173.
- Lafuste, M.L.J., Pavillon, M.J., 1976. Mise en évidence d'Eifélien daté au sein des terrains métamorphiques des zones internes des Cordillères bétiques. Intérêt de ce nouveau repère stratigraphique. *C. R. Acad. Sci. Paris* 283(2), 1015-1018.
- Lanari, P., Duisterhoef, E., 2019. Modeling Metamorphic Rocks using Equilibrium Thermodynamics and Internally Consistent Databases: Past Achievements, Problems and Perspectives. *Journal of Petrology*, DOI:10.1093/ptrology/egy105.
- Lanari, P., Engi, M., 2017. Local bulk composition effects on metamorphic mineral assemblages, *Rev. Mineral. Geochem.* 83, 55-102.
- Lanari, P., Giuntoli, F., Loury, C., Burn, M., Engi, M., 2017. An inverse modeling approach to obtain P-T conditions of metamorphic stages involving garnet growth and resorption. *Eur. J. Mineral.* 29, 181-199.
- Lanari, P., Riel, N., Guillot, S., Vidal, O., Schwartz, S., Pêcher, A., Hattori, K., 2013. Deciphering high-pressure metamorphism in collisional context using microprobe-mapping methods: application to the Stak eclogitic massif (NW Himalaya). *Geology* 41, 111-114.
- Lanari, P., Vho, A., Bovay, T., Airaghi, L., Centrella, S., 2018. Quantitative compositional mapping of mineral phases by electron probe micro-analyser. *Geol. Soc. London Spec. Publ.* 478, 29 March 2018.
- Lanari, P., Vidal, O., De Andrade, V., Dubacq, B., Lewin, E., Grosch, E.G., Schwartz, S., 2014. XMapTools: a MATLAB-B©-based program for electron microprobe X-ray image processing and geothermobarometry. *Comput. Geosci.*, 62, 227-240.
- Laurent, V., Lanari, P., Naïr, I., Augier, R., Lahfid, A., Jolivet, L., 2018. Exhumation of eclogite and blueschist (Cyclades, Greece): Pressure-temperature evolution determined by thermobarometry and garnet equilibrium modelling. *J. Metamorph. Geol.* 36, 769-798.
- Leech, M.L., Singh, S., Jain, A.K., Klempner, S.L., Manickavasagam, R.M., 2005. The onset of India–Asia continental collision: early, steep subduction required by the timing of UHP metamorphism in the western Himalaya. *Earth Planet. Sci. Lett.*, 234, 83-97.
- Li, B., Massonne, H. J., 2018. Two Tertiary metamorphic events recognized in high-pressure metapelites of the Nevado-Filábride Complex (Betic Cordillera, S Spain). *J. Metamorph. Geol.* 36, 603-630.
- Li, B., Massonne, H.J., 2018. Two Tertiary metamorphic events recognized in high-pressure metapelites of the Nevado-Filábride Complex (Betic Cordillera, S Spain). *J. Metamorph. Geol.* 36, 603-630.
- Linhout, K., Vissers, R.L.M., 1979. On the classification of tectonic units in the Nevado-Filábride Complex of the Northern Sierra de los Filabres, Betic Cordilleras, SE Spain. *Geol. Mijnbouw* 58, 1, 49-56.
- Litty, C., Lanari, P., Burn, M., Schlunegger, F. 2017. Climate-controlled shifts in sediment provenance inferred from detrital zircon ages, Western Peruvian Andes. *Geology* 45, 59-62.
- Lonergan, L., White, N., 1997. Origin of the Betic-Rif mountain belt. *Tectonics* 16, 504-522.
- López Sánchez-Vizcaíno, V., Rubatto, D., Gómez-Pugnaire, M.T., Tommsdorff, V., Müntener, O., 2001. Middle Miocene high-pressure metamorphism and fast exhumation of the Nevado-Filábride Complex, SE Spain. *Terra Nova* 13, 327-332.
- López Sánchez-Vizcaíno, V., Trommsdorff, V., Gómez-Pugnaire, M.T., Garrido, C.J., Müntener, O., Connolly, J.A.D., 2005. Petrology of titanian clinohumite and olivine at the high-pressure breakdown of antigorite serpentinite to chlorite harzburgite (Almirez Massif, S. Spain). *Contrib. Mineral. Petr.* 149, 627-646.

- Loury, C., Rolland, Y., Cenki-Tok, B., Lanari, P., Guillot, S., 2016. Late Paleozoic evolution of the South Tien Shan: Insights from P–T estimates and allanite geochronology on retrogressed eclogites (Chatkal range, Kyrgyzstan). *J. Geodyn.* 96, 62-80.
- Linnemann, U., Pereira, F., Jeffries, T.E., Drost, K., Gerdes, A., 2008. The Cadomian Orogeny and the opening of the Rheic Ocean: the diachrony of geotectonic processes constrained by La-ICP-MS U-Pb zircon dating (Ossa-Morna and Saxo-Thuringian Zones, Iberian and Bohemian Massifs). *Tectonophysics* 461, 21-43.
- Ludwig, K., 2008. User's Manual for Isoplot 3.6: A Geochronological Toolkit for Microsoft Excel, Berkeley Geochronology Centre. Spec. Pub. 4, 1-71.
- Mäkel, G.H., 1985. The geology of the Malaguide Complex and its bearing on the geodynamic evolution of the Betic-Rif orogen (southern Spain and northern Morocco). *GUA papers of Geology. Ser. 1*, 22, 263.
- Martínez, F.J., Dietsch, C., Aleinikoff, J., Cirés, J., Arboleya, M.L., Reche, J., Gómez-Gras, D., 2016. Provenance, age, and tectonic evolution of Variscan flysch, southeastern France and northeastern Spain, based on zircon geochronology. *Geol. Soc. Am. Bull.* 128, 842-859.
- Martínez-Martínez, J.M., 1986. Evolución tectono-metamórfica del Complejo Nevado-Filábride en el sector de unión entre Sierra Nevada y Sierra de los Filabres (Cordilleras Béticas). *Cuadernos de Geología. Universidad de Granada* 13, 1-194.
- Martínez-Martínez, J.M., Soto, J.I., Balanyá, J.C., 2002. Orthogonal folding of extensional detachments: Structure and origin of the Sierra Nevada elongated dome (Betics, SE Spain). *Tectonics* 21, 1-22.
- Martínez-Martínez, J.M., Torres-Ruiz, J., Pesquera, A., Gil-Crespo, P.P., 2010. Geological relationships and U-Pb zircon and $40\text{Ar}/39\text{Ar}$ tourmaline geochronology of gneisses and tourmalinites from the Nevado-Filábride Complex (western Sierra Nevada, Spain): tectonic implications. *Lithos* 119, 238-250.
- McNaughton, N.J., Rasmussen, B., Fletcher, I.R., 1999. SHRIMP Uranium-Lead Dating of Diagenetic Xenotime in Siliclastic Sedimentary Rocks. *Science* 285, 5424, 78-80.
- Meinhold, G., Morton, A.C., Avigad, D., 2013. New insights into peri-Gondwana paleogeography and the Gondwana super-fan system from detrital zircon U–Pb ages. *Gondwana Res.* 23, 2, 661-665.
- Merlet, C., 1994. An accurate computer correction program for quantitative electron-probe microanalysis. *Microchim. Acta* 114, 363-376.
- Monié, P., Galindo-Zaldívar, J., González-Lodeiro, F., Goffé, B., Jabaloy, A., 1991. $40\text{Ar}/39\text{Ar}$ geochronology of Alpine tectonism in the Betic Cordilleras (southern Spain). *J. Geol. Soc. London* 148, 288-297.
- Monié, P., Torres-Roldán, R-L., García-Casco, A., 1994. Cooling and exhumation of the western Betic Cordilleras, $40\text{Ar}/39\text{Ar}$ thermochronological constraints on a collapsed terrane. *Tectonophysics* 238, 353-79.
- Morley, C.K., 1993. Discussion of origins of hinterland basins to the Rif-Betic Cordillera and Carpathians. *Tectonophysics* 226, 359-376.
- Nance, R.D., Murphy, J.B., 1994. Contrasting basement isotopic signatures and the palinspastic restoration of peripheral orogens: example from the Neoproterozoic Avalonian–Cadomian belt. *Geology* 22, 617-620
- Nelder, J.A., Mead, R., 1965. A simplex method for function minimization. *Comput. J.* 7, 308-313.
- Nelson, D.R., 2001. An assessment of the determination of depositional ages for Precambrian clastic sedimentary rocks by U-Pb dating of detrital zircon. *Sediment. Geol.* 141-142, 37-60.
- Nieto, J.M., 1996. Petrología y geoquímica de los ortogneises del complejo del Mulhacén, Cordilleras Béticas. Universidad de Granada, Granada.
- Nieto, J.M., Puga, E., Monié, P., Díaz de Federico, A., Jagoutz, E., 1997. High-pressure metamorphism in metagranites and orthogneisses from the Mulhacén Complex (Betic Cordillera, Spain). *Terra Nova* 9 (Supl. 1), 22-23 abstract.
- Nijhuis, H.J., 1964. On the stratigraphy of the Nevado-Filábride units as exposed in the eastern Sierra de los Filabres (SE

- Spain). *Geol. Mijnbouw* 43, 321-325.
- O'Brien, P.J., 2001. Subduction followed by collision: Alpine and Himalayan examples. *Phys. Earth Planet. Inter.* 127, 277-291.
- Padrón-Navarta, J.A., Hermann, J., Garrido, C.J., López Sánchez-Vizcaíno, V., Gómez-Pugnaire, M.T., 2010. An experimental investigation of antigorite dehydration in natural silica-enriched serpentinite. *Contrib. Mineral. Petrol.* 159, 25-42.
- Pastor-Galán, D., Gutiérrez-Alonso, G., Murphy, J.B., Fernández-Suárez, J., Hoffman, M., Linnemann, U., 2013. Provenance analysis of the Paleozoic sequences of the northern Gondwana margin in NW Iberia: passive margin to Variscan collision and orocline development. *Gondwana Res.* 23, 1089-1103.
- Pereira, M.F., Chichorro, M., Johnston, S.T., Gutiérrez-Alonso, G., Silva, J.B., Linnemann, U., Hofmann, M., Drost, K., 2012. The missing Rheic Ocean magmatic arcs: provenance analysis of Late Paleozoic sedimentary clastic rocks of SW Iberia. *Gondwana Res.* 3-4 (22), 882-891.
- Pérez-Cáceres, I., Martínez-Poyatos, D., Simancas, J.F., Azor, A., 2017. Testing the Avalonian affinity of the South Portuguese Zone and the Neoproterozoic evolution of SW Iberia through detrital zircon populations. *Gondwana Res.* 42, 177-192.
- Petersen, K.D., Buck, W.R., 2015. Eduction, extension, and exhumation of ultrahigh-pressure rocks in metamorphic core complexes due to subduction initiation. *Geochem. Geophys.* 16, 2564-2581.
- Platt, J.P., Anczkiewicz, R., Soto, J.I., Kelley, S.P., Thirlwall, M., 2006. Early Miocene continental subduction and rapid exhumation in the western Mediterranean. *Geology* 34, 981-984.
- Platt, J.P., Behr, W.M., Johansen, K., Williams, R., 2013. The Betic-Rif Arc and its Orogenic Hinterland: A Review. *Annu. Rev. Earth Planet. Sci.* 41, 313-357.
- Platt, J.P., Behrmann, J.H., 1986. Structures and fabrics in a crustal-scale shear zone, Betic Cordillera, SE Spain. *J. Struct. Geol.* 8, 15-33.
- Platt, J.P., Kelley, S.P., Carter, A., Orozco, M., 2005. Timing of tectonic events in the Alpujarride Complex, Betic Cordillera, S. Spain. *J. Geol. Soc. London* 162, 451-462.
- Platt, J.P., Vissers, R.L.M., 1989. Extensional collapse of thickened continental lithosphere: A working hypothesis for the Alboran Sea and Gibraltar Arc. *Geology* 17, 540-543.
- Platt, J.P., Whitehouse, M.J., Kelley, S.P., Carter, A., Hollick, L., 2003. Simultaneous extensional exhumation across the Alboran Basin: Implications for the causes of late orogenic extension. *Geology* 31(3), 251-254.
- Priem, H.N.A., Boelrijk, N.A., Hebeda, E.H., Verschure, R.M., 1966. Isotopic age determinations on tourmaline granite-gneiss and a metagranite in the Eastern Betic Cordilleras, SE Spain. *Geol. Mijnbouw* 45, 184-187.
- Puga, E., 1971. Investigaciones petrológicas en Sierra Nevada Occidental. Thesis Univ. Granada, nº 133: 273 p.
- Puga, E., 1976. Investigaciones petrológicas en Sierra Nevada Occidental. Tesis Doctoral, Universidad de Granada. Secretariado de Publicaciones Univ. Granada, 269 p.
- Puga, E., 1977. Sur l'existence dans le complexe de la Sierra Nevada (Cordillère Bétique, Espagne du sud) d'éclogites et sur leur origine probable à partir d'une croûte océanique mésozoïque. *C. R. Acad. Sci.* 285, 1379-1382.
- Puga, E., Díaz de Federico, A., 1976. Pre-Alpine metamorphism in the Sierra Nevada Complex (Betic Cordilleras Spain). *Cuad. Geol. Univ. Granada* 7, 161-171.
- Puga, E., Díaz de Federico, A., 1978. Metamorfismo polifásico y deformaciones alpinas en el Complejo de Sierra Nevada (Cordillera Bética). Implicaciones geodinámicas. In: Reunión sobre la Geodinámica de las Cordilleras Béticas y el Mar de Alborán. Universidad de Granada, Secretariado de Publicaciones: Spain, 79-111.
- Puga, E., Díaz de Federico, A., Fanning, M., Nieto, J., Rodríguez Martínez-Conde, J., Díaz Puga, M., Lozano, J., Bianchini, G., Natali, C., Beccaluva, L., 2017. The Betic Ophiolites and the Mesozoic Evolution of the Western Tethys.

- Geosciences 7, 1-31.
- Puga, E., Díaz de Federico, A., Fontboté, J.M., 1974. Sobre la individualización y sistematización de las unidades profundas de la Zona Bética. *Estudios Geológicos* 30, 543-548.
- Puga, E., Díaz de Federico, A., Nieto, J.M., 2002. Tectonostratigraphic subdivision and petrological characterisation of the deepest complexes of the Betic zone: a review. *Geodin. Acta* 15, 23-43.
- Puga, E., Fanning, M., Díaz de Federico, A., Nieto, J.M., Beccaluva, L., Bianchini, G., 2011. Petrology, geochemistry and U-Pb geochronology of the Betic Ophiolites: Inferences for Pangaea break-up and birth of the westernmost Tethys Ocean. *Lithos* 124, 255-272.
- Puga, E., Fanning, M., Nieto, J.M., Díaz de Federico, A., 2003. Datación U-Pb con SHRIMP de circones de la eclogitas ofiolíticas del Complejo Mulhacén (Cordillera Bética). *Geogaceta* 33, 131-134.
- Puga, E., Fontboté, J.M., Martín-Vivaldi, J.L., 1975. Kyanite pseudomorphs after andalusite in polymetamorphic rocks of the Sierra Nevada (Betic Cordillera, Southern Spain). *Schweizerische Mineralogische und Petrographische Mitteilungen* 55, 227-241.
- Puga, E., Nieto, J.M., De Federico, A.D., 2000. Contrasting P-T paths in eclogites of the Betic Ophiolitic Association, Mulhacén Complex, southeastern Spain. *Can. Mineral.* 38, 1137-1161.
- Puga, E., Fanning, M., Nieto, J.M., Díaz de Federico, A., 2005. Recrystallization textures in zircon generated by ocean-floor and eclogite-facies metamorphism: a cathodoluminescence and U-Pb SHRIMP study, with constrains from REE elements. *Can. Mineral.* 43, 183-202.
- Regis, D., Rubatto, D., Darling, J., Cenki-Tok, B., Zucali, M., Engi, M., 2014. Multiple Metamorphic Stages within an Eclogite-facies Terrane (Sesia Zone, Western Alps) Revealed by Th-U-Pb Petrochronology. *J. Petrol.* 55 (7), 1429-1456.
- Rodríguez-Cañero, R., Jabaloy-Sánchez, A., Navas-Parejo, P., Martín-Algarra, A., 2018. Linking Palaeozoic palaeogeography of the Betic Cordillera to the Variscan Iberian Massif: new insight through the first conodonts of the Nevada-Filábride complex. *Int. J. Earth Sci.* 107 (5), 1791-1806.
- Rolland, Y., Lardeaux, J.M., Jolivet, L., 2012. Deciphering orogenic evolution. *J. Geodyn.* 5, 6-57.
- Rónadh, C., Coleman, D.S., Chokel, C.B., DeOreo, S.B., Wooden, J.L., Collins, A.S., De Waele, B., Kröner, A., 2004. Proterozoic Tectonostratigraphy and Paleogeography of Central Madagascar Derived from Detrital Zircon U-Pb Age Populations. *J. Geol.* 112, 4, 379-399.
- Rosell, O., Martí, A., Marcuello, À., Ledo, J., Queralt, P., Roca, E., Campanyà, J., 2011. Deep electrical resistivity structure of the northern Gibraltar Arc (western Mediterranean): evidence of lithospheric slab break-off. *Terra Nova* 23, 179-186.
- Rosenbaum, G., Lister, G.S., Duboz, C., 2002. Relative motions of Africa, Iberia and Europe during Alpine orogeny. *Tectonophysics* 359, 117-129.
- Royden, L.H., 1993. Evolution of retreating subduction boundaries formed during continental collision. *Tectonics* 12, 629-638.
- Rubatto, D., 2017. Zircon: the metamorphic mineral. *Rev. Mineral. Geochem.* 83, 261-295.
- Rubatto, D., 2002. Zircon trace element geochemistry: partitioning with garnet and the link between U-Pb ages and metamorphism. *Chem. Geol.* 184(1-2), 123-138.
- Rubatto, D., Regis, D., Hermann, J., Boston, K., Engi, M., Beltrando, M., McAlpine, S., 2011. Yo-Yo subduction recorded by accessory minerals in Italian Western Alps. *Nat. Geosci.* 4, 338-342.
- Rubatto, D., Scambelluri, M., 2003. U-Pb dating of magmatic zircon and metamorphic baddeleyite in the Ligurian eclogites (Voltri Massif, Western Alps). *Contrib. Mineral. Petrol.* 146(3), 341-355.
- Rubatto, D., Schaltegger, U., Lombardo, B., Colombo, F., Compagnoni, R. 2001. Complex Paleozoic magmatic and me-

- tamorphic evolution in the Argentermassif (Western Alps), resolved with U-Pb dating. *Schweiz Mineral. Petrogr. Mitt.* 81, 213-228.
- Ruiz-Cruz, M.D, Sanz de Galdeano, C., 2017. Genetic significance of zircon in orthogneisses from Sierra Nevada (Betic Cordillera, Spain). *Mineral. Mag.* 81(1), 77-101.
- Ruiz-Cruz, M.D., Sanz de Galdeano, C., Santamaría, A., 2015. Petrology and thermobarometric estimates for metasediments, orthogneisses, and eclogites from the Nevado-Filábride Complex in the Western Sierra Nevada (Betic Cordillera, Spain). *Can. Mineral.* 53 (6), 1083-1107.
- Sánchez Martínez, S., De la Horra, R., Arenas, R., Gerdes, A., Galán-Abellán, A.B., López- Gómez, J., Barrenechea, J.F., Arche, A., 2012. U-Pb ages of detrital zircons from the Permo-Triassic series of the Iberian ranges: a record of variable provenance during rift propagation. *J. Geol.* 120, 135-154.
- Sánchez-Rodríguez, L., Gebauer, D., 2000. Mesozoic formation of pyroxenites and gabbros in the Ronda area (southern Spain), followed by Early Miocene subduction metamorphism and emplacement into the middle crust: U-Pb sensitive high-resolution ion microprobe dating of zircon. *Tectonophysics* 316, 19-44.
- Santamaría-López, A., Sanz de Galdeano, C., 2018. SHRIMP U-Pb detrital zircon dating to check subdivisions in metamorphic complexes: a case of study in the Nevado-Filábride complex (Betic Cordillera, Spain). *Int. J. Earth Sci.* 107(7), 2539-2552.
- Sanz de Galdeano, C., 1990. Geologic evolution of the Betic Cordilleras in the Western Mediterranean, Miocene to the present. *Tectonophysics* 172, 107-119.
- Sanz de Galdeano, C., El Kadiri, K., Simancas, F., Rachid, H., López-Garrido, A. C., El Mrihi, A., Chalouan, A., 2006. Paleogeographical reconstruction of the Malaguide-Ghomaride Complex (Internal Betic-Rifian Zone) based on Carboniferous granitoid pebble provenance. *Geol. Carpath.* 57, 327-336.
- Sanz de Galdeano, C., López-Garrido, A.C., 1999. Estratigrafía y estructura de las unidades alpujarrides en el borde occidental de Sierra Nevada (Granada, España). *J. Geol. Soc. Spain.* 12(2), 187-198.
- Sanz de Galdeano, C., López-Garrido, A.C., 2016. The Nevado-Filábride Complex in the western part of Sierra de los Filabres (Betic Internal Zone). Structure and lithological succession. *Boletín Geológico y Minero* 127, 4, 823-836.
- Sanz de Galdeano, C., López-Garrido, A.C., Santamaría-López, A., 2016. Major scale structure of the marbles situated between Cóbdar and Macael (Nevado-Filábride Complex, Betic Cordillera, Almería province, Spain), and general stratigraphic arrangement. *J. Geol. Soc. Spain.* 29, 2, 107-116.
- Sanz de Galdeano, C., Santamaría-López, A., 2019. The lithological sequence of the Nevado-Filábride Complex (Betic Internal Zone) in the sierras Nevada and Filabres. *Revista de la Sociedad Geológica de España*, 32 (1): in press.
- Schoene, B., 2014. U-Th-Pb geochronology. In: Holland, H.D., Turekian, K.K. (eds). *Treatise on Geochemistry*. Elsevier, Oxford, pp 341-378.
- Simancas, J.F., 2018. A reappraisal of the Alpine structure of the Alpujarride Complex in the Betic Cordillera: Interplay of shortening and extension in the westernmost Mediterranean. *J. Struct. Geol.* 115, 231-242.
- Sláma, J., Košler, J., Condon, D.J., Crowley, J.L., Gerdes, A., Hanchar, J.M., Horstwood, M.S., Morris, G.A., Nasdala, L., Norberg, N., 2008. Plešovice zircon – a new natural reference material for U-Pb and Hf isotopic microanalysis. *Chem. Geol.* 249, 1-35.
- Sosson, M., Morillon, A.C., Bourgois, J., Feraud, G., Poupeau, G., Saint-Marc, P., 1998. Late exhumation stages of the Alpujarride Complex (western Betic Cordilleras, Spain); new thermochronological and structural data on Los Reales and Ojen nappes. *Tectonophysics* 285, 253-73.
- Spear, F.S., 1988. Metamorphic fractional crystallization and internal metasomatism by diffusional homogenization of zoned garnets. *Contributions to Mineralogy and Petrology* 99(4), 507-517.
- Spakman, W., Wortel, R., 2004. A Tomographic View on Western Mediterranean Geodynamics. In: Cavazza, W., Roure, F.M., Spakman, W., Stampfli, G.M., Ziegler, P.A. (eds). *The TRANSMED Atlas. The Mediterranean Region from Crust to Mantle*. Springer, Berlin, pp 31-52.

- Stampfli, G.M., 2000. Tethyan oceans. In: Bozkurt, E., Winchester, J.A., Piper, J.D.A. (eds). *Tectonics and Magmatism in Turkey and the Surrounding Area*. Geol. Soc. London Spec. Publ. 173, 1-23.
- Talavera, C., Montero, P., Martínez Poyatos, D., Williams, I.S., 2012. Ediacaran to Lower Ordovician age for rocks ascribed to the Schist-Graywacke Complex (Iberian Massif, Spain): Evidence from detrital zircon SHRIMP U-Pb geochronology. *Gondwana Res.* 22, 928-942.
- Tendero, J.A., Martín-Algarra, A., Puga, E., Díaz de Federico, A., 1993. Lithostratigraphie des métasédiments de l'association ophiolitique Nevado-Filábride (SE Espagne) et mise en évidence d'objets ankéritiques évocant des foraminifères planctoniques du Crétacé: conséquences paléogéographiques. *C. R. Acad. Sci. Paris* 316, 1115-1122.
- Thiebot, E., Gutscher, M.A., 2006. The Gibraltar Arc seismogenic zone (part 1): constraints on a shallow east dipping fault plane source for the 1755 Lisbon earthquake provided by seismic data, gravity and thermal modeling. *Tectonophysics* 426, 135-152.
- Thompson, A.B., England, P.C., 1984. Pressure temperature time paths of regional metamorphism. 2. Their inference and interpretation using mineral assemblages in metamorphic rocks. *J. Petrol.* 25, 929-955.
- Thomson, K.D., Stockli, D.F., Clark, J.D., Puigdefàbrega, C., Fildani, A., 2017. Detrital zircon (U-Th)/(He-Pb) double-dating constraints on provenance and foreland basin evolution of the Ainsa Basin, south-central Pyrenees, Spain. *Tectonics* 36, 1352-1375.
- Tinkham, D.K., Ghent, E.D., 2005. Estimating P-T conditions of garnet growth with isochemical phase-diagrams sections and the problem of effective bulk-composition. *Can. Mineral.* 43(1), 35-50.
- Vai, G.B., Boriani, A., Rivalenti, G., Sassi, F.P., 1984. Catena ercinica e Paleozoico nelle Alpi Meridionali. *Cento Anni di Geologia Italiana*. Vol. Giub. I. Centenario SGI, Bologna, pp. 133-154.
- Valle Aguado, B.V., Azevedo, M.R., Schaltegger, U., Catalan, J.R.M., Nolan, J., 2005. U-Pb zircon and monazite geochronology of Variscan magmatism related to syn-convergence extension in Central Northern Portugal. *Lithos* 82, 169-184.
- Van Bemmelen, R.W., 1927. Bijdrage tot de bouw der betische ketens in de Provincie Granada, Spanje. Thesis Tech. Univ. Delft p. 176.
- van Hinsbergen, D.J.J., Vissers, R.L.M., Spakman, W., 2014. Origin and consequences of western Mediterranean subduction, rollback, and slab segmentation. *Tectonics* 33, 393-419.
- Vera, J.A., Martín-Algarra, A., 2004. Cordillera Bética. In: Vera, J.M. (ed). *Geología de España*. IGME-Sociedad Geológica de España, Madrid, pp 345-464.
- Vergés, J., Fernández, M., 2012. Tethys-Atlantic interaction along the Iberia-Africa plate boundary: The Betic-Rif orogenic system. *Tectonophysics* 579, 144-172.
- Vermeesch, P., 2012. On the visualization of detrital age distributions. *Chem. Geol.* 312-313, 190-94.
- Vissers, R.L.M., 1977. Data on the tectonic and metamorphic evolution of the central Sierra de los Filabres, SE Spain. *Geologische Rundschau* 66, 1, 81-90.
- Vissers, R.L.M., 1981. A structural study of the Central Sierra de los Filabres (Betic Zone, SE Spain), with emphasis on deformational process and their relation to the Alpine Metamorphism. *GUA Papers on Geology, Series 1*, 15, 154 pp.
- Vissers, R.L.M., 2012. Extension in a convergent tectonic setting: a lithospheric view on the Alboran system of SW Europe. *Geol. Belg.* 15(1-2), 53-72.
- Vissers, R.L.M., Platt, J.P., van der Wal, D., 1995. Late orogenic extension of the Betic Cordillera and the Alborán Domain: a lithospheric view. *Tectonics* 14, 786-803.
- Warren, C.J. 2013. Exhumation of (ultra-)high-pressure terranes: concepts and mechanisms. *Solid Earth* 4, 75-92.
- Williams, J.R., Platt, J.P., 2018. A new structural and kinematic framework for the Alborán Domain (Betic-Rif arc, western Mediterranean orogenic system). *J. Geol. Soc. London* 175 (3), 465-496.

- Worley, B., Powell, R., 2000. High-precision relative thermobarometry: theory and a worked example. *J. Metamorph. Geol.* 18(1), 91-101.
- Wortel, M., Spakman, W., 2000. Subduction and slab detachment in the Mediterranean- Carpathian region. *Science* 290, 1910-1917.
- Wu, Y., Zheng, Y., 2004. Genesis of zircon and its constraints on interpretation of U-Pb age. *Chinese Sci. Bull.* 49, 15, 1554-1569.
- Xu, W.-C., Zhang, H.-F., Parrish, R., Harris, N., Guo, L., Yuan, H.-L., 2010. Timing of granulite-facies metamorphism in the eastern Himalayan syntaxis and its tectonic implications. *Geology* 485 (1-4), 231–244.
- Yakymchuk, C., Clark, C., White, R., 2017. Phase Relations, Reaction Sequences and Petrochronology: Methods and Applications. *Rev. Mineral. Geochem.* 83, 13-53.
- Zeck, H., 1996. Betic-Rif orogeny: Subduction of Mesozoic Tethys lithosphere under eastward drifting Iberia, slab detachment shortly before 22 Ma, and subsequent uplift and extensional tectonics. *Tectonophysics* 254, 1-16.
- Zeck, H.P., Whitehouse, M.J., 2002. Repeated age resetting in zircons from Hercynian–Alpine polymetamorphic schists (Betic–Rif tectonic belt, S. Spain)—a U–Th–Pb ion microprobe study. *Chem. Geol.* 182, 2-4, 275-292.

Appendix

Appendix 1 UTM coordinates of studied samples (chapters 5 and 6).

Sample	Formation	Band: 30S		Area of study
SF-1	Dark schists Fm	464424	4106792	Peñones de San Francisco (western part of Sierra Nevada)
SF-2	Schists and marbles Fm	462710	4107880	
10.1	Dark schists Fm	465766	4105274	
16.8	Tahal Fm	462668	4107906	
16.16	Schists and marbles Fm	462705	4107860	
RA-0	Tahal Fm	501530	4096400	La Ragua (Central part of Sierra Nevada)
RA-1	Dark schists Fm	498284	4103669	
RA-2	Dark schists Fm	500104	4099243	
RA-3	Tahal Fm	501534	4096508	
VE-1	Dark schists Fm	551198	4111193	Velefique (Central part of Sierra de los Filabres)
VE-2	Dark schists Fm	552063	4118932	
VE-3	Tahal Fm	551490	4121466	

Appendix 2 U-Th-Pb Geochron analytical procedure used in the SHRIMP IIe/mc instrument of the IBERSIMS lab (UGR).

Zircon grains were separated using panning and magnetic techniques. Hand-picked zircons from the studied samples, several grains of the TEMORA-1 standard (for isotope ratios; Black et al., 2003), one grain of the SL13 zircon standard (for U concentration, Claoué-Long et al., 1995), plus a few grains of the REG zircon (plenty of common lead, for calibrating the masses) were cast on a 3.5 cm diameter epoxy mount (megamount), polished and documented using optical (reflected and transmitted light) and scanning electron microscopy (secondary electrons and cathodoluminescence). After extensive cleaning, mounts were coated with ultra-pure gold (8-10 nanometers-thick) and inserted into the SHRIMP for analysis.

The analytical method followed that described by Williams and Claesson (1987). Each selected spot was rastered with the primary beam for 120 s prior to analysis, and then analysed 6 scans, following the isotope peak sequence $^{196}\text{Zr}2\text{O}$, ^{204}Pb , $^{204.1}$ background,

^{206}Pb , ^{207}Pb , ^{208}Pb , ^{238}U , ^{248}ThO , ^{254}UO . Every peak of every scan was measured sequentially 10 times with the following total counting times per scan: 2 s for mass 196; 5 s for masses 238, 248, and 254; 15 s for masses 204, 206, and 208; and 20 s for mass 207. The primary beam, composed of single charged, double $^{16}\text{O}^{\text{ions}}$, was set to an intensity of about 5 nA, with a 120 microns Kohler aperture, which generates 17 x 20 micron elliptical spots on the target. The secondary beam exit slit was fixed at 80 microns, achieving a resolution of about 5000 at 1% peak height.

All calibration procedures were performed on the standards included on the same mount. Mass calibration was done on the REG zircon (ca. 2.5 Ga, very high U, Th and common lead content). Every analytical session started measuring the SL13 zircon, which was used as a concentration standard (238 ppm U). The TEMORA-1 zircon (416.8 ± 1.1 Ma), used as isotope ratios standard, was then measured every 4 unknowns.

Data reduction was done with the SHRIMPTOOLS software (available from www.ugr.es/~fbea), specifically developed for IBERSIMS by F. Bea. This software is a new implementation of the original PRAWN software developed for the SHRIMP, and has been extensively checked against PRAWN and Ludwig's SQUID. SHRIMPTOOLS is platform-independent and runs on any Windows, Mac or Unix computer regardless of language, time, and date system settings. It has been written in the programming language of the STATA commercial package which implements powerful algorithms for robust regression, outlier detection and time-series analysis. The software calculates the intensity of each measured isotope in two steps. First, it uses the STATA letter-value display algorithm to find outliers in the ten replicates measured in each peak during each scan, discarding them and averaging the rest. Then, the blank, measured at 204.1 mass is subtracted from each peak. This may produce negative values in mass 204 when it recorded next to zero counts. Once normalized to the SBM measurements, the software calculates the 204/206, 207/206, 208/206, 254/238 ratios using Dodson's (1978) double linear interpolation method. The 206/238, 206/195, 238/195, and 248/254 ratios are calculated by dividing the value at the mid-time of the analysis of each isotope calculated from the robust regression lines of the peak average of each scan vs the time at which it was measured. Errors for Dodson interpolated ratios are calculated as the standard error of the (scans-1) interpolations for each ratio. Errors for the isotope ratios calcu-

lated by regression result from propagating accordingly the standard error of the linear prediction at the mid-point of the analysis. $^{206}\text{Pb}/^{238}\text{U}$ is calculated from the measured $^{206}\text{Pb}+^{238}\text{U}$ and $\text{UO}+/\text{U}+$ following the method described by Williams (1998). The error reported for $^{206}\text{Pb}/^{238}\text{U}$ includes (1) the error in $\text{UO}+/\text{U}+$ (2) the error in the regression line $\ln(\text{UO}+/\text{U}+)$ vs $\ln(^{206}\text{Pb}/^{238}\text{U})$ (3) the standard error in the replicate measurements of the TEMORA zircon. For high-U zircons ($\text{U} > 2500$ ppm) $^{206}\text{Pb}/^{238}\text{U}$ is further corrected using the algorithm of Williams and Hergt (2000). Though seldom necessary, the software also permits correction for instrumental drift with time using the sequence of replicate measurements of the TEMORA zircon.

References

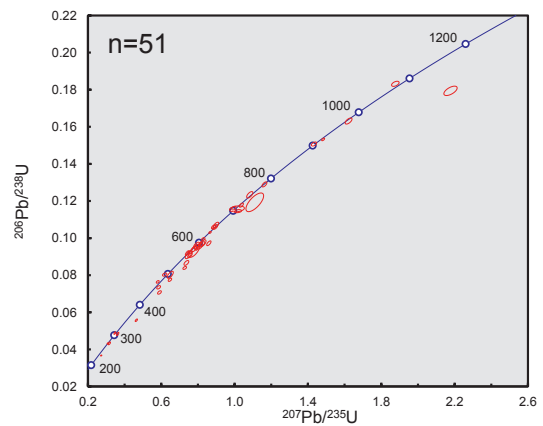
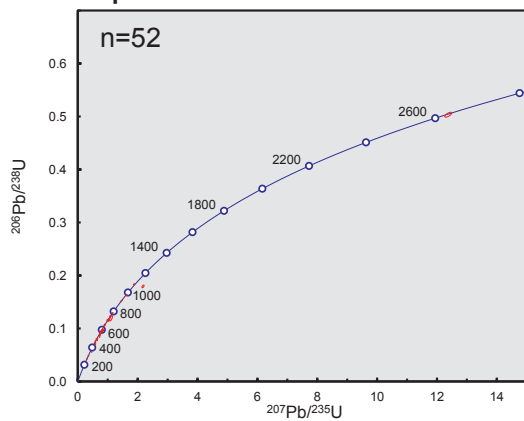
- Black, L. P., Kamo, S. L., Allen, C. M., Aleinikoff, J. A., Davis, D. W., Korsch, J. R., Foudolis, C., 2003. TEMORA 1: a new zircon standard for Phanerozoic U-Pb geochronology. *Chemical Geology* 200, 155-170.
- Claoué-Long, J. C., Compston, W., Roberts, J., Fanning, C. M. (1995). Two Carboniferous ages: a comparison of SHRIMP zircon dating with conventional zircon ages and $^{40}\text{Ar}/^{39}\text{Ar}$ analysis. In: Berggren, W. A., Kent, D. V., Aubry, M. P., Hardenbol, J. (Eds.), *Geochronology Time Scales and Global Stratigraphic Correlation*. SEPM (Society for Sedimentary Geology) Special Publication No. 4. (pp. 3-21).
- Dodson, M. H. (1978) A linear method for second-degree interpolation in cyclical data collection. *Journal of Physics E: Scientific Instruments* 11, 296.
- Williams, I. S., & Claesson, S. (1987). Isotopic evidence for the Precambrian provenance and Caledonian metamorphism of high grade paragneisses from the Seve Nappes, Scandinavian Caledonides. II: Ion microprobe zircon U-Th-Pb. *Contribution to Mineralogy and Petrology*, 97, 205-217
- Williams, I. S., Hergt, J. M. (2000). U-Pb dating of Tasmanian dolerites: a cautionary tale of SHRIMP analysis of high-U zircon. In: Woodhead, J. D., Hergt, J. M., Noble, W. P. (Eds.), *Beyond 2000: New Frontiers in Isotope Geoscience*, Lorne, 2000; Abstracts and Proceedings. (pp. 185-188).
- Williams, I. S. (1998). U-Th-Pb Geochronology by Ion Microprobe. In: McKibben, M. A., Shanks III, W. C., Ridley, W. I. (Eds.), *Applications of microanalytical techniques to understanding mineralizing processes*. *Reviews in Economic Geology* v.7. (pp. 1-35).

Appendix 3 Optical and cathodoluminescence images of the studied zircons (chapter 5) can be found in the digital version of this Ph.D. Thesis (CD). Circles and numeric codes correspond to selected points analyzed in the SHRIMP sessions.

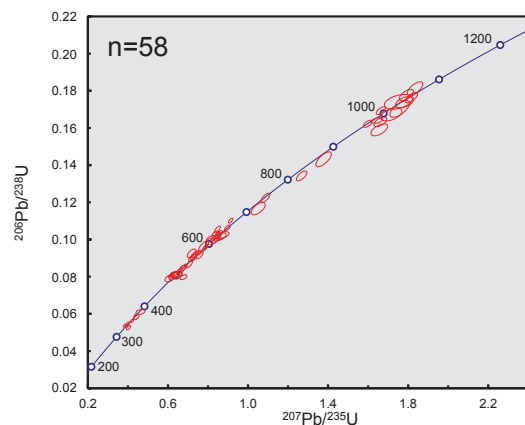
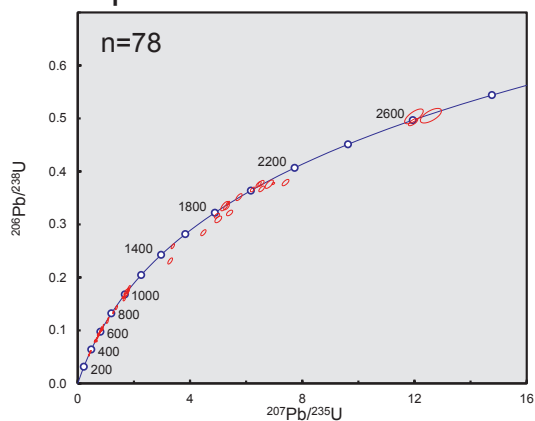
Appendix 4 Tables comprising the SHRIMP U-Th-Pb analytical data of zircons (chapter 5) can be found in the digital version of this Ph.D. Thesis (CD).

Appendix 5 Wetherill plots of the SHRIMP U-Pb detrital zircon dating (chapter 5).

Sample SF-2

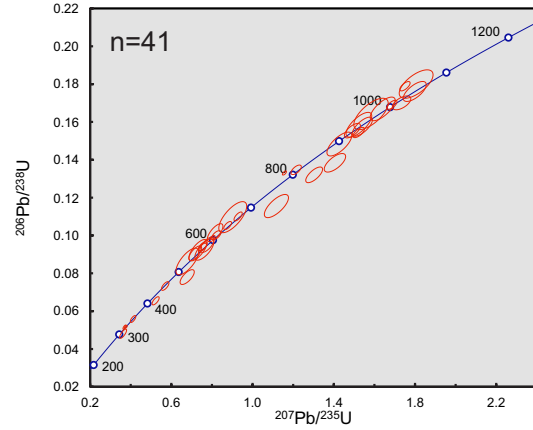
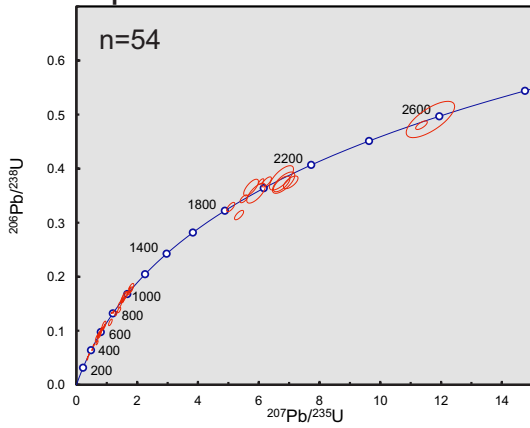


Sample SF-1

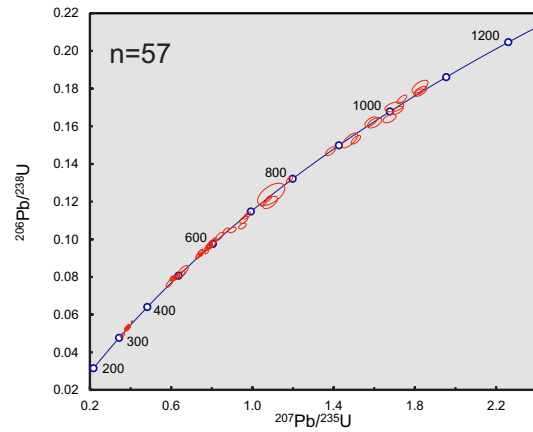
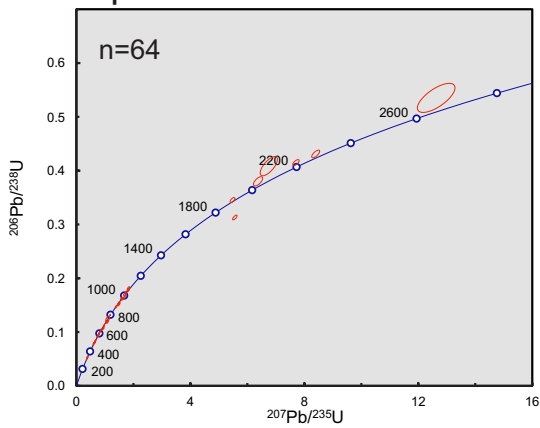


Appendix 5 (cont.)

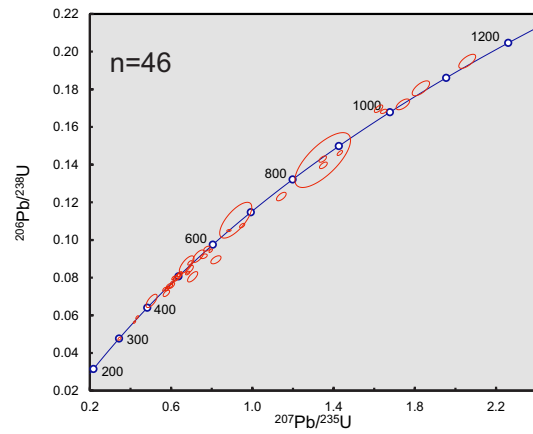
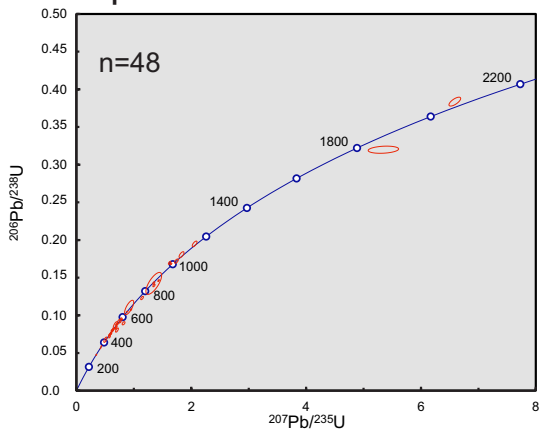
Sample RA-3



Sample RA-2

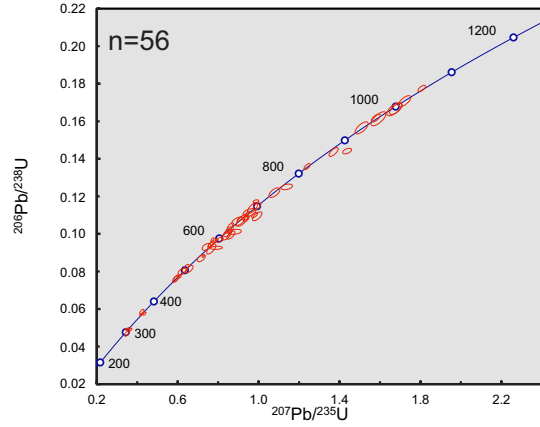
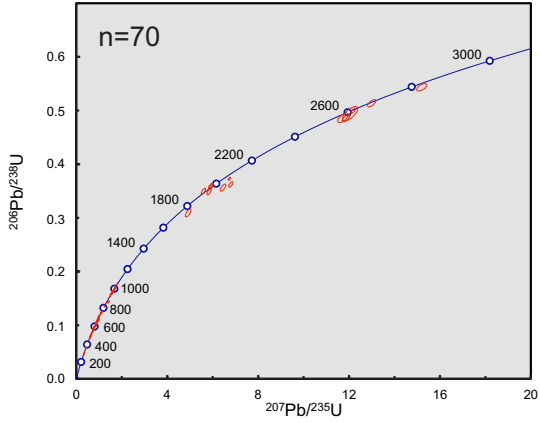


Sample RA-1

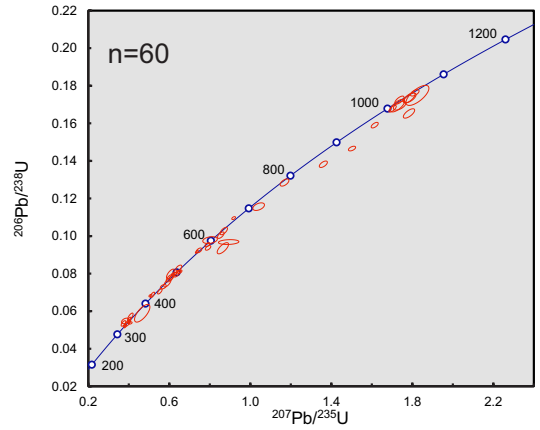
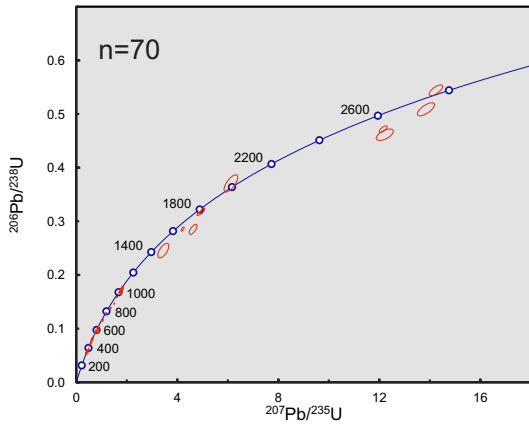


Appendix 5 (cont.)

Sample VE-3



Sample VE-2



Sample VE-1

